Dissertation

submitted to the
Combined Faculty of Mathematics, Engineering and Natural Sciences
of Heidelberg University, Germany
for the degree of

Doctor of Natural Sciences

put forward by

M.Sc. Jacqueline Fedyk

born in Solingen, Germany

Oral examination:

June 12th, 2023

On the Theory of double ICD
and
Applications of ICD

Referees: Prof. Dr. Dr. h.c. mult. Lorenz S. Cederbaum
Prof. Dr. Jochen Schirmer

Abstract

Interatomic or intermolecular Coulombic decay (ICD) is an efficient relaxation pathway on the femtosecond timescale, where after inner-valence ionization of an atom or molecule, the initial vacancy is filled by an outer-valence electron and the excess energy is transferred radiationlessly to its neighbor, leading to its ionization. In this thesis, ICD-related phenomena are studied. Therefore, the work is divided into two main parts. Part I treats the new decay channel double ICD (dICD), where after the relaxation of the system, the excess energy exceeds the double ionization threshold of the neighboring species, resulting in its double ionization. We derive an asymptotic and perturbative expression for the dICD decay width as an indicator of efficiency. In Part II, nuclear dynamics during ICD and pre-ICD in NeKr and Ar_2 dimers are investigated focusing on different aspects. In pre-ICD, the excess energy is only sufficient for the excitation of the neighboring atom or molecule and additional energy has to be provided for its ionization. While the study about NeKr dimers undergoing ICD mostly concentrates on interference effects, the main goal of the pre-ICD in Ar_2 dimers study is to understand the nuclear motions and their appearance in the corresponding spectrum.

Kurzfassung

Der interatomare oder intermolekulare Coulomb-Zerfall (ICD) ist ein effizienter Zerfallskanal auf der Femtosekunden-Zeitskala, bei dem nach der inneren Valenzschalen-Ionisation eines Atoms oder Moleküls die entstandene Fehlstelle durch ein Elektron der äußeren Valenzschale gefüllt und die dabei frei werdende Energie strahlungslos auf den Nachbarn übertragen wird, was zu seiner Ionisation führt. In dieser Doktorarbeit werden ICD-bezogene Phänomene untersucht. Daher gliedert sich die Arbeit in zwei Hauptteile. Teil I behandelt den neuen Zerfallskanal Doppel-ICD (dICD), bei dem nach der Abregung des Systems die überschüssige Energie die Doppelionisationsschwelle der benachbarten Spezies übersteigt, was zu derer Doppelionisation führt. Wir leiten einen asymptotischen und störungstheoretischen Ausdruck für die dICD-Zerfallsbreite als Indikator für die Effizienz her. In Teil II wird die Kerndynamik während ICD und Prä-ICD in NeKr- und Ar_2-Dimeren auf verschiedene Aspekte untersucht. Bei Prä-ICD reicht die überschüssige Energie nur zur Anregung des benachbarten Atoms oder Moleküls aus und es muss zusätzliche Energie für dessen Ionisation aufgebracht werden. Während sich die Studie über ICD im NeKr-Dimere hauptsächlich auf Interferenzeffekte konzentriert, ist das Hauptziel der Studie über Prä-ICD in Ar_2-Dimeren die Kernbewegungen und ihr Auftreten im dazugehörigen Spektrum zu verstehen.

Contents

Appendix

Chapter 1

Introduction

Interatomic or intermolecular Coulombic decay (ICD) was originally predicted in 1997, see Ref. [1], as a highly efficient electronic energy-transfer mechanism in weakly bound systems on a femtosecond timescale, where after inner-valence ionization of an atom or molecule, the initial vacancy of the ion is filled by an outer-valence electron and the emerging excess energy is transferred radiationlessly by dipole-dipole coupling to a neighboring atom or molecule resulting in its ionization. After the ICD process, two positively charged ions with outer-valence vacancies remain. As they repel each other, the system usually disintegrates in a Coulomb explosion. A few years after its theoretical prediction, ICD was also experimentally confirmed in neon dimers and clusters [2–4]. Since then, the process has been intensively studied, establishing ICD over the last two decades as an important relaxation pathway in atomic and molecular clusters, see Refs. [5–8]. Thereby, the work interests ranged from ICD in weakly bound systems like the He dimer [9, 10], to other van der Waals clusters like Ne_n [2–4, 11–14], NeAr [15–19], ArKr [20] and NeHe [21–23], hydrogen-bonded clusters of H_2O and HF [1, 24–27], biological relevant systems [28–30], as well as quantum dots [31–34] and cavities [35]. Additionally, ICD inspired the investigations of further related mechanisms as resonant ICD (rICD) [36–38], ICD from electronic to vibrational states [39], ICD after Auger decay [40–46], electron transfer mediated decay (ETMD) [15, 45, 47–50] and interatomic Coulomb electron capture (ICEC) [51–57]. It was also demonstrated that the process can be initiated by ion [58–60] and electron impact [61–63]. In this thesis, we add to this body of work the theory development of double ICD [64] as well as studies regarding nuclear dynamics in the NeKr and the Ar_2 dimers undergoing ICD [65] and pre-ICD [66], respectively.

These further investigations of ICD-related phenomena divide the work into two parts. Part I is about double ionization by ICD (dICD) [64, 67–70], where if the excess energy of the initially ionized atom or molecule exceeds the double ionization threshold of its neighbor, the latter emits two electrons. We developed a theory to describe and investigate this new decay channel by deriving an asymptotic and perturbative expression for the dICD decay width. The here shown results are taken from Ref. [64]. In Part II, nuclear dynamics of dimers, which undergo ICD and pre-ICD, are studied. Therefore, photoelectron (PE), ICD-electron, and kinetic-energy-release

(KER) spectra were computed and analyzed. The presented methods and the discussion about nuclear dynamics during ICD and pre-ICD in NeKr and Ar_2 are reported in Refs. [65] and [66].

Beginning with Part I, among the processes which lead to correlated emission of two electrons after absorption of one photon single-photon double-ionization (SPDI) [71–75] and double Auger (dA) decay [76–80] are the best known. In the former, the two electrons escape directly following the photon absorption; in the latter, they escape in the decay of a metastable core-ionized state. The concerted double electron emission is primarily due to the electron correlation in the final ionized state [72]. It is common to describe the effect of correlation in terms of shake-off and knock-out mechanisms [72, 73, 81]. In the shake-off mechanism, the first electron is emitted rapidly. The sudden change in the potential is felt by the remaining electrons, and their subsequent relaxation leads to the ejection of the second electron. Accordingly, the signature of the shake-off process in the electron kinetic-energy spectrum appears as peaks at high (first electron) and low (second electron) electron energies [80, 82]. In contrast, the knock-out mechanism can be seen as an impact ionization, whereby the first emitted electron collides inelastically with a bound electron as it exits the collision region, with the result that both electrons are ejected into the continuum. Its signature in the electron spectrum is flatter, although it shows a preference for one slow and one fast electron peak.

In single-photon double-ionization, the knock-out dominates at photon energies near the double-ionization threshold [71, 81, 83], while the shake-off mechanism becomes dominant for high photon energies. Both mechanisms also appear in the double Auger decay, and it has been shown that the knock-out mechanism dominates [77–79]. The effectiveness of the process can be gauged by comparing it to the single ionization analogue. The ratios of the single-photon double-ionization to single-ionization cross sections usually amount to a few percentage points near the double-ionization threshold [75, 81, 84–86]. The branching ratios of the double to the normal Auger decay [77, 78, 83, 87, 88] are comparable to the typical SPDI to single ionization ratios. For large photon energies over 200 eV, these ratios can reach values up to 80 % in some systems [83, 89].

In both of these processes, electron emission occurs at the atom or molecule which absorbs the photon. However, a non-local process was suggested [67], whereby the absorption of a photon and emission of two electrons occur on different weakly interacting species, specifically a guest atom and a C_{60} cage of an endohedral fullerene. For example, removing a 2p electron of Mg in Mg@C_{60} creates an electronically unstable state. As a result, C_{60} can be ionized in an electronic-energy transfer between the excited $Mg^+(2p^{-1})$ ion and the carbon cage. For single ionization, this process is known as interatomic Coulombic decay (ICD) [1, 5–8]. However, since the transferred energy in this example is larger than the double-ionization threshold of C_{60}, two electrons can also be emitted into the continuum in a process, which was named double interatomic (intermolecular) Coulombic decay (dICD) [67].

The dICD process is formally related to both the double Auger decay and the single-photon double-ionization processes. As in the double Auger decay, the initial state of the ICD process is a resonance state, whose decay leads to double-electron emission. In the above example of Mg@C_{60}, the magnesium atom is initially ionized, forming the metastable $Mg^+(2p^{-1})$. In the presence of C_{60}, this ion can transfer its excess energy (by relaxing to $Mg^+(3s^{-1})$) to the fullerene cage and doubly ionize it. ICD involves radiationless energy transfer between the excited species and its neighbor, which at large distances between them can be described as the transfer of a virtual photon [90–93]. Since the absorption of the virtual photon by the neighbor leads to the emission of two electrons, dICD is related to SDPI. As a result, the discussion of the dICD process can also be carried out in terms of the knock-out, shake-off, and the less efficient ground-state-correlation mechanisms.

The dICD process was recently demonstrated in experiments on He droplets doped with alkali dimers [68]. The droplets were irradiated by XUV photons, which led to the photoexcitation of the He atoms. The energy released in the subsequent relaxation of He was transferred to the dimers attached to the droplet's surface, resulting in their ionization. The electron spectra display peaks at lower and higher electron energy, which have the characteristic U-shape profile and indicate that two electrons are emitted in concert in the interatomic decay step. Apart from demonstrating the existence of dICD, the experiment indicates that its efficiency is comparable to that of ICD so that the dICD to ICD branching ratio is much larger than the branching ratios commonly seen for the double Auger or SPDI processes.

Recently, resonant dICD in $Li^{2+}He$ was investigated theoretically [69]. Resonant photoexcitation of Li^{2+} ($1s \rightarrow 2p$) leads to the radiationless transfer of its excess energy (91.8 eV) to the neighboring atomic He, which is doubly ionized. dICD was shown to be more efficient than SPDI, and for random interatomic orientation, it was found that the averaged angular distribution of resonant dICD qualitatively differs from the one of SPDI.

Recently, triple ionization of benzene trimers by dICD, and their subsequent fragmentation were tracked using triple-coincidence ion momentum spectroscopy, see Ref. [70]. After electron collision, one of the benzene molecules is C2s ionized $C_6H_6^{+*}(C2s^{-1})(C_6H_6)_2$. Afterward, the inner-valence vacancy is filled by an outer-valence electron, and the excess energy is utilized to singly ionize the two neighboring benzene molecules. Because the three benzene molecules repel each other, the system undergoes Coulomb explosion, resulting in the fragmentation of the benzene trimer $C_6H_6^+$ $C_6H_6^+$ $C_6H_6^+$. Ab-initio calculations of the ionization cross sections after electron impact demonstrated that the dICD decay channel is an important one.

Motivated by these results of [67–70], we investigate, in the present work, the general theory of the dICD process and put it in relation to the common ICD process. For this purpose, we derive the expression for the decay width of dICD, Γ_{dICD}. In Chap. 3, we develop an asymptotic formula, assuming that the system which initially carryies the excess energy and its neighbor, which is doubly ionized in the energy transfer process, are spatially well separated and can be treated as independent entities. Afterward, in Chap. 4, we discuss the dICD width and its ratio to the ICD width for a palette of atomic and molecular systems, making explicit use of the derived asymptotic formula. Beyond this approximation, we also derive in Chap. 5 a general analytical expression for the decay width of the dICD process employing perturbation theory in second order. The numerical evaluation of the resulting expression is rather involved and beyond the scope of the present work. Nevertheless, one can identify in this expression several mechanisms which constitute dICD and explicitly recover the asymptotic expression. In Chap. 6, we finally discuss our findings and further research potential. We complete our studies by Chap. 7. Throughout Part I electrostatic units are used.

Returning to Part II, typical lifetimes of inner valence states which undergo ICD are of the order of femtoseconds. Although the characteristic timescales of nuclear motion are usually longer than the ICD lifetime, in cases where they are comparable, the nuclear dynamics have to be considered when ICD is investigated. The coherent population of vibrational states, their broadening due to the partial decay widths, and the quantum superposition in their decay also give rise to interference effects, which have to be considered. Experimentally and thus also theoretically preferred systems for such studies are noble gas dimers such as the homoatomic Ne_2 [2, 3, 11, 13, 94–96] and He_2 [9, 10, 97, 98], as well as the heteroatomic NeAr [19, 99] and NeKr [100], where the impact of nuclear dynamics on ICD-electron and kinetic-energy-release (KER) ionic spectra were investigated. Periodic structures were observed which can be related to the nodal structures of the corresponding vibrational ground-state wave functions. If experimental and theoretical data are available, a satisfying agreement between the measured and computed ICD-electron spectra will be achieved.

Recently, the nuclear dynamics during ICD initiated by Ne$2s$ ionization of a NeKr dimer were tracked experimentally [100]. The measuring method applied in Ref. [100] is based on the post-collision interaction technique [101, 102], using the deceleration of the slow photoelectron $\mathbf{e}^-_{PE}$ when it gets overtaken by the fast ICD electron $\mathbf{e}^-_{ICD}$. The two singly charged cations and the electron produced in the ICD process, as well as the photoelectron, were detected in coincidence using a COLTRIMS reaction microscope [103]. Time-resolved photoelectron (PE) and KER spectra, as well as the survival probability of the decaying state, were measured and compared to theoretical simulations, which provided insight into the evolution of the vibrational wave packet during the ICD process. Although a good agreement between the theoretical and experimental spectra was obtained, the theoretical methodology used in Ref. [100] does not account for the interference effects in the PE and ICD spectra.

In the present work [65], we concentrate on the interference effects during ICD in NeKr, and how they appear in the spectra of the emitted particles. Furthermore, we investigate the impact of vibrationally selected ICD, where the electronic ground state is vibrationally excited, on the ICD-electron spectra. Although related, the sources of interference effects are different in the PE, ICD-electron, and KER spectra and reflect different aspects of the decay dynamics. As the decay width of the $Ne^+(2s^{-1})Kr$ state depends on the distance between neon and krypton, the photoelectron spectrum is not simply a sum of Lorentzians [104], reflecting the decay width of every populated vibrational state of the cation, but contains an additional interference-like term [105]. Moreover, if the decay is fast, the broadening of the vibrational states can be so large that the states overlap, causing interferences. Therefore, the PE spectrum is highly sensitive to changes in the potential energy curve (PEC) of the 2s ionized state. An *ab initio* computation of the respective resonance PEC, accurate enough to describe well the nuclear dynamics in the inner-valence ionized state, is beyond the means of existing numerical methods. Therefore, we fitted this PEC by a Morse potential and determined its parameters in a way that the computed PE spectrum and the experimental one [100] coincide satisfyingly well. The resulting PEC is used for all the following calculations. Finally, the wave-packet dynamics during the ICD process and the follow-up Coulomb explosion are additional sources of interference effects. The ICD-electron and KER spectra reflect the dynamics on the PECs of the final and of the decaying state, respectively, where different portions of the wave packet can interfere with one another while propagating in the corresponding potentials. Besides the observed interference effects, we were motivated by the previous results, see Refs. [13, 96, 99], regarding the vibrationally excited electronic ground state. Consequently, the vibrationally selected ICD-electron spectra for NeKr are computed, and their structures are interpreted. Furthermore, the impact of different temperatures on the ICD-electron spectrum is discussed. To complete our studies, the KER spectra are directly calculated and compared to the mirror image of the corresponding vibrationally selected ICD-electron spectrum.

Recently, the ultrafast energy transfer in argon dimers was experimentally observed by a time-resolved pump-probe experiment [106]. In the XUV-pump step, one of the monomers is 3s ionized. The system deexcite and the energy is transferred to the neighboring argon atom, resulting in its 4s or 4p excitation. The subsequent nuclear dissociation dynamics were tracked by a time-delayed IR-probe pulse, which causes the ionization of the excited argon atom. The measured pump-probe delay-dependent KER spectrum provided insight into the relaxation dynamics, and an energy-transfer time of about 824 fs could be subtracted. Because the investigated fast relaxation pathway energetically lies below the ICD threshold, it is called pre-ICD. Furthermore, a pump-probe delay-dependent KER spectrum was semi-classically computed using Monte-Carlo simulations, which gives great agreement with the experimental one but does not feature all the observed phenomena.

In our work [66], we perform a quantum-mechanical computation of the pump-probe delay-dependent KER spectrum to reproduce the experimental spectrum. As expected, the structures in the experimental spectrum are caused by nuclear dynamics. We analyze the occurrence of these quantum effects by separately computing the distributions of the gerade and ungerade transitions of the total spectrum. Furthermore, we show the impact of form and position of the PECs on the spectrum and use this knowledge to optimize the PEC of the 3s-hole state to achieve good agreement between theory and experiment.

Part II is structured as follows. In Chap. 8, we present the derivations of the time-independently computed PE spectrum and of the time-dependently computed ICD-electron and KER spectra based on Refs. [104, 105, 107–112]. We continue showing, in Chap. 9, the numerical tools needed to implement the previous-derived equations. Finally, we compute PE, ICD-electron, and the KER spectra of the NeKr dimer and time-delay dependent KER spectra of the Ar_2 dimer in Chaps. 10 and 11. The spectra are analyzed for the aspects introduced and motivated above, see Refs. [65] and [66]. Chap. 12 completes our studies with a conclusion. Throughout Part II atomic units are used.

Part I

On the Theory of double ICD

Chapter 2

Motivation

Interatomic Coulombic decay (ICD) was established over the last decades as a well-known decay mechanism due to several experimental and theoretical studies, Refs. [1, 5–8]. Double interatomic Coulombic decay (dICD) is related to ICD, but represents a significant extension to the original decay process. We investigated this new decay mechanism in Ref. [64] and present our results here. How ICD and dICD differ from each other is schematically shown in Fig. 2.1.

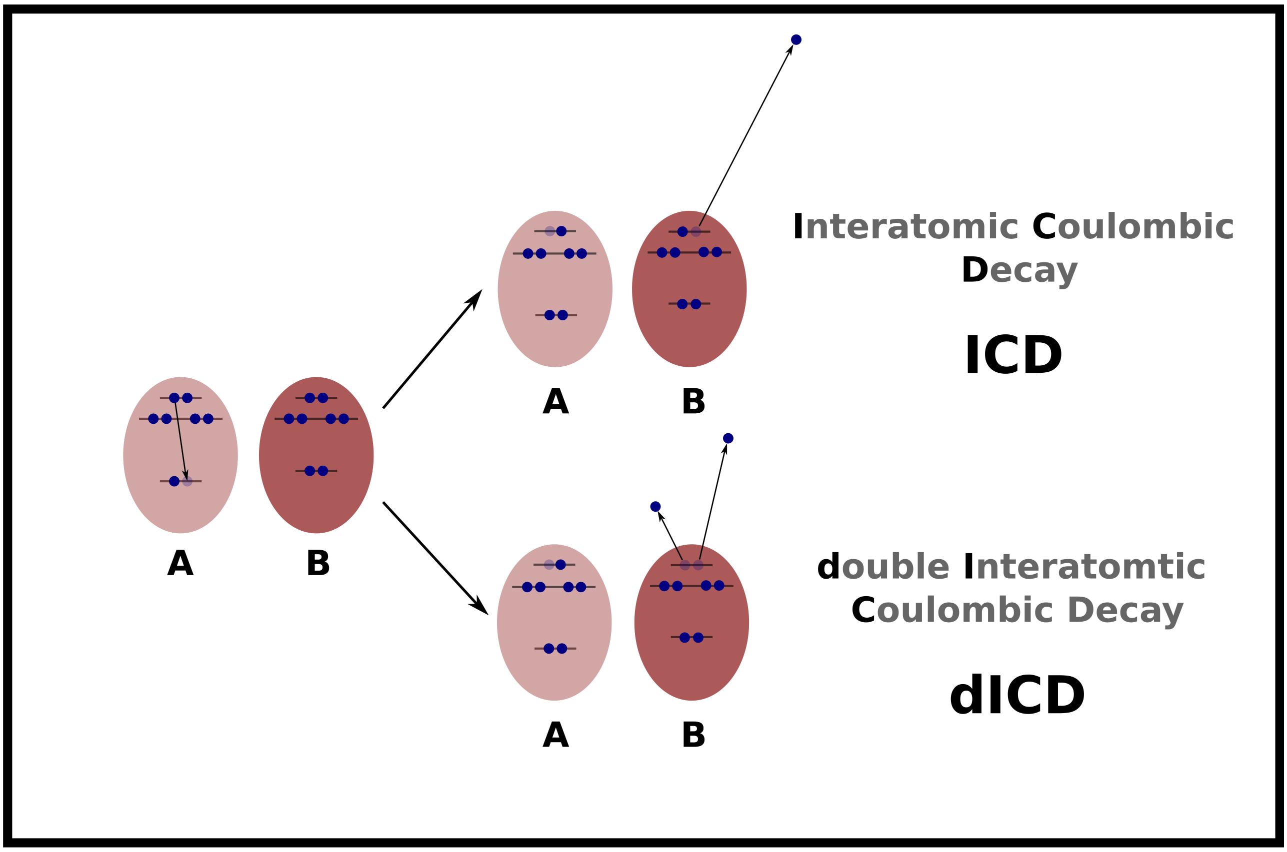

Figure 2.1: Simplified scheme of interatomic and double interatomic Coulombic decay (ICD and dICD). While in ICD after relaxation of the initially ionized species A, one electron of species B is emitted, in dICD two electrons of species B are simultaneously rejected.

For simplicity, we consider a system consisting of two species A and B separated by an internuclear distance R, where A and B can be atoms or molecules. The initial ionization on species A results in removing an electron from an inner-valence orbital. If the energy of the excited ionic state is larger than the ionization threshold of B, the system can undergo ICD, where after the relaxation of species A, the energy is transferred radiationlessly to species B, which is ionized and emits one outer-valence electron. If the excess energy even exceeds the double-ionization threshold of the combined system, the resulting excited ion can decay via the new dICD mechanism, in which relaxation of the initial excitation is accompanied by radiationless energy transfer and simultaneous ejection of two electrons from the outer-valence shell of species B into the continuum. Thus, the considered dICD mechanism reads

$$\mathrm{A}^{+*} + \mathrm{B} \longrightarrow \mathrm{A}^{+} + \mathrm{B}^{++} + e + e^{'}, \tag{2.1}$$

where e and $e^{'}$ are the two ICD electrons. Inner-valence ionization of a neutral species is not the only mechanism for producing electronically excited states, which might decay in an interatomic process. Electronically excited neutral or multiply ionized atoms or molecules were shown to undergo ICD [1, 2, 4, 7, 21, 26, 27, 45, 113–115]. However, to keep the presentation simple, we will continue the discussion in terms of the inner-valence ionized states. The generalization to other types of excitations is usually straightforward.

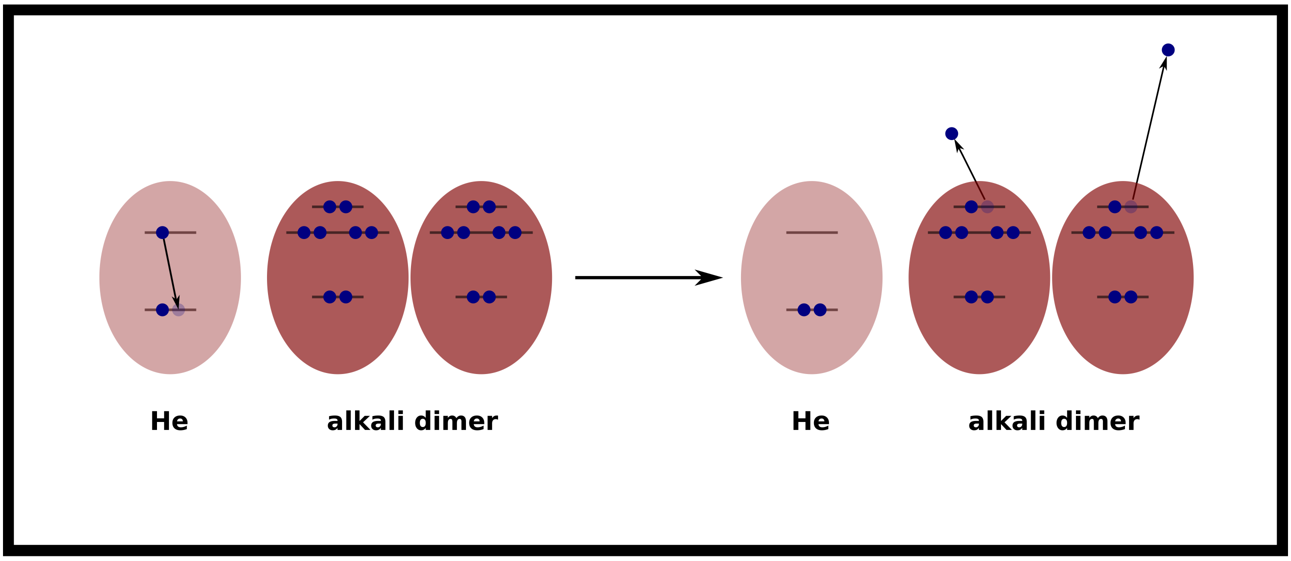

Figure 2.2: Simplified scheme of dICD in an alkali dimer attached to a helium droplet. After excitation and subsequent relaxation, the excited He*(1s2s) decays. The excess energy of 20.6 eV is transferred to the attached alkali dimer, which simultaneously emits two electrons to the continuum. The corresponding measurements were reported in Ref. [68].

A few years ago, dICD was experimentally demonstrated in alkali dimers attached to helium droplets [68]. The He droplet absorbes a photon of 21.6 eV resulitng in the excitation of a He atom. Subsequently, the excited He*(1s2p) relaxes to the metastable 1s2s state and decays. The excess energy of 20.6 eV is transferred radiationlessly to the attached alkali dimer, leading to the emission of two electrons in the continuum. The above-described process is schematically visualized in Fig. 2.2.

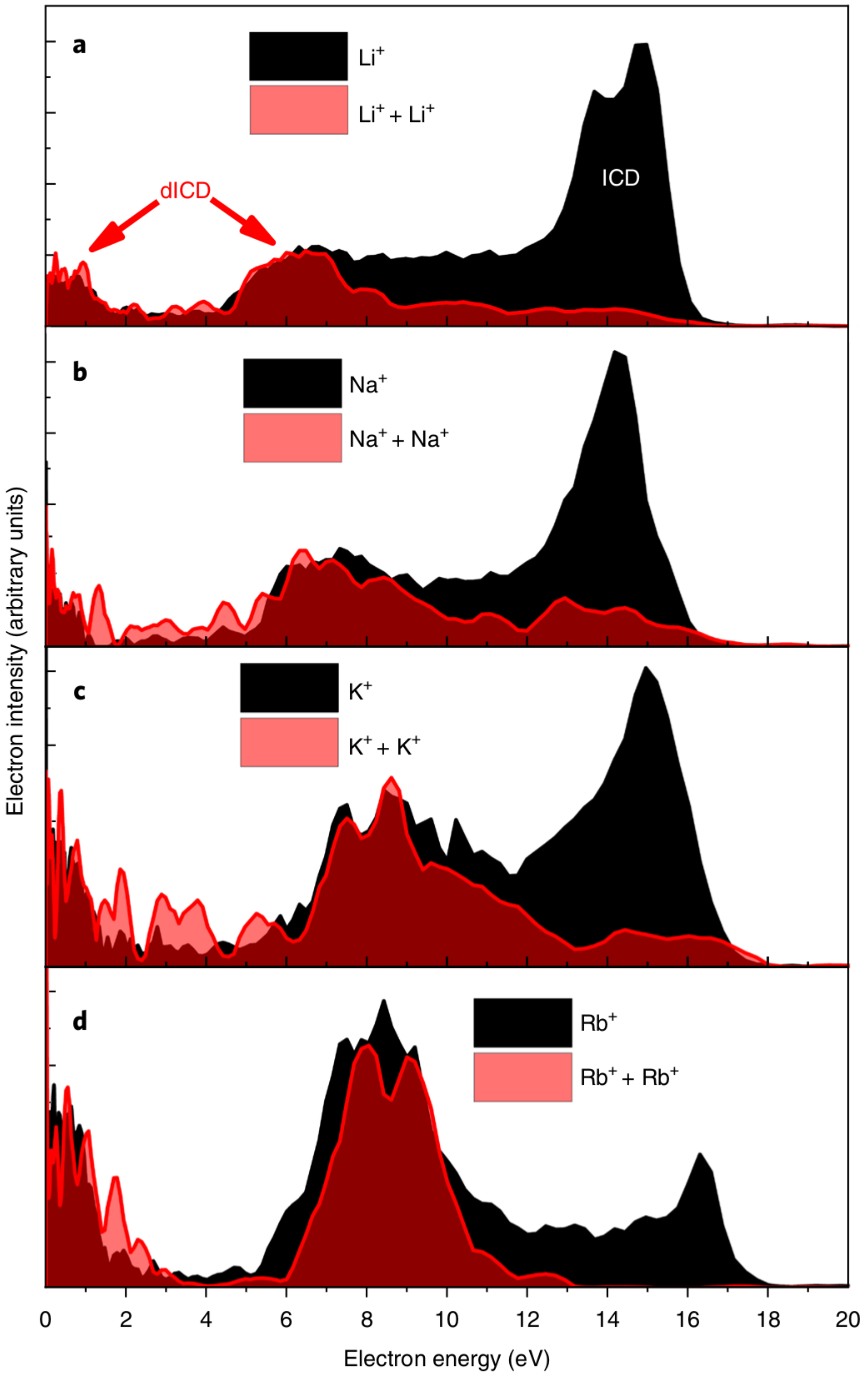

Figure 2.3: Electron spectra for Li (a), Na (b), K (c), and Rb (d) dimers attached to helium droplets taken from Ref. [68]. After the excited He*(1s2s) atoms decay, the systems undergo ICD and dICD, respectively. The red-filled lines are measured in triple coincidence (e^-, Ak$^+$, Ak$^+$) and give only the contribution of dICD. The black-filled lines are taken in double coincidence (e^-, Ak$^+$) and exhibit both ICD and dICD. e^- is the ejected electron, and Ak$^+$ denotes the ionized alkali dimer.

The corresponding electron spectra for Li, Na, K, and Rb dimers attached to helium droplets are given in Fig. 2.3, which is taken from Ref. [68]. The red-filled curves were measured in double-ion coincidence, and therefore, one can only observe dICD. The black-filled curves were taken in single-ion coincidence and, consequently, present both ICD and dICD, which are separated in kinetic energy. The ICD peaks are between 14 eV and 16 eV depending on the alkali dimer. The heavier the alkali dimer, the lower the ionization threshold, and consequently, the ICD peak is shifted to higher electron energies. The same applies to the two dICD peaks, where one appears between 0 eV and 2 eV and the other between 6 eV and 8 eV. The resulting U-shape profiles are characteristic for correlated emission mechanisms such as shake off and in a flatter form knock out [72, 73, 81], which are known from the local processes such as double Auger (dA) decay [76–80] and single-photon double-ionization (SPDI) [71–75].

After emission of the first electron in the shake-off mechanism, the system relaxes and the sudden change in the potential triggers the ejection of the second electron. Because the first electron is high in energy and the energy of the second electron barely exceeds the ionization threshold, the shake off leads to a distinct U-shape profile in the electron kinetic-energy spectrum, where one peak is close to the threshold and the other peak is located at higher energies. In contrast, the knock-out mechanism is comparable to impact ionization, where the first emitted electron knocks out another electron while leaving the atom. The two ejected electrons are closer in energy than the emitted electrons in the shake-off process, but still separated in kinetic energy.

In dA, an atom or molecule is initially core ionized. The vacancy is filled by a valence electron, and the corresponding excess energy is utilized to eject two electrons in the continuum. In SPDI, the investigated species is directly doubly ionized. In these two local processes, the ratios of the double- to the corresponding single-ionization process usually amount only to several percents for energies close to threshold, see Refs. [75, 77, 78, 81, 83–88]. Remarkable is now that the efficiency of dICD appears to be comparable to that of ICD and even exceeds it, as seen in Fig. 2.3. So, the question arises why dICD is so efficient.

The efficiency of dICD is determined by its decay rate, and we present in the following chapters some approaches for its computation. We start with the asymptotic approach, where we assume that the two species are well separated so that we can treat them as independent. Experimentally measurable quantities are used to put the asymptotic decay width into a practical form, which is subsequently applied to several atomic and molecular systems known from the literature. To complete our studies, we also show the perturbative approach, where the two species are no longer far away from each other. Due to perturbation theory, which considers the orbital overlap between the two species, we obtain further insight into the different intra- and interatomic mechanisms resulting in dICD.

Chapter 3

Asymptotic Approach

In this chapter, we derive the asymptotic partial decay width $\Gamma_{dICD}(\omega)$ expressed by experimentally measurable quantities of isolated monomers, where $\hbar\omega$ is the transferred energy or the energy of the virtual photon. The derivation shown below is based on Ref. [64]. We assume that the two species are well separated so that we can make two crucial assumptions. First, we will write the states of the combined system as products of the states of the isolated subsystems A and B, and second, we will represent the Coulomb operator, which describes the interaction between the electrons of A and B, as the multipole expansion. In Sec. 3.1, we introduce the corresponding states, the electronic Hamiltonian, and the expansion of the interaction Hamiltonian in multipole terms. Subsequently, the expression of the transition amplitude in terms of dipole operators is derived in Sec. 3.2. Averaging of the transition amplitude over the initial states and summing over the final states is done in Sec. 3.3. Finally, in Sec. 3.4, the expression of the decay width expressed in terms of experimentally measurable quantities is derived. Electrostatic units are used, as is seen from the form of the Coulomb term (see Eq. (3.3)).

3.1 States and Hamiltonians

We assume that the interatomic distance R is fixed. Following the excitation step, the system A-B is found in a decaying electronic state $|\Psi_D\rangle$, which comprises the excited inner-valence ionized species A^{+*} and the neighbor B. This decaying state lies energetically in the double-continuum corresponding to the relaxed ion A^+ and a doubly ionized state of B. We denote the energies of the two electrons in the continuum as ε_k and $\varepsilon_{k'}$. The final state of the system, can be written as $|\Psi_{E_\gamma,\varepsilon,\varepsilon_{k'}}\rangle$, where E_γ is the energy of the remaining ion (A^+B^{2+}) in the state γ, which is accessible in the decay, and $\varepsilon = \varepsilon_k + \varepsilon_{k'}$. The electronic part of the final state at fixed R is energy-normalized in ε and $\varepsilon_{k'}$, i.e., $\langle\Psi^*_{E'_\gamma,\varepsilon',\varepsilon'_{k'}}|\Psi_{E_\gamma,\varepsilon,\varepsilon_{k'}}\rangle = \delta_{\gamma\gamma'}\,\delta(\varepsilon-\varepsilon')\delta(\varepsilon_{k'}-\varepsilon'_{k'})$. Due to the large separation of A and B, the subsystems can be seen as isolated, which allows us to approximate the states of interest as direct products of the states of A and B. The resulting expressions read

$$|\Psi_D\rangle = |\Psi_D^{(A)}\rangle\,|\Psi_0^{(B)}\rangle\,, \tag{3.1a}$$

$$|\Psi_{E_\gamma,\varepsilon,\varepsilon_{k'}}\rangle = |\Psi_{E_{\gamma_A}}^{(A)}\rangle\,|\Psi_{E_{\gamma_B},\varepsilon,\varepsilon_{k'}}^{(B)}\rangle\,, \tag{3.1b}$$

where $|\Psi_D^{(A)}\rangle$ represents species A in an inner-valence ionized state, while we assume that $|\Psi_0^{(B)}\rangle$ is the ground state of species B. The double ionization of species B by radiationless energy transfer can then be conceptualized as proceeding via absorbing a single virtual photon emitted in deexcitation of A^{+*}. A final state of the system is a product of the energetically accessible low-lying state of the ion A^+, $|\Psi_{E_{\gamma_A}}^{(A)}\rangle$, and a state $|\Psi_{E_{\gamma_B},\varepsilon,\varepsilon_{k'}}^{(B)}\rangle$ which describes the doubly charged ion of B^{2+} with two emitted electrons in the continuum.

Let us continue with the electronic Hamiltonian, which can be written as

$$\hat{H} = \hat{H}_A + \hat{H}_B + \hat{W}_{AB} + \hat{V}_{AB}, \tag{3.2}$$

where $\hat{H}_A$ and $\hat{H}_B$ are the full electronic Hamiltonians of isolated A and B, respectively, $\hat{W}_{AB}$ is the interaction of the electrons of A with the nuclei of B and vice versa, and $\hat{V}_{AB}$ is the Coulomb interaction between the electrons of A and B. The states of the isolated subsystems of A and B are eigenstates of the Hamiltonians $\hat{H}_A$ and $\hat{H}_B$, respectively. The transition from $|\Psi_D\rangle$ to $|\Psi_{E_\gamma,\varepsilon,\varepsilon_{k'}}\rangle$ is effected already in second-order perturbation theory due to the interatomic (intermolecular) two-electron term $\hat{V}_{AB}$, while the coupling of the excited state to the double-continuum of the neighbor via the one-particle operator $\hat{W}_{AB}$ arises only in higher orders and can be neglected.

Before we evaluate the transition amplitude in Eq. (3.8) in the asymptotic limit, we focus on the Coulomb operator $\hat{V}_{AB}$, which is given as

$$\hat{V}_{AB} = \sum_{i\in A}\sum_{j\in B} \frac{e^2}{|\boldsymbol{r}_j^{(B)} - \boldsymbol{r}_i^{(A)}|}. \tag{3.3}$$

The corresponding system is schematically depicted in Fig. 3.1, where the center of species A is placed at the origin, and the vector $\boldsymbol{R} = R\,\boldsymbol{e}_R$ connects the centers of the species A and B.

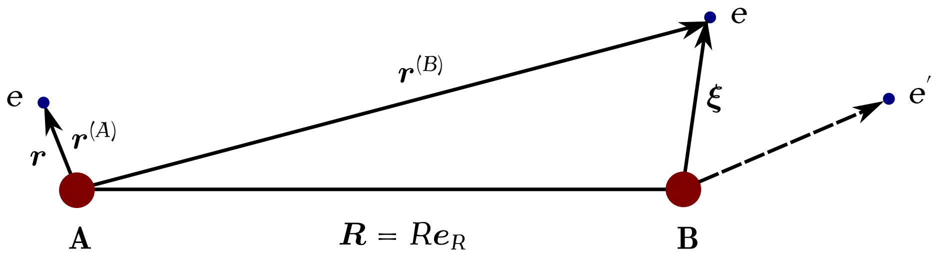

Figure 3.1: Schematical configuration of species A and species B at distance R. The coordinates $\boldsymbol{r}^{(A)}$ and $\boldsymbol{r}^{(B)}$ describe the positions of electrons localized on A or B with respect to the species A, while $\boldsymbol{r}$ and $\boldsymbol{\xi}$ are the corresponding coordinates to A and B, respectively. Electron $\boldsymbol{e}$ recieves the energy following the relaxation of A and shares it with $\mathbf{e}'$ by correlations.

The electron coordinates in A and B relative to the origin are $\boldsymbol{r}_i^{(A)}$ and $\boldsymbol{r}_j^{(B)}$, where $\boldsymbol{i}$ enumerates the electrons of A and $\boldsymbol{j}$ labels the electrons of B. The vectors $\boldsymbol{r}_i$ and $\boldsymbol{\xi}_j$ are the electron coordinates relative to the centers of A and B, respectively. We assume that in the case of atoms, their centers coincide with the nuclei, while for molecules they are located at the respective centers of electronic charge.

At large internuclear distances R, where $|\boldsymbol{r}_i^{(A)}| << |\boldsymbol{r}_j^{(B)}|$ holds and the Coulomb term can be represented as multipole expansion, whereby only the leading terms are retained. Inserting, $\boldsymbol{r}_j^{(B)}=\boldsymbol{R}+\boldsymbol{\xi}_j$ into Eq. (3.3) (see Fig. 3.1), and carrying out the multipole expansion in powers of $1/R$, gives

$$\begin{aligned}\hat{V}_{AB} &= \sum_{i\in A}\sum_{j\in B}\frac{e^2}{|(\boldsymbol{R}+\boldsymbol{\xi}_j)-\boldsymbol{r}_i|}\\ &= \frac{e^2}{R} - e^2\sum_{i\in A}\sum_{j\in B}\frac{(\boldsymbol{\xi}_j-\boldsymbol{r}_i)}{R^2}\boldsymbol{e}_{\boldsymbol{R}} + \frac{e^2}{2}\sum_{i\in A}\sum_{j\in B}\left[-\frac{(\boldsymbol{\xi}_j-\boldsymbol{r}_i)^2}{R^3} + 3\frac{((\boldsymbol{\xi}_j-\boldsymbol{r}_i)\boldsymbol{R})^2}{R^5}\right] + O\Big(\frac{1}{\boldsymbol{R}^4}\Big).\end{aligned} \tag{3.4}$$

Because only terms containing both the coordinates of A ($\boldsymbol{r}_i$) and B ($\boldsymbol{\xi}_j$) can couple electrons of A and B, the first surviving term in Eq. (3.4) is the third term, where only contributions, which behave as $1/R^3$, remain. Neglecting higher orders, gives the following approximation for the interaction Coulomb operator

$$\hat{V}_{AB} \approx \frac{e^2}{R^3}\sum_{i\in A}\sum_{j\in B}\big[\boldsymbol{\xi}_j\boldsymbol{r}_i - 3(\boldsymbol{\xi}_j\boldsymbol{e}_{\boldsymbol{R}})(\boldsymbol{r}_i\boldsymbol{e}_{\boldsymbol{R}})\big]. \tag{3.5}$$

3.2 Transition Amplitude and Decay Width

The *differential partial decay width* $\Gamma_{E_\gamma}(\varepsilon, \varepsilon_{k'})$ [73, 76], which corresponds to the decay of the state $|\Psi_D\rangle$ to the state $|\Psi_{E_\gamma,\varepsilon,\varepsilon_{k'}}\rangle$ is given by the following equation

$$\Gamma_{E_\gamma}(\varepsilon, \varepsilon_{k'}) = 2\pi |\langle \Psi_{E_\gamma,\varepsilon,\varepsilon_{k'}} | \hat{H} | \Psi_D \rangle|^2, \tag{3.6}$$

where $\hat{H}$ denotes the full electronic Hamiltonian, and neither $|\Psi_D\rangle$ nor $|\Psi_{E_\gamma,\varepsilon,\varepsilon_{k'}}\rangle$ is an eigenstate of $\hat{H}$. Eq. (3.6) is related to Fermi's golden rule, which gives the probability per unit time P for transitions caused by time-independent perturbations, by $P = \frac{\Gamma_{E_\gamma}(\varepsilon, \varepsilon_{k'})}{\hbar}$, see Ref. [116]. Because the final states are energy-normalized, see Sec. 3.1, the corresponding prefactors of the continuum states cancel the density of the final states, which reduces to $\rho(E_{E_\gamma,\varepsilon,\varepsilon_{k'}}) = 1$.

By integrating $\Gamma_{E_\gamma}(\varepsilon, \varepsilon_{k'})$ over $\varepsilon_{k'}$, we get an expression for the decay width which corresponds to one specific decay on A accompanied by the emission of two electrons with the combined energy ε from specific orbitals of B. We call this expression *partial decay width for a given channel*

$$\Gamma_{E_\gamma}(\varepsilon) = \int_0^{\varepsilon} \Gamma_{E_\gamma}(\varepsilon, \varepsilon_{k'})\, d\varepsilon_{k'}. \tag{3.7}$$

As discussed before, if the interatomic distance R between the two centers A and B is considered at the limit $R \to \infty$, several simplifying assumptions will become valid, and we will be able to derive an analytical expression for the asymptotic decay width [90–93]. This allows us to expand the Coulomb interaction, which is the only contributing operator of the electronic Hamiltonian. Consequently, the differential partial decay width reads

$$\Gamma_{E_\gamma}(\varepsilon, \varepsilon_{k'}) = 2\pi |\langle \Psi^{(A)}_{E_{\gamma_A}} | \langle \Psi^{(B)}_{E_{\gamma_B},\varepsilon,\varepsilon_{k'}} | \hat{V}_{AB} | \Psi^{(A)}_D \rangle | \Psi^{(B)}_0 \rangle|^2, \tag{3.8}$$

where the approximated Coulomb interaction in Eq. (3.5) can be used for evaluating the dICD transition amplitude

$$\begin{aligned} M_{FI} &= \langle \Psi^{(A)}_{E_{\gamma_A}} | \langle \Psi^{(B)}_{E_{\gamma_B},\varepsilon,\varepsilon_{k'}} | \hat{V}_{AB} | \Psi^{(A)}_D \rangle | \Psi^{(B)}_0 \rangle \\ &\approx \frac{e^2}{R^3} \sum_{i \in A} \sum_{j \in B} \Big[\langle \Psi^{(A)}_{E_{\gamma_A}} | \boldsymbol{r}_i | \Psi^{(A)}_D \rangle \langle \Psi^{(B)}_{E_{\gamma_B},\varepsilon,\varepsilon_{k'}} | \boldsymbol{\xi}_j | \Psi^{(B)}_0 \rangle \\ &\quad - 3 \langle \Psi^{(A)}_{E_{\gamma_A}} | \boldsymbol{r}_i \boldsymbol{e}_R | \Psi^{(A)}_D \rangle \langle \Psi^{(B)}_{E_{\gamma_B},\varepsilon,\varepsilon_{k'}} | \boldsymbol{\xi}_j \boldsymbol{e}_R | \Psi^{(B)}_0 \rangle \Big]. \end{aligned} \tag{3.9}$$

By introducing the dipole operators

$$\hat{\boldsymbol{D}}_{\boldsymbol{A}} = -\sum_{i \in A} e\, \boldsymbol{r}_i, \tag{3.10a}$$

$$\hat{\boldsymbol{D}}_{\boldsymbol{B}} = -\sum_{j \in B} e\, \boldsymbol{\xi}_j, \tag{3.10b}$$

which act only on the electron coordinates of either A or B, we can write the interaction in a form that emphasizes the dipole-dipole coupling between A and B clearly

$$M_{FI} = \frac{1}{R^3}\left[\boldsymbol{D}^{(A)}\boldsymbol{D}^{(B)} - 3(\boldsymbol{e}_R\,\boldsymbol{D}^{(A)})(\boldsymbol{e}_R\,\boldsymbol{D}^{(B)})\right], \tag{3.11}$$

where the transition dipole amplitudes $\boldsymbol{D}^{(A)}$ and $\boldsymbol{D}^{(B)}$ are

$$\boldsymbol{D}^{(A)} = \langle \Psi^{(A)}_{E_{\gamma_A}} | \hat{\boldsymbol{D}}_A | \Psi^{(A)}_{D} \rangle\,, \tag{3.12a}$$

$$\boldsymbol{D}^{(B)} = \langle \Psi^{(B)}_{E_{\gamma_B},\varepsilon,\varepsilon_{k'}} | \hat{\boldsymbol{D}}_B | \Psi^{(B)}_{0} \rangle\,. \tag{3.12b}$$

Choosing the z-axis along $\boldsymbol{e_R}$, we obtain the following expression for the absolute value squared of the transition amplitude

$$|M_{FI}|^2 = \frac{1}{R^6}|D^{(A)}_x D^{(B)}_x + D^{(A)}_y D^{(B)}_y - 2\,D^{(A)}_z D^{(B)}_z|^2, \tag{3.13}$$

where D_x, D_y, D_z denote the transition matrix elements belonging to the corresponding component of the dipole operator.

3.3 Isotropic Transition Amplitude

In the following, we consider the isotropic transition amplitude by averaging over the initial states and summing over the final states, which is required to compute the *total decay width* Γ_{dICD}. Due to the absence of an external field, we assume that no direction in space is favored and that the atoms can be with equal probability in any angular momentum substates characterized by M_A and M_B. For a diatomic system A-B the states of interest can be written in terms of atomic quantum numbers

$$|\Psi_D\rangle = |\gamma_A E_A J_A M_A\rangle\,|\gamma_B E_B J_B M_B\rangle\,, \tag{3.14a}$$

$$|\Psi_{E_\gamma \varepsilon \varepsilon_{k'}}\rangle = |\gamma'_A E'_A J'_A M'_A\rangle\,|\gamma'_B E'_B J'_B M'_B\rangle\,, \tag{3.14b}$$

where E is the energy of the respective atomic state, J is the total angular momentum, M is its projection, and γ denotes all other quantum numbers. It follows for the transition matrix elements

$$\begin{aligned} D^{(A)}_k &= \langle \gamma'_A E'_A J'_A M'_A | \hat{D}^{(A)}_k | \gamma_A E_A J_A M_A \rangle\,, \\ D^{(B)}_k &= \langle \gamma'_B E'_B J'_B M'_B | \hat{D}^{(B)}_k | \gamma_B E_B J_B M_B \rangle\,, \end{aligned} \tag{3.15}$$

where $\boldsymbol{k} = x, y, z$. We average over the projections of the total angular momentum of A and B in the initial state, M_A and M_B, and sum over the final states, M'_A and M'_B, to get the isotropic transition amplitude [39, 117]

$$\overline{|M_{FI}|^2} = \frac{1}{2J_A+1}\frac{1}{2J_B+1}\sum_{M_A M'_A}\sum_{M_B M'_B}|M_{FI}|^2. \tag{3.16}$$

The expressions above can be simplified by using the concept of reduced matrix elements [117]

$$\begin{aligned}\sum_{M_A,M'_A}|\langle\gamma'_A E'_A J'_A M'_A|\hat{D}^{(A)}_k|\gamma_A E_A J_A M_A\rangle|^2 &= \frac{1}{3}|(\gamma'_A E'_A J'_A||\hat{\boldsymbol{D}}_A||\gamma_A E_A J_A)|^2,\\ \sum_{M_B,M'_B}|\langle\gamma'_B E'_B J'_B M'_B|\hat{D}^{(B)}_k|\gamma_B E_B J_B M_B\rangle|^2 &= \frac{1}{3}|(\gamma'_B E'_B J'_B||\hat{\boldsymbol{D}}_B||\gamma_B E_B J_B)|^2,\end{aligned} \tag{3.17}$$

where $(\gamma'_A E'_A J'_A||\hat{\boldsymbol{D}}_A||\gamma_A E_A J_A)$ and $(\gamma'_B E'_B J'_B||\hat{\boldsymbol{D}}_B||\gamma_B E_B J_B)$ denote the reduced matrix elements. Note that the terms of different dipole matrix components arising in the absolute square give no contribution, see Ref. [117]. Finally, the isotropic transition amplitude is given by

$$\overline{|M_{FI}|^2} = \frac{1}{2J_A+1}\frac{1}{2J_B+1}\frac{2}{3\,R^6}|(\gamma'_A E'_A J'_A||\hat{\boldsymbol{D}}_A||\gamma_A E_A J_A)(\gamma'_B E'_B J'_B||\hat{\boldsymbol{D}}_B||\gamma_B E_B J_B)|^2. \tag{3.18}$$

In our case, we assume that atom B initially in its non-degenerate ground state with $J_B = 0$, thus $\frac{1}{2J_B+1}$ reduces to 1. Finally, the differential partial decay width averaged over the projections of the angular momentum becomes

$$\Gamma_{E_\beta}(\varepsilon,\varepsilon_{k'}) = \frac{4\pi}{3R^6}\frac{1}{2J_A+1}|(\gamma'_A E'_A J'_A||\hat{\boldsymbol{D}}_A||\gamma_A E_A J_A)(\gamma'_B E'_B J'_B||\hat{\boldsymbol{D}}_B||\gamma_B E_B\,0)|^2. \tag{3.19}$$

We use Eq. (3.19) to obtain the partial decay width $\Gamma_{E_\gamma}(\varepsilon)$ (see Eq. (3.7)). By summing the latter over all final states, we obtain the total decay width of dICD,

$$\Gamma_{dICD} = \frac{4\pi}{3R^6}\sum_{F_A F_B}\int_0^{\varepsilon} d\varepsilon_{k'}\,\frac{1}{2J_A+1}\,|(\gamma'_A E'_A J'_A||\hat{\boldsymbol{D}}_{\boldsymbol{A}}||\gamma_A E_A J_A)(\gamma'_B E'_B J'_B||\hat{\boldsymbol{D}}_{\boldsymbol{B}}||\gamma_B E_B\,0)|^2, \tag{3.20}$$

whereby F_A (F_B) enumerates the energetically accessible final states of A (B).

3.4 Experimentally Measurable Quantities

In the special case where there is only one suitable transition on A, we can express the *partial decay width* $\Gamma_{dICD}(\omega)$ through experimentally measurable quantities of the isolated subsystems A and B. To do that, we write for the radiative decay rate on atom A [117]

$$w_A = \frac{4\omega^3}{3\hbar c^3}\frac{1}{2J_A+1}|(\gamma'_A E'_A J'_A||\hat{\boldsymbol{D}}_A||\gamma_A E_A J_A)|^2, \tag{3.21}$$

where the transition energy $\hbar\omega$ is the energy of the virtual photon,

$$\hbar\omega = E'_A - E_A = E'_B - E_B. \tag{3.22}$$

The radiative lifetime corresponding to the transition $(\gamma_A E_A J_A) \rightarrow (\gamma'_A E'_A J'_A)$ on A reads

$$\tau_A = \frac{1}{w_A}. \tag{3.23}$$

Furthermore, the transition moment $|(\gamma'_B E'_B J'_B||\hat{\boldsymbol{D}}_B||\gamma_B E_B J_B)|^2$ can be replaced by the *single-differential one-photon double-ionization cross section* of atom B, $\frac{d\sigma_B^{++}(\omega)}{d\varepsilon_{k'}}$, in the length gauge with photons of energy $\hbar\omega$ [72–74],

$$\frac{d\sigma_B^{++}(\omega)}{d\varepsilon_{k'}} = \frac{4\pi^2}{3}\frac{\omega}{c}\sum_{F_B}|(\gamma'_B E'_B J'_B||\hat{\boldsymbol{D}}_B||\gamma_B E_B J_B)|^2, \tag{3.24}$$

where F_B denotes all energetically possible final states on B, which is initially in its non-degenerate ground state. The resulting formula for the partial decay width $\Gamma_{dICD}(\omega)$ of dICD in a system of two atoms defined by measurable quantities for one specific virtual photon energy $\hbar\omega$, finally reads

$$\Gamma_{dICD}(\omega) = \frac{3\hbar}{4\pi}\left(\frac{c}{\omega}\right)^4 \frac{\tau_A^{-1}\sigma_B^{++}(\omega)}{R^6}. \tag{3.25}$$

Note that the partial decay width $\Gamma_{dICD}(\omega)$ considers different transitions on species B for one specific virtual photon energy, while the partial decay width for a given channel $\Gamma_{E_\gamma}(\varepsilon)$ considers only one transition on B for a given decay on A.

In the asymptotic derivation of the partial decay width, the dipole operators appear naturally in the length gauge, since they arise through the expansion of the Coulomb interaction. Therefore, whenever *ab initio* radiative lifetimes and single-photon double-ionization cross sections are used in Eq. (3.25), the length gauge should be preferred if the respective transition moments depend on the gauge chosen.

Furthermore, Eq. (3.25) is not only valid for atomic systems. It is also valid for systems, which consist of a decaying atomic species and a molecular species as neighbor, if we average over the orientation of the molecule in space [118, 119].

Chapter 4

Atomic and Molecular Systems

In this chapter, we apply the asymptotic expression, see Eq. (3.25), to investigate dICD and compare its efficiency to that of ICD and other decay processes. The results presented here are taken from Ref. [64]. For ICD, it has been shown that at shorter distances R, where the respective asymptotic expression loses its validity, the ICD rates obtained by this expression can be much smaller than the true rates due to orbital overlap and can be seen as a lower bound to the latter [90]. Since two electrons are emitted in dICD and at least two orbitals of the neighbor are involved in the process, one can expect that orbital overlap may have an even larger impact on the rate than found for ICD. Thus, at smaller R, the rates obtained by the asymptotic expression are also to be seen as lower bounds to the true, but yet unknown, rates.

4.1 Asymptotic ICD and dICD Rates in Comparison

Following the first observation that dICD is possible in Mg@C_{60} [67], we start the discussion with the fullerene C_{60} as a neighbor. It is well known that C_{60} and other fullerenes accommodate foreign atoms and molecules [120–122]. Here, we shall concentrate on the endohedral fullerenes Ne@C_{60}, Mg@C_{60} and He@C_{60}.

We start with Ne@C_{60} after 2s ionization of Ne. The excess energy (see Tab. 4.1) is 26.9 eV and, of course, suffices to ionize via ICD the C_{60} cage. However, due to the large Coulomb repulsion of 8.4 eV between Ne^+ and the resulting C_{60}^{++}, dICD is just not possible. Here, the ICD rate was computed by *ab initio* methods [67] and we use this fact to compare the result with that of the asymptotic expression. The asymptotic expression for the ICD rate reads [90]

$$\Gamma_{ICD} = \frac{3\hbar}{4\pi}\left(\frac{c}{\omega}\right)^4 \frac{\tau_A^{-1}\sigma_B^+}{R^6}. \tag{4.1}$$

As can be seen from Tab. 4.1, the lifetime of the $Ne^+(2s^{-1})$ ion decreases from the lifetime of the isolated ion of 0.2 ns to only 7 fs due to ICD. The reported *ab initio* value is smaller and amounts to 2 fs [67].

Ne@C_{60}	R = 3.4 Å [120]		
$Ne^+(2s^12p^6 \rightarrow 2s^22p^5)$	E_{vp} = 26.9 eV [123]	$w_A = 5.5 \cdot 10^9 \frac{1}{s}$[123]	$\tau_A = 1.9 \cdot 10^{-10}$ s
C_{60} [124–126]	DIP = 19 eV		σ_B^+ (26.9 eV) $= 5.7 \cdot 10^2$ Mb
ICD	$\Gamma_{ICD} = 9.3 \cdot 10^{-2}$ eV	$\Gamma_{ICD} = 1.4 \cdot 10^{14} \frac{1}{s}$	$\tau_{ICD} = 7.1 \cdot 10^{-15}$ s
Mg@C_{60}	R = 3.5 Å [127]		
$Mg^+(2p^53s^2 \rightarrow 2p^63s)$	E_{vp} = 50.2ẽV [123]	$w_A = 4.7 \cdot 10^9 \frac{1}{s}$	$\tau_A = 2.1 \cdot 10^{-10}$ s [128]
C_{60} [124–126]	DIP = 19 eV	$\sigma_B^{++} = 2.2 \cdot 10^1$ Mb	$\sigma_B^+ = 8.9 \cdot 10^1$ Mb
ICD	$\Gamma_{ICD} = 8.6 \cdot 10^{-4}$ eV	$\Gamma_{ICD} = 1.3 \cdot 10^{12} \frac{1}{s}$	$\tau_{ICD} = 7.7 \cdot 10^{-13}$ s
dICD	$\Gamma_{dICD} = 2.1 \cdot 10^{-4}$ eV	$\Gamma_{dICD} = 3.2 \cdot 10^{11} \frac{1}{s}$	$\tau_{dICD} = 3.1 \cdot 10^{-12}$ s
He@C_{60}	R = 3.3 Å [120]		
$He^*(1s2p \rightarrow 1s^2)$	E_{vp} = 21.2 eV [123]	$w_A = 1.8 \cdot 10^9 \frac{1}{s}$ [123]	$\tau_A = 5.6 \cdot 10^{-10}$ s
C_{60} [124–126]	DIP = 19 eV	$\sigma_B^{++} = 1.4$ Mb	$\sigma_B^+ = 1.2 \cdot 10^3$ Mb
ICD	$\Gamma_{ICD} = 2.0 \cdot 10^{-1}$ eV	$\Gamma_{ICD} = 2.9 \cdot 10^{14} \frac{1}{s}$	$\tau_{ICD} = 3.5 \cdot 10^{-15}$ s
dICD	$\Gamma_{dICD} = 2.3 \cdot 10^{-4}$ eV	$\Gamma_{dICD} = 3.5 \cdot 10^{11} \frac{1}{s}$	$\tau_{dICD} = 2.9 \cdot 10^{-12}$ s

Table 4.1: ICD and dICD rates for endohedral fullerenes. For each system the first row shows the data of the guest atom and the second row the data of C_{60} at the respective virtual photon energy. The third row reports the desired rates for the respective endohedral fullerene. Note that the dICD channel is not open for Ne@C_{60} due to the Coulomb repulsion in the final state. E_{vp} is the excess energy (virtual photon energy), w_A is the radiative rate, τ_A is the respective radiative lifetime of the isolated guest atom, DIP is the double-ionization potential of C_{60}, σ_B^{++} and σ_B^+ are the double- and single-ionization cross sections at the corresponding virtual photon energies, Γ_{ICD} and Γ_{dICD} are the ICD and dICD decay rates, and τ_{ICD} and τ_{dICD} are the resulting lifetimes due to the process indicated.

As noted in Ref. [67], the dICD channel is open in Mg@C_{60} after 2p ionization of Mg. As indicated in Tab. 4.1, the excess energy of $Mg^+(2p^{-1})$ is above 50 eV and by far suffices for dICD to take place. To be able to easily compute the ICD and dICD rates, we express the decay width in practical units

$$\Gamma_{dICD}[eV] = 2.38 \cdot 10^{-5} \frac{1}{(E_{vp}[eV])^4} \frac{(\tau_A[s])^{-1} \sigma_B^{++}[Mb]}{(R[\text{Å}])^6}, \tag{4.2}$$

as well as the relationship between lifetime and width

$$\tau[s] = 6.58 \cdot 10^{-16} \frac{1}{\Gamma[eV]}. \tag{4.3}$$

The radiative lifetime of $Mg^+(2p^{-1})$ is 0.2 ns , while due to ICD alone the lifetime of this ion inside C_{60} becomes 770 fs. Even dICD alone, would reduce the lifetime of $Mg^+(2p^{-1})$@C_{60} to the ps time regime (3.1 ps). Clearly, dICD is a relevant process in Mg@C_{60} after 2p ionization. For completeness, we mention that the ion $Mg^+(2p^{-1})$, unlike $Ne^+(2s^{-1})$, can also decay by autoionization [129, 130].

Having seen that dICD can be an efficient decay pathway in Mg@C_{60}, we now turn to He@C_{60} where after the lowest excitation 1s → 2p of He, ICD as well as dICD are open decay channels.

Since there is no Coulomb repulsion in the final state, the excess energy of 21.2 eV is sufficient to trigger the double ionization of C_{60} by energy transfer. Here, except for radiative decay, there is no competition to ICD and dICD by other decay mechanisms. ICD is very efficient for this system; its lifetime is only 3.5 fs as compared to the radiative lifetime of 0.56 ns in the isolated excited He atom. Keeping in mind that the asymptotic expression overestimates ICD lifetimes, the correct value might be sub fs. dICD is also efficient and would by itself lead the short lifetime of 0.29 ps, more than two orders of magnitude shorter than the radiative lifetime.

4.2 Ratios of the dICD to ICD Rates

Having seen that dICD, depending on the system and neighbor chosen, can be an efficient process, orders of magnitude faster than radiative decay, we concentrate in the following on the ratio of the dICD and ICD rates. From the asymptotic expressions for these rates, it is obvious that their ratio is simply provided by the ratio of the double- to single-ionization cross sections at the respective excess energy

$$\frac{\Gamma_{dICD}}{\Gamma_{ICD}} = \frac{\sigma_B^{++}}{\sigma_B^{+}}. \tag{4.4}$$

Consequently, the dICD to ICD ratio is determined by the cross sections of the neighbor alone, while the state of the decaying system determines the photon energy at which these cross sections have to be taken. Keeping this in mind, we discuss in the following further simple examples of systems with high dICD to ICD ratios.

Tab. 4.2 gives an overview of doubly ionized species, their double-ionization potential (DIP), their single-photon double-ionization (SPDI) to photoionization (PI) ratio at a specific photon energy and lists the corresponding publications from which the data was taken. The SPDI to PI ratio can be either the ratio of cross sections $\sigma_B^{++}/\sigma_B^{+}$ or the ratio of doubly to singly ionized ions M^{2+}/M^{+}. For C_{60} the respective cross sections are available, but not for the hydrocarbons listed in Tab. 4.2. In the absence of autoionization, the amount of singly and doubly charged ions is proportional to their respective cross sections, and thus, the ratio of doubly to singly charged ions is equivalent to the ratio of the SPDI to PI cross sections and we will not distinguish between them in the following [81, 89, 134–137]. The photon energy of 68.3 eV used in most of the entries of the table, is the excess energy of $Xe^{+}(4d^{-1})$ and just chosen as an example. Many more values are available in the literature cited. Before proceeding with the discussion, a brief comment on the ratios of Mg and Ca in the table is in order. Both ratios are the highest ones in the measured or calculated photon energy range. The SPDI cross section of Mg is measured and calculated from threshold to about 54 eV [75, 84–86, 125, 138], and the ratio reaches its highest point of 0.9 % at 36.5 eV. The ratio for Ca is calculated up to 43 eV and has its highest value of 4 % at 28.5 eV [84, 138].

As seen in Tab. 4.2, aromatic hydrocarbons: benzene, naphthalene, anthracene, pentacene,

Species	DIP [eV]	$\frac{\sigma_B^{++}(\omega)}{\sigma_B^{+}(\omega)} \cdot 100$ [%] $^{a)}$	References
Na	52.4 eV	0.9 % (68.3 eV)	[131–133]
K	36.0 eV	40 % (68.3 eV)	[132]
Be	27.5 eV	2.4 % (47.5 eV)	[84, 85]
Mg	22.7 eV	0.9 % (36.5 eV)	[75, 84–86]
Ca	18.0+eV	4.0 % (28.5 eV)	[84]
C_6 H_6	26.1 eV	23 % (68.3 eV) $^{a)}$	[89]
C_6 H_3 D_3	26.0 eV	5 % (68.3+eV) $^{a)}$	[83, 89]
selenophene	24.2 eV	80 % (275 eV) $^{a)}$	[83, 89]
pyrrole	24.2 eV	11.2 % (68.3 eV) $^{a)}$	[83, 89]
furan	25.2 eV	7.8 % (68.3 eV) $^{a)}$	[83, 89]
naphthalene	21.4 eV	9 % (68.3 eV) $^{a)}$	[83, 89]
anthracene	20.1 eV	13 % (68.3 eV) $^{a)}$	[83, 89]
pentacene	18.6 eV	31 % (68.3 eV) $^{a)}$	[83, 89]
coronene	18.8 eV	27.5 % (68.3 eV) $^{a)}$	[83, 89, 125]
pyrene	19.3 eV	19 % (68.3 eV) $^{a)}$	[83, 89, 125]
C_{60}	19.0 eV	49 % (68.3 eV)	[124, 126]

Table 4.2: Ratio of the photoionization to single-photon double-ionization cross sections for selected atoms and molecules. In the first column are the atomic or molecular species listed, in the second are their double-ionization potentials (DIP), in the third are the single-photon double-ionization (SPDI) to photoionization (PI) ratios at specific photon energies and the last contains the corresponding references. Data at other photon energies can be found in the respective references. The single-photon double-ionization to photoionization ratios are ratios of the respective cross sections or, if not available, ratios of the respective doubly to singly charged ions, whereby the second case is marked with an $^{a)}$.

pyrene, coronene, pyrrole, furan, and selenophene are suitable neighbors and offer rather low-lying double-ionization thresholds, ranging from 18.6 eV to 26.1 eV. These molecules play an important role in astrophysics [139–141]. Experimental investigations, as in Refs. [83, 89], show that the ratios of doubly charged to singly charged ions can reach values up to nearly 80 % (selenophene) for photon energies above 200 eV. For a photon energy of 68.3 eV, which is the excess energy of the $4d^{-1}$ vacancy of Xe, the ratio is distinctly smaller, but still reaches 23 % for benzene, 31 % for pentacene and even 49 % for C_{60}.

For even smaller excess energies, the SPDI to PI ratio typically further decreases. Nevertheless, dICD can still be efficient. In the following, we discuss briefly two sets of examples.

In the first, the decaying system is Ne^+ in the state $2s^2 2p^4(^1D)3s$ which has an excess energy of 30.5 eV [123] and its radiative rate is $w_A = 1.4 \cdot 10^9 \ \frac{1}{s}$ [142]. This state is populated by Auger decay [143–145]. We focus on the systems Ne^+-coronene, Ne^+-pyrene and Ne^+-pentacene. Intermolecular distances between Ne^+ and aromatic hydrocarbons typically range from 3 Å to 3.5 Å [146–148]. Coronene has a double-ionization threshold of 18.8 eV, while that of pyrene is 19.3 eV. Their ratios of SPDI to PI or the dICD to ICD ratios at 30.5 eV are about 5.9 % and

9 %, respectively [83, 89, 125]. The double-ionization threshold of pentacene lies at 18.6 eV and the SPDI to PI ratio at 30.5 eV reaches 10 % [83, 89, 125]. Even for photon energies near the threshold, the dICD to ICD ratios are sizable for aromatic hydrocarbons. We would like to stress that Ne^+ in the state $2\mathrm{s}^2 2\mathrm{p}^4(^1\mathrm{D})3\mathrm{s}$ cannot undergo autoionization and hence there are no competitive processes.

In the second set of examples, we combine the excited (1s → 2p) helium ion He^+ [149] with coronene, pyrene and pentacene. This ion was utilized to investigate ICD in the extreme He dimer [9, 10]. The 2p → 1s transition provides an excess energy of 40.8 eV. The dICD to ICD ratios for this virtual photon energy become: 13.7 % for coronene, 12.1 % for pyrene and even 19 % for pentacene [83, 89, 125].

These high ratios make clear that dICD can be a significant percentage of ICD for photon energies not too close to the double-ionization threshold. Since SPDI compared to photoionization can be more dominant at larger photon energies (see, e.g., selenophene in Tab. 4.2), the dICD to ICD ratio can become large for these energies. However, as the excess energy enters the asymptotic expression to the fourth power in the denominator of Eq. (3.25), the absolute impact of dICD is still expected to be small at high values of the energy.

Chapter 5

Perturbative Approach

After showing the derivation of the asymptotic dICD decay width under the assumption that the two species are well separated by an approximated internuclear distance $R \to \infty$, in the following chapter, we assume that the decay occurs in a weakly bound cluster A-B, where the characteristic values of R are a few Ångströms, and where A and B mostly retain the character of isolated species. The here presented results are taken from Ref. [64]. In contrast to the derivation of the asymptotic dICD width, we have to use now time-dependent perturbation theory to obtain an expression for the decay width Γ_{dICD}. Therefore, we introduce in Sec. 5.1 the states and Hamiltonians in the Hartree Fock approximation using second quantization. In Sec. 5.2, the derivation of the differential partial dICD decay width using second-order perturbation theory is shown. Subsequently, in Sec. 5.3, the corresponding transition amplitude and its computation are explained and discussed. In Sec. 5.4, the transition amplitude is used to derive the partial and total dICD decay width. To complete our studies, we finally show in Sec. 5.5 how the perturbatively derived transition amplitude reduces to the asymptotic one at the limit $R \to \infty$.

5.1 States and Hamiltonians in the Hartree Fock Approximation

The electronic Hamiltonian is divided into an unperturbed Hamiltonian $\hat{H}_0$ and an interaction Hamiltonian $\hat{H}_{int}$, which describes the perturbation,

$$\hat{H} = \hat{H}_0 + \hat{H}_{int}. \tag{5.1}$$

We select $\hat{H}_0$ as the Hartree-Fock (HF) Hamiltonian and $\hat{H}_{int} = \hat{V} - \hat{v}^{HF}$ is the interaction Hamiltonian, which contains the Coulomb Operator $\hat{V}$ and the average Hartree-Fock potential $\hat{v}^{HF}$. The Hartree-Fock Hamiltonian is given as $\hat{H}_0 = \sum_i \hat{f}(\boldsymbol{r}_i)$, where $\hat{f}$ stands for a one-electron Fock operator and the sum runs over all electrons in the system. The eigenfunctions φ_n and eigenvalues ε_n of the Fock operator are the spin-orbitals and the orbital energies.

In the following, we consider N-electron systems with a closed-shell electronic ground state. The decaying state is produced by removing an inner-valence electron, while the final states consist of the triply ionized system with two electrons in the continuum. To describe these states using the perturbation theory, one needs one-hole (1h), one-particle-two-hole (1p2h), and two-particle-three-hole (2p3h) unperturbed states. They are constructed by acting with the physical excitation operators on the HF ground state $|\Phi_0\rangle$:

$$|\Phi_i\rangle = c_i |\Phi_0\rangle , \tag{5.2a}$$

$$|\Phi_{ij}^a\rangle = c_a^\dagger c_i c_j |\Phi_0\rangle , \tag{5.2b}$$

$$|\Phi_{ijk}^{ab}\rangle = c_a^\dagger c_b^\dagger c_i c_j c_k |\Phi_0\rangle , \tag{5.2c}$$

where c_n and $c_n^\dagger$ are annihilation and creation operators for an electron in the orbital φ_n. Thereby, the indices a and b enumerate the particle orbitals and i, j, and k the hole orbitals. Note that the indices refer to spin-orbitals.

The unperturbed states are eigenstates of the unperturbed Hamiltonian $\hat{H}_0$, according to

$$\hat{H}_0 |\Phi_i\rangle = (E_0^{(0)} - \varepsilon_i) |\Phi_i\rangle = E_i^{(0)} |\Phi_i\rangle , \tag{5.3a}$$

$$\hat{H}_0 |\Phi_{ij}^a\rangle = (E_0^{(0)} + \varepsilon_a - \varepsilon_i - \varepsilon_j) |\Phi_{ij}^a\rangle = E_{aij}^{(0)} |\Phi_{ij}^a\rangle , \tag{5.3b}$$

$$\hat{H}_0 |\Phi_{ijk}^{ab}\rangle = (E_0^{(0)} + \varepsilon_a + \varepsilon_b - \varepsilon_i - \varepsilon_j - \varepsilon_k) |\Phi_{ijk}^{ab}\rangle = E_{abijk}^{(0)} |\Phi_{ijk}^{ab}\rangle , \tag{5.3c}$$

where $E_0^{(0)}$ is the zeroth-order energy of the ground state: $\hat{H}_0 |\Phi_0\rangle = E_0^{(0)} |\Phi_0\rangle$.

We derive the expression for the dICD width for a cluster consisting of two weakly bound components A and B, which we assume initially to be in their closed-shell ground state. Because the bonding is weak for the R of interest, the hole orbitals are just weakly perturbed orbitals of isolated A and B. Therefore, we will retain the indices A and B in denoting the orbitals, to indicate that they are mostly localized on the respective species. The decaying state has a hole in an inner-valence orbital $iv_A \equiv iv_A\eta$ ($\eta = \pm 1/2$ is the spin projection). In the final state, there are three holes that occupy the outer-valence orbitals $ov_A \equiv ov_A\lambda$, $ov_B \equiv ov_B\mu$, and $ov_B' \equiv ov_B'\sigma$, while the two particles occupy the continuum orbitals $\varepsilon_k \equiv \varepsilon_k\delta$ and $\varepsilon_{k'} \equiv \varepsilon_{k'}\nu$. We denote the initial state as $|\Phi_{iv_A}\rangle$ and the final state as $|\Phi_{ov_A ov_B ov_B'}^{\varepsilon_k \varepsilon_{k'}}\rangle$, where the spin indices are suppressed for clarity. The total spin of the decaying state is $S = 1/2$, and it is conserved in the decay, since $\hat{H}_{int}$ is spin-free.

5.2 Second-order Perturbation Theory

In contrast to the asymptotic approach, where the approximation of two well-separated species allows us the expansion of the interaction Coulomb operator and, consequently, the use of experimentally measurable quantities to describe the processes on A and B, we now have to adjust Fermi's Golden to compute the dICD rate without these assumptions. Fermi's Golden rule is nothing else than the time-dependent first-order perturbation theory at its limit t→ ∞, which removes the time dependency. Since the transition between the unperturbed decaying and final state is forbidden in first order, we use the time-dependent second-order expansion to obtain the differential partial dICD decay width. The general derivation of the time-dependent second-order perturbation theory is presented below, see also Refs. [116, 150].

The eigenstates $|\Phi_N\rangle$ of the unperturbed Hamiltonian, $\hat{H}_0 |\Phi_N\rangle = E_N^{(0)} |\Phi_N\rangle$, form a complete basis, which expands the time-dependent wave function as

$$\Psi(t) = \sum_N c_N(t) \exp(-\frac{i}{\hbar} E_N^{(0)} t) |\Phi_N\rangle . \tag{5.4}$$

Here, $c_N(t)$ is the time-dependent expansion coefficient. At the time t_0 the system is in the eigenstate $|\Phi_I\rangle$ of $\hat{H}_0$ resulting in the initial condition $c_N(t_0) = \delta_{NI}$. At later time t the probability of finding the system in the eigenstate $|\Phi_F\rangle$ of $\hat{H}_0$ is given by $w_{F\leftarrow I}(t) = |c_F(t)|^2$. To determine the coefficients $c_N(t)$, the expansion of the wave function is inserted into the time-dependent Schrödinger equation, $\hat{H} |\Psi(t)\rangle = i\hbar \frac{d |\Psi(t)\rangle}{dt}$, where $\hat{H}$ is the full Hamiltonian as defined in Eq. (5.1). Multiplying from the left $\langle \Psi_M|$ and integrating over $\int_{t_0}^{t}$, gives the implicit solution for the expansion coefficient

$$\begin{aligned} c_M(t) &= c_M(t_0) + \frac{1}{i\hbar} \int_{t_0}^{t} \sum_N H_{MN}^{int} \exp\left[\frac{i}{\hbar}(E_M^{(0)} - E_N^{(0)})t'\right] c_N(t')\, dt' \\ &= c_M(t_0) + \frac{1}{i\hbar} \int_{t_0}^{t} dt' \sum_N H_{MN}^{int} \exp\left[\frac{i}{\hbar}(E_M^{(0)} - E_N^{(0)})t'\right] c_N(t_0) \\ &\quad + \frac{1}{(i\hbar)^2} \int_{t_0}^{t} dt' \sum_N H_{MN}^{int} \exp\left[\frac{i}{\hbar}(E_M^{(0)} - E_N^{(0)})t'\right] \\ &\qquad \int_{t_0}^{t'} dt'' \sum_L H_{NL}^{int} \exp\left[\frac{i}{\hbar}(E_N^{(0)} - E_L^{(0)})t'\right] c_L(t'') + ..., \end{aligned} \tag{5.5}$$

where $H_{MN}^{int} = \langle \Phi_M | \hat{H}_{int} | \Phi_N \rangle$ is the corresponding matrix element of the interaction Hamiltonian. Here, the expression for the transition amplitude $c_F(t)$ to the final state $|\Phi_F\rangle$ is given by the second order and is obtained by inserting $c_L(t'')$ and applying the initial condition, which cancels the sum over L

$$c_F(t) = \frac{1}{(i\hbar)^2} \sum_N H_{FN}^{int} H_{NI}^{int} \int_{t_0}^{t} dt' \exp\left[\frac{i}{\hbar}(E_F^{(0)} - E_N^{(0)})t'\right] \int_{t_0}^{t'} dt'' \exp\left[\frac{i}{\hbar}(E_N^{(0)} - E_I^{(0)})t''\right]. \tag{5.6}$$

In the following, we compute the transition amplitude at its limits. Therefore, we define $t = \infty$ and $t_0 = -\infty$. The integration over t'' can be immediately performed, while the relation $\int_{-T/2}^{T/2} dt \exp\left[\frac{i}{\hbar}(E_F^{(0)} - E_I^{(0)})t\right] = 2\pi\hbar\delta(E_F^{(0)} - E_I^{(0)})$ [150] is used for the second integral resulting in

$$c_F(t \to \infty) = i2\pi \sum_N \frac{H^{int}_{FN} H^{int}_{NI}}{(E^{(0)}_N - E^{(0)}_I)} \delta(E^{(0)}_F - E^{(0)}_I) \tag{5.7}$$

The probabilty to find the system at infinite times in the eigenstate $|\Phi_F\rangle$ is obtained by using $[2\pi\hbar\delta(E^{(0)}_F - E^{(0)}_I)]^2 = 2\pi\hbar\delta(E^{(0)}_F - E^{(0)}_I)T$ [150]. The square of the absolute value can be written as

$$|c_F(t \to \infty)|^2 = w_{F\leftarrow I}(t \to \infty) = \frac{2\pi}{\hbar} \Big| \sum_N \frac{H^{int}_{FN} H^{int}_{NI}}{(E^{(0)}_N - E^{(0)}_I)} \Big|^2 \delta(E^{(0)}_F - E^{(0)}_I) t \tag{5.8}$$

To determine the probability per unit time, $\dfrac{w_{F\leftarrow I}(t \to \infty)}{t}$ is integrated over an infinitesimal energy range around the initial energy $E^{(0)}_I$

$$\begin{aligned} P_{F\leftarrow I} &= \lim_{\eta \to 0} \int_{E^{(0)}_I - \eta}^{E^{(0)}_I + \eta} \frac{2\pi}{\hbar} \Big| \sum_N \frac{H^{int}_{FN} H^{int}_{NI}}{(E^{(0)}_N - E^{(0)}_I)} \Big|^2 \delta(E^{(0)}_F - E^{(0)}_I) \rho(E^{(0)}_F) \, dE^{(0)}_F \\ &= \frac{2\pi}{\hbar} \Big| \sum_N \frac{H^{int}_{FN} H^{int}_{NI}}{(E^{(0)}_N - E^{(0)}_I)} \Big|^2 \rho(E^{(0)}_F = E^{(0)}_I), \end{aligned} \tag{5.9}$$

where for energy-normalized final states, the density of the final states becomes $\rho(E^{(0)}_F) = 1$. The relation between the probability per unit time and the decay width is given by $\Gamma = \hbar P$. After showing the general derivaiton, we return to dICD, where the initial state is the 1h-state $|\Phi_{iv_A}\rangle$ and the final state is the 2p3h-state $|\Phi^{\varepsilon_k \varepsilon_{k'}}_{ov_A ov_B ov'_B}\rangle$ as defined in Sec. 5.1. Finally, the differential partial dICD decay width reads

$$\Gamma_{ov_A ov_B ov'_B}(\varepsilon, \varepsilon_{k'}) = 2\pi \Big| \sum_N \frac{\langle \Phi^{\varepsilon_k \varepsilon_{k'}}_{ov_A ov_B ov'_B} | \hat{H}_{int} | \Phi_N \rangle \langle \Phi_N | \hat{H}_{int} | \Phi_{iv_A} \rangle}{(E^{(0)}_N - E^{(0)}_{iv_A})} \Big|^2 . \tag{5.10}$$

Note that due to energy conservation the initial energy equals the final energy, $E^{(0)}_{iv_A} = E^{(0)}_{\varepsilon_k \varepsilon_{k'} ov_A ov_B ov'_B}$ (see Eq. (5.9)). Furthermore, $E^{(0)}_N \neq E^{(0)}_{iv_A}$ and $E^{(0)}_N \neq E^{(0)}_{\varepsilon_k \varepsilon_{k'} ov_A ov_B ov'_B}$ because the first order gives no contribution, $\langle \Phi^{\varepsilon_k \varepsilon_{k'}}_{ov_A ov_B ov'_B} | \hat{H}_{int} | \Phi_N \rangle = 0$. Alternatively to expanding the Hamiltonian by using time-dependent perturbation theory, we can also adjust Fermi's golden rule (Eq. (3.6)) by expanding directly the initial and final state in the framework of many-body perturbation theory [151] resulting in the same expression for the differential partial dICD decay width as Eq. (5.10), see App. A.

5.3 Transition Amplitude

To evaluate the second-order transition amplitude in Eq. (5.10),

$$T^{(2)}_{\varepsilon_k \varepsilon_{k'} ov_A ov_B ov'_B : iv_A} = \sum_N \frac{\langle \Phi^{\varepsilon_k \varepsilon_{k'}}_{ov_A ov_B ov'_B} | \hat{H}_{int} | \Phi_N \rangle \langle \Phi_N | \hat{H}_{int} | \Phi_{iv_A} \rangle}{(E^{(0)}_N - E^{(0)}_{iv_A})}, \tag{5.11}$$

the summation over the eigenstates $|\Phi_N\rangle$ of the unperturbed Hamiltonian and the corresponding eigenenergies $E_N^{(0)}$ is performed, where only 1p2h- and 2p3h-states give a contribution, see App. A. The resulting expression for the transition amplitude 5.11 consists of eighteen terms, which can be interpreted in terms of known physical processes. The complete list of the terms and the details of their derivation can be found in App. A. In the following, we discuss the structure and the physical meaning of four characteristic terms.

We begin with the term, which arises when the coupling proceeds via the unperturbed virtual state $\sum_{p_B} |\Phi^{p_B}_{ov_A ov_B}\rangle \langle \Phi^{p_B}_{ov_A ov_B}|$ (see Tab. A.1 combination 1 in App. A). The sum $\sum_{p_B}$ runs overall particle orbitals of B including bound and continuum states. The term reads

$$\sum_{p_B} + \frac{V_{\varepsilon_k \varepsilon_{k'}[ov'_B p_B]}}{\left(\varepsilon_k + \varepsilon_{k'} - \varepsilon_{ov'_B} - \varepsilon_{p_B} + i0^+\right)} V_{p_B iv_A ov_B ov_A}. \tag{5.12}$$

After the electron transition from the outer-valence orbital ov_A to the inner-valence orbital iv_A, an electron of B is ejected from the outer-valence orbital ov_B. The emitted electron p_B interacts with another bound electron of B in the outer-valence orbital ov'_B knocking it out, which leads to two electrons ε_k and ε'_k in the continuum. This process encoded in the amplitude in Eq. (5.12) (see Fig. 5.1(a)) can be interpreted as an ICD step followed by knock-out ionization of B. The energy denominator has a singularity for the limiting case, if one of the emitted electrons takes the whole excess energy: $\varepsilon_{p_B} = \varepsilon_k + \varepsilon_{k'} - \varepsilon_{ov'_B}$. Therefore, an infinitesimal imaginary part $+i0^+$ has to be added to the energy denominator. The process is analogous to that describing knock-out mechanism in double Auger decay or SPDI, where it is the dominant mechanism for photon energies near the double-ionization threshold [72–80].

Next, we consider the term (see Fig. 5.1(b)), obtained by inserting the unperturbed virtual state $\sum_{h_B} |\Phi^{\varepsilon_k}_{ov_A h_B}\rangle \langle \Phi^{\varepsilon_k}_{ov_A h_B}|$ into the dICD transition amplitude in Eq. (5.11) (see Tab. A.1 combination 1 in App. A). The result reads

$$\sum_{h_B} -V_{iv_A \varepsilon_k ov_A h_B} \frac{V_{h_B \varepsilon_{k'}[ov_B ov'_B]}}{\left(\varepsilon_{h_B} + \varepsilon_{k'} - \varepsilon_{ov_B} - \varepsilon_{ov'_B}\right)}, \tag{5.13}$$

where the summation runs over all hole orbitals on B. The first matrix element is the ICD amplitude, which corresponds to the relaxation of the initial vacancy on A and the first ionization of B. The second matrix element describes the relaxation of B accompanied by the emission of the second electron. In other words, following the energy transfer in ICD, the electron of B is ejected from h_B to the continuum with the energy ε_k. Because of this sudden ionization, the potential on B changes rapidly, and the orbital relaxation leads to the emission of another electron from ov'_B, which has the kinetic energy $\varepsilon_{k'}$, see Fig. 5.1(b). This mechanism is analogous to shake-off processes, which appear in double Auger decay and SPDI.

In the last two examples, we focus on the unperturbed virtual 2p3h-states, $\sum_{p_1 p_2 h_1 h_2 h_3} |\Phi^{p_1 p_2}_{h_1 h_2 h_3}\rangle \langle \Phi^{p_1 p_2}_{h_1 h_2 h_3}|$.

The presented terms arise by inserting the unperturbed states $|\Phi^{p_B\varepsilon_{k'}}_{ov_B ov'_B iv_A}\rangle$ and $|\Phi^{\varepsilon_k\varepsilon_{k'}}_{ov'_B h_B iv_A}\rangle$ (see Tab. A.2 configuration 5 and 3 in App. A) into the dICD transition amplitude (see Eq. (5.11))

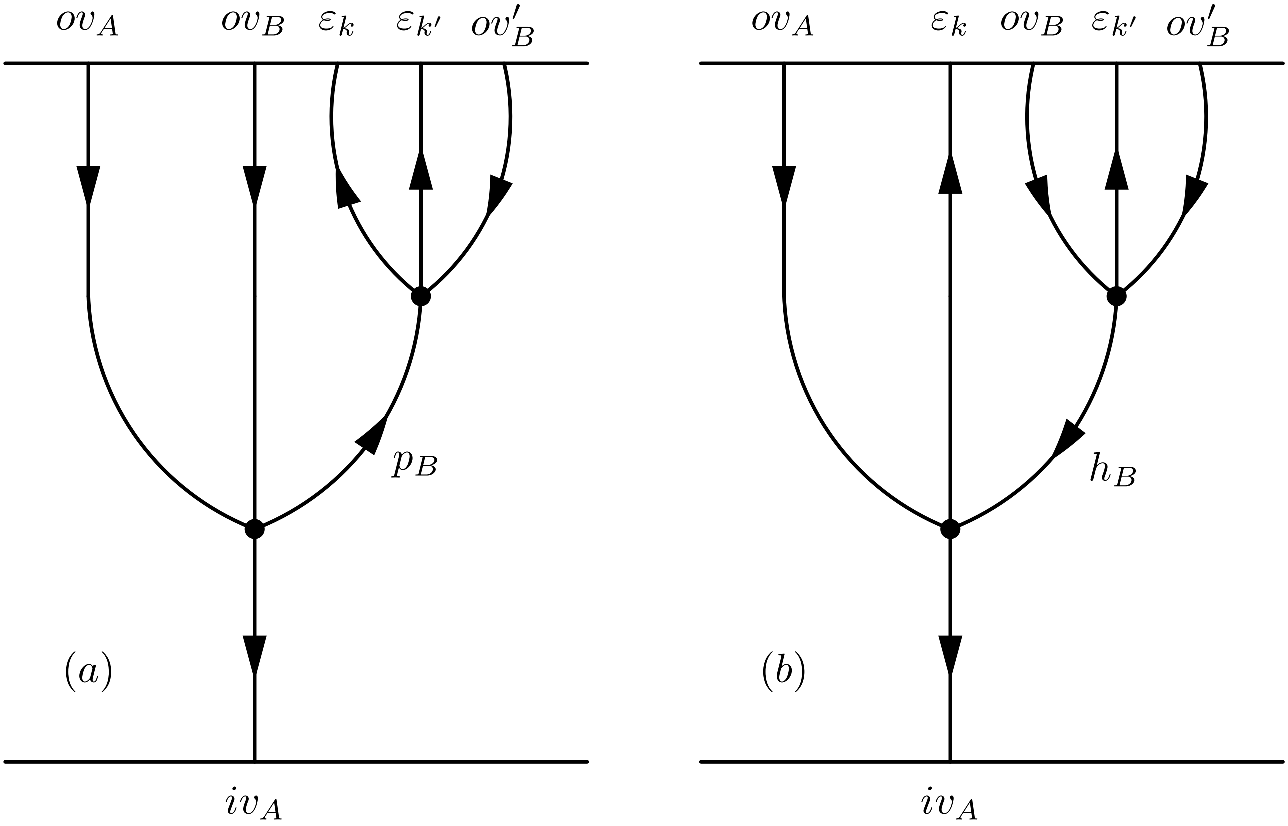

Figure 5.1: Diagrammatic representation of the dICD transition amplitudes which correspond to the knock-out (a) and the shake-off (b) mechanisms. The horizontal lines represent the initial and the final states. The dots describe the interaction. The arrows pointed downwards denote occupied (hole) orbitals, while the arrows pointed upwards denote unoccupied (particles) orbitals.

$$\sum_{p_B} -V_{iv_A\varepsilon_k ov_A p_B}\frac{V_{p_B\varepsilon_{k'}[ov_B ov'_B]}}{\left(\varepsilon_{p_B}+\varepsilon_{k'}-\varepsilon_{ov_B}-\varepsilon_{ov'_B}\right)}, \tag{5.14}$$

$$\sum_{h_B} +\frac{V_{\varepsilon_k\varepsilon_{k'}[ov'_B h_B]}}{\left(\varepsilon_k+\varepsilon_{k'}-\varepsilon_{ov'_B}-\varepsilon_{h_B}\right)}V_{h_B iv_A ov_B ov_A}. \tag{5.15}$$

Both terms include the electron transition from ov_A to iv_A and the direct double ionization of B, where the coupling between the two species proceeds in Eq. (5.14) via particle and in Eq. (5.15) via hole orbitals. These two mechanisms can be understood as stemming from the ground-state correlations of the two species participating in dICD (see Fig. 5.2). These double-ionization pathways due to ground-state correlations are known from SPDI, where they arise from the perturbative expansion of the ground state of an atom or a molecule being ionized. Similar mechanisms also appear in double Auger decay when unperturbed 2p3h-states are used in the first-order expansion of the core-hole state.

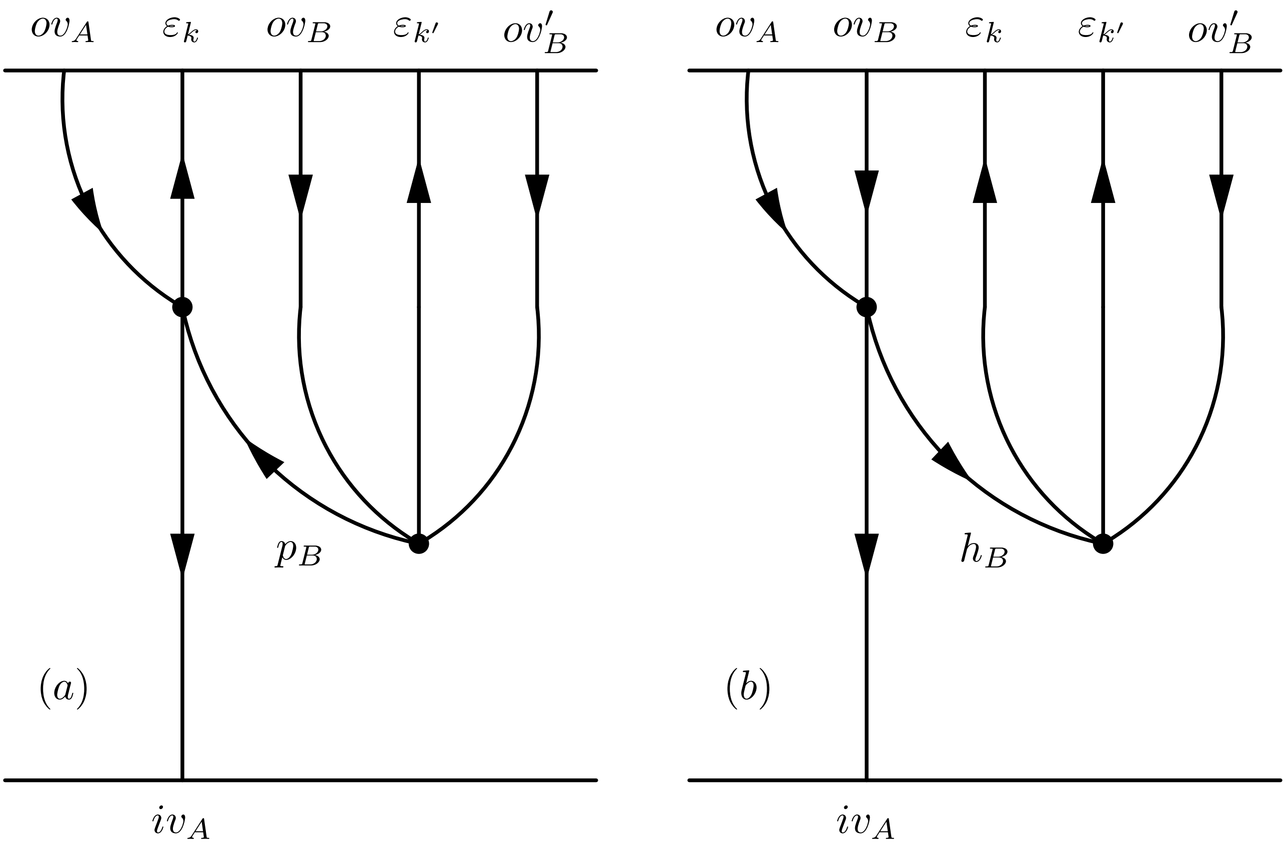

Figure 5.2: Diagrammatic representation of the dICD transition amplitude which corresponds to the initial state correlations: initial state correlation via a particle p_B (a) and initial state correlation via a hole h_B (b). The horizontal lines represent the initial and the final states. The dots describe the interaction. The arrows pointed downwards denote occupied (hole) orbitals and The arrows pointed upwards denote unoccupied (particles) orbitals.

5.4 Total dICD Decay Width

The transition amplitude $T^{(2)}_{\varepsilon_k\varepsilon_{k'}ov_Aov_Bov'_B;iv_A}$ (see App. A) refers to a specific set of spin-orbitals. To construct the differential partial decay width $\Gamma_{ov_Aov_Bov'_B}(\varepsilon,\varepsilon_{k'})$ for a state-to-state transition according to Eq. (5.10), one has to deal with both spin and spatial degeneracies of the involving orbitals. This means that for a final state characterized by spatial orbitals ov_A, ov_B, and ov'_B one has to average over initial state and to sum over final state degeneracies [117]. In the case of an atomic system the orbitals iv_A ov_A ov_B and ov'_B are described by orbital angular momenta l and the respective degeneracies are given by the magnetic quantum numbers m_l. Consequently, the absolute value squared reads

$$\overline{|T^{(2)}_{\varepsilon_k\varepsilon_{k'}ov_Aov_Bov'_B;iv_A}|^2} = \frac{1}{2\,l_{iv_A}+1}\frac{1}{2\,s_{iv_A}+1}\sum_{\substack{m_{l_{iv_A}}m_{l_{ov_A}}\\ m_{l_{ov_B}}m_{l_{ov'_B}}}}\sum_{\eta\lambda\delta\nu\mu\sigma}|T^{(2)}_{\varepsilon_k\varepsilon_{k'}ov_Aov_Bov'_B;iv_A}|^2. \tag{5.16}$$

It follows for the differential partial decay width according to Eq. (5.10):

$$\Gamma_{ov_Aov_Bov'_B}(\varepsilon,\varepsilon_{k'}) = 2\pi\,\overline{|T^{(2)}_{\varepsilon_k\varepsilon_{k'}ov_Aov_Bov'_B;iv_A}|^2}. \tag{5.17}$$

By integrating the differential partial decay width over the energy of one of the emitted electrons and by summing over different degenerate final states of B we obtain the partial decay width which corresponds to some virtual photon energy $\hbar\omega$ (see also Eq. (3.25))

$$\Gamma_{dICD}(\omega) = \sum_{ov_B ov'_B} \int_0^{\varepsilon} \Gamma_{ov_A ov_B ov'_B}(\varepsilon, \varepsilon_{k'})\, d\varepsilon_{k'}. \tag{5.18}$$

For the total decay width of dICD, the summation over the spin-orbital ov_A is added. The sum $\sum_{ov_A ov_B ov'_B}$ includes different relaxation pathways of A and thus different virtual photon energies. Consequently, it contains all energetically possible transitions on B for the given virtual photon energies. The total decay width of dICD reads

$$\Gamma_{dICD} = \sum_{ov_A ov_B ov'_B} \int_0^{\varepsilon} \Gamma_{ov_A ov_B ov'_B}(\varepsilon, \varepsilon_{k'})\, d\varepsilon_{k'}. \tag{5.19}$$

Once the values of the two-electron integrals and the orbital energies are known, the various widths can be computed numerically.

5.5 Derivation of the asymptotic expression from the perturbatively derived transition amplitude

In this subsection, we show that the expression Γ_{dICD} in Eq. (5.19) correctly reduces to Eq. (3.25) for $R \to \infty$. The total Coulomb operator $\hat{V}$ is rewritten as

$$\hat{V} = \hat{V}_A + \hat{V}_B + \hat{V}_{AB}. \tag{5.20}$$

$\hat{V}_A$ and $\hat{V}_B$ are the electron repulsion operators of A and B, which are responsible for local processes, while $\hat{V}_{AB}$ represents the interaction between the electrons of A and B. The amplitudes, which involve electron transfer, decay exponentially with R and can be neglected [15]. Furthermore, the interaction Coulomb operator $\hat{V}_{AB}$ is expanded (see Eq. (3.5)). The effect of these two approximations is to reduce the number of terms in the transition amplitude from eighteen to eight, see App. B, which represents the four different mechanisms: knock-out (KO), shake-off (SO) and the two types of ground-state correlations (GSC_p and GSC_h) as described above.

After the multipole expansion of the interaction Coulomb operator $\hat{V}_{AB}$ the Coulomb integrals of the surviving eight terms of the form $V_{p_B iv_A h_B ov_A}$ read

$$V_{p_B iv_A h_B ov_A} \approx \frac{1}{R^3}\Big[\langle \varphi_{iv_A}|\hat{\boldsymbol{d}}_A|\varphi_{ov_A}\rangle \langle \varphi_{p_B}|\hat{\boldsymbol{d}}_B|\varphi_{h_B}\rangle - 3\cdot \langle \varphi_{iv_A}|\hat{\boldsymbol{d}}_A \boldsymbol{e_R}|\varphi_{ov_A}\rangle \langle \varphi_{p_B}|\hat{\boldsymbol{d}}_B \boldsymbol{e_R}|\varphi_{h_B}\rangle\Big]. \tag{5.21}$$

Inserting this expansion into the surviving eight terms of the transition amplitude (see Eq. (B.1) in App. B) and averaging its absolute value squared over the degeneracies, allows us to represent the width via quantities related to isolated A and B. The dICD transition amplitude becomes a product of the dipole transition amplitude on A, $\langle \varphi_{iv_A} | \hat{\boldsymbol{d}}_A | \varphi_{ov_A} \rangle$, and of the double-ionization amplitude of B, $(\boldsymbol{T}(KO) + \boldsymbol{T}(SO) + \boldsymbol{T}(GSC_p) + \boldsymbol{T}(GSC_h))$. For details of the derivation, see App. B. The total decay width Γ_{dICD} of dICD (see Eq. (5.19)) expressed by the various individual transition amplitudes reads

$$\Gamma_{dICD} = 2\pi \frac{2}{3R^6} \sum_{ov_A} \overline{\left| \langle \varphi_{iv_A} | \hat{\boldsymbol{d}}_A | \varphi_{ov_A} \rangle \right|^2} \sum_{ov_B ov'_B} \int_0^{\varepsilon} d\varepsilon_{k'} \, \overline{\left| (\boldsymbol{T}(KO) + \boldsymbol{T}(SO) + \boldsymbol{T}(GSC_p) + \boldsymbol{T}(GSC_h)) \right|^2}, \tag{5.22}$$

where the overlines denote that the absolute values squared of the corresponding transition amplitudes are averaged over degeneracies. $\boldsymbol{T}(KO)$ and $\boldsymbol{T}(SO)$ are respectively the knock-out and the shake-off amplitudes, while $\boldsymbol{T}(GSC_p)$ and $\boldsymbol{T}(GSC_h)$ appear due to the ground-state correlations. The sum of these transition amplitudes equals the total amplitude of the SPDI cross section [72, 73]. Employing Eq. (3.24), we rewrite the single-differential SPDI cross section to be in our nomenclature [72–74]:

$$\frac{d\sigma_B^{++}(\omega)}{d\varepsilon_{k'}} = \frac{4\pi^2}{3} \frac{\omega}{c} \sum_{ov_B ov'_B} \overline{\left| (T(KO) + T(SO) + T(GSC_p) + T(GSC_h)) \right|^2}. \tag{5.23}$$

The explicit SPDI amplitudes in our nomenclature can be found in App. C.

As in Chap. 3, the lifetime τ_A (see Eq. (3.23)) and the single-differential single-photon double-ionization cross section $\frac{d\sigma_B^{++}(\omega)}{d\varepsilon_{k'}}$ (see Eq. (5.23)) can be identified in the expression for the dICD rate (see Eq. (5.22)). As $\frac{d\sigma_B^{++}(\omega)}{d\varepsilon_{k'}}$ takes only one virtual photon energy into account, one can consider a single relaxation pathway of A and finally arrive at the asymptotic partial decay width

$$\Gamma_{dICD}(\omega) = \frac{3\hbar}{4\pi} \left(\frac{c}{\omega} \right)^4 \frac{\tau_A^{-1} \sigma_B^{++}(\omega)}{R^6}, \tag{5.24}$$

which coincides with the expression for the dICD rate derived above directly from Fermi's Golden rule [116] at large R (see Eq. (3.25) in Chap. 3).

Chapter 6

Discussion and Outlook

The discussed ideas and future prospects are based on Ref. [64].

As shown in Chap. 4, the asymptotic dICD decay width in Eq. (3.25) builts the lower bound of the actual decay width, which is confirmed by Ref. [90], where is shown that the decay width increases for decreasing internuclear distances. Furthermore, due to the fact that it is expressed by experimentally measurable quantities, the asymptotic dICD decay width is a useful equation, providing a quick estimate of the dICD decay width. Although the ratio of the asymptotic dICD to the asymptotic ICD decay width reduces to the ratio of double to single ionization, the ratio can be significantly large depending on the system, which also demonstrates the relevance of dICD.

While the asymptotic dICD width accounts only for processes like knock-out, shake-off, and ground-state correlations, which are familiar from the discussion of the single-photon double-ionization, the perturbative dICD width covers further mechanisms which are important at shorter interatomic distances. To finally answer our question, we asked at the beginning, of why dICD is so efficient in comparison to the local processes such as SPDI and dA, perturbation theory has to be implemented. We need to understand, if these further mechanisms are the reason for the efficiency of dICD, seen in Ref. [68], but the computation is a large effort by itself because of the two electrons in the continuum of a non-spherical system.

At the moment, there are no approaches to simultaneously overcome both of these difficulties, but methods to describe the double ionization of an atom or the single ionization of a molecule are already known. The single-center expansion can be used to approximate a non-spherical system in the case of involved molecules, see Refs. [152, 153]. The easiest way to define double-continuum states is the use of 2C wave functions [154], which are antisymmetrized products of two Coulomb wave functions. They are easy to construct but not very precise because the interaction between the two emitted electrons is not considered, leading to the preference that both electrons are emitted in the same direction. If the two ejected electrons are close in energy, as in the knock-out mechanism, the interaction can be approximated by the Gamov factor as in Refs. [69, 155, 156], where less numerical effort is needed than for the computation of 3C wave functions [157–159] or other model wave functions, which take the interactions in the three-body Coulomb problem into account, for an overview see [160]. In these models, the two electrons moving in the double continuum of the nucleus are represented by three non-interacting two-body subsystems. Widely applied numerical methods to compute the SPDI and dA cross sections are based on the close-coupling approximation as convergence close coupling (CCC) [161, 162], time-dependent close coupling (TDCC) [163] and the R-Matrix formalism [164, 165]. In general, dealing with electron correlations remains difficult. Therefore, the double ionization process is often approximated as single ionization with subsequent electron-impact ionization. All introduced methods to describe double continua are only applied in small systems including hydrogen or helium [53, 157–159, 166–168] and heliumlike atoms [169] as alkaline-earth metals [84–86, 170, 171], which can be approximated as two-electron systems. Furthermore, some promising numerical approaches exist, which might have the potential to compute the dICD decay width in the future. The Fano-ADC method, which belongs to a family of *ab initio* techniques for computing electronic decay widths, was successfully applied to various ICD processes [172–175]. Furthermore, an ADC(2,2) approximation was introduced which has the potential to describe dICD of singly ionized states [176]. Recently, a new method was developed to compute double- and single-ionization cross sections using a fully correlated close-coupling approach and a Dyson orbital analysis [166]. The new approach was tested in antiproton-helium and even antiproton–molecular hydrogen collisions in the keV range. Further development and implementation of these numerical techniques are necessary to investigate the qualitative and quantitative influence of these additional processes. It is beyond the scope of the present work and is left for the future.

To complete our dICD studies and finally answer the question of the beginning regarding the efficiency of dICD, the electron spectra in Ref. [68] have to be computed. After implementing the transition amplitude, which is a large effort for the reasons explained above, the differential partial decay width (see Eq. (5.17)) can be used to determine the dICD spectra. To compare with experiment, one has also to take into account the impact of the nuclear motion in the system undergoing dICD as done before for ICD. This requires additional method development. However, in many cases, a comparison can be done without the inclusion of the nuclear motion, if we assume instantaneous decay and small energy broadening due to the distribution of the interatomic distances in the vibrational wave packet compared to the total energy of the two emitted electrons. Both assumptions hold for the systems we considered. The total decay width is of the order of several meV and is larger than the characteristic frequencies in the decaying state, while the total energy of the emitted electrons is larger than several eV. Under these assumptions, we may resort to Eq. (5.17) as such. We briefly mention that beyond the dICD electron spectra, triply differential cross sections can be computed as well from the absolute value squared of the dICD amplitude (see Eq. (5.16)) analogously to the case of one-photon double-ionization process as shown in [177–179].

Once these technical difficulties are resolved, one can think about studying dICD in bigger systems and about new processes related to dICD. The three examples below are taken from Ref. [64].

After having demonstrated that dICD can be a significant decay channel depending on the system and its neighbor, we discuss the influence of several neighbors. For ICD it has been shown that the decay width of the system increases with increasing number N of the surrounding neighbors [4, 12, 180, 181]. A linear behavior with N was found in $NeHe_N$ and $CaHe_N$ clusters [180], while in $Na^+(H_2O)_N$ and $Mg^{2+}(H_2O)_N$ it was shown that the decay width deviates from a linear behavior [181], due to the polarization of water by the charged ions. Each water molecule becomes polarized by the alkali ion and shields the ion's charge from the other water molecules. Every additional water molecule becomes less polarized due to the shielding of the charge and gives a smaller contribution to the total ICD width. Consequently, further water molecules get less and less polarized and their contributions decrease with increasing N. The effect increases for higher-charged ions. However, for a small number of neighbors, a linear increase of the ICD width scaling with N can be assumed [180, 181]. From the asymptotic equation, one obtains a linear growth with the number N of equivalent neighbors of the rate of dICD as well as long as the neighbors do not interact with each other. Once the neighbors do interact with each other and/or the intermolecular distances are too short for the asymptotic expression to be valid, the dICD rate grows with N, but the behavior as a function of N will depend on the situation at hand and has still to be investigated.

Large virtual photon energies are present in core ionization and excitation processes, which preferentially decay by Auger. In clusters and condensed phases, however, core-ICD competes with Auger decay. In rare gas clusters, the ICD to Auger decay ratio has recently been found to nevertheless amount to around 1 % in Ar and to a few percent in Xe clusters [149, 182]. The timescale of the core level ICD was determined to be 33 fs for the 2p core hole of aqueous Ca^{2+} implying that the ICD to Auger decay ratio can be around 10 % [183]. All of this gives hope that dICD may be a relevant process in core ionization and excitation in extended systems.

For completeness, we finally briefly mention other interatomic/intermolecular processes where two electrons can be emitted. As explained above for $Ne@C_{60}$, the excess energy of Ne after 2s ionization is insufficient for dICD to take place. However, another process can take place which has been termed dETMD [67] (ETMD stands for electron transfer mediated decay [15]). The process $Ne^+(2s^{-1})@C_{60} \rightarrow Ne@C_{60}^{3+} + 2e^-$ gives rise to a neutral Ne and a triply charged C_{60} cage, whereby two electrons have been emitted in concert [67]. Doubly excited states, for instance of He [184, 185], possess sufficient excess energy to undergo dICD with various neighbors. Since two electrons are excited, the process is expected to be sequential rather than non-sequential in this case. Another interesting two-step process can also take place with doubly excited species. The doubly excited species can first autoionize and the resulting ion can then undergo ETMD with a neighbor [186]. As a consequence, two electrons have been emitted, one from the species carrying the excess energy and one from the neighbor.

Besides the fact that dICD is due to its efficiency an interesting topic by itself - especially as long as the question if the additional mechanisms contribute significantly to the dICD decay width stays unanswered - dICD opens a field to a variety of new applications and related processes.

Chapter 7

Conclusion

The double-ionization mechanism by interatomic or intermolecular Coulombic decay, briefly called dICD, is investigated, where the presented results are reported in Ref. [64]. Motivated by the findings of Ref. [68] that the efficiency of dICD is comparable to the one of ICD although in the case of competing local processes the ratios of the double- to the single-ionization channel amount only to a few percent, we derived the dICD decay width in different ways as an indicator for the efficiency of the new decay channel.

For large separations between the ionized atom or molecule and its neighbor, an explicit asymptotic expression for the decay rate of dICD was derived, which solely depends on experimentally measurable quantities. Within the asymptotic expressions, the dICD to ICD ratio equals the ratio of the cross sections of single-photon double- and single-ionization. Therefore, the decay width provides a lower bound to the full dICD width and is a useful estimate of the exact total dICD width. The asymptotic expression was applied to several examples showing, that dICD depending on the system is a relevant decay channel. Furthermore, the knowledge of these ratios for various photon energies can thus help to choose atoms and molecules for which the ratio of dICD to ICD is favorable. The probability that an atom absorbs a resonant photon and emits a virtual photon is much higher than that to directly doubly ionize an atom or molecule by the same photon. Consequently, doubly ionizing a system in an environment via dICD can become a more relevant process than SPDI. As for ICD, it is argued that the dICD rate grows substantially with the number of neighbors which can be doubly ionized by the available excess energy. This fact can make dICD important in true environments, where the number of available neighbors is usually high.

Apart from the analysis of the asymptotic expression, we developed an analytical expression for the dICD decay width which is valid for smaller distances between the species by using perturbation theory. This results in a comprehensive expression for the total decay width of dICD, allowing one to distinguish various intra- and interatomic and molecular processes. To further analyze the resulting perturbative decay width, we considered it at the limit of separated subsystems, which reduces the expression to the asymptotic formula. The asymptotic decay width only contains the terms reflecting the processes, which are already known from SPDI. This confirms the suspicion that the additional terms arising in the perturbative dICD expression are also responsible for the efficiency of the dICD channel, besides the higher probability of absorbing a photon and emitting a virtual photon in comparison to the direct double ionization. The numerical computation of the perturbative dICD decay is still an effort by itself due to the double continuum of a non-spherical system, but it is needed to finally answer the question regarding the dICD efficiency, which makes further investigations necessary.

In general, dICD is an interesting decay channel due to its efficiency in comparison to competing local processes. Even the asymptotic decay width shows that, depending on the system, dICD is a relevant decay channel, although its real decay width is estimated to be higher. Furthermore, deriving the perturbative dICD decay width provides an insight into the corresponding intra- and interatomic and molecular mechanisms leading to dICD. Finally, as a new decay mechanism, dICD opens a field to further investigations regarding dICD itself or applications and related processes.

Part II

Applications of ICD

Chapter 8

Theoretical Framework

In this chapter, the analytical expressions of the photoelectron (PE), the interatomic Coulombic decay (ICD)-electron, as well as the kinetic-energy-release (KER) spectrum for dimers undergoing ICD after ionization are derived. The underlying theory is based on Refs. [104, 105, 107–112], which can be consulted for more detailed explanations. Furthermore, parts of the derivations were published in Refs. [65] and [66] .

This chapter is divided into three sections. In Sec. 8.1, the investigated ICD mechanism is described. Sec. 8.2 deals with the computation of the time-independently derived PE spectrum, where scattering theory is applied. In Sec. 8.2, a time-dependent formalism for the ICD-electron and KER spectra is developed. This approach is also based on scattering theory, but the expressions derived before are now extended by a time-dependent treatment and combined with wave-packet dynamics. Throughout Part II atomic units are used.

8.1 Interatomic Coulombic Decay in Dimers

After one of the atoms has been inner-valence ionized, the vacancy is filled by an outer-valence electron and the excess energy is transferred radiationlessly to the neighboring atom, which is ionized and emits an outer-valence electron. Two singly charged ions remain, and due to the repelling force, the system undergoes Coulomb explosion. In the framework of nuclear motion, ICD can be described as a population (probability density) transfer between potential-energy curves (PEC) of the involved states. Initially, the population is transferred from the ground-state PEC V_{gs} to the PEC V_d of the singly ionized dimer. This state is metastable and decays. Thus, the propagation on the decaying-state PEC is accompanied by the simultaneous transfer of population to the final-state PEC V_f due to the decay. The final state corresponds to the two ions formed after the dimer has undergone ICD. Because these ions repel each other, the final state is dissociative. This simplified ICD mechanism for dimers in the framework of nuclear dynamics is shown in Fig. 8.1.

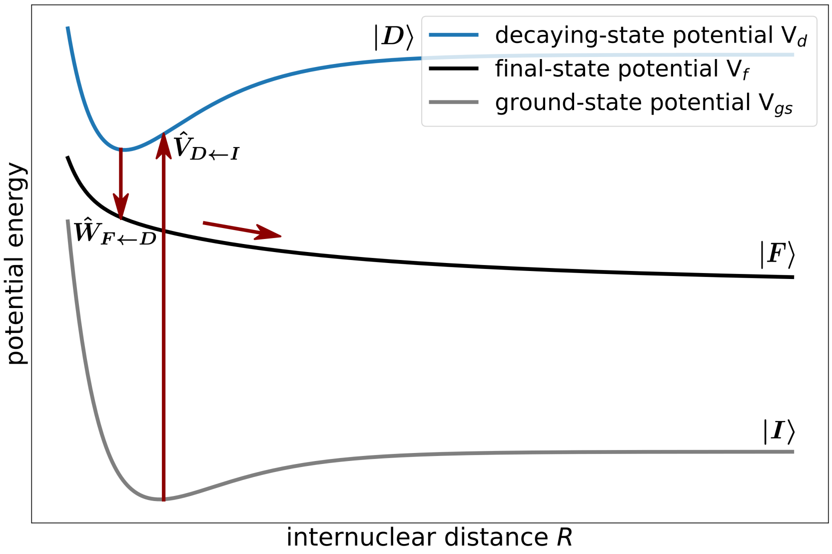

Figure 8.1: Schematic representation of ICD in a dimer. The gray, blue, and black curves are the PECs of the ground state V_{gs}, the decaying state V_d, and the final state V_f, which are associated with the initial $|I\rangle$, the decaying $|D\rangle$ and the final state $|F\rangle$. The red arrows mark the transfer of population between the states and the propagation on the PECs. Initially, one of the dimer species is ionized. The ionization denoted by the transition operator $\hat{V}_{D\leftarrow I}$ is accompanied by the transfer of population from the PEC of the electronic ground state V_{gs} (gray) to the PEC of the ionized state V_d (blue), which is metastable and decays. Consequently, besides wave-packet propagation on the PEC of the decaying state, the population is transferred to the PEC of the final state V_f (black) described by the transition operator $\hat{W}_{F\leftarrow D}$. The decay and transfer of the population to the final state pertain to the deexcitation of the ionized species and the ionization of its neighbor. The repellency of the remaining two ions leads to the final state being dissociative.

The corresponding Hamiltonian, describing the process, can be written as a sum of an unperturbed part $\hat{H}_0$ and a perturbation denoted by the interaction Hamiltonian $\hat{H}_{int}$

$$\hat{H} = \hat{H}_0 + \hat{H}_{int}. \tag{8.1}$$

The unperturbed Hamiltonian $\hat{H}_0$ consists of the Hamiltonians of the initial $\hat{H}_I$, the decaying $\hat{H}_D$ and the final $\hat{H}_F$ state

$$\hat{H}_0 = \hat{H}_I + \hat{H}_D + \hat{H}_F, \tag{8.2}$$

which represent the molecular motion (electronic and nuclear) in the initial $|I\rangle$, the decaying $|D\rangle$ and the final $|F\rangle$ state, respectively, compare Fig. 8.1.

The interaction Hamiltonian $\hat{H}_{int}$ causing the transitions between the electronic states is defined as

$$\hat{H}_{int} = \hat{V}_{D\leftarrow I} + \hat{W}_{F\leftarrow D} + \hat{V}^{\dagger}_{D\leftarrow I} + \hat{W}^{\dagger}_{F\leftarrow D}, \tag{8.3}$$

where the transition operators $\hat{V}_{D\leftarrow I}$ and $\hat{W}_{F\leftarrow D}$ denote the transitions from the initial to the decaying and from the decaying to the final state, respectively. The adjoint transition operators $\hat{V}^{\dagger}_{D\leftarrow I}$ and $\hat{W}^{\dagger}_{F\leftarrow D}$ correspond to the inverse transitions, see Fig. 8.1. These transitions between the three involved states read

$$\hat{V}_{D\leftarrow I}\left|I\right\rangle = \left|D\right\rangle, \qquad \hat{V}^{\dagger}_{D\leftarrow I}\left|D\right\rangle = \left|I\right\rangle, \tag{8.4a}$$

$$\hat{W}_{F\leftarrow D}\left|D\right\rangle = \left|F\right\rangle, \qquad \hat{W}^{\dagger}_{F\leftarrow D}\left|F\right\rangle = \left|D\right\rangle, \tag{8.4b}$$

where the backward transition from the decaying to the initial state is excluded due to the weak-field approximation. All other combinations of transition operators and states vanish by definition: $\hat{V}_{D\leftarrow I}\left|D\right\rangle = \hat{V}_{D\leftarrow I}\left|F\right\rangle = \hat{V}^{\dagger}_{D\leftarrow I}\left|I\right\rangle = \hat{V}^{\dagger}_{D\leftarrow I}\left|F\right\rangle = \hat{W}_{F\leftarrow D}\left|I\right\rangle = \hat{W}_{F\leftarrow D}\left|F\right\rangle = \hat{W}^{\dagger}_{F\leftarrow D}\left|I\right\rangle = \hat{W}^{\dagger}_{F\leftarrow D}\left|D\right\rangle = 0$.

8.2 Photoelectron Spectrum

In this section, the time-independent derivation of the cross section for the PE spectrum based on scattering theory is shown. A time-independent approach is used because in Chap. 10, where we apply the formulas derived here, we focus only on time-independent quantum effects such as interferences resulting from the overlap between vibrational states. The section is structured as follows. After presenting the states and the Hamiltonians in the Born-Oppenheimer approximation describing the investigated system, see Fig. 8.1, the basics of scattering theory are introduced. By developing the corresponding T-matrix element, the probability per unit time is computed, which is used to finally derive the cross section of the PE spectrum. The time-independent formalism explained in more detail can be found in Refs. [104, 107, 110, 112].

8.2.1 States and Hamiltonians in the Born-Oppenheimer Approximation

Here, the general molecular states and Hamiltonians introduced in Sec. 8.1 are worked out and presented in Born-Oppenheimer approximation [187], which is valid, if the electronic states are energetically well separated and the electrons move relatively quickly in comparison to the nuclei. Since the electrons are lighter than the nuclei by three orders of magnitude, the nuclear motion is much slower than the electronic motion. We can therefore assume that the electrons follow the nuclear motion instantaneously. Consequently, the nuclei are fixed from the electrons' perspective and the electronic wave functions depend only parametrically on the nuclear positions but not on their velocities. Due to the strong separation of timescales between the electronic and the nuclear motion, the initial $\left|I\right\rangle$, the decaying $\left|D\right\rangle$ and the final $\left|F\right\rangle$ state involved in the ICD mechanism can be written in product form

$$|I\rangle = |p\rangle\,|\phi_i\rangle\,|n_i\rangle\,, \tag{8.5a}$$
$$|D\rangle = |vac\rangle\,|\phi_d, E_{k_0}\rangle\,|n_d\rangle\,, \tag{8.5b}$$
$$|F\rangle = |vac\rangle\,|\phi_f, E_{k_0}, E_{k_0'}\rangle\,|E_{n_f}\rangle\,, \tag{8.5c}$$

where each total state is a product of the photonic, the electronic, and the nuclear state. The initial state $|I\rangle$ is the ground state with one incoming photon $|p\rangle$ causing the ionization. $|\phi_i\rangle$ and $|n_i\rangle$ denote the electronic and the vibrational ground state, respectively. In the decaying state $|D\rangle$ and the final state $|F\rangle$, only the photon vacuum $|vac\rangle$ is left. Due to ionization and ICD, the electronic states not only comprise the ionic contributions $|\phi_d\rangle$ and $|\phi_f\rangle$, but also those of the emitted photoelectron $|E_{k_0}\rangle$ and the emitted ICD electron $|E_{k_0'}\rangle$. $|E_{k_0}\rangle$ and $|E_{k_0'}\rangle$ will also be referred to as the first and second ejected electron, respectively. $|n_d\rangle$ denotes the vibrational states of the electronically decaying state. As the final state is dissociative, $|E_{n_f}\rangle$ is chosen to mark the final vibrational states. The normalizations of the electronic and nuclear states introduced above are given by

$$\langle\phi_i'|\phi_i\rangle = \delta_{i'i}, \tag{8.6a}$$
$$\langle\phi_d', E_{k_0}'|\phi_d, E_{k_0}\rangle = \delta_{d'd}\delta(E_{k_0}' - E_{k_0}), \tag{8.6b}$$
$$\langle\phi_f', E_{k_0}', E_{k_0'}'|\phi_f, E_{k_0}, E_{k_0'}\rangle = \delta_{f'f}\delta(E_{k_0}' - E_{k_0})\delta(E_{k_0'}' - E_{k_0'}), \tag{8.6c}$$

$$\langle n_i'|n_i\rangle = \delta_{n_i'n_i}, \tag{8.7a}$$
$$\langle n_d'|n_d\rangle = \delta_{n_d'n_d}, \tag{8.7b}$$
$$\langle E_{n_f}'|E_{n_f}\rangle = \delta(E_{n_f}' - E_{n_f}), \tag{8.7c}$$

where the normalization of bound states is given by Kronecker deltas and the normalization of continuum states involves delta functions. The continuum functions are energy-normalized.

Within the assumption of the Born-Oppenheimer approximation, the nuclei are not directly affected by the instantaneous position of the electrons, but they move in the electron potential. Therefore, the total unperturbed Hamiltonians $\hat{H}_I$, $\hat{H}_D$ and $\hat{H}_F$ are represented in the photonic-electronic basis $\{|p\rangle\,|\phi_i\rangle\,, |vac\rangle\,|\phi_d, E_{k_0}\rangle\,, |vac\rangle\,|\phi_f, E_{k_0}, E_{k_0'}\rangle\}$

$$\langle p|\,\langle\phi_i|\,\hat{H}_I\,|\phi_i\rangle\,|p\rangle = \omega_p + \hat{H}_i, \tag{8.8a}$$
$$\langle\phi_d, E_{k_0}|\,\hat{H}_D\,|\phi_d, E_{k_0}\rangle = E_{k_0} + \hat{H}_d, \tag{8.8b}$$
$$\langle\phi_f, E_{k_0}, E_{k_0'}|\,\hat{H}_F\,|\phi_f, E_{k_0}, E_{k_0'}\rangle = E_{k_0} + E_{k_0'} + \hat{H}_f, \tag{8.8c}$$

where the photon vacuum states reduce to $\langle vac|vac\rangle = 1$ and are therefore immediately left out. $\hat{H}_i$, $\hat{H}_d$ and $\hat{H}_f$ are the nuclear Hamiltonians of the corresponding electronic states, ω_p denotes the photon energy, and E_{k_0} and $E_{k_0'}$ are the energies of the first and second emitted electron, respectively.

The actions of the unperturbed Hamiltonians in Born-Oppenheimer approximation (see Eqs. (8.8)) on the vibrational states $|n_i\rangle$, $|n_d\rangle$ and $|E_{n_f}\rangle$ read

$$(\omega_p + \hat{H}_i)\,|n_i\rangle = (\omega_p + E_{n_i})\,|n_i\rangle = E_I\,|n_i\rangle\,, \tag{8.9a}$$

$$(E_{k_0} + \hat{H}_d)\,|n_d\rangle = (E_{k_0} + E_{n_d})\,|n_d\rangle = E_D\,|n_d\rangle\,, \tag{8.9b}$$

$$(E_{k_0} + E_{k_0'} + \hat{H}_f)\,|E_{n_f}\rangle = (E_{k_0} + E_{k_0'} + E_{n_f})\,|E_{n_f}\rangle = E_F\,|E_{n_f}\rangle\,. \tag{8.9c}$$

Here, E_I, E_D, and E_F depict the total energies of the initial $|I\rangle$, decaying $|D\rangle$ and final $|F\rangle$ state in the Born-Oppenheimer approximation, respectively, which consist of the vibrational energies E_{n_i}, E_{n_d} and E_{n_f}, and depending on the state of the photon energy ω_p or the energies of the first E_{k_0} and second $E_{k_0'}$ emitted electron.

Turning to the interaction Hamiltonian $\hat{H}_{int}$, the representations of the transition operators in the photonic-electronic basis $\{|p\rangle\,|\phi_i\rangle\,, |vac\rangle\,|\phi_d, E_{k_0}\rangle\,, |vac\rangle\,|\phi_f, E_{k_0}, E_{k_0'}\rangle\}$ read

$$\hat{V}_{d\leftarrow i}(E_{k_0}) = \langle vac|\,\langle\phi_d, E_{k_0}|\hat{V}_{D\leftarrow I}|\phi_i\rangle\,|p\rangle\,, \tag{8.10a}$$

$$\hat{W}_{f\leftarrow d}(E_{k_0'}) = \langle\phi_f, E_{k_0'}|\hat{W}_{F\leftarrow D}|\phi_d\rangle\,. \tag{8.10b}$$

For $\hat{W}_{f\leftarrow d}(E_{k_0'})$, the photonic part including only the photon vacuum $\langle vac|vac\rangle = 1$ is left out. Note that there is no non-adiabatic coupling due to the different amounts of electrons associated with the electronic states. However, the decaying and final state are coupled by the decay, whose theoretical formalism is introduced in the next section.

8.2.2 Transition Probability and T-Matrix

To derive the PE spectrum in the framework of scattering theory, see Ref. [105], we computed the transition from the initial state $|I\rangle$ to the final $|F\rangle$ state (see Eqs. (8.5)) by the transition probability per unit time P_{FI}, which is given by

$$P_{FI} = 2\pi\,\big|\,\langle F|\hat{T}|I\rangle\,\big|^2\,\delta(E_I - E_F). \tag{8.11}$$

Here, E$_I$ and E$_F$ are the energies of the initial and final state, respectively (see Eqs. 8.9), and the matrix element

$$T_{FI} = \langle F|\hat{T}|I\rangle\,, \tag{8.12}$$

is called the T-matrix element. $\hat{T}$ is the transition operator, which is defined by the Lippmann-Schwinger equation, see Ref. [188],

$$\hat{T}(E_I) = \hat{H}_{int} + \hat{H}_{int}\hat{G}_0(E_I)\hat{T}(E_I), \tag{8.13}$$

where $\hat{G}_0(E_I)$ is the free Green's operator, $\hat{G}_0(E_I) = \lim_{\eta\to 0}[E_I - \hat{H}_0 + i\eta]^{-1}$. $\hat{H}_0$ and $\hat{H}_{int}$ are the unperturbed and interaction Hamiltonian, respectively, as introduced in Sec. 8.1, see Eqs. (8.2) and (8.3), and represented in the Born-Oppenheimer approximation in Sec. 8.2, compare Eqs. (8.8) and (8.10). The expansion of the transition operator can be rewritten as

$$\begin{aligned}\hat{T}(E_I) &= \hat{H}_{int} + \hat{H}_{int}\hat{G}_0(E_I)\hat{H}_{int} + \hat{H}_{int}\hat{G}_0(E_I)\hat{H}_{int}\hat{G}_0(E_I)\hat{H}_{int} + \ldots,\\ &= \sum_{n=0}^{\infty}(\hat{H}_{int}\hat{G}_0(E_I))^n\hat{H}_{int}.\end{aligned} \tag{8.14}$$

Inserting the general interaction Hamiltonian $\hat{H}_{int}$ as defined in Eq. (8.3) into Eq. (8.14) shows that only every second term including an equal number of interaction Hamiltonians contributes to the T-matrix element (see Eq. (8.12))

$$T_{FI} = \langle F|\,\hat{W}_{F\leftarrow D}\hat{G}_0(E_I)\hat{V}_{D\leftarrow I}\,|I\rangle + \langle F|\,\hat{W}_{F\leftarrow D}\hat{G}_0(E_I)\hat{W}^{\dagger}_{F\leftarrow D}\hat{G}_0(E_I)\hat{W}_{F\leftarrow D}\hat{G}_0(E_I)\hat{V}_{D\leftarrow I}\,|I\rangle + \ldots, \tag{8.15}$$

where the choice of transition operators is unambiguous. $\hat{V}_{D\leftarrow I}\,|I\rangle$ and $\langle F|\,\hat{W}_{F\leftarrow D}$ are the only options giving a non-zero contribution and, therefore, defining the first contributing term, which describes the direct population transfer from the initial to the decaying to the final state. Since the backward transition from the decaying to the initial state is excluded, higher contributing terms are associated with the backward transfer of population from the final to the decaying state followed by an additional decay as the second contributing term shows, compare Eq. (8.15). By introducing a sum over the operators effecting the forward and subsequent backward population transfer between the final and decaying state, the T-matrix element can be rewritten as

$$T_{FI} = \langle F|\,\hat{W}_{F\leftarrow D}\sum_{m=0}^{\infty}(\hat{G}_0(E_I)\hat{W}^{\dagger}_{F\leftarrow D}\hat{G}_0(E_I)\hat{W}_{F\leftarrow D})^m\hat{G}_0(E_I)\hat{V}_{D\leftarrow I}\,|I\rangle\,. \tag{8.16}$$

Note that the sum now runs over the index m, which only accounts for the contributing terms of the expansion of the transition operator Eq. (4.2).

The resolution of identity

$$\mathbb{1} = \sum_{n_i} |I\rangle\langle I| + \sum_{n_d} \int dE_k \, |D\rangle\langle D| + \int dE_{n_f} \int dE_k \int dE_{k'} \, |F\rangle\langle F| \tag{8.17}$$

is inserted. Due to the decay, the energy is conserved but not well defined between the initial and final state, as can be seen in Eq. (8.11). Consequently, the intermediate states inserted with the resolution of identity also cover off-resonant energies. Therefore, the states are used as defined in Eqs. (8.5), but the energies of the first and second emitted electrons are renamed E_k and $E_{k'}$.

The resolution of identity is inserted in front and behind the free Green's operator $\hat{G}_0(E_I)$, where only the decaying states contribute and the definitions of the transition operators in the photonic-electronic basis, $\hat{V}_{d\leftarrow i}(E_k)$ and $\hat{W}_{f\leftarrow d}(E_{k'})$, are applied, see Eqs. (8.10). The T-matrix element for $m = 0$ finally reads

$$\begin{aligned} T_{FI}^{(m=0)} &= \langle F|\hat{W}_{F\leftarrow D}\hat{G}_0(E_I)\hat{V}_{D\leftarrow I}|I\rangle \\ &= \int dE'_k \int dE''_k \sum_{n'_d, n''_d} \langle E_{n_f}| \, \hat{W}_{f\leftarrow d}(E_{k'_0}) \, \langle E_{k_0}|E'_k\rangle \, |n'_d\rangle \, \langle n'_d| \, \langle \phi_d| \, \langle E'_k| \\ &\qquad \hat{G}_0(E_I) \, |E''_k\rangle \, |\phi_d\rangle \, |n''_d\rangle \, \langle n''_d|\hat{V}_{d\leftarrow i}(E''_k)|n_i\rangle \, , \end{aligned} \tag{8.18}$$

where the integration over the photon-vacuum states is immediately performed. After the sum over the vibrational states has been executed, the free Green's operator is inserted and the unperturbed Hamiltonian $\hat{H}_0$ acts on the remaining states, see Eqs. (8.8). The temporary expression for the first contributing term to the T-matrix element becomes

$$T_{FI}^{(m=0)} = \lim_{\eta\to 0} \int dE'_k \int dE''_k \, \langle E_{n_f}| \, \hat{W}_{f\leftarrow d}(E_{k'_0}) \, \langle E_{k_0}|E'_k\rangle \, \langle E'_k| \, [E_I - E''_k - \hat{H}_d + i\eta]^{-1} \, |E''_k\rangle \, \hat{V}_{d\leftarrow i}(E''_k) \, |n_i\rangle \, , \tag{8.19}$$

where the integration over the electronic decaying state has already been performed, $\langle \phi_d|\phi_d\rangle = 1$. The normalization conditions for the continuum electrons (see Eqs. (8.6)) are used and the integrations over the emitted photoelectrons are executed, where only E_{k_0} contributes. As a result, the final expression of the first term of the T-matrix element reads

$$T_{FI}^{(m=0)} = \lim_{\eta\to 0} \langle E_{n_f}| \, \hat{W}_{f\leftarrow d}(E_{k'_0})[E_I - E_{k_0} - \hat{H}_d + i\eta]^{-1}\hat{V}_{d\leftarrow i}(E_{k_0}) \, |n_i\rangle \, . \tag{8.20}$$

After inserting the time-independent states, the resolutions of identity, the definitions of the transition operators, the summations over the vibrational decaying states and the integration over the vibrational final states are performed. Subsequently, the free Green's operator is applied and the normalization conditions (see Eqs. (8.6)) for the emitted electrons are used. The second term of the T-matrix element is given by

$$T_{FI}^{(m=1)} = \lim_{\eta\to 0} \langle E_{n_f}|\, \hat{W}_{f\leftarrow d}(E_{k_0'})[E_I - E_{k_0} - \hat{H}_d + i\eta]^{-1}$$
$$\Big(\int dE_{k'}\ \hat{W}^{\dagger}_{f\leftarrow d}(E_{k'})[E_I - E_{k_0} - E_{k'} - \hat{H}_f + i\eta]^{-1}\hat{W}_{f\leftarrow d}(E_{k'})\Big)$$
$$[E_I - E_{k_0} - \hat{H}_d + i\eta]^{-1}\hat{V}_{d\leftarrow i}(E_{k_0})\,|n_i\rangle\,, \tag{8.21}$$

where all but one integral over the energy of the second emitted electron are carried out using the normalization condition for continuum states. The remaining one is set in parentheses.

The same procedure is applied to all terms, $T_{FI} = T_{FI}^{(m=0)} + T_{FI}^{(m=1)} + T_{FI}^{(m=2)} + ...$, resulting in the following expression for the T-matrix element

$$T_{FI} = \lim_{\eta\to 0} \langle E_{n_f}|\, \hat{W}_{f\leftarrow d}(E_{k_0'}) \sum_{m=0}^{\infty}\Big([E_I - E_{k_0} - \hat{H}_d + i\eta]^{-1} \int dE_{k'}\ \hat{W}^{\dagger}_{f\leftarrow d}(E_{k'})[E_I - E_{k_0} - E_{k'} - \hat{H}_f + i\eta]^{-1}$$
$$\hat{W}_{f\leftarrow d}(E_{k'})\Big)^m [E_I - E_{k_0} - \hat{H}_d + i\eta]^{-1}\hat{V}_{d\leftarrow i}(E_{k_0})\,|n_i\rangle\,, \tag{8.22}$$

where the sum is a converging geometric series. After some algebraic operations, the final expression for the T-matrix element reads

$$T_{FI} = \lim_{\eta\to 0} \langle E_{n_f}|\, \hat{W}_{f\leftarrow d}(E_{k_0'})\big[E_I - E_{k_0} - \hat{H}_d - \int dE_{k'}\ \hat{W}^{\dagger}_{f\leftarrow d}(E_{k'})[E_I - E_{k_0} - E_{k'} - \hat{H}_f + i\eta]^{-1}$$
$$\hat{W}_{f\leftarrow d}(E_{k'}) + i\eta\big]^{-1}\hat{V}_{d\leftarrow i}(E_{k_0})\,|n_i\rangle\,. \tag{8.23}$$

In the following, an effective Hamiltonian for the decaying state,

$$\hat{\mathcal{H}}_d = \hat{H}_d + \int dE_{k'}\ \hat{W}^{\dagger}_{f\leftarrow d}(E_{k'})[E_I - E_{k_0} - E_{k'} - \hat{H}_f + i\eta]^{-1}\hat{W}_{f\leftarrow d}(E_{k'}), \tag{8.24}$$

is introduced. For definiteness of the integration, the energy denominator $\mathcal{D}$ is augmented by an infinitesimally small factor $\mathcal{D} + i\eta$. Principal value integration can now be executed according to $(\mathcal{D} + i\eta)^{-1} = \mathcal{P}\mathcal{D}^{-1} - i\pi\delta(\mathcal{D})$, which gives

$$\hat{\mathcal{H}}_d = \hat{H}_d + \Delta_d - i\frac{\hat{\Gamma}_d}{2}. \tag{8.25}$$

The energy shift Δ_d and the total decay width of the decaying state $\hat{\Gamma}_d$ are defined as

$$\Delta_d = \mathcal{P}\int dE_{k'}\ \hat{W}^{\dagger}_{f\leftarrow d}(E_{k'})[E_I - E_{k_0} - E_{k'} - \hat{H}_f]^{-1}\hat{W}_{f\leftarrow d}(E_{k'}), \tag{8.26a}$$

$$\hat{\Gamma}_d = 2\pi\int dE_{k'}\ \hat{W}^{\dagger}_{f\leftarrow d}(E_{k'})\delta(E_I - E_{k_0} - E_{k'} - \hat{H}_f)\hat{W}_{f\leftarrow d}(E_{k'}). \tag{8.26b}$$

Now, the local approximation is applied [189–191], where the decay width does not depend on the energy E but only on the internuclear distance R, $\hat{\Gamma}_d(E = E_I - E_{k_0} - \hat{H}_f) = \hat{\Gamma}_d(R)$. Note that the decay width as shown above also depends explicitly on R due to the transition operator $\hat{W}_{f\leftarrow d}(E_{k'})$. The local approximation typically works well when the decaying state is well above threshold, which means that the decaying and final state energetically are far away from each other so that no further interactions between the particles besides the decay and the subsequent ionization of the neighbor have to be considered. In the present case, this condition is satisfied as the ICD process emits electrons of more than 8 eV. This allows to freeze the movement of the nuclei and to introduce a local energy E', which depends on the internuclear distance R and replaces the original energy dependency. Furthermore, the decay width has to vary rather slowly in the range of the potential-well width in order for the original decay width, depending on the energy, to be approximated sufficiently well. In general, interactions involving highly vibrational levels are hard to describe because the states may overlap with the continuum due to the decay width introduced broadening. For more details, see Ref. [191]. For notational simplicity, we refer to the decay width $\hat{\Gamma}_d(R)$ in the following as $\hat{\Gamma}_d$. Applying the local approximation, the R-dependent decay width reads

$$\hat{\Gamma}_d = 2\pi \hat{W}^{\dagger}_{f\leftarrow d}(E_{k'})\hat{W}_{f\leftarrow d}(E_{k'}) \approx 2\pi |\hat{W}_{f\leftarrow d}|^2. \tag{8.27}$$

Finally, the effective Hamiltonian $\hat{\mathcal{H}}_d$ of the decaying state in local approximation takes on the form

$$\hat{\mathcal{H}}_d = \hat{H}_d - i\frac{\hat{\Gamma}_d}{2}, \tag{8.28}$$

where the energy shift Δ_d is incorporated into the real Hamiltonian $\hat{H}_d$. $\hat{\mathcal{H}}_d$ is a complex symmetric non-Hermitian Hamiltonian and its eigenvalues ε_{n_d} and eigenstates $|\tilde{n}_d\rangle$ are both complex. For more details on non-Hermitian quantum mechanics, see Ref. [192]. The corresponding time-independent Schrödinger equation reads

$$\hat{\mathcal{H}}_d \left|\tilde{n}_d\right\rangle = \varepsilon_{n_d} \left|\tilde{n}_d\right\rangle. \tag{8.29}$$

Usually, the complex nuclear eigenstates $|\tilde{n}_d\rangle$ are written in round brackets $|n_d)$ to denote that they are complex and differently normalized. Here, when using angular brackets, we add ˜ to mark that these states have a complex component. As the left and the right eigenvector of a complex symmetric matrix are not adjoints but just transposes of each other, the orthogonality relation is now a c-product, $\langle \tilde{n}^*_d|\tilde{n}^{'}_d\rangle = (n_d|n^{'}_d) = \delta_{n_d n^{'}_d}$, and the resolution of identity reads $\sum_{n_d} |n_d)(n_d| = \mathbb{1}$ (for a detailed discussion, see Ref. [192]). The corresponding eigenvalues ε_{n_d} are given by

$$\varepsilon_{n_d} = e_{n_d} - i\frac{\Gamma_{n_d}}{2}, \tag{8.30}$$

where Γ_{n_d} is the partial decay width of the nuclear state n_d and can be imagined as a broadening of the energy level e_{n_d}, which also includes the contribution of the energy shift and, consequently, differs from the solution of the time-independent Schrödinger equation of the real

Hamiltonian of the decaying state

$$\hat{H}_d \left| n_d \right\rangle = E_{n_d} \left| n_d \right\rangle . \tag{8.31}$$

8.2.3 Time-independently computed Photoelectron Spectrum

Returning to the transition probability per unit time Eq. (8.11) and inserting the final T-matrix element (8.23), gives

$$P_{FI} = 2\pi \left| \langle E_{n_f} | \hat{W}_{f \leftarrow d}(E_{k_0'}) [E_I - E_{k_0} - \hat{\mathscr{H}}_d]^{-1} \hat{V}_{d \leftarrow i}(E_{k_0}) | n_i \rangle \right|^2 \delta(E_I - E_F), \tag{8.32}$$

where the initial energy E_I is similar to the photon energy ω_p neglecting the vibrational energy of the ground state (see. Eqs. (8.9)) and the final energy is $E_F = E_{n_f} + E_{k_0} + E_{k_0'}$. While $E_{k_0'}$ is the energy of the ICD electron associated with a real transition and thereby fulfilling the energy conservation, $E_{k'}$ denotes the energy of the ICD electron from a virtual transition, and is off-resonant. $E_{k_{ICD}}$ is introduced to combine $E_{k_0'}$ and $E_{k'}$. Integrating Eq. (8.32) over the final vibrational states $|E_{n_f}\rangle$ as well as over the energy of the second emitted electron $E_{k_0'}$ gives the following expression for the photoelectron spectrum $\sigma_{PE}(E_I - E_{k_0})$:

$$\sigma_{PE}(E_I - E_{k_0}) = 2\pi \int dE_{k_0'} \int dE_{n_f} \left| \langle E_{n_f} | \hat{W}_{f \leftarrow d} [E_I - E_{k_0} - \hat{\mathscr{H}}_d]^{-1} \hat{V}_{d \leftarrow i}(E_{k_0}) | n_i \rangle \right|^2 \delta(E_I - E_F). \tag{8.33}$$

After the integration has been performed and the square of the absolute value was written out, the total decay width (8.27) can be inserted. Furthermore, $E_I - E_{k_0}$ is replaced by the binding energy ω_b. The resulting expression for the PE spectrum reads

$$\sigma_{PE}(\omega_b) = \langle n_i | \hat{V}^{\dagger}_{d \leftarrow i}(E_{k_0}) [E_I - E_{k_0} - \hat{\mathscr{H}}^{\dagger}_d]^{-1} \hat{\Gamma}_d [E_I - E_{k_0} - \hat{\mathscr{H}}_d]^{-1} \hat{V}_{d \leftarrow i}(E_{k_0}) | n_i \rangle . \tag{8.34}$$

The resolution of identity $\mathbb{1} = \sum_{n_d} |n_d)(n_d|$ is inserted in front of and behind the total decay width. Additionally, the double sum is split into the sums $\sum_{n_d = n_d'}$ and $\sum_{n_d \neq n_d'}$ so that the expression of the PE spectrum contains two separate terms

$$\sigma_{PE}(\omega_b) = \sum_{n_d} \frac{\left| \langle n_i | \, \hat{V}^{\dagger}_{d \leftarrow i}(E_{k_0}) | n_d^*) \right|^2 (n_d^* | \hat{\Gamma}_d | n_d)}{(\omega_b - e_{n_d})^2 + (\hat{\Gamma}_{n_d}/2)^2} + \sum_{n_d \neq n_d'} \frac{\langle n_i | \, \hat{V}^{\dagger}_{d \leftarrow i}(E_{k_0}) | n_d^*) (n_d^* | \hat{\Gamma}_d | n_d') (n_d' | \hat{V}_{d \leftarrow i}(E_{k_0}) \, | n_i \rangle}{(\omega_b - \varepsilon^*_{n_d})(\omega_b - \varepsilon_{n_d'})} . \tag{8.35}$$

The second sum $\sum_{n_d \neq n_d'}$ can be further simplified because the imaginary part vanishes, if the summation is performed. The imaginary parts of cross terms of the form, $n_d = 0$, $n_{d'} = 1$ and $n_d = 1$, $n_{d'} = 0$, cancel each other, while the real parts of the cross terms give the same contributions. Consequently, only half of the calculations have to be performed, which also lowers the computational costs. The final expression for the PE spectrum reads

$$\sigma_{PE}(\omega_b) = \sum_{n_d} \frac{|\langle n_i|\, \hat{V}^{\dagger}_{d\leftarrow i}(E_{k_0})|n_d^*)|^2 (n_d^*|\hat{\Gamma}_d|n_d)}{(\omega_b - E_{n_d})^2 + (\Gamma_{n_d}/2)^2}$$

$$+ 2\,Re \sum_{n_d > n_d^{'}} \frac{\langle n_i|\, \hat{V}^{\dagger}_{d\leftarrow i}(E_{k_0})|n_d^*)(n_d^*|\hat{\Gamma}_d|n_d^{'})(n_d^{'}|\hat{V}_{d\leftarrow i}(E_{k_0})\,|n_i\rangle}{(\omega_b - \varepsilon^*_{n_d})(\omega_b - \varepsilon_{n_d^{'}})}, \tag{8.36}$$

where the first sum describes the PE spectrum without interference effects, while the second sum is associated with interference effects. These interference effects are caused by the huge partial decay widths Γ_{n_d}, which broaden the energy levels and lead to overlaps. Consequently, the vibrational levels of the decaying state interfere with each other, which affects the PE spectrum.

8.3 Interatomic-Coulombic-Decay-Electron Spectrum and Kinetic-Energy-Release Spectrum

In the following section, phenomena stemming from nuclear motions are investigated, and therefore, the application of a time-dependent approach is required. These phenomena can be observed in the ICD-electron and KER spectra in Chaps. 10 and 11. Before we start with the derivation of the time-dependently computed ICD-electron and KER spectrum, we want to show the relation between the time-dependent and the time-independent formalism. The time-dependent nuclear wave functions are expanded in sets of the time-independent eigenstates

$$|\psi_d(E_{k_0}, t)\rangle = \sum_{\tilde{n}_d} c_{n_d}(E_{k_0}, t)\,|\tilde{n}_d\rangle = \sum_{\tilde{n}_d} c_{n_d}(t) e^{-i(E_{k_0}+\varepsilon_{n_d})t}\,|\tilde{n}_d\rangle\,, \tag{8.37}$$

$$\begin{aligned} |\psi_f(E_{k_0}, E_{k_0^{\prime}}, t)\rangle &= \int_0^{\infty} dE_{n_f}\, c_{E_{n_f}}(E_{k_0}, E_{k_0^{\prime}}, t)\,|E_{n_f}\rangle \\ &= \int_0^{\infty} dE_{n_f}\, c_{E_{n_f}}(t) e^{-i(E_{k_0}+E_{k_0^{\prime}}+E_{n_f})t}\,|E_{n_f}\rangle\,, \end{aligned} \tag{8.38}$$

where $|\tilde{n}_d\rangle$ and $|E_{n_f}\rangle$ are the eigenstates of the time-independent nuclear Hamiltonians $\hat{\mathcal{H}}_d$ and $\hat{H}_f$. ε_{n_d} and E_{n_f} are the corresponding eigenenergies, and E_{k_0} and $E_{k_0^{\prime}}$ are the energies of the first and second ejected electrons. For a detailed explanation regarding the time-independent states, see Sec. 8.2. The time-dependent coefficients $c_{n_d}(t)$ and $c_{E_{n_f}}(t)$ equal the total coefficients $c_{n_d}(E_{k_0}, t) = \langle\tilde{n}_d|\psi_d(E_{k_0}, t)\rangle$ and $c_{E_{n_f}}(E_{k_0}, E_{k_0^{\prime}}, t) = \langle E_{n_f}|\psi_f(E_{k_0}, E_{k_0^{\prime}}, t)\rangle$ reduced by the energy contribution, respectively.

8.3.1 Wave-packet Dynamics

To derive the ICD-electron and KER spectrum, we start with nuclear wave-packet dynamics to get the time evolution of the states. Therefore, we have to define the time-dependent Hamiltonian, which is separated into an electronic, a nuclear, and an external-field contribution

$$\hat{H}(t) = \hat{T}_{nuc} + \hat{H}_{el} + \hat{V}_{nuc} + \hat{\boldsymbol{D}} \cdot \boldsymbol{E}(t), \tag{8.39}$$

where $\hat{T}_{nuc}$ is the kinetic-energy operator of the nuclei, $\hat{H}_{el}$ is the electronic Hamiltonian and $\hat{V}_{nuc}$ is the potential of the nuclei. These three operators are time-independent and describe the molecular system, while the last part of the Hamiltonian is time-dependent and denotes the interaction with an external field, which leads to the ionization of the system. $\hat{\boldsymbol{D}}$ is the dipole operator and $\boldsymbol{E}(t)$ is the external electric field.

The total time-dependent wave function consists of the electronic $|\phi\rangle$ as well as the nuclear $|\psi(t)\rangle$ wave functions and can be written as a product of them. Consequently, the total wave function is a sum of the product states involved in the ICD process and reads

$$\begin{aligned} |\Psi(t)\rangle = |\phi_i\rangle\,|\psi_i(t)\rangle &+ \int_0^\infty dE_{k_0}\,|\phi_d, E_{k_0}\rangle\,|\psi_d(E_{k_0}, t)\rangle \\ &+ \int_0^\infty dE_{k_0} \int_0^\infty dE_{k'_0}\;|\phi_f, E_{k_0}, E_{k'_0}\rangle\,|\psi_f(E_{k_0}, E_{k'_0}, t)\rangle\,. \end{aligned} \tag{8.40}$$

The electronic wave functions $|\phi_i\rangle$, $|\phi_d, E_{k_0}\rangle$ and $|\phi_f, E_{k_0}, E_{k'_0}\rangle$ are associated with the electronic ground state, the decaying state of the ionized system with the first emitted electron and the final state with the two remaining ions as well as the first and second emitted electron, respectively. The time-dependent nuclear wave functions are $|\psi_i(t)\rangle$, $|\psi_d(E_{k_0}, t)\rangle$ and $|\psi_f(E_{k_0}, E_{k'_0}, t)\rangle$ describing the nuclear dynamics in the corresponding electronic state. Because the decaying state and the final state are associated with one electron and two electrons in the continuum, respectively, it has to be integrated over the energies of the corresponding ejected electrons E_{k_0} and $E_{k'_0}$.

The total Hamiltonian Eq. (8.39) and the total wave function Eq. (8.40) are inserted into the time-dependent Schrödinger equation $i\frac{\partial}{\partial t}|\Psi(t)\rangle = \hat{H}\,|\Psi(t)\rangle$. The electronic states $\langle\phi_i|$, $\langle\phi_d, E_k|$ and $\langle\phi_f, E_{k_0}, E_{k'_0}|$ are multiplied from the left, respectively, where is taken advantage of the energy normalization Eq. (8.6) of the electronic continuums states. Note that the vibrational wave functions $|\psi(t)\rangle$ as well as $\hat{T}_{nuc}$ and $\hat{V}_{nuc}$ depend on the nuclear coordinate R, while the electronic states $|\phi\rangle$ and the electronic Hamiltonian $\hat{H}_{el}$ depend on the electronic coordinates $\boldsymbol{r}_n$. Consequently, the nuclear operators act only on the vibrational wave functions, and the electronic Hamiltonian acts only on the electronic states, which results in the following set of differential equations

$$i\,|\dot{\psi}_i(t)\rangle = \hat{H}_i\,|\psi_i(t)\rangle + \hat{F}^\dagger(E_{k_0}, t)\,|\psi_d(E_{k_0}, t)\rangle\,, \tag{8.41a}$$

$$\begin{aligned} i\,|\dot{\psi}_d(E_{k_0}, t)\rangle &= \hat{F}(E_{k_0}, t)\,|\psi_i(t)\rangle + (E_{k_0} + \hat{H}_d)\,|\psi_d(E_{k_0}, t)\rangle \\ &\quad + \int_0^\infty dE_{k'_0}(E_{k_0} + \hat{W}^\dagger_{f\leftarrow d}(E_{k'_0}))\,|\psi_f(E_{k_0}, E_{k'_0}, t)\rangle\,, \end{aligned} \tag{8.41b}$$

$$\begin{aligned} i\,|\dot{\psi}_f(E_{k_0}, E_{k'_0}, t)\rangle &= (E_{k_0} + \hat{W}_{f\leftarrow d}(E_{k'_0}))\,|\psi_d(E_{k_0}, t)\rangle \\ &\quad + (E_k + E_{k'_0} + \hat{H}_f)\,|\psi_f(E_{k_0}, E_{k'_0}, t)\rangle\,, \end{aligned} \tag{8.41c}$$

which describe the wave-packet propagation in the initial, the decaying, and the final state, respectively. Eqs. 8.41 are our temporary working equations, which will be further simplified below. The Hamiltonians $\hat{H}_i$, $\hat{H}_d$ and $\hat{H}_f$ are associated with the nuclear motion in the corresponding electronic potential, respectively, and are consequently given by

$$\hat{H}_{i/d/f} = \hat{T}_{nuc} + \hat{V}_{i/d/f}, \tag{8.42a}$$

$$\hat{V}_{i/d/f} = \langle \phi_{i/d/f} | \hat{H}_{el} | \phi_{i/d/f} \rangle + \hat{V}_{nuc}, \tag{8.42b}$$

where $\hat{T}_{nuc}$ is the kinetic-energy operator of the nuclei and $\hat{V}_{i/d/f}$ is the potential-energy operator in the corresponding state. $\hat{F}(E_{k_0}, t)$ and $\hat{W}_{f\leftarrow d}(E_{k'_0})$ also represent matrix elements concerning the electronic functions. The corresponding transition operators in the space of the nuclear wave functions are defined as

$$\hat{F}(E_{k_0}, t) = \langle \phi_d, E_{k_0} | \hat{D} | \phi_i \rangle \cdot \boldsymbol{E}(t) = \hat{V}_{d\leftarrow i}(E_{k_0}) \cdot g(t), \tag{8.43a}$$

$$\hat{W}_{f\leftarrow d}(E_{k'_0}) = \langle \phi_f, E_{k'_0} | \hat{H}_{el} | \phi_d \rangle, \tag{8.43b}$$

where $\hat{F}(E_{k_0}, t)$ describes the transition from the initial to the decaying state, driven by an external electric field, and $\hat{W}_{f\leftarrow d}(E_{k'_0})$ is responsible for the transition from the decaying to the final state, which is due to the decay width. The time-independent contribution to $\hat{F}(E_{k_0}, t)$ and the time-independent transition operator $\hat{W}_{f\leftarrow d}(E_{k'_0})$ are already known from Sec. 8.2.

In the following, dressed states are introduced, see Refs. [108, 111, 112]. By adding a phase to the wave functions, one gets rid of the photoelectron energy E_{k_0}. If the photon energy just exceeds the threshold, the photoelectron energy will be comparatively small, which only shifts the PECs a little bit. This allows the use of dressed states

$$|\tilde{\psi}_d(E_{k_0}, t)\rangle = e^{iE_{k_0}t} |\psi_d(E_{k_0}, t)\rangle, \tag{8.44a}$$

$$|\tilde{\psi}_d(E_{k_0}, E_{k'_0}, t)\rangle = e^{iE_{k_0}t} |\psi_f(E_{k_0}, E_{k'_0}, t)\rangle. \tag{8.44b}$$

The dressed states Eq. (8.44) are inserted into the temporary working equations Eq. (8.41). Furthermore, the weak-field approximation is applied, which forbids the backward transition of the population from the decaying to the initial state. Consequently, $\hat{F}^{\dagger}(E_{k_0}, t)\,|\psi_d(E_{k_0}, t)\rangle$ is canceled. The new working equations read

$$
\begin{aligned}
i\,|\dot{\psi}_i(t)\rangle &= \hat{H}_i\,|\psi_i(t)\rangle\,, && \text{(8.45a)}\\
i\,|\dot{\tilde{\psi}}_d(E_{k_0},t)\rangle &= \hat{F}(E_{k_0},t)\,|\psi_i(t)\rangle + \hat{H}_d\,|\tilde{\psi}_d(E_{k_0},t)\rangle \\
&\qquad + \int_0^\infty dE_{k'_0}\;\hat{W}^\dagger_{f\leftarrow d}(E_{k'_0})\,|\tilde{\psi}_f(E_{k_0},E_{k'_0},t)\rangle\,, && \text{(8.45b)}\\
i\,|\dot{\tilde{\psi}}_f(E_{k_0},E_{k'_0},t)\rangle &= \hat{W}_{f\leftarrow d}(E_{k'_0})\,|\tilde{\psi}_d(E_{k_0},t)\rangle \\
&\qquad + (E_{k'_0} + \hat{H}_f)\,|\tilde{\psi}_f(E_{k_0},E_{k'_0},t)\rangle\,, && \text{(8.45c)}
\end{aligned}
$$

The initial ionization $\hat{F}(E_{k_0},t)$ depends on E_{k_0}, and consequently, the nuclear wave functions of the decaying state $|\psi_d(E_{k_0},t)\rangle$ and of the final state $|\psi_f(E_{k_0},E_{k'_0},t)\rangle$ do so, too. Instead of using an external field, the transfer from the initial to the decaying state can be approximated by broad-band ionization. Thereby, the whole population is immediately brought to the decaying-state PEC. One can imagine this procedure as a δ-pulse Ref. [187] at propagation time $t = 0$ fs, which is sharp in time and broad in the energy domain. In practice, this means that one (or an incoherent sum) of the vibrational eigenfunctions of the ground state is taken as the initial wave function for the decaying state. The mathematical formulation of the initial condition at $t = 0$ fs reads $|\psi_d(t=0)\rangle = \hat{V}_{d\leftarrow i}(E_{k_0})\,|n_i\rangle$. Consequently, the term associated with the ionization of the ground state via the external field, is canceled. Furthermore, there is no propagation in the initial state and the time development of the initial state can be neglected completely. Therefore, $|\tilde{\psi}_d(E_{k_0},t)\rangle$ and $|\tilde{\psi}_f(E_{k_0},E_{k'_0},t)\rangle$ do not any longer depend on E_{k_0} and can be rewritten to $|\psi_d(t)\rangle$ and $|\psi_f(E_{k'_0},t)\rangle$. The new coupled time-dependent Schrödinger equations read

$$
\begin{aligned}
i\,|\dot{\psi}_d(t)\rangle &= \hat{H}_d\,|\psi_d(t)\rangle + \int_0^\infty dE_{k'_0}\;\hat{W}^\dagger_{f\leftarrow d}(E_{k'})\,|\psi_f(E_{k'_0},t)\rangle\,, && \text{(8.46a)}\\
i\,|\dot{\psi}_f(E_{k'_0},t)\rangle &= \hat{W}_{f\leftarrow d}(E_{k'_0})\,|\psi_d(t)\rangle + (E_{k'_0} + \hat{H}_f)\,|\psi_f(E_{k'_0},t)\rangle\,. && \text{(8.46b)}
\end{aligned}
$$

As in Sec. 8.2, the local approximation is applied, where the transition operator $\hat{W}_{f\leftarrow d}(E_{k'_0})$ is assumed to be R-dependent by freezing the nuclei and separating the energy-dependency $\hat{W}_{f\leftarrow d}(E_{k'_0}) \rightarrow f(E_{k'_0})\hat{W}_{f\leftarrow d}$. For more details about the local approximation, see Ref. [191]. Consequently, the effective Hamiltonian $\hat{\mathcal{H}}_d$ is given by

$$
\begin{aligned}
\hat{\mathcal{H}}_d\,|\psi_d(t)\rangle =& \hat{H}_d\,|\psi_d(t)\rangle - i\int_0^\infty dE_{k'_0}\;\hat{W}^\dagger_{f\leftarrow d}(E_{k'_0})\int_{-\infty}^t dt' e^{i(\hat{H}_f+E_{k'_0})(t'-t)}\,\hat{W}_{f\leftarrow d}(E_{k'_0})\,|\psi_d(t')\rangle \\
=& \hat{H}_d\,|\psi_d(t)\rangle - i\frac{\hat{\Gamma}_d}{2}\,|\psi_d(t)\rangle\,, \qquad \text{(8.47)}
\end{aligned}
$$

which is the same expression for the effective Hamiltonian as in the time-independent approach, see Eq. (8.28) in Sec. 8.2. Again, the Hamiltonian of the decaying state $\hat{H}_d$ is expanded by a complex component, which includes the decay width $\hat{\Gamma}_d$ and is responsible for the decay of the state. As explained before, the decay width in the local approximation depends on the nuclear coordinate R. By introducing the effective Hamiltonian of the decaying state $\hat{\mathcal{H}}_d$, the differential equations in Eq. (8.46) decouple,

$$i\,|\dot{\psi}_d(t)\rangle = \hat{\mathcal{H}}_d\,|\psi_d(t)\rangle\,, \tag{8.48a}$$

$$i\,|\dot{\psi}_f(E_{k_0'},t)\rangle = \hat{W}_{f\leftarrow d}\,|\psi_d(t)\rangle + (\hat{H}_f + E_{k_0'})\,|\psi_f(E_{k_0'},t)\rangle\,. \tag{8.48b}$$

The first equation describes the propagation in the decaying state, while the second equation is associated with the nuclear motion in the final electronic state, where two contributions of the population define the time evolution. The first contribution to the final state $\hat{W}_{f\leftarrow d}\,|\psi_d(t)\rangle$ describes the transfer of population from the decaying state to the final state at each time step. The wave packet is then propagated on the final PEC by $(\hat{H}_f + E_{k_0'})\,|\psi_f(E_{k_0'},t)\rangle$, while the population in the decaying state constantly decays and interferes with the already existing population in the final state. Furthermore, in the last equation, the ICD-electron energy $E_{k_0'}$ is added to the Hamiltonian of the final state $\hat{H}_f$ to ensure energy conservation between the decaying and final state and to simulate the continuum for the ejected ICD electrons. The PEC of the final state is shifted by this energy, influencing the nuclear dynamics.

In the following, the time evolutions of the wave functions are needed for the computations of the spectra.

8.3.2 Coincidence Spectrum

To derive the expression of the coincidence spectrum, we return to the time-independent approach. The transition probability Eq. (8.32) is now integrated over the energy of the photoelectron to generate a spectrum, which includes the information on the decay process. In the following, we refer to this spectrum as the coincidence spectrum

$$\sigma_{coin} = 2\pi \int dE_{k_0} |\,\langle E_{n_f}|\hat{W}_{f\leftarrow d}[E_I - E_{k_0} - \hat{\mathcal{H}}_d]^{-1}\hat{V}_{d\leftarrow i}(E_{k_0})|n_i\rangle\,|^2 \delta(E_I - E_F). \tag{8.49}$$

The integration over the δ-function, $\delta(E_I - E_F) = \delta(E_I - E_{n_f} - E_{k_0} - E_{k_0'}) = \delta\big([E_I - E_{k_0}] - [E_{n_f} + E_{k_0'}]\big)$, is performed, and all additional arising factors are incorporated into the transition operators. Therefore, the expression for the time-independent coincidence spectrum $\sigma_{coin}(E_{n_f}, E_{k_0'})$ reads

$$\sigma_{coin}(E_{n_f}, E_{k_0'}) = |\,\langle E_{n_f}|\hat{W}_{f\leftarrow d}[E_{n_f} + E_{k_0'} - \hat{\mathcal{H}}_d]^{-1}\hat{V}_{d\leftarrow i}(E_{k_0})|n_i\rangle\,|^2. \tag{8.50}$$

The time-dependent coincidence spectrum can be developed from Eq. (8.50) by rewriting the energy denominator as

$$[E_{n_f} + E_{k_0'} - \hat{\mathcal{H}}_d]^{-1} = -i \int_0^{\infty} e^{i(E_{n_f} + E_{k_0'} - \hat{\mathcal{H}}_d)t} \, dt. \tag{8.51}$$

Furthermore, $E_{k_{ICD}}$ is inserted for the energy of the first emitted electron $E_{k_0'}$ and the vibrational energy of the final state E_{n_f} is replaced by the KER energy $E_{n_f} = E_{KER} + V_f^{\infty}$, where V_f^{∞} is the final-state PEC at infinite internuclear distances. Finally, the time-dependent coincidence spectrum reads

$$\sigma_{coin}(E_{KER}, E_{k_{ICD}}, t) = | \langle E_{n_f} | \hat{W}_{f \leftarrow d} (-i) \int_0^{\infty} dt \, e^{i(E_{KER} + V_f^{\infty} + E_{k_{ICD}} - \hat{\mathcal{H}}_d)t} \hat{V}_{d \leftarrow i}(E_{k_0}) | n_i \rangle |^2. \tag{8.52}$$

The ICD-electron spectrum is computed by integrating the coincidence spectrum over the energy of the final state E_{n_f} or the KER E_{KER} and the KER spectrum is obtained by integrating the coincidence spectrum over the energy of the ICD electron $E_{k_{ICD}}$

$$\sigma_{ICD}(E_{k_{ICD}}, t) = \int_0^{\infty} \sigma_{coin}(E_{KER}, E_{k_{ICD}}, t) \, dE_{KER}, \tag{8.53a}$$

$$\sigma_{KER}(E_{KER}, t) = \int_0^{\infty} \sigma_{coin}(E_{KER}, E_{k_{ICD}}, t) \, dE_{k_{ICD}}. \tag{8.53b}$$

8.3.3 Time-dependently computed Interatomic-Coulombic-Decay-Electron Spectrum

Before deriving the ICD-electron spectrum by performing the integration in Eq. (8.53), the time-dependent Schrödinger equations (Eq. (8.48)) need to be solved. As usual, the exponential ansatz is applied. Its solutions are the wave functions associated with the decaying and final state, which are needed later. The vibrational decaying and final state read

$$|\psi_d(t)\rangle = e^{-i\hat{\mathcal{H}}_d t} \hat{V}_{d \leftarrow i}(E_{k_0}) \, |n_i\rangle \, , \tag{8.54a}$$

$$|\psi_f(E_{k_0'}, t)\rangle = -i \int_0^{t} dt' e^{i(\hat{H}_f + E_{k_0'})(t'-t)} \hat{W}_{f \leftarrow d} e^{-i\hat{\mathcal{H}}_d t} \hat{V}_{d \leftarrow i}(E_{k_0}) \, |n_i\rangle \, . \tag{8.54b}$$

As explained above, to get the ICD-electron spectrum, one has to integrate the coincidence spectrum Eq. (8.53) over the final states. Note that $|E_{n_f}\rangle = |E_{KER}\rangle$. This leads to the following expression for the coincidence spectrum

$$\begin{aligned} \sigma_{coin}(E_{k_{ICD}}, t) = \int dE_{KER} \, \langle n_i | \, \hat{V}_{d \leftarrow i}^{\dagger}(E_{k_0}) \big(i \int_0^{\infty} dt' e^{-i(E_{KER} + V_f^{\infty} + E_{k_{ICD}} - \hat{\mathcal{H}}_d)t'} \big) \hat{W}_{f \leftarrow d}^{\dagger} \, |E_{n_f}\rangle \\ \langle E_{n_f} | \, \hat{W}_{f \leftarrow d} \big(-i \int_0^{\infty} dt'' e^{i(E_{KER} + V_f^{\infty} + E_{k_{ICD}} - \hat{\mathcal{H}}_d)t''} \big) \hat{V}_{d \leftarrow i}(E_{k_0}) \, |n_i\rangle \, . \end{aligned} \tag{8.55}$$

The time-independent Schrödinger equation is applied, $E_{n_f} \, |E_{n_f}\rangle = E_{KER} + V_f^{\infty} \, |E_{n_f}\rangle = \hat{H}_f \, |E_{n_f}\rangle$, and afterward, the integration over the vibrational final states is performed, leading to

$$
\begin{aligned}
\sigma_{coin}(E_{k_{ICD}}, t) = \langle n_i | \, \hat{V}^{\dagger}_{d\leftarrow i}(E_{k_0}) i & \int_0^{\infty} dt' \mathrm{e}^{-i(\hat{H}_f + E_{k'_0})t'} \hat{W}^{\dagger}_{f\leftarrow d} \mathrm{e}^{i\hat{\mathfrak{H}}^{\dagger}_d t'} \\
& (-i) \int_0^{\infty} dt'' \mathrm{e}^{i(\hat{H}_f + E_{k'_0})t''} \hat{W}_{f\leftarrow d} \mathrm{e}^{-i\hat{\mathfrak{H}}_d t''} \hat{V}_{d\leftarrow i}(E_{k_0}) \, | n_i \rangle \\
& \mathrm{e}^{-i(\hat{H}_f + E_{k_{ICD}})t} \mathrm{e}^{i(\hat{H}_f + E_{k_{ICD}})t} . \qquad (8.56)
\end{aligned}
$$

By expanding Eq. (8.56) by $\mathrm{e}^{-i(\hat{H}_f + E_{k_{ICD}})t} \mathrm{e}^{i(\hat{H}_f + E_{k_{ICD}})t}$ the solution of the final state's Schrödinger equation Eq. (8.54) can be identified. Therefore, the ICD-electron spectrum finally reads

$$
\sigma_{ICD}(E_{k_{ICD}}) = \lim_{t\to\infty} \langle \psi_f(E_{k_{ICD}}, t) | \psi_f(E_{k_{ICD}}, t) \rangle \, , \qquad (8.57)
$$

and the time-resolved ICD-electron spectrum is given by

$$
\sigma_{ICD}(E_{k_{ICD}}, t) = \langle \psi_f(E_{k_{ICD}}, t) | \psi_f(E_{k_{ICD}}, t) \rangle \, . \qquad (8.58)
$$

The total ICD-electron spectrum equals the population of the final state accumulated to infinite times, while the time-resolved ICD-electron spectrum displays the final state population at each time step.

8.3.4 Time-dependently computed Kinetic-Energy-Release Spectrum

As explained above, the coincidence spectrum Eq. (8.52) is used to derive the KER spectrum. Inserting the initial condition $|\psi_d(t)\rangle = \mathrm{e}^{-i\hat{\mathfrak{H}}_d t} \hat{V}_{d\leftarrow i}(E_{k_0}) \, |n_i\rangle$ and solving the square of the amount results in

$$
\begin{aligned}
\sigma_{coin}(E_{KER}, E_{k_{ICD}}, t) = & \int_0^{\infty} dt' \mathrm{e}^{-i(E_{KER} + V_f^{\infty} + E_{k_{ICD}})t'} \int_0^{\infty} dt \, \mathrm{e}^{i(E_{KER} + V_f^{\infty} + E_{k_{ICD}})t} \\
& \langle \psi_d(t') | \hat{W}^{\dagger}_{f\leftarrow d} | E_{n_f} \rangle \, \langle E_{n_f} | \hat{W}_{f\leftarrow d} | \psi_d(t') \rangle \, . \qquad (8.59)
\end{aligned}
$$

Subsequently, the coincidence spectrum is integrated (see Eq. (8.53)) over the energy of the ICD electron $E_{k_{ICD}}$. The energy of the ICD electron is per definition positive, so we can easily expand the integral bounds without changing the result

$$
\sigma_{KER}(E_{KER}, t) = \int_{-\infty}^{\infty} dE_{k_{ICD}} \int_0^{\infty} dt' \int_0^{\infty} dt \, \mathrm{e}^{i(E_{KER} + V_f^{\infty} + E_{k_{ICD}})(t-t')} \langle \psi_d(t') | \hat{W}^{\dagger}_{f\leftarrow d} | E_{n_f} \rangle \, \langle E_{n_f} | \hat{W}_{f\leftarrow d} | \psi_d(t') \rangle \, . \qquad (8.60)
$$

To perform the integration, the energies and the times are substituted by $E = E_{KER} + V_f^{\infty} + E_{k_{ICD}}$ and $T = t - t'$ resulitng in

$$
\sigma_{KER}(E_{KER}, t) = \int_{-\infty}^{\infty} dE \int_0^{\infty} dt' \int_{-t'}^{\infty} dT \; \mathrm{e}^{iET} \langle \psi_d(t') | \hat{W}^{\dagger}_{f\leftarrow d} | E_{n_f} \rangle \, \langle E_{n_f} | \hat{W}_{f\leftarrow d} | \psi_d(T + t') \rangle \, . \qquad (8.61)
$$

By replacing the integration over E with a δ-function the expression above can be further simplified. The corresponding relation $\int_{-\infty}^{\infty} dE\, e^{iET} = 2\pi\delta(T)$ is inserted, and leads to

$$\sigma_{KER}(E_{KER}, t) = 2\pi \int_0^\infty dt' \int_{-t'}^{\infty} dT\, \delta(T) \langle \psi_d(t') | \hat{W}^\dagger_{f\leftarrow d} | E_{n_f} \rangle \langle E_{n_f} | \hat{W}_{f\leftarrow d} | \psi_d(T + t') \rangle\,. \tag{8.62}$$

Performing the time integration over T gives the final expression for the KER spectrum

$$\sigma_{KER}(E_{KER}) = \lim_{t\to\infty} 2\pi \int_0^t |\langle E_{n_f} | \hat{W}_{f\leftarrow d} | \psi_d(t') \rangle|^2\, dt', \tag{8.63}$$

whereas the time-resolved KER spectrum reads

$$\sigma_{KER}(E_{KER}, t) = 2\pi \int_0^t |\langle E_{n_f} | \hat{W}_{f\leftarrow d} | \psi_d(t') \rangle|^2\, dt'. \tag{8.64}$$

The KER spectrum can be interpreted as accumulated Franck-Condon factors between the decaying and the final state.

Chapter 9

Numerical Methods

In Chap. 8, the time-independent formalism of the PE spectrum and the time-dependent formalism of the ICD-electron as well as the KER spectrum is derived by introducing an arbitrary dimer, which is ionized and, subsequently undergoes ICD. The aim of the following two Chaps. 10 and 11 is to apply these expressions determined before to real systems - namely the NeKr and the Ar_2 dimer. For their implementations, numerical tools are required, which are the focus of this chapter. Two main tasks have to be solved in order to compute the spectra: The solutions of the time-independent and the time-dependent Schrödinger equation have to be found. The time-independent Schrödinger equation is an eigenvalue problem, which can be solved by diagonalization of the Hamiltonian matrix. Therefore, we need to choose a basis, in which the Hamiltonian and, consequently, also the eigenstates can be presented. An appropriate candidate is the discrete variable representation (DVR), which allows the computation of the potential-energy matrix directly on grid points, while a unitary transformation has to be performed to finally get the kinetic-energy operator in grid basis. Once the eigenvalues and eigenvectors are found, the PE spectrum can be time-independently computed, and we turn to the time-dependent approach, which is used for the ICD-electron and the KER spectrum. The time-dependent Schrödinger equation Eq. (8.48) is a system of first-order differential equations and is numerically solved by the Heidelberger MCTDH package, see Ref. [193], using the complex short iterative Lanczos integrator (CSIL), see Ref. [194]. Its solutions are the wave functions associated with the decaying and final state, necessary to compute the spectra. Because the final state is dissociative, the wave packet propagates along the final PEC and reaches the end of the grid after a short propagation time. To avoid reflection at the end of the grid, complex absorbing potentials (CAPs) are introduced and set at the end of the grid, which locally imitates the propagation of the population leaving the grid area by absorbing it. Furthermore, the CAP is used to determine the flux of a wave function through a dividing surface (into the CAP), which appears in the ICD-electron spectrum expressed by Eq. (8.56).

The following sections introducing the DVR (Sec. 9.1) and the CAP (Sec. 9.2) are based on Refs. [187, 195, 196] and [197], respectively. In general, DVRs and CAPs are comprehensive topics by themselves, and a detailed investigation would exceed the scope of this work.

Therefore, we only introduce the concept and the mathematical formulation by concentrating on the aspects required for the application in the following Chaps. 10 and 11. Studies about DVRs and CAPs can be found in the literature, for example, see Refs. [198–201] and [202–204], respectively. Sec. 9.3 about computational detail of the spectrum calculations completes the chapter.

9.1 Discrete Variable Representation

In the spectral method, a complete set of orthonormal functions $\{\varphi_i(x)\}_{i=0}^{\infty}$ is chosen as a basis. Furthermore, $\varphi_i, x\varphi_i, \frac{d}{dx}\varphi_i \in \mathcal{L}^2$ is demanded to guarantee the presentation of the wave function ψ, the potential-energy $\hat{V}$ and the kinetic-energy operator $\hat{T}$, whose matrix element $\langle\varphi_i|\hat{T}|\varphi_j\rangle$ has to be known analytically. By introducing the projector $\hat{P} = \sum_{i=0}^{N-1} |\varphi_i\rangle\langle\varphi_i|$, we can express the wave function and any operator as $\psi(x) = \sum_{i=0}^{N-1} c_i\varphi_i(x)$ and $\hat{O} = \sum_{i,j=1}^{N-1} |\varphi_i\rangle O_{ij}\langle\varphi_j|$, where $c_i = \langle\varphi_i|\psi\rangle$ is a vector element and $O_{ij} = \langle\varphi_i|\hat{O}|\varphi_j\rangle$ is a matrix element. Consequently, the action of any operator on the wave function reduces to matrix-vector multiplication: $\hat{O}\psi \rightarrow \boldsymbol{O}\boldsymbol{c}$. For the numerical realization, we cannot use an infinite number of functions, and therefore, we have to reduce the set to N functions $\{\varphi_i(x)\}_{i=0}^{N-1}$, which leads to the so-called basis-truncation error, but as long as $||(1 - \hat{P}|\psi\rangle||$ is small, the error is negligible. This representation of the wave function and operators is called the variational-basis representation (VBR). The matrix elements of kinetic-energy and the potential-energy operator now read

$$T_{ij}^{VBR} = \langle\varphi_i|\hat{T}|\varphi_j\rangle, \tag{9.1a}$$

$$V_{ij}^{VBR} = \langle\varphi_i|\hat{V}|\varphi_j\rangle = \int \varphi_i^* \; V(x) \; \varphi_j \; dx. \tag{9.1b}$$

While T_{ij}^{VBR} is known analytically, $N(N+1)/2$ integrals have to be solved to compute the potential energy matrix V^{VBR}, which is numerically expensive. Instead of the spectral method, a grid-based method can be used to overcome this problem, where a set of equidistant grid points $\{x_\alpha\}_{\alpha=0}^{N-1}$ is taken at which the wave function is stored: $\psi(x) \approx \{\psi(x_\alpha)\}$. Furthermore, the operation of the potential energy operator $\hat{V}$ on the wave function ψ is only given at the grid points x_α: $[\hat{V}\psi](x) \approx (V(x_1)\psi(x_1), ..., V(x_N)\psi(x_N))^T$. Consequently, the matrix of the potential energy operator can be directly constructed as a diagonal matrix with the potential energies evaluated at the grid points x_α as entries $\boldsymbol{V}^{Grid} = \mathrm{diag}(V(x_\alpha))$. For the representation of the kinetic-energy operator in the equidistant grid basis, where it is not known analytically, the Laplacian matrix ($\boldsymbol{T}^{Grid} = -\frac{1}{2m(\Delta x)^2}\boldsymbol{L}$) can be used, which is easy to compute but not very precise. In the following, we combine the benefits of the spectral method (T_{ij}) known analytically and the grid-based method ($V(x_\alpha)$) by introducing pseudo-spectral methods with a focus on the sine-DVR, which is used for the computations of the spectra.

9.1.1 Pseudo-Spectral Methods

For the pseudo-spectral method, a set of orthonormal functions $\{\varphi_i(x)\}_{i=0}^{N-1}$ has to be chosen as in the spectral method, in which the wave function ψ can be expanded. The grid-based method comes into play by the requirement that the expanded wave function ψ is exact at a number of points $\{x_\alpha\}$. This approach is called collocation and the wave function reads

$$\psi(x_\alpha) = \sum_i c_i \varphi_i(x_\alpha), \tag{9.2}$$

where the expansion coefficients $c_i = \langle \varphi_i(x_\alpha) | \psi(x_\alpha) \rangle$ are the elements of the vector $\boldsymbol{c}$, which is finally saved as a representation of the wave function in the above-introduced basis denoted by $\boldsymbol{b}$. In the following, $\boldsymbol{g}$ marks the grid representation, where the grid points $\{x_\alpha\}$ built the basis. Note that the grid points do not have to be equidistantly distributed. The above equation of the collocation wave function Eq. (9.2) can be rewritten in matrix-vector notation by introducing the matrix $G_{\alpha i} = \varphi_i(x_\alpha)$, which allows us to change between the grid $\boldsymbol{g}$ and basis $\boldsymbol{b}$ representation

$$\boldsymbol{\psi}^g = \boldsymbol{G}\boldsymbol{c}, \qquad \boldsymbol{c} = \boldsymbol{G}^{-1}\boldsymbol{\psi}^g. \tag{9.3}$$

We return to the representation of the Hamiltonian, and especially to that of the kinetic-energy operator. While the kinetic-energy operator in the VBR is given analytically, the easily implemented solution for the kinetic-energy operator in the equidistant-grid basis, the Laplacian matrix, is not precise. It is beneficial to check if a better representation can be found using Eq. (9.3). Therefore, the action of the kinetic-energy operator on the wave function is determined in the grid basis

$$(\boldsymbol{T}\boldsymbol{\psi})^g = \boldsymbol{G}(\boldsymbol{T}\boldsymbol{\psi})^b = \boldsymbol{G}\boldsymbol{T}^b\boldsymbol{c} = \boldsymbol{G}\boldsymbol{T}^b\boldsymbol{G}^{-1}\boldsymbol{\psi}^g \qquad \rightarrow \boldsymbol{T}_1^g = \boldsymbol{G}\boldsymbol{T}^b\boldsymbol{G}^{-1}, \tag{9.4}$$

where Eq. (9.3) is used for the algebraic transformations and one finally gets the definition $\boldsymbol{T}_1^g$ for the kinetic energy in the grid basis. Alternatively, the two arbitrary wave functions are used

$$|\phi\rangle = \sum_i k_i \, |\varphi_i\rangle \,, \qquad |\psi\rangle = \sum_i c_i \, |\varphi_i\rangle \,, \tag{9.5}$$

to compute the matrix element of the kinetic energy operator in the grid basis

$$\langle \phi | \hat{T} | \psi \rangle = \boldsymbol{k}^\dagger \boldsymbol{T}^b \boldsymbol{c} = (\boldsymbol{G}^{-1}\boldsymbol{\phi}^g)^\dagger \boldsymbol{T}^b \boldsymbol{G}^{-1}\boldsymbol{\psi}^g = \boldsymbol{\phi}^{g^\dagger}\boldsymbol{G}^{-1^\dagger}\boldsymbol{T}^b\boldsymbol{G}^{-1}\boldsymbol{\psi}^g \qquad \rightarrow \boldsymbol{T}_2^g = \boldsymbol{G}^{\dagger^{-1}}\boldsymbol{T}^b\boldsymbol{G}^{-1}. \tag{9.6}$$

One sees, apparently, the definitions of the kinetic energy in grid representation $\boldsymbol{T}_1^g$ and $\boldsymbol{T}_2^g$ do not coincide. This inconsistency is caused by the fact that for the derivation of Eq. (9.6) an integration has to be performed. By examining the scalar product of two collocation wave functions a volume element type of weight is defined, which makes the two definitions consistent

$$\begin{aligned}\langle\phi|\psi\rangle &= \boldsymbol{k}^{\dagger}\boldsymbol{c} = \boldsymbol{\phi}^{g^{\dagger}}\boldsymbol{G}^{-1^{\dagger}}\boldsymbol{G}^{-1}\boldsymbol{\psi}^{g} = \boldsymbol{\phi}^{g^{\dagger}}(\boldsymbol{G}\boldsymbol{G}^{\dagger})^{-1}\boldsymbol{\psi}^{g} \\ &= \sum_{\alpha\beta}\phi^{*}(x_{\alpha})(\boldsymbol{G}\boldsymbol{G}^{\dagger})^{-1}_{\alpha\beta}\psi(x_{\beta}) = \sum_{\alpha\beta}\phi^{*}(x_{\alpha})W_{\alpha\beta}\psi(x_{\beta}),\end{aligned} \tag{9.7}$$

where again Eq. (9.3) is used and $W_{\alpha\beta} = (\boldsymbol{G}\boldsymbol{G}^{\dagger})^{-1}_{\alpha\beta}$ is introduced. By demanding that $\boldsymbol{W}$ is diagonal, Eq. (9.8) becomes a Gaussian quadrature type of scalar product

$$W_{\alpha\beta} = \omega_{\alpha}\delta_{\alpha\beta}, \qquad \langle\phi|\psi\rangle = \sum_{\alpha}\omega_{\alpha}\phi^{*}(x_{\alpha})\psi(x_{\alpha}) = \boldsymbol{\phi}^{g^{\dagger}}\boldsymbol{W}\boldsymbol{\psi}^{g}. \tag{9.8}$$

Gaussian quadrature is a numerical method to integrate functions of orders up to $2N-1$ with only N points. Therefore, N quadrature weights $\{\omega_{\alpha}\}$ and points $\{x_{\alpha}\}$ have to be determined, respectively. As basis functions, a set of orthonormal polynomials of order $N-1$ is chosen, $\{\psi_i\}_{i=0}^{N-1}$. After a polynomial division by the corresponding polynomial of order N, the integral can be rewritten and the orthonormality of the set of polynomials leads to the analytical elimination of one part of the new integral. The quadrature weights and points are chosen in a way that this part also numerically vanishes, which finally leads to the replacement of the initial integral of a function of order $2N-1$ by an integral over a function of order $N-1$. The quadrature weights are given by the orthonormality relation of the set of polynomials and the quadrature points are the roots of the polynomial of order N, which is not in the basis $\{\psi_i\}_{i=0}^{N-1}$. A detailed explanation regarding Gaussian quadrature can be found in Ref. [187, 205]. For the remainder of this work, it is sufficient to know that the quadrature weights and quadrature points are taken to diagonalize $\boldsymbol{W}$. Under the assumption that $\boldsymbol{W}$ is diagonal, the two definitions of the kinetic-energy operator in grid basis become consistent due to the extra weight of the quadrature

$$\langle\phi|\hat{T}|\psi\rangle = \langle\phi|\hat{T}\psi\rangle = \boldsymbol{\phi}^{\dagger}\boldsymbol{W}\underbrace{\boldsymbol{G}\boldsymbol{T}^{b}\boldsymbol{G}^{-1}}_{\boldsymbol{T}^{g}_{1}}\boldsymbol{\psi} = \boldsymbol{\phi}^{\dagger}(\boldsymbol{G}\boldsymbol{G}^{\dagger})^{-1}\boldsymbol{G}\boldsymbol{T}^{b}\boldsymbol{G}^{-1}\boldsymbol{\psi} = \boldsymbol{\phi}^{\dagger}\underbrace{\boldsymbol{G}^{\dagger^{-1}}\boldsymbol{T}^{b}\boldsymbol{G}^{-1}}_{\boldsymbol{T}^{g}_{2}}\boldsymbol{\psi}. \tag{9.9}$$

Furthermore, only if $\boldsymbol{W}$ is diagonal the last interchange of $\boldsymbol{G}$ and $\boldsymbol{W}^{1/2}$ is allowed

$$\begin{aligned}&\boldsymbol{G}\boldsymbol{G}^{\dagger} = \boldsymbol{W}^{-1}, \\ &\boldsymbol{W}^{1/2}\boldsymbol{G}\boldsymbol{G}^{\dagger}\boldsymbol{W}^{1/2} = \mathbb{1}, \\ &(\boldsymbol{W}^{1/2}\boldsymbol{G})(\boldsymbol{G}\boldsymbol{W}^{1/2})^{\dagger} = (\boldsymbol{W}^{1/2}\boldsymbol{G})(\boldsymbol{W}^{1/2}\boldsymbol{G})^{\dagger} = \mathbb{1},\end{aligned} \tag{9.10}$$

and one can find the matrices $\boldsymbol{U}$ and $\boldsymbol{U}^{\dagger}$, which perform a unitary transformation from grid to basis and from basis to grid representation, respectively

$$\boldsymbol{U}^{\dagger} = \boldsymbol{W}^{1/2}\boldsymbol{G}, \qquad \boldsymbol{U} = \boldsymbol{G}^{\dagger}\boldsymbol{W}^{1/2}, \qquad U_{i\alpha} = \omega_{\alpha}^{1/2}\varphi_i(x_{\alpha}), \tag{9.11}$$

where $U_{i\alpha}$ describes the matrix elements. As a unitary matrix, $\boldsymbol{U}$ fulfills the relation for discrete orthogonality of the basis functions $(\boldsymbol{U}\boldsymbol{U}^{\dagger})_{ij} = \sum_{\alpha}\omega_{\alpha}\varphi_i^{*}(x_{\alpha})\varphi_j(x_{\alpha}) = \delta_{ij}$ and discrete completeness on the grid points $(\boldsymbol{U}^\dagger\boldsymbol{U})_{\alpha\beta} = \sum_i (\omega_\alpha\omega_\beta)^{1/2}\varphi_i(x_\alpha)\varphi_i^*(x_\beta) = \delta_{\alpha\beta}$, and is, therefore, orthogonal, which means that row (discrete orthogonality) and column (discrete completeness) vectors are orthonormal by forming the scalar products, respectively. Here, the scalar product of the discrete completeness relation is the completeness relation of the orthonormal polynomials $\{\varphi_i(x)\}_{i=0}^{N-1}$ written as Gaussian quadrature. Consequently, the points $\{x_\alpha\}$ and weights $\{\omega_\alpha\}$ of an N-Gaussian quadrature have to be taken to get the unitary transformation matrix $\boldsymbol{U}$, which is the orthogonal version of the collocation matrix.

This pseudo-spectral method related to the spectral basis by an orthogonal collocation matrix $\boldsymbol{U}$, which is based on Gaussian quadrature points and weights, is called discrete variable representation (DVR). In the following, the DVR functions $\{\chi_\alpha(x)\}$ of order $N-1$ are introduced. Besides building our new basis, they are used to define the quadrature weights and to find the quadrature points $\{x_\alpha\}$, which diagonalize $\boldsymbol{W}$ and, subsequently, give the unitary transformation $\boldsymbol{U}$. Therefore, N linear combinations of the polynomials $\{\varphi_i\}_{i=0}^{N-1}$ are constructed, which share the same roots, except one at x_α, with φ_N, respectively,

$$\chi_\alpha(x) = \sum_i U_{i\alpha}\varphi_i(x) = \sum_i \omega_\alpha^{1/2}\varphi_i^*(x_\alpha)\varphi_i(x). \tag{9.12}$$

Evaluating $\chi_\alpha(x_\beta)$ at point ω_β and using the orthonormality of the polynomials, define the quadrature weights

$$\chi_\alpha(x_\beta) = \sum_i \omega_\alpha^{1/2}\varphi_i^*(x_\alpha)\varphi_i(x_\beta) = \omega_\beta^{-1/2}\sum_i \omega_\alpha^{1/2}\omega_\beta^{1/2}\varphi_i^*(x_\alpha)\varphi_i(x_\beta) = \omega_\beta^{-1/2}\sum_i U_{i\alpha}U_{i\beta} = \omega_\alpha^{-1/2}\delta_{\alpha\beta}. \tag{9.13}$$

Furthermore, the set of the DVR functions is orthonormal as well, $\langle\chi_\alpha|\chi_\beta\rangle = \delta_{\alpha\beta}$, and forms a basis. To determine the quadrature points, the following matrix elements are calculated

$$\langle\chi_\alpha|x|\chi_\beta\rangle = \sum_\gamma \omega_\gamma\chi_\alpha^*(x_\gamma)x_\gamma\chi_\beta(x_\gamma) = x_\alpha\delta_{\alpha\beta}, \tag{9.14}$$

whereby using Eq. (9.13) one can see that the above equation is only non-zero if $\alpha = \beta = \gamma$. Consequently, $\{\chi_\alpha\}$ are eigenfunctions of $\boldsymbol{X}$ in the basis $\{\varphi_i\}_{i=0}^{N-1}$ with eigenvalues $\{x_\alpha\}$. Because the eigenvalues are independent of the basis, one can construct

$$X_{ij} = \langle\varphi_i|x|\varphi_i\rangle\,. \tag{9.15}$$

$\boldsymbol{X}$ is tri-diagonal because of the form of the recursion relation, which is fulfilled by the orthogonal polynomials $\{\varphi_i\}_{i=0}^{N-1}$. As a consequence, the eigenvalues of $\boldsymbol{X}$ are roots of φ_N. Diagonalizing $\boldsymbol{X}$ gives the eigenvalues $\{x_\alpha\}$ and the eigenvectors, which can be combined to form the transformation matrix $\boldsymbol{U}$

$$\boldsymbol{X} = \boldsymbol{U}\boldsymbol{D}\boldsymbol{U}^{\dagger}, \qquad \boldsymbol{D} = \boldsymbol{diag}(x_{\alpha}). \tag{9.16}$$

Returning to the Hamiltonian, see Eq. (9.1), we introduce the finite-basis representation (FBR). If the matrix element of the potential-energy operator cannot be calculated exactly and is evaluated by using Gaussian quadrature, the corresponding potential-energy operator is no longer expressed in the VBR but in the FBR basis due to the quadrature-induced error. $\boldsymbol{T}^{VBR} = \boldsymbol{T}^{FBR}$ is known analytically and can be easily expressed in the DVR basis by applying the unitary transformation operator: $\boldsymbol{T}^{DVR} = \boldsymbol{U}^{\dagger}\boldsymbol{T}^{FBR}\boldsymbol{U}$. Of course, the potential-energy operator in FBR can also be written in DVR by unitary transformation and vise verse. For the sake of consistency, this is shown:

$$\boldsymbol{V}_{ij}^{FBR} = \sum_{\alpha=0}^{N-1} \omega_{\alpha}\varphi_{i}^{*}(x_{\alpha})V(x_{\alpha})\varphi_{j}(x_{\alpha}) = \sum_{\alpha=0}^{N-1} U_{i\alpha}V(x_{\alpha})U_{j\alpha}^{*} = (\boldsymbol{U}\boldsymbol{V}^{DVR}\boldsymbol{U}^{\dagger})_{ij}. \tag{9.17}$$

Note that the integration, see Eq. (9.1b) is performed by Gaussian quadrature and is, therefore, expressed in FBR. Furthermore, the potential-energy operator can now be directly computed in the DVR basis $\{\chi_{\alpha}\}$

$$\boldsymbol{V}_{\alpha\beta}^{DVR} = \langle\chi_{\alpha}|\hat{V}|\chi_{\beta}\rangle = \langle\chi_{\alpha}|\hat{V}(x)|\chi_{\beta}\rangle = \int \chi_{\alpha}^{*}(x)V(x)\chi_{\beta}(x)dx \approx \sum_{\gamma=0}^{N-1} \omega_{\gamma}\chi_{\alpha}^{*}(x_{\gamma})V(x_{\gamma})\chi_{\beta}(x_{\gamma}) = V(x_{\alpha})\delta_{\alpha\beta}. \tag{9.18}$$

Consequently, the potential-energy matrix reduces to a diagonal matrix with the potential energy evaluated at the quadrature points, which simplifies the computation enormously. The task of DVR is to find a unitary transformation operator, which can be used to transform the analytically known kinetic-energy operator in FBR to DVR and - more importantly - which diagonalizes the potential-energy operator in DVR such that the potential only needs to be evaluated on N points instead of solving $N(N+1)/2$ integrals.

9.1.2 Sine-DVR

For $\{\varphi_{i}\}_{i=0}^{N-1}$, different sets of orthonormal functions can be used, where the choice usually depends on the potential-energy operator. For example, Hermite polynomials are chosen for systems similar to the one of the harmonic oscillator. Because they are the eigenfunctions of the Harmonic oscillator, the potential-energy operator can be well represented in the corresponding DVR. The grid points are not equidistantly distributed, and their distribution becomes denser at the end of the grid. Thus, fewer grid points are necessary to describe the Hamiltonian. Because we only investigate systems with one degree of freedom, saving memory does not restrict the computation and, therefore, allows using the sine-DVR. Our basis functions are then eigenfunctions of the quantum mechanical 1D “Particle in a box” problem, which are sine functions,

$$\varphi_i(x) = \sqrt{\frac{2}{L}}\sin\Big(\frac{i\pi(x-x_0)}{L}\Big). \tag{9.19}$$

The eigenfunctions are defined for $i = 1, \ldots, N$. The grid points are equally distributed between the starting point x_0 and $x_0 + L$, where L denotes the box length or, here, the grid length. As a result, compared to other DVRs more grid points are required to represent the Hamiltonian correctly. However, the huge advantage is that not only the kinetic-energy operator in FBR,

$$\langle\varphi_i|\hat{T}|\varphi_j\rangle = \frac{1}{2m}\langle\varphi_i|\frac{\partial^2}{\partial x^2}|\varphi_j\rangle = \frac{1}{2m}\Big(\frac{j\pi}{L}\Big)^2\langle\varphi_i|\varphi_j\rangle = \frac{j^2\pi^2}{2mL^2}\delta_{ij}, \tag{9.20}$$

but also the unitary transformation matrix $\boldsymbol{U}$, the quadrature points $\{x_\alpha\}$ and the weights $\{\omega_\alpha\}$ are known analytically. As explained above, the quadrature points have to equal the roots of φ_N and can be found by diagonalizing $\boldsymbol{X}$, which has to be tri-diagonal. There is no recursion rule for x, but for $f(x) = \cos\big(\frac{\pi(x-x_0)}{L}\big)$, and therefore, the corresponding matrix $\boldsymbol{F}$ has to be diagonalized in order to find the quadrature points, which are now roots of φ_{N+1} due to the choice of the basis functions. Since the inverse function is formed later, $f(x)$ must be monotonic in $[x_0, x_0 + L]$. If follows

$$f(x)\varphi_i(x) = \sqrt{\frac{2}{L}}\frac{1}{2}\sin\Big(\frac{(i-1)\pi(x-x_0)}{L}\Big) + \sqrt{\frac{2}{L}}\frac{1}{2}\sin\Big(\frac{(i+1)\pi(x-x_0)}{L}\Big) = \frac{1}{2}(\varphi_{i+1}(x) + \varphi_{i-1}), \tag{9.21}$$

where the relation between the product of sine and cosine is used. Because the recursion rule is fulfilled, one can construct the tri-diagonal matrix $\boldsymbol{F}$, whose elements read $F_{ij} = \langle\varphi_i|f(x)|\varphi_j\rangle$. By diagonalizing $\boldsymbol{F}$, the eigenvectors with the elements $U_{i\alpha}$ and the eigenvalues f_α are obtained

$$U_{i\alpha} = \sqrt{\frac{2}{N+1}}\sin\Big(\frac{i\alpha}{N+1}\Big), \tag{9.22}$$

$$f_\alpha = \cos\Big(\frac{\alpha\pi}{N+1}\Big). \tag{9.23}$$

By applying the inverse function f^{-1}, the grid points read

$$x_\alpha = f^{-1}(f_\alpha) = x_0 + \frac{L}{\pi}\arccos(f_\alpha) = x_0 + \alpha\frac{L}{N+1} = x_0 + \alpha\Delta x. \tag{9.24}$$

Furthermore, the weights can be computed using the definition of $U_{i\alpha}$,

$$\omega_\alpha^{1/2} = \frac{U_{i\alpha}}{\varphi_i^*(x_\alpha)} = \sqrt{\frac{L}{N+1}} = \sqrt{\Delta x_\alpha}. \tag{9.25}$$

The equations above are used to implement the nuclear Hamiltonians, see Eq. (8.42), in DVR in Python3, which are subsequently diagonalized. Their eigenvalues and eigenvectors are used to time-independently compute the PE spectrum (Eq. (8.36)) and to time-dependently compute the ICD-electron as well as the KER spectrum, see Eqs. (8.57) and (8.63).

9.2 Complex Absorbing Potential and Flux

After the ionized dimer has undergone ICD, two cations are left, which repel each other and form the dissociative final state together with the two emitted electrons. While slower parts of the wave packet are still in the interaction region, faster parts of the wave packet propagate along the grid to larger internuclear distances. When they reach the end of the grid, nonphysical reflections occur, which do not belong to the investigated process. One solution is to increase the grid size, but a huge grid and many grid points are numerically expensive. A more convenient way includes the introduction of a complex absorbing potential (CAP), which extends the considered Hamiltonian of the final state $\hat{H}_f$ by a complex component

$$\hat{\hat{H}}_f = \hat{H}_f - i\hat{W}_{CAP}. \tag{9.26}$$

It annihilates the population at the end of the grid in the region $[R_c, L]$, where L denotes the length of the grid

$$W_{CAP}(R) = \eta(R - R_c)^n \theta(R - R_c). \tag{9.27}$$

$W_{CAP}(R)$ is a polynomial of order n, which is switched on at the internuclear distance R_c by the Heaviside step function $\theta(R - R_c)$. η denotes the strength of the CAP and controls the speed of the population annihilation. Furthermore, the CAP also causes reflections. To avoid those, one has to choose a rather small values for η, which gives a weak CAP leading to the transmission of the population. The length of the CAP has to be adapted by optimizing the CAP parameters. In general, the CAP is located at the end of the grid outside the region of physical relevance.

By adding a CAP to the Hamiltonian in Eq. (9.26) becomes non-Hermitian, which means that the norm is no longer conserved

$$\frac{d}{dt}\langle\psi_f|\psi_f\rangle = i\langle\psi_f|\hat{\hat{H}}_f^\dagger - \hat{\hat{H}}_f|\psi_f\rangle = -2\langle\psi_f|\hat{W}_{CAP}|\psi_f\rangle. \tag{9.28}$$

The decreasing norm in Eq. (9.28) reflects the annihilation of the final state population. Consequently, the loss of population has to be considered, when computing the ICD-electron spectrum, and therefore, the original expression (see Eq. (8.57)) is extended. Based on Refs. [193, 197], we derived a working equation for the ICD-electron spectrum by having in mind that for time $t = \infty$ the whole population has left the interaction region and has reached the CAP at R_c,

$$\sigma_{ICD}(E_{k_0'}) = \lim_{t\to\infty}\int_{R_c}^{\infty} dR\, |\psi_f(R, E_{k_0'}, t)|^2 = \int_0^{\infty} dt \int_{R_c}^{\infty} dR\, \frac{d}{dt}|\psi_f(R, E_{k_0'}, t)|^2. \tag{9.29}$$

where the limit value is replaced by a time integral and a time derivative. Eq. (9.29) can be further simplified by rewriting the integral over the nuclear coordinate using the step function $\theta(R - R_c)$. Furthermore, the time derivation is performed by inserting the time-dependent Schrödinger equation, leading to

$$= \int_0^\infty dt \frac{d}{dt} \langle \psi_f(R, E_{k'_0}, t)|\theta|\psi_f(R, E_{k'_0}, t)\rangle = i \int_0^\infty dt \, \langle \psi_f|[\hat{H}_f, \theta]|\psi_f\rangle \,. \tag{9.30}$$

The flux operator is introduced,

$$\hat{F} = i[\hat{H}_f, \theta] = i\hat{H}_f\theta - i\theta\hat{H}_f = i\hat{\tilde{H}}_f^\dagger\theta - i\theta\hat{\tilde{H}}_f + 2\hat{W}_{CAP}, \tag{9.31}$$

where $\theta\hat{W}_{CAP} = \hat{W}_{CAP}\theta = \hat{W}_{CAP}$ holds. The flux operator can now be inserted into Eq. (9.30), which transforms the ICD-electron spectrum to

$$\sigma_{ICD}(E_{k'_0}) = \int_0^\infty dt \frac{d}{dt} \langle \psi_f(t)|\theta|\psi_f(t)\rangle + \int_0^\infty dt \, \langle \psi_f(t)|2\hat{W}_{CAP}|\psi_f(t)\rangle = \int_0^\infty dt \, \langle \psi_f(t)|2\hat{W}_{CAP}|\psi_f(t)\rangle \,, \tag{9.32}$$

where the first integral vanishes because at $t = 0$ is no population on the PEC and at $t = \infty$ is the population annihilated by the CAP. However, in practice, we propagate to some fixed time $t = T$, which is defined by the time of the decay and the time the final state population needs to leave the interaction region. For clarity, $E_{k'_0}$ is replaced by $E_{k_{ICD}}$ and our final ICD-electron spectrum reads

$$\sigma_{ICD}(E_{k_{ICD}}) = \langle \psi_f(T)|\theta|\psi_f(T)\rangle + \int_0^T dt \, \langle \psi_f(t)|2\hat{W}_{CAP}|\psi_f(t)\rangle \,, \tag{9.33}$$

where the first term describes the transmitted population, which is still in the CAP region $[R_c, L]$ and the second part gives the annihilated population. Eq. (9.33) can be understood as an extension of Eq. (8.57). Assuming that at $t = T$, the whole population has reached the CAP, only the region of the CAP has to be considered. Therefore, the transmitted population is the population on the final grid and equals Eq. (8.57), which is finally extended by the contribution of the annihilated population.

9.3 Computational Details

For the computation of the PE spectrum, the matrices of the ground and decaying state Hamiltonian $\boldsymbol{H}_i$ and $\boldsymbol{\mathcal{H}}_d$ have to be diagonalized to obtain the corresponding eigenvalues and eigenvectors. Therefore, the Hamiltonians were represented in the DVR basis, for whose implementation a Python3 module was used, see Ref. [196]. The diagonalization was also realized in Python3. Most diagonalization routines use the Euclidean norm, as required for the eigenvectors of $\boldsymbol{H}_i$. Because $\boldsymbol{\mathcal{H}}_d$ is non-Hermitian, its eigenvectors should fulfill the orthogonality relation for complex eigenvectors, which equals a c-product, see Sec. 8.2. Consequently, we had to renormalize the eigenvectors. After the eigenvalues and eigenvectors have been found in the DVR basis, the implementation of the PE spectrum including interference effects (see Eq. (8.36)) in Python3 is straightforward.

For the implementation of the ICD-electron and the KER spectrum, see Eqs. (8.57) and (8.63), the time-dependent Schrödinger equations in Eq. (8.48) were solved by using the Heidelberger MCTDH package, see Ref. [193], which is a Fortran-based algorithm developed to solve multidimensional nuclear-dynamic problems. Besides multidimensional dynamical calculations, numerically exact calculations can be performed for low-dimensional systems. We investigated dimers, which exhibit only one vibrational degree of freedom, given by the internuclear distance R. Although the MCTDH package is a tool much more powerful than our system requires, we decided to use the algorithm because it is well established, and we benefit from its reliability. We applied the *exact* calculation option implemented in the MCTDH algorithm, where our time-dependent wave functions are expanded in the primitive basis, to execute the propagation in the decaying and the final state and to determine the quantum flux, which is needed for the computation of the ICD-electron spectrum Eq. (8.57).

As already mentioned, the working equations form a set of first-order differential equations. The corresponding time-dependent Schrödinger equation in matrix notation reads

$$i \cdot \begin{pmatrix} |\dot{\psi}_d(t)\rangle \\ |\dot{\psi}_f(E_{k_0'}, t)\rangle \end{pmatrix} = \begin{pmatrix} \hat{\mathcal{H}}_d & 0 \\ \hat{W}_{f\leftarrow d} & (\hat{H}_f + E_{k_0'}) \end{pmatrix} \cdot \begin{pmatrix} |\psi_d(t)\rangle \\ |\psi_f(E_{k_0'}, t)\rangle \end{pmatrix} . \tag{9.34}$$

The initial condition for $t = 0$ fs is given by

$$\begin{pmatrix} |\psi_d(t_0)\rangle \\ |\psi_f(E_{k_0'}, t_0)\rangle \end{pmatrix} = \begin{pmatrix} \hat{V}_{d\leftarrow i}(E_{k_0})\,|n_i\rangle \\ |0\rangle \end{pmatrix} , \tag{9.35}$$

where the whole population of the ground state is immediately transferred to the decaying state, and the final state is still unpopulated. Because $|n_i\rangle$ is a vibrational eigenstate of the electronic ground state, the initial condition can easily be determined by diagonalizing the matrix of the ground state Hamiltonian $\boldsymbol{H}_i$, which is represented in sine-DVR. The wave functions $|\psi_d(t)\rangle$ and $|\psi_f(E_{k_0'}, t)\rangle$ are propagated on a combined grid, which is defined by the primitive basis consisting of the vibrational degree of freedom R as well as the two electronic states $|\phi_d\rangle$ and $|\phi_f\rangle$. Because the sine-DVR is used, the $N = 1024$ grid points are equidistantly distributed over the grid of the internuclear distance R, which ranges from 2 to 12.23 Å. For the propagation in time, the set of first order-differential Schrödinger equations (Eq. (9.34)) has to be solved. Due to the non-Hermiticity of the decaying state Hamiltonian $\hat{\mathcal{H}}_d$, we have to use the complex short iterative Lanczos (CSIL) integrator, which is based on the Lanczos-Arnoldi algorithm, see Ref. [194].

When the wave functions propagated in time are known, we can determine the ICD-electron and the KER spectrum, see Eqs. (8.57) and (8.63). Of course, in practice, we cannot propagate until infinite times. Therefore, we chose a time range, in which the whole population of the decaying state completely decays to the final state. A higher vibrationally excited ground state causes a more delocalized initial wave function. Since the decay width decreases with increasing nuclear distance, the propagation time from different vibrationally selected ICD pathways varies between 1500 fs ($\nu = 0$) and 45000 fs ($\nu = 4$). Because the final state is dissociative, the population propagates on the corresponding PEC along the grid in the direction of higher internuclear distances. Consequently, longer propagation times also require a bigger grid. Because practically, our grid size is limited, a complex absorbing potential (CAP) is introduced. This third-order CAP is located at the end of the grid to simulate the propagation of the population out of the defined grid area and to avoid reflections, see Sec. 9.2.

After performing the propagation, the wave function at each time step of the decaying state $\psi_d(t)$ is output by the analysis program *showspf* and can be subsequently used for the implementation of Eq. (8.63), for which we used Python3. The ICD-electron spectrum can nearly be fully determined within the MCTDH package by using the analysis program *flux*. Therefore, the third-order CAP is set at the end of the grid $R_c = 18$ au ≈ 9.53 Å. Note that for the tracking of time-resolved spectra, the CAP has to be set in the interaction region. Applying the analysis program, creates the file *iwtt*, which contains the accumulated population of the final state absorbed and transmitted by the CAP for each time step, see Eq. (9.31). Plotting the accumulated final state population against the propagation time, gives a converged curve. The last value approximates the population at infinite times for a given energy of the ICD electron and is, therefore, one point of the ICD-electron spectrum, see Eq. (8.57). Because the wave function of the final state depends solely parametrically on $E_{k_{ICD}}$, the propagation and the flux analysis have to be performed separately for each ICD-electron energy to finally obtain the ICD-electron spectrum.

Chapter 10

ICD in NeKr

In this chapter, we study the Ne2s ionization and the subsequent ICD in the NeKr dimer. After the ionization of the Ne atom, where the photoelectron e^-_{PE} is ejected, the 2s vacancy is filled by a 2p electron, and the excess energy is transferred radiationlessly to the neighboring Kr atom, which results in its 4p ionization via the emission of the ICD electron e^-_{ICD}. The photon energy of 48.68 eV is only slightly above the threshold, and therefore, the ejected ICD-electron is higher in kinetic energy than the previously ejected photoelectron. Besides the two electrons, the two cations Ne^+ and Kr^+ remain. Due to their positive charge, they repel each other and drift apart, which leads to a Coulomb explosion. The described mechanism is shown below

$$\mathrm{NeKr} + \hbar\omega \longrightarrow \mathrm{Ne}^+(2\mathrm{s}^{-1})\mathrm{Kr} + e^-_{PE} \longrightarrow \mathrm{Ne}^+(2\mathrm{p}^{-1}) + \mathrm{Kr}^+(4\mathrm{p}^{-1}) + e^-_{PE} + e^-_{ICD}. \tag{10.1}$$

We investigate the above-explained process by computing time-independently the PE spectra and time-dependently the ICD-electron and KER spectra. The PE spectra exhibit interferences, which occur due to the coherently populated vibrational levels for the $\mathrm{Ne}^+(2\mathrm{s}^{-1})\mathrm{Kr}$ state and their partial decay widths, causing the vibrational levels to overlap. A different source of interferences affects the ICD-electron spectrum. The population is continuously transferred from the decaying to the final state, where it interferes with the population, which is already in the final state and propagates. To get full insight into the nuclear dynamics during ICD, we also investigate vibrationally selected ICD, where the population is initially prepared in one of the excited vibrational eigenstates of the electronic ground state. The results shown in this chapter were reported in Ref. [65].

A convenient way to describe the dynamics of the process in Eq. (10.1) is the wave-packet propagation formulation of the electronic decay, see Refs. [109, 110, 112]. For this purpose, we need to introduce the PECs of all electronic states involved in the process and their corresponding vibrational eigenstates with their partial decay widths, see Fig. 10.1.

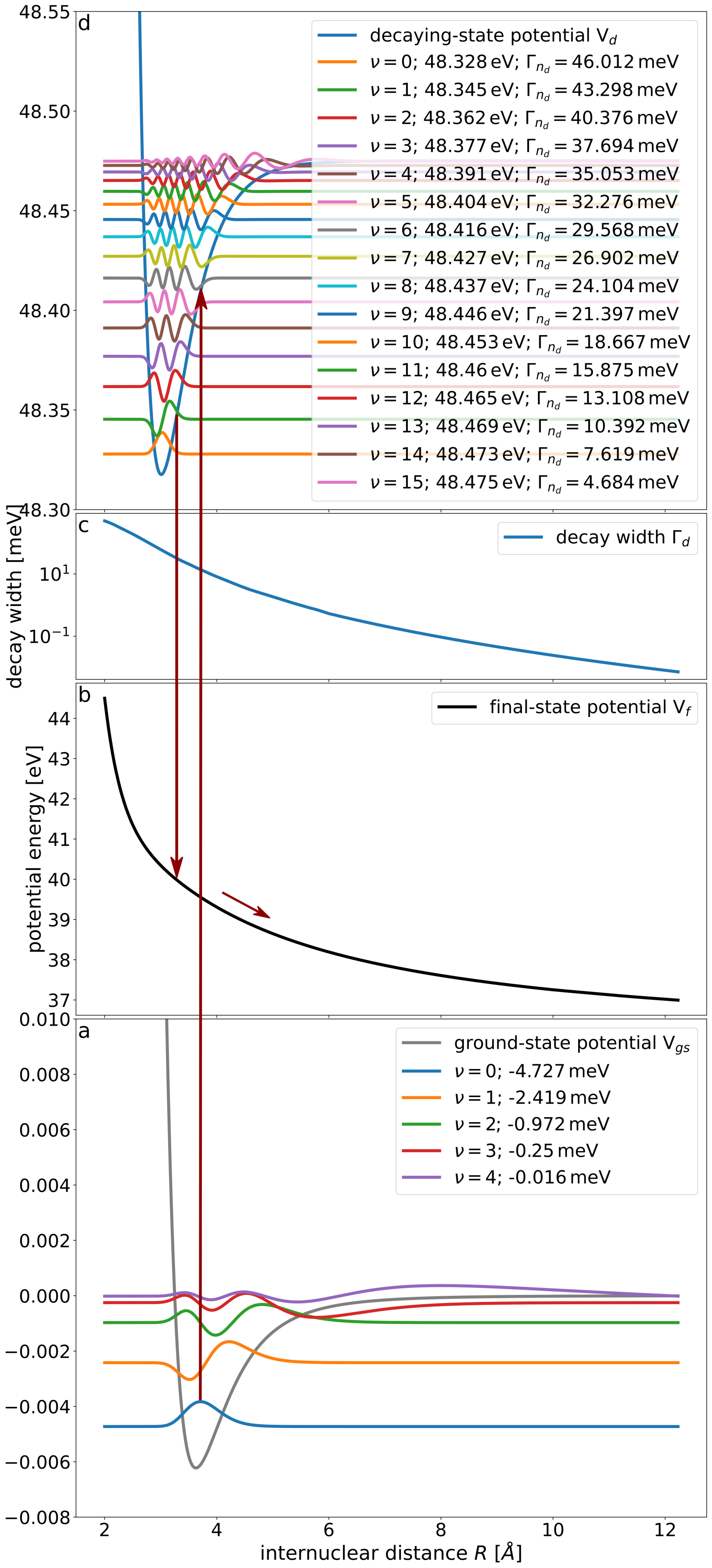

Figure 10.1: PECs and decay width of the NeKr dimer and schematics of the ICD process. Panel a shows the electronic ground state (V_{gs}) and its five vibrational states with the corresponding eigenenergies and eigenfunctions. By a broad-band ionization, the population is vertically transferred to the Ne$^+$(2s^{-1})Kr electronic state (V_d), shown in panel d, that decays by ICD and thus its potential has a complex contribution. The energies of the vibrational states and their corresponding decay widths are given in the legend. The total decay width is shown on a logarithmic scale in panel c. The final ICD state Ne$^+$(2p^{-1})Kr$^+$(4p^{-1}), depicted in panel b, is dissociative (V_f).

Initially, the NeKr dimer is in its electronic ground state $|\phi_i\rangle$. The corresponding PEC denoted as V_{gs} is an interatomic potential of the Hartree-Fock dispersion (HFD-B) form shown in Fig. 10.1a, and taken from Ref. [206]. It has its minimum at 3.63 Å and, as can be seen in Fig. 10.1a, supports five bound vibrational states. If absolute zero temperature is assumed, only its vibrational ground state will be populated.

Then the dimer is ionized, leading to the population of the Ne$^+$(2s^{-1})Kr state. We assume a broad-band ionization of Ne, which is represented by a vertical transfer (red vertical arrow in Fig. 10.1) of the ground-state vibrational wave function of NeKr to the PEC of the decaying state V_d, which is shown in Fig. 10.1d. The latter PEC was computed using the third-order algebraic-diagrammatic-construction scheme for approximating the one-particle Green's function [ADC(3)] [207, 208], employing aug-cc-pCVQZ basis set on Ne and aug-cc-pVQZ basis set on Kr. The corresponding electronic state is denoted as $|\phi_d, E_{k_0}\rangle$, where $|\phi_d\rangle$ is the electronic wave function of the singly ionized Ne$^+$(2s^{-1})Kr dimer and $|E_{k_0}\rangle$ corresponds to the emitted photoelectron. As the state is electronically unstable, its energy as a function of the internuclear distance is complex with an imaginary part being half of the decay width Γ_d. The decay width (Fig. 10.1c)) was computed with the Fano-ADC-Stieltjes approach [172], as described in Ref. [100]. The decaying-state PEC supports 16 vibrational states, and each of them acquires a partial decay width Γ_{n_d}. Those widths are listed in Fig. 10.1d. The minimum of the decaying state PEC is located at 3.01 Å, i.e., slightly shifted to smaller internuclear distances compared to that of the ground-state PEC.

The decay width of the decaying state Γ_d describes the rate with which the population is transferred to the final electronic states Ne$^+$(2p^{-1})Kr$^+$(4p^{-1}). The latter states were computed with the second-order two-hole propagator ADC(2) method [209] using aug-cc-pVQZ basis sets on both atoms. In the range of internuclear distances relevant for the dynamics studied here, the PECs of the final states differ only slightly (see Fig. 1 of Ref. [100]). Consequently, the nuclear dynamics on the different final PECs are very similar, and the resulting electron and KER spectra will be practically indistinguishable. For simplicity and clarity, we thus use, in the present study, a single final PEC obtained by averaging over all final states of interest. It is shown in Fig. 10.1b and denoted as V_f. The final state is dissociative and at large internuclear distances, the corresponding PEC becomes purely Coulombic, as can be expected for two repelling cations, Ne$^+$ and Kr$^+$. The electronic final state can be written as $|\phi_f, E_{k_0}, E_{k_{0'}}\rangle$, where $|\phi_f\rangle$ gives the contribution of the repelling cations, $|E_{k_0}\rangle$ and $|E_{k_{0'}}\rangle$ correspond to the emitted photoelectron and the ICD electron, respectively.

As already shown in Ref. [100], the PE spectrum is sensitive to the form of the PEC of the decaying state V_d. Therefore, we first fitted the *ab initio* PEC by a Morse potential and then determined its parameters such that the computed spectra reproduce best the experimental ones.

10.1 Interference Effects in the Photoelectron Spectrum

As discussed, the decaying state is formed by ionization, where a Ne2s electron of the NeKr dimer is ejected. As the populated state is a decaying one, it is intuitively clear that the photoelectron carries also information on the decay. Therefore, the photoelectron (PE) spectrum contains not only the total decay width of the decaying electronic state but also information on its vibrational structure and partial decay widths, i.e., on the subsequent decay dynamics. In this section, we will discuss the PE spectrum, focusing on the interference effects which can occur and get imprinted within it. The interferences arise due to the different partial decay widths of the coherently populated vibrational levels of the decaying state [105]. The different decay widths, in turn, appear as a result of the dependence of the total decay width on the internuclear distance, $\Gamma_d = \Gamma_d(R)$. If Γ_d is constant, every vibrational state will have the same decay width and the PE spectrum will be given by the standard formula, i.e., a sum of Lorentzians, one for every populated vibrational state, weighted by the corresponding Franck-Condon factors. Moreover, the decay widths can be larger than the energy spacing between the vibrational states, and therefore, the populated states overlap in energy causing an additional interference effect.

In general, the PE spectrum depends on the eigenstates of the decaying state and, consequently, reacts very sensitively to changes in the corresponding PEC and the respective partial decay widths. Before we start our investigation of the interference effects in the PE spectrum, we want to make sure that our computed spectra reproduce the measured ones of Ref. [100] well, and thus, we optimized the PEC of the decaying state as well as the decay width.

Although the PEC was obtained by the high-level *ab initio* method [ADC(3)], highly excited and, moreover, decaying states of weakly bound van der Waals clusters are very difficult to compute. Obtaining electronic decay widths, especially for interatomic processes, poses even larger difficulties. Discrepancies of 20 % [210] and even larger [46] were reported for decay widths obtained by Fano-ADC-Stieltjes method, used to compute the decay width of the Ne$^+$(2s^{-1})Kr state. These computational difficulties give us some flexibility in the choice of the PEC and the decay width.

By comparing the experimental and theoretical survival probabilities it was already shown in Ref. [100] that the *ab initio* decay width of Ne$^+$(2s^{-1})Kr is overestimated. We, therefore, scaled the *ab initio* decay width by the constant factor of 0.8 (sc = 0.8), which gives the best agreement with the experimentally observed survival probability. We note that even after this rescaling, the follow up ICD process is still ultrafast. The decay width at the equilibrium geometry is 16 meV, corresponding to a lifetime of about 41 fs. We can now use the experimental spectra and adjust the PEC of the decaying state, assuming a scaled decay width.

We approximated the PEC of the decaying state with a Morse potential and redefined its parameters. Therefore, we fitted a Morse potential to the original *ab initio* date, which is given as

$$V_d(R) = D_e \left(1 - e^{-\alpha(R-R_e)}\right)^2, \tag{10.2}$$

where D_e is the depth, R_e marks the equilibrium position, and α controls the width of the potential well. The fit to the *ab initio* data gives the initial guess for the parameters defining the Morse potential. Subsequently, a grid search was performed, where for each combination of parameters (D_e, R_e, and α), the PE spectrum is computed and compared to the experimental one. This procedure is repeated until the difference between computed and measured data is minimized. Because in the experiment the photon energy of 48.68 eV is slightly above the ionization threshold, post-collision interactions (PCI) can be observed. In PCI, the fast ICD electron overtakes the slow photoelectron, which is decelerated due to the missing shielding from the remaining ions by the ICD electron. Simultaneously, the ICD electron is accelerated. This PCI effect appears as a tail in the low-energy part of the PE spectrum, see App. D. In our calculations, we do not take PCI effects into account, and therefore, we compared the computed PE spectrum only to the higher photoelectron energy part starting behind the intensity maximum of the experimental data. To achieve better agreement, our theoretical investigations consider the reported experimental resolution of ± 15 meV by convolving the computed PE spectrum with a Gaussian of 30 meV width.

Due to numerous parameter combinations, many local minima exist, and consequently, several Morse potentials lead to a satisfactory agreement with the measured data. Therefore, we determined the Morse-potential parameters by computing the KER spectrum and comparing it with the experimental one. A more detailed explanation of the impact of the Morse potential shape on the PE and the KER spectrum is illustrated in App. D. The parameters corresponding to the best agreement with the experiment are $D_e = 0.16$ eV, $R_e = 3.01$ Å, $\alpha = 1.09$ au^{-1}, and the originally computed decay width is scaled by 0.8 (sc = 0.8). In the following, we refer to this PEC as the working Morse potential. The PE spectra computed with the working Morse potential with and without interference effects are shown in Fig. 10.2 together with the high-energy part of the experimental result for a photon energy of 48.68 eV [100].

We can see that the PE spectrum, which takes interference effects into account (blue curve) and the data points (blue dots) of the measurement satisfactorily coincide and that the standard PE spectrum has a similar form, but is slightly shifted to lower energies. Before analyzing the interference effects in the PE spectrum in more detail, we now briefly discuss the impact of the nuclear mass. The mass of a dimer is usually approximated by calculating the reduced mass of each isotope combination and, subsequently, averaging over the different isotopic compositions. The spectra for the fit represented in Fig. 10.2 are obtained by computing a spectrum for each isotope-mass combination and then summing these PE spectra, which are weighted by the natural abundance of the respective isotope composition. A demonstration of the impact of mass on the PE spectrum can be found in App. E. For our theoretical study, we use in the following the mass of the isotopic combination, which occurs most frequently in nature (reduced mass 16.15 AMU).

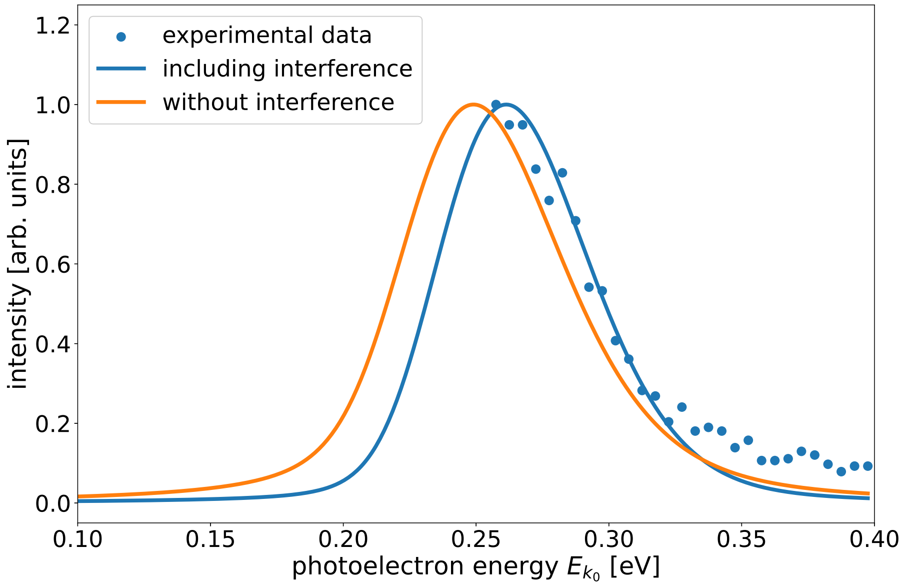

Figure 10.2: Computed PE spectra with and without interference effects in comparison to experimental data for the NeKr dimer. The blue curve is the PE spectrum including interference effects, while the orange curve describes the standard PE spectrum without interference effects. The former is calculated by Eq. (8.36) and the latter is determined by the standard PE spectrum equation, which is the first sum of Eq. (8.36). The blue dots belong to the measurements of Ref. [100], where Ne^+ and Kr^+ ions and low-energy photoelectrons were measured in coincidence after photoionization followed by ICD. The photon energy is 48.68 eV. Because of the high kinetic energy of the ICD electron, the slow photoelectron is overtaken by it. Consequently, the photoelectron is decelerated because the ICD electron does not shield it any longer, and it experiences the attractive force of the positive doubly charged NeKr dimer. The potential of the decaying state is described by a Morse potential, whose parameters are optimized so that the PE spectrum including interferences and the experimental results satisfactory agree ($D_e = 0.16\,\mathrm{eV}$, $R_e = 3.01\,\text{Å}$, $\alpha = 1.09\ \mathrm{au}^{-1}$ and $\mathrm{sc} = 0.8$). Furthermore, the PE spectrum is convolved by a Gaussian with a full-width half-maximum of 30 meV to consider the resolution of the laser of ± 15 meV. By using only the part of the spectrum of the fast photoelectrons, the effects of the post-collision interaction (PCI) on the PE spectrum are minimized. The spectra are computed for all different combinations of isotopic masses and, subsequently, weighted by their abundance in nature summed. The spectra are scaled by their maximum intensities.

After the excursion about the construction of the PEC of the decaying state, we return to the interference effects. In Fig. 10.2, the PE spectrum including interference effects is computed by Eq. (8.36), whereas for the standard PE spectrum without interference effects only the first sum is taken into account. Both are scaled to make their shapes comparable. One can see that the PE spectra with and without interference have approximately the same shape and that the spectrum, which does not take interference effects into account, is slightly shifted to lower photoelectron energies. But where does this difference come from? For answering this question, we separately compute the PE spectrum including interferences (Eq. (8.36)) and its individual components, which are the standard PE spectrum (first sum in Eq. (8.36)), and the interference term (second sum in Eq. (8.36)). The scaling factor is now defined by the highest intensity of the PE spectrum without interference. The scaling shows the contribution of the interference term to the total PE spectrum. Furthermore, we assume a photoelectron energy of 48.68 eV, as in Ref. [100], and a reduced mass of 16.15 AMU according to the most frequently occurring NeKr isotope in nature. Because this is a theoretical investigation, we do not convolve the PE spectra any longer with a Gaussian to take the experimental resolution into account. Furthermore, unless described differently, we assume that the whole population is initially only in the vibrational ground state ($\nu = 0$).

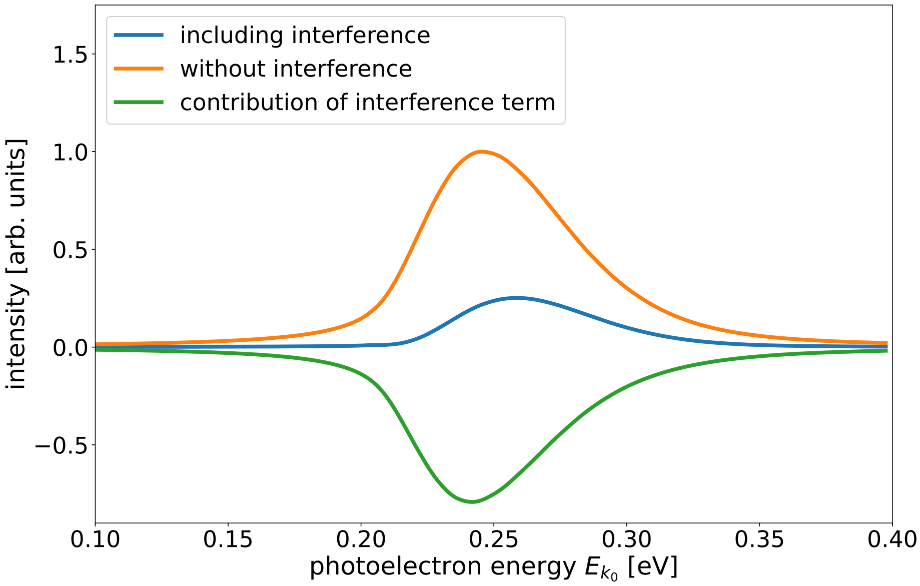

Figure 10.3: Computed PE spectra of the NeKr dimer with (blue) and without (orange) interference effects and the contribution of the interference (green) term. The PE spectrum including interferences is computed by Eq. (8.36), while the standard PE spectrum without interferences is calculated by the first sum and the contribution of the interference term by the second sum of Eq. (8.36). The spectra are computed for the NeKr dimer with a reduced mass of 16.15 AMU (the most frequently occurring isotope-mass combination) assuming that before ionization the system is in its vibrational ground state $\nu = 0$. Furthermore, they are scaled by the highest value of the PE spectrum without interference effects. A photon energy of 48.68 eV is taken.

As seen in Fig. 10.3, the contribution of the interference term is negative and thus associated with destructive interferences. Consequently, the total PE spectrum is of lower intensities and slightly shifted to higher photoelectron energies compared to the standard spectrum. Since Γ_d decreases for larger internuclear distances, the higher-lying vibrational states have a smaller partial decay width. This favors the contributions of the lower-lying vibrational states, which occur at lower photoelectron energies in the PE spectrum. In the present case, the R-dependence is monotonic (at large internuclear distances $\Gamma_d \sim R^{-6}$ [90]) making that the interference term causes mostly a shift in the PE spectrum. A more involved dependency of the decay width on the internal degrees of freedom of the system can lead to a more dramatic effect of the interference term in the PE spectrum.

In the present case, the interference effects are a combination of the coherent population of vibrational states with different partial decay widths (R-dependence of Γ_d) and their overlap in energy due to the large partial decay widths Γ_{n_d} and the small energy difference between the states (shallow potential). The impact of these interferences on the PE spectrum can be illustrated by computing the PE spectrum and its contributions again assuming a scaling factor of sc = 0.4 and sc = 0.2, see Figs. 10.4 and 10.5.

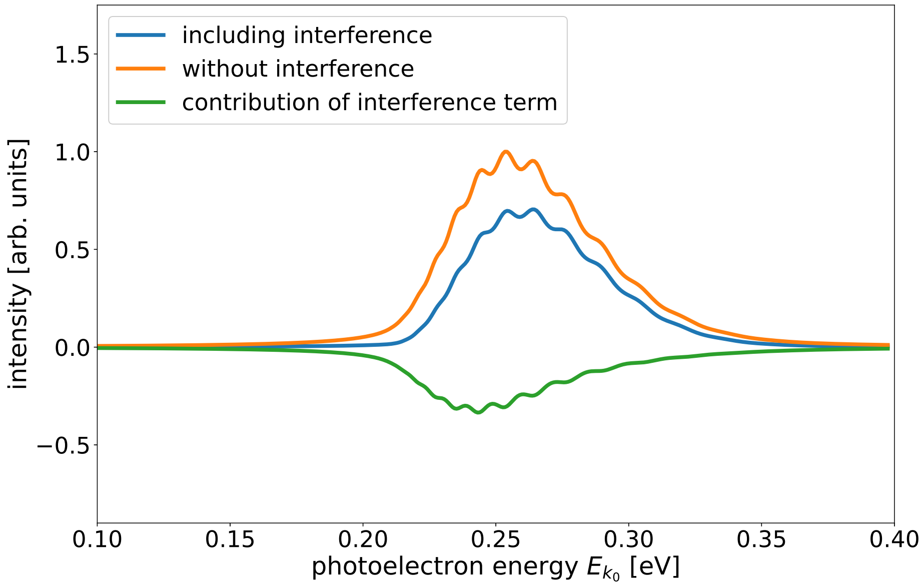

Figure 10.4: Computed PE spectra for the NeKr dimer with (blue) and without (orange) interference effects and the contribution of the interference (green) term. The total decay width is scaled by sc = 0.4. The PE spectrum including interferences is computed by Eq. (8.36), while the standard PE spectrum without interferences is calculated by the first sum and the contribution of the interference term by the second sum of Eq. (8.36). The spectra are computed for the NeKr dimer with a reduced mass of 16.15 AMU (the most frequently occurring isotope-mass combination) assuming that before ionization the system is in its vibrational ground state $\nu = 0$. Furthermore, they are scaled by the highest value of the PE spectrum without interference effects. A photon energy of 48.68 eV is taken.

While in Fig. 10.3, the large total decay width and the small energy spacing between the vibrational states suppress any structure in the PE spectrum, the smaller partial decay widths cause less overlapping vibrational states, which leads to more structured PE spectra, where each populated vibrational state gives one peak in the spectrum. Furthermore, the interference terms decrease with decreasing decay width, at least when Γ_d monotonically decreases, and the PE spectrum including interferences and the standard PE spectrum differ less. In situations where the decay width has a complicated functional dependence on the system geometry and combinations of overlapping and non-overlapping vibrational states are populated, accounting for the interference effects can be crucial for understanding the PE spectrum.

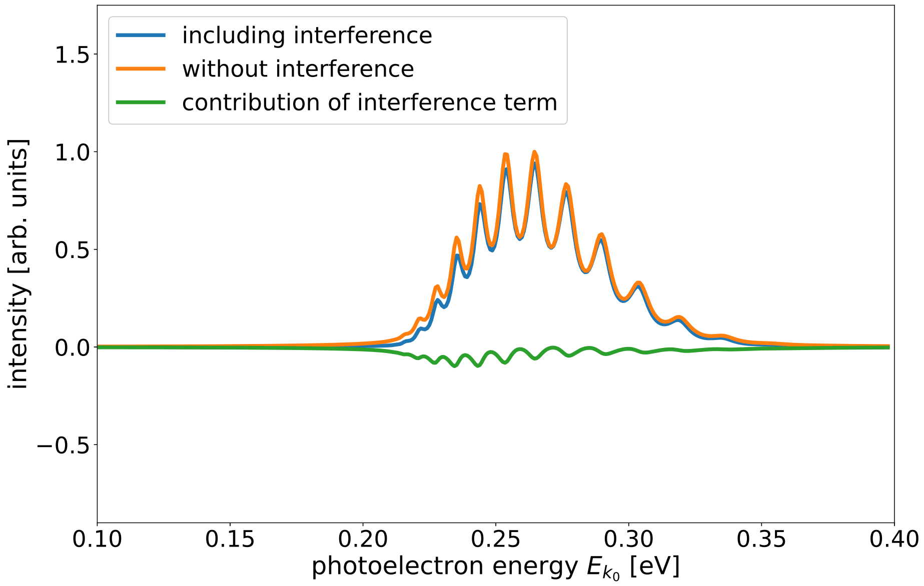

Figure 10.5: Computed PE spectra with (blue) and without (orange) interference effects and the contribution of the interference (green) term. The total decay width is scaled by sc = 0.2. The PE spectrum including interferences is computed by Eq. (8.36), while the standard PE spectrum without interferences is calculated by the first sum and the contribution of the interference term by the second sum of Eq. (8.36). The spectra are computed for the NeKr dimer with a reduced mass of 16.15 AMU (the most frequently occurring isotope-mass combination) assuming that before ionization, the system is in its vibrational ground state $\nu = 0$. Furthermore, they are scaled by the highest value of the PE spectrum without interference effects. A photon energy of 48.68 eV is taken.

In all the computations above, the initial population is assumed to be in the vibrational ground state ($\nu = 0$). Preparing the initial population in the excited vibrational states of the electronic ground state shows that the impact of interferences on the PE spectra decreases with increasing vibrational quantum number ν. The higher the vibrational excitation, the more delocalized is the corresponding wave function. Besides the total decay width, which is lower at higher internuclear distances, also more vibrational levels of the decaying state with smaller partial decay widths contribute to the PE spectra. Therefore, the total decay widths decrease with increasing vibrational excitation and fewer interferences can be observed in the vibrationally selected PE spectra.

10.2 Vibrationally selected Interatomic Coulombic Decay

In this section, we continue our study with the analysis of the ICD-electron spectrum. After the Ne2s photoionization, the Ne$^+$(2s^{-1})Kr state decays via emission of an ICD-electron. The corresponding spectrum of the ejected ICD-electron is obtained using Eq. (8.57). The ICD process assuming that the NeKr dimer is initially in its vibrational ground state was studied already in Ref. [100]. Therefore, here we concentrate mostly on vibrationally selected ICD. We investigate the process, assuming that the population is initially in one vibrationally excited state of the electronic ground state. This will also allow us to study how the cluster temperature affects the ICD-electron spectrum.

As mentioned above, five bound states are associated with the electronic ground state, which are marked by the quantum number ν. Thereby, $\nu = 0$ stands for the vibrational ground state, while ν = 1-4 present the vibrationally excited states. The vibrationally selected ICD-electron spectra are computed by assuming that the whole population is initially prepared in one of the five vibrational levels of the electronic ground state. The result is seen in Fig. 10.6.

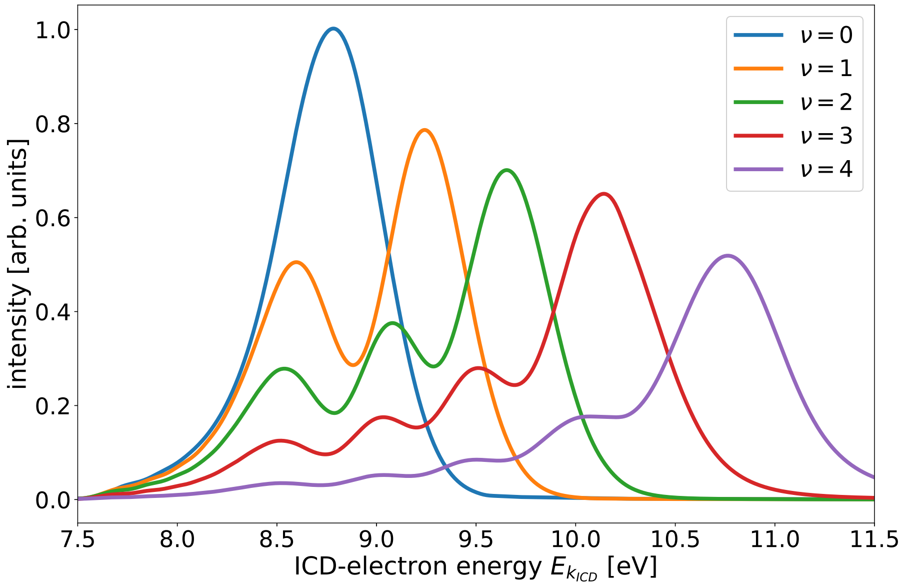

Figure 10.6: Computed vibrationally selected ICD-electron spectra of the NeKr dimer. The spectra are calculated using Eq. (8.57) and assuming that the system is initially in one of the five vibrational levels of the electronic ground state, $\nu = 0$ to 4. The corresponding vibrational quantum numbers ν are displayed in the legend. Because the spectrum, which corresponds to the initially populated vibrational ground state, is the most localized one and has consequently the highest intensity contribution, its maximum value is used for the scaling of the other spectra. The most frequently occurring isotope-mass combination of 16.15 AMU (reduced mass) is used for the computation.

The ICD-electron spectrum of the selectively populated vibrational ground-state corresponds to the most localized initial vibrational wave function. Therefore, it provides the highest intensity and is used for the scaling of the other vibrationally selected ICD-electron spectra. While the wave function of the vibrational ground state is located at comparable lower nuclear distances, for increasing quantum number ν, the initial wave function is more extended over the grid. This leads to an increase of the ICD-electron energy range in the corresponding ICD-electron spectrum.

As the ICD is fast, the wave packet created in the decaying state has practically no time to evolve on the V_d potential and is nearly immediately transferred to the final state. This makes the ICD-electron spectrum practically a direct image of the population of the initial vibrational state. This can be confirmed by comparing the spectra shown in Fig. 10.6 with the probability densities, or the modulus square of the respective vibrational wave functions, shown in Fig. 10.7. As we see, the vibrationally selected ICD-electron spectra clearly reflect the nodal structures of the corresponding initial vibrational wave functions.

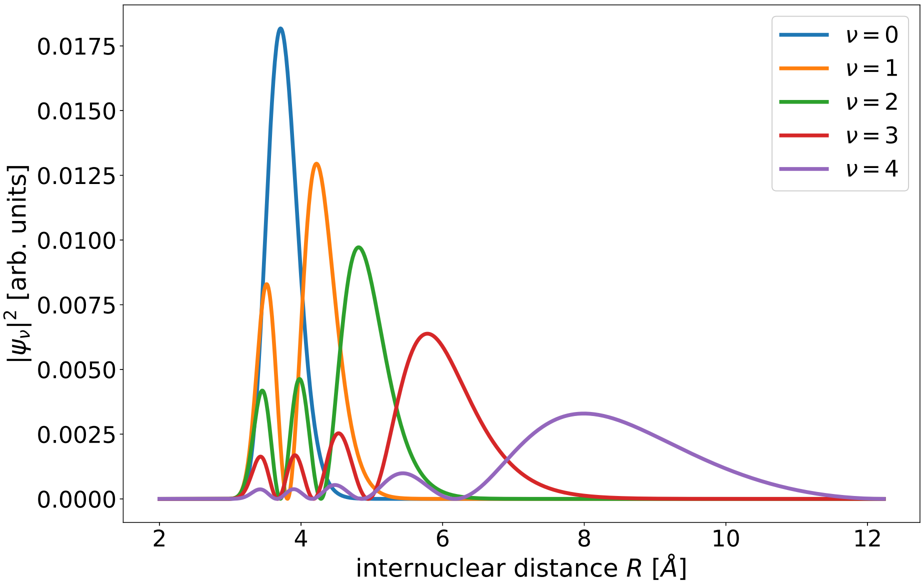

Figure 10.7: Probability densities of all 5 bound vibrational states of the electronic ground state of the NeKr dimer. The blue curve belongs to the vibrational ground state and the orange, the green, the red and the purple ones depict the vibrationally excited ones in rising order. The eigenfunctions are normalized. The legend shows the corresponding vibrationally excited states by the vibrational quantum numbers ν. The most frequently occurring isotope-mass combination of 16.15 AMU (reduced mass) is taken for the NeKr dimer.

Let us now return to the role of the interference effects during the ionization and the subsequent decay in the NeKr dimer. As explained in Sec. 10.1, interferences can result from effects on the decaying and the final state. Of course, the interference effects of the decaying state always indirectly affect the propagation in the final state. Even without final-state interferences, the ICD-electron spectrum would not simply display the inverse population of the decaying state. Energy conservation applies to the initial and the final state (compare Eq. (8.11)), but as shown in Sec. 8.2, intermediate states can also be off-resonance, and consequently, the energy of the decaying state is not well defined due to the decay width Γ_d. However, the ICD-electron spectrum reflects the nuclear dynamics of the final state because it is given by the population in the final state accumulated over time, see Eq. (8.48). The interference effects in the final state occur due to the continuous transfer of population from the decaying to the final state, which means that portions of the wave packet arriving at later times can interfere with portions of the wave packet already propagating on the final-state PEC. Clearly, these effects can lead to noticeable modifications of the spectra, if the decay is slower and allows for the time evolution of the wave packet in the decaying and the final state. The nodal structures of the vibrationally selected ICD-electron spectra in Fig. 10.6 demonstrate that no strong interference effects can be observed, as the lifetime of the decaying state is too short. Consequently, the whole population of the decaying state decays nearly immediately, and there is not enough time for the different portions of the wave function in the final state to interfere during the propagation.

Depending on the way of their preparation (usually by supersonic co-expansion), the rare mixed gas clusters may have a different temperature. The vibrationally selected ICD provides the possibility to analyze the dependence of the spectra on the temperature.

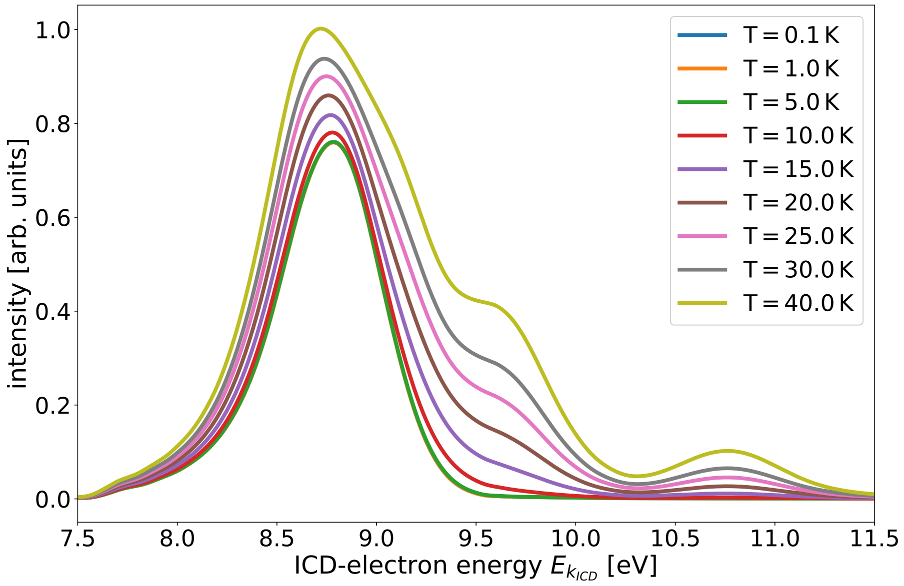

Figure 10.8: Computed ICD-electron spectra of the NeKr dimer at different temperatures. The spectra are calculated by using Eq. (8.57) in combination with the Boltzman distribution explained in the text. The spectrum at the highest temperature exhibits the biggest maximum and is therefore used for scaling the spectra. The different temperatures at which the spectra are determined are given in the legend. The most frequently occurring isotope-mass combination of 16.15 AMU (reduced mass) is used for the NeKr dimer.

It is usually assumed that before ionization the dimer is in its vibrational ground state, which is certainly the case at $T = 0$ K. At higher temperatures, however, the population is statistically distributed to higher-lying vibrational states. Therefore, we introduce the impact of temperature in our computations by weighting the vibrationally selected ICD-electron spectra by the Boltzmann distribution $w_\nu = e^{-\beta E_\nu}$. Here, $\beta = (k_B T)^{-1}$ is the Boltzmann factor including the Boltzmann constant k_B, and E_ν corresponds to the energy difference between the vibrational ground state and the vibrationally excited state ν. Subsequently, the weighted vibrationally selected ICD-electron spectra are incoherently summed. The ICD-electron spectra at different temperatures are given in Fig. 10.8.

Note that the spectra are scaled by the highest intensity of the ICD-electron spectrum computed at the highest temperature. The impact of the temperature starts to become noticeable at about 10 K, which is the estimated temperature of the dimers in the experiment reported in Ref. [100], but this increase in intensity at about 9.5 eV is too small to be experimentally resolvable. More noticeable differences start to appear at temperatures higher than 20 K, where the main peak develops a clear shoulder and a second peak at 10.8 eV appears. We can therefore conclude that for the NeKr dimer, the approximation that only the vibrational ground state is initially populated is valid for temperatures of up to about 20 K. This corresponds to population rates of 26 % for the first vibrationally excited state, and still over 11 % and 7 % for the second and third one. In comparison, at 10 K only 7 % of the population is in the first excited vibrational state, and only 1 % in the second one .

We would like to conclude our study by examining the KER spectrum of the Coulomb exploding dimer, again concentrating on the interference effects. While the ICD-electron spectrum records the propagation on the final state, the KER spectrum reflects the nuclear dynamics in the decaying state by projecting the decaying-state wave packet on the final state, see Eq. (8.63). Therefore, the ICD and the KER spectrum carry complementary information [111]. In the classical picture, however, the KER and the ICD-electron spectra are mirror images of each other (mirror-image approximation) when converting the energy of the ICD-electron to the associated KER energy. Although this is often used in practice, it was shown [111, 112] that due to quantum effects the mirror-image principle breaks down and is a good approximation only in cases of a small decay width and no or negligible nuclear dynamics on the decaying state. Due to the very shallow potential V_d, the dynamics in the decaying state of NeKr are not fast. However, the decay width of our system is rather large. We observe interference effects in the PE spectrum due to the massive broadening of the vibrational energy levels and their corresponding overlaps. Furthermore, the vibrationally selected ICD-electron spectra reflect the nodal structures of the vibrational ground-state wave functions, which implies a short lifetime of the decaying state and, consequently, a large decay width Γ_d. Can such an intermediate situation lead to noticeable deviations from the mirror image approximation?

The KER spectra as results from vibrationally selected ICD processes, as well as the KER spectra at various temperatures, can be found in Appendix F. They were computed using

Eq. (8.63). The results show that the directly computed KER spectra and the mirror image of the ICD-electron spectra show good agreement, at least if solely the vibrational ground state is initially populated, see Fig. 10.9. The comparisons of the KER spectra and the mirror image of the ICD-electron spectra corresponding to the higher vibrationally excited states, however, show discrepancies at higher KER energies. An example of an ICD process initiated from the third excited vibrational state of the electronic ground state is shown in Fig. 10.10. The mirror image of the ICD-electron spectrum is lower in intensity than the directly computed KER spectrum, and the deviation increases with increasing KER, which implies destructive interferences.

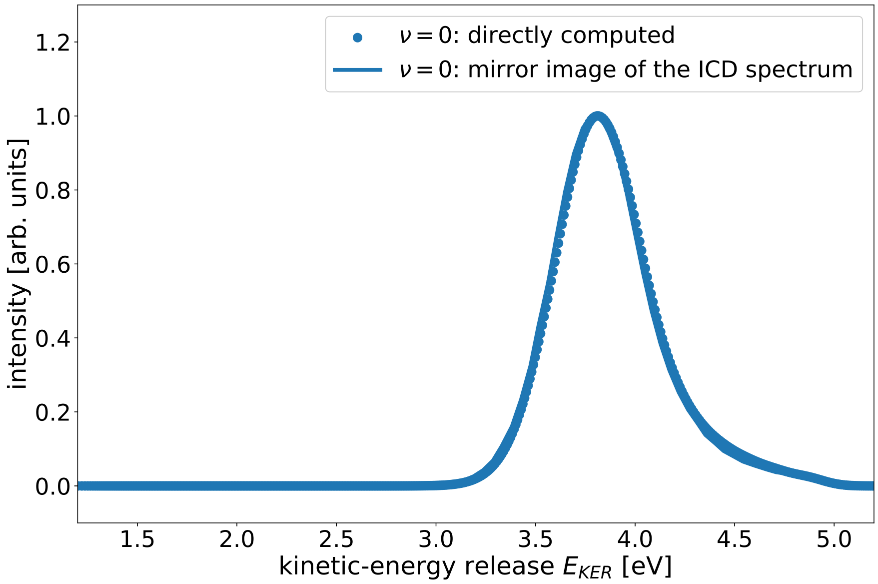

Figure 10.9: Comparison of the directly computed KER spectrum (dots) and the mirror image of the ICD-electron spectrum (line). The spectra are determined by Eqs. (8.57) and (8.63), where the energy of the ICD electron is transferred to the KER for the ICD mirror image. The population is assumed initially to be in the vibrational ground state $\nu = 0$. The spectra are scaled by their highest values. The most frequently occurring isotope-mass combination of 16.15 AMU (reduced mass) is employed for the NeKr dimer.

While the KER spectrum only reflects the dynamics and the corresponding interference effects in the decaying state, the ICD-electron spectrum carries more information. It gives insight into the wave-packet motion in the final state, which also depends on the dynamics in the decaying state, see Eq. (8.48). The propagation in the final state is accompanied by leakages from the decaying state that interfere with the final-state wave packet. Because the KER spectrum does not display these final-state interferences, we may conclude that they need to be small to ensure that the mirror image is a good approximation.

In the case of the initially populated vibrational ground state, this is guaranteed by the large decay width. Due to the fast decay, the entire population of the decaying state is nearly immediately transferred to the final state, leaving practically no time for the different portions of the wave packet to propagate and interfere in the final state. Returning to the vibrationally selected ICD in Fig. 10.10, we see the reason for the discrepancies between the mirror image and the directly computed KER spectrum. The third excited vibrational state is more delocalized compared to the ground state, and therefore, higher vibrational states of the decaying state are populated, which have smaller partial decay widths (the total decay width decreases with R). Therefore, for some parts of the wave packet, there is more time for the propagation on the decaying- and, consequently, also on the final-state PEC, which leads to interferences. We can thus conclude that final-state interferences can be suppressed by a short lifetime of the decaying state and increased by somewhat longer decay times.

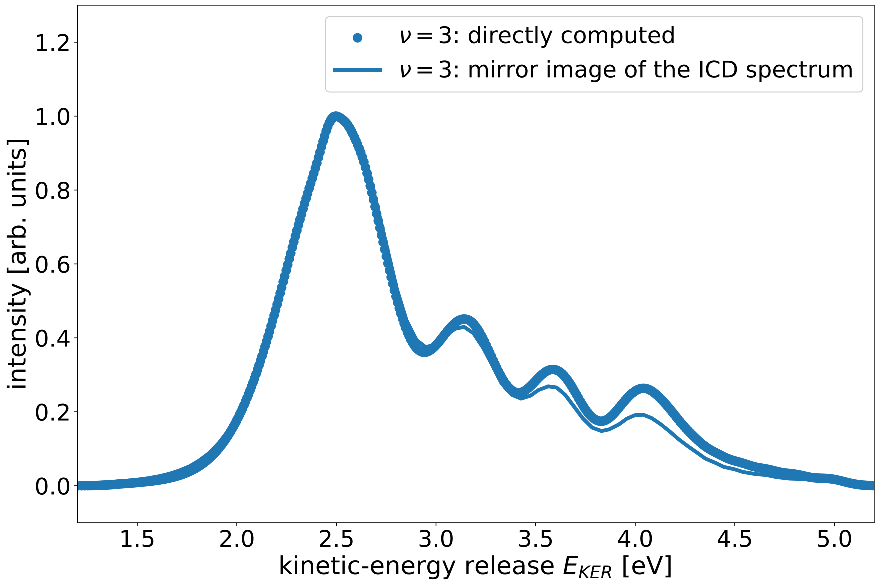

Figure 10.10: Directly computed KER spectrum (dots) in comparison to the mirror image of the ICD-electron spectrum (line). The spectra are determined by Eqs. (8.57) and (8.63), where the energy of the ICD electron is transferred to the KER for the ICD mirror image. The population is initially assumed to be in the third vibrationally excited state $\nu = 3$ of the electronic ground state. The spectra are scaled by their highest values. The most frequently occurring isotope-mass combination of 16.15 AMU (reduced mass) is used.

Chapter 11

Pre-ICD in Ar_2

In this chapter, we investigate the nuclear dynamics in ultrafast electronic relaxation by an energy transfer in Ar_2 dimers below the threshold of ICD. After inner-valence 3s ionization of one of the argon atoms, the relaxation dynamics of the system lead to 4s and 4p excitations of the neighboring argon. This process is called pre-ICD (or frustrated ICD) [211, 212] because additional energy is needed to also ionize the neighboring argon atom and to create a dissociative system consisting of two repelling cations similar to the resulting state of ICD. Time-resolved photoion-photoion coincidence spectroscopy and classical Monte-Carlo simulations were used to track and understand the nuclear dynamics in the Ar_2 dimer during the system undergoes pre-ICD [106] [66]. Motivated by these previous findings, we performed quantum dynamic simulations to gain more insight into the relaxation dynamics of this ultrafast energy-transfer mechanism. We computed the time-resolved pump-probe delay-dependent KER spectrum to study the obtained structures in the experimental spectrum and to explain their occurrence.

The chapter is structured as follows. In Sec. 11.1, we introduce a previous study [106] regarding pre-ICD in the Ar_2 dimer to motivate our investigations and to separate our work from what has been done before. In the following, Sec. 11.2, the computational method based on wave-packet propagation is explained and the corresponding KER spectrum is presented. The chapter is completed by Sec. 11.3, with adjusting our computed spectrum to the measured one. The results discussed here are also found in Ref. [66].

11.1 State of the Art

For all homonuclear noble-gas dimers heavier than neon, the ICD channel of the inner-valence hole state is energetically closed. In Ar_2 dimers, for example, the 3s-ionization energy is 29.24 eV, which is below the threshold for ICD at 31.52 eV [211]. However, recently, a study [106] revealed that although the relaxation energy of the 3s hole in argon is not enough to ionize its neighboring atom, it is sufficient to excite the electron of its neighboring atom to some Rydberg states, creating the predissociative Ar^+-Ar^* system. This ultrafast transfer of excitation energy, called pre-ICD, was observed in a time-resolved extreme ultraviolet (XUV)-

pump infrared (IR)-probe experiment in Ar_2 dimers. The process itself and the involved PECs are illustrated in Fig. 11.1.

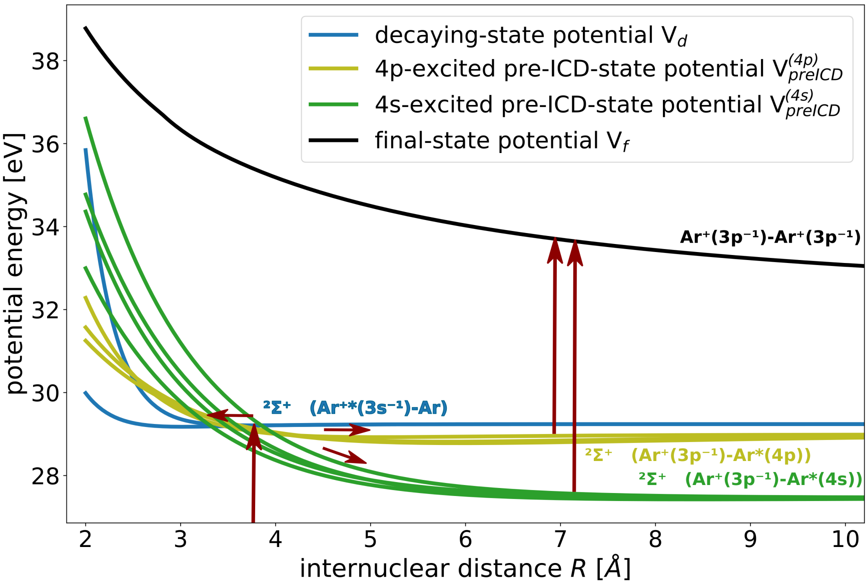

Figure 11.1: Schematic representation of the pre-ICD mechanism in Ar_2 by the corresponding PECs. The PECs are taken from Refs. [106, 213]. The red arrows mark the population transfer between states and the propagation on the PECs. After one argon atom is 3s ionized by an XUV pulse and the population is transferred to the PECs of the $^2\Sigma^+_{g,u}$ $(Ar^{+*}(3s^{-1})$-$Ar)$ states V_d (blue), the population propagates on the PECs and oscillates around the minima of the PECs. Simultaneously, the 3s-ionized argon deexcites, and the excess energy is utilized to 4s or 4p excite the neighboring argon atom, $^2\Sigma^+_{g,u}$ $(Ar^+(3p^{-1})$-$Ar^*(3p^{-1}4s))$ and $^2\Sigma^+_{g,u}$ $(Ar^+(3p^{-1})$-$Ar^*(3p^{-1}4p))$. These pre-ICD states are pre-dissociative and the corresponding PECs are denoted by V_{preICD} (dark and light green). Afterward, the excited argon is ionized by an IR pulse and the population is transferred to the PEC of the final state V_f (black), $Ar^+(3p^{-1})$-$Ar^+(3p^{-1})$. The ionization initiates a Coulomb explosion of the two remaining cations.

One of the argon atoms in the dimer is ionized by an XUV pulse, creating a 3s hole. Within the picture of wave-packet propagation, this signifies the transfer of population from the ground-state PEC to the PECs V_d of the singly ionized $Ar^{+*}(3s^{-1})Ar$ states, see the blue curves in Fig. 11.1. The wave packet starts to propagate along the PECs in the direction of the minimum, where it passes the curve-crossing points of the 3s-hole states V_d with the PECs of the pre-dissociative Ar^+-$Ar^*(3p^{-1}4s$ and $3p^{-1}4p)$ states, to which we refer in the following also as 4s- and 4p-excited states, see the dark and the light green curves V_{preICD}. This transfer of population between the PECs at these curve-crossing points corresponds to the ultrafast transfer of excitation energy to the neighboring argon, resulting in its excitation. While a part of the population stays close to the curve-crossing points of the 3s-hole states V_d, other parts propagate along the PECs of the 4s- and 4p-excited states. A delayed IR pulse can then ionize the excited neighboring argon atom. This ionization is accomplished by the transfer of population from the 4s- and 4p-excited states to the final PEC V_f of the ICD state, $Ar^+(3p^{-1})Ar^+(3p^{-1})$, see the black curve. The remaining two cations repel each other, resulting in a Coulomb explosion. Consequently, the process is dissociative and the corresponding PEC is monotonically decreasing. The pump-probe reaction is described by

$$\mathrm{Ar}_2 \xrightarrow{XUV} \mathrm{Ar}^{+*}(3\mathrm{s}^{-1})\mathrm{Ar} \longrightarrow \mathrm{Ar}^{+}(3\mathrm{p}^{-1})\mathrm{Ar}^{*}(3\mathrm{p}^{-1}4\mathrm{s}/4\mathrm{p}) \xrightarrow{IR} \mathrm{Ar}^{+}(3\mathrm{p}^{-1})\mathrm{Ar}^{+}(3\mathrm{p}^{-1}). \tag{11.1}$$

To track the nuclear dynamics, a time-resolved KER spectrum, which depends on the pump-probe delay time, was reconstructed after measuring the singly charged argon atoms in coincidence, see Fig. 11.2a. Furthermore, the experimental data were confirmed by the corresponding computed KER spectrum, which was determined by performing a Monte-Carlo simulation, see Fig. 11.2b.

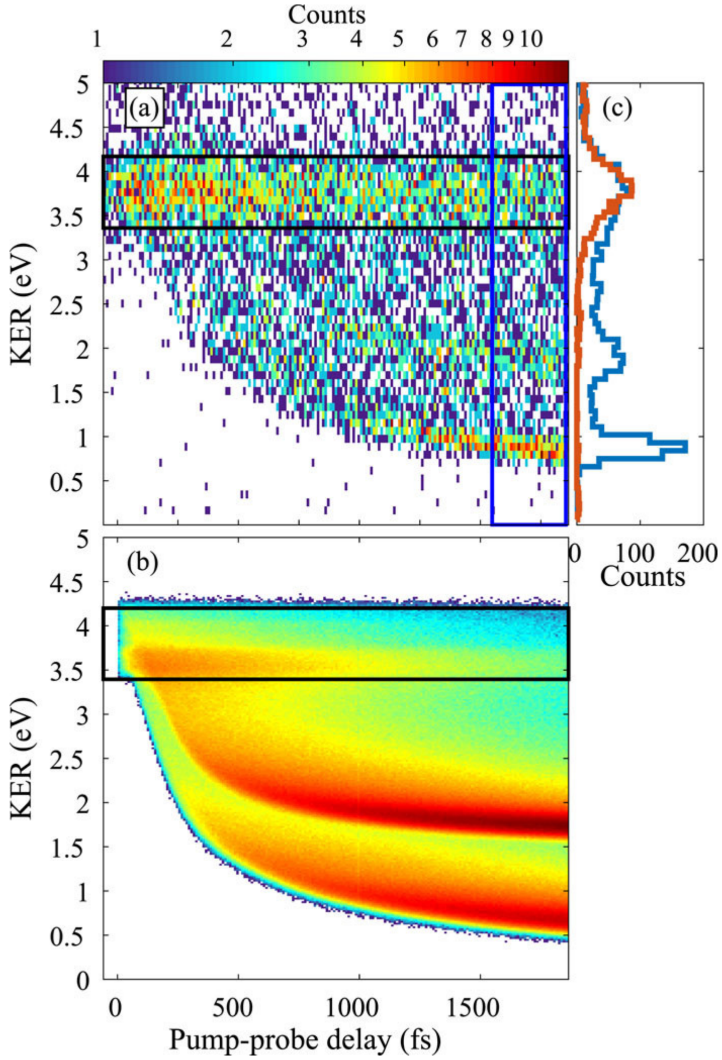

Figure 11.2: The figure is taken from Ref. [106]. Logarithmic color scales are used. (a) Measured time-resolved KER spectrum of Ar$_2$ depending on the pump-probe delay. Time-resolved photoion-photoion coincidence spectroscopy was used. (b) Time-resolved KER spectrum of Ar$_2$, depending on the pump-probe delay, computed by a classical Monte-Carlo simulation. The black box marks the region over which is integrated to determine the energy transfer time. (c) Blue curve: Projection onto the KER axis for pump-probe delay times between 1550 fs and 1850 fs (see blue box). Red curve: KER spectrum of another measurement using only XUV pulses, scaled to the maximum of the blue curve for better comparison.

The measured and the semi-classically computed time-resolved KER spectrum are in good agreement. In Fig. 11.2c, the time delays between 1550 fs and 1850 fs (blue box) are projected on the KER axis (blue curve) to interpret the observed structures in the spectra. The corresponding projection curve exhibits three dominant peaks, where the peaks at 0.8 eV and 1.9 eV reflect the relaxation pathway via the 4p- and 4s-excited states, respectively, and the peak around 3.8 eV originates from the population directly probed after the transition to these pre-dissociative states (black box). Both spectra show these three main structures. Note that the pre-ICD itself (i.e., XUV-only case (red curve)) does not contribute to the Coulomb explosion signal in contrast to the ICD process of satellite states $\mathrm{Ar}^{+*}(3\mathrm{p}^{-2}\,\mathrm{nl})$-Ar created by shake-up ionization [213–215]. Therefore, a time-independent background exists in the KER range between 3.4 eV and 4.2 eV, which should be rather small due to the low cross-section of the shake-up ICD channel in the XUV-energy regime. It could also be shown that the relaxation of the 3s-hole state is the dominant channel. In previous studies, signals at higher KERs were reported resulting from other satellite states below the ICD threshold [211, 212] and double ionized states at one site, which decay via the radiative charge transfer (RCT) process, $\mathrm{Ar}^{2+}(3\mathrm{p}^{-2})\text{-Ar} \rightarrow \mathrm{Ar}^{+}\text{-}\mathrm{Ar}^{+}$ [216, 217] when the internuclear distance is decreasing, corresponding to a KER peak centered at 5.2 eV. The measured KER spectrum does not exhibit structures at higher KERs. Consequently, the population of satellite states $\mathrm{Ar}^{+*}(3\mathrm{p}^{-2}\,\mathrm{np})$-Ar and double ionized states at one site Ar^{2+}-Ar can be neglected in the computation. Additionally, it could be extracted an energy transfer time τ_{3s} of the 3s-hole to the pre-dissociative 4s- and 4p-excited states by analyzing the theoretical and experimental data. Because the internuclear-distance dependent IR-ionization probability is not known, the count rate of the KER range between 3.4 eV and 4.2 eV is used. The KER is restricted to this range because the corresponding KERs belong to the parts of the population, which are at the curve-crossing points on the PECs of the 4s- and 4p-excited states and are immediately transferred to the final state by the IR-pulse. Therefore, the internuclear-distance dependent IR-ionization probability can be assumed to be constant in this range. The restricted count rate is projected on the time-delay axis and an exponential fit $e^{t/\tau_{3s}}$ gives the energy transfer time, which can be seen as the lifetime of the 3s-hole state τ_{3s}. Overall, a good agreement between experimental and computed data was archived, and the lifetime was determined as $\tau_{3s} = 824 \pm 183$ fs in Ref. [106].

Recently, time-resolved photoion-photoion coincidence spectroscopy was performed by Wörner and co-workers to track the nuclear dynamics of Ar_2 dimers undergoing pre-ICD, see Ref. [66]. The XUV-pump IR-probe experiment was realized in a COLd Target Recoil Ion Momentum Spectroscopy (COLTRIMS) spectrometer [103, 218]. The measured time-resolved KER spectrum is given in Fig. 11.3. In comparison with the study [106] introduced above, the result validates that there are two clearly visible decay channels approaching 0.8 eV and 1.9 eV at the largest pump-probe delays, which are identified as contributions of the 4p- and 4s-excited states, respectively.

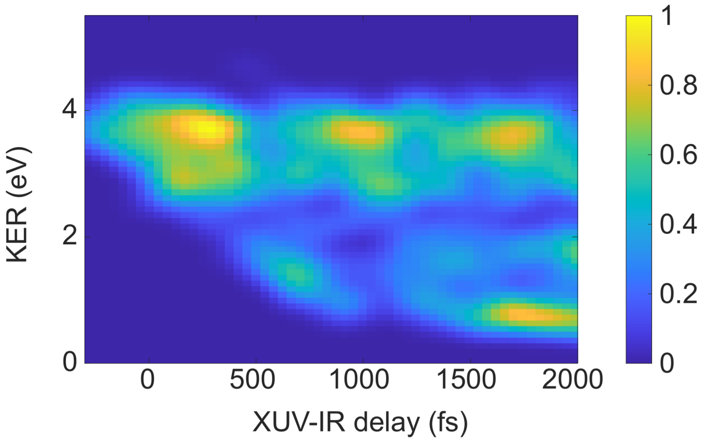

Figure 11.3: The figure is taken from Ref. [66]. Time-resolved KER spectrum of Ar$_2$ depending on the pump-probe delay measured by time-resolved photoion-photoion coincidence spectroscopy.

What is observed exclusively is the periodical modulation of the main islands around 3.8 eV. The oscillation period is about 800 fs, a typical timescale of vibrational motions in noble-gas dimers. This is reminiscent of the nuclear dynamics in this ultrafast inter-atomic energy transfer process. To explain these new features in the measured time-resolved KER spectrum, quantum effects have to be considered as well. In a collaboration with Wörner and co-workers, we quantum-mechanically computed the time-resolved pump-probe delay-time dependent KER spectrum by using a method based on wave-packet propagation to interpret the experimental results, see Ref. [66].

11.2 Time-resolved Kinetic-Energy-Release Spectrum

To interpret the experimental results [66], we performed quantum dynamic simulations of the process and computed the time-dependent KER spectrum in the framework of nuclear wave-packet propagating on the PECs of the involved states, see Fig. 11.1. The *ab initio* PECs for the ground state and the final Ar$^+$(3p^{-1})-Ar$^+$(3p^{-1}) state are taken from Ref. [213], where for the PECs of the latter the configuration interaction method was applied, comprising all single and double excitations from the reference configuration (CISD). The cc-pVDZ basis set augmented with two diffuse s functions, two diffuse d functions, and two compact d functions was used. The PECs of the 3s-hole state and the 4s- and 4p- excited states refer to Ref. [106] and were determined by the non-Dyson ADC(3) method and the cc-pVTZ basis set augmented with a set of 3s, 3p, and 3d functions of the KBJ-type. The electronic structure calculations were performed using adiabatic bases. In the adiabatic picture, the energy transfer proceeds via avoided crossings by non-adiabatic couplings. Here, the PECs in the adiabatic basis were used to construct the PECs [106, 213] in Fig. 11.1, leading to curve crossings. Note that the PECs are no results of electronic structure calculations assuming diabatic bases.

The PECs of the pre-dissociative states still feature minima around 7-8 Å and 5 Å, respectively, but their corresponding potential wells are comparatively shallow caused by the outer-valence excitation. However, the 4s- and 4p-excited states show dissociative behavior, where the pre-dissociative-state designation comes from. Consequently, the wave packet does not oscillate localized in the potential well, but rather propagates along the grid. Usually, one can locate a CAP, see Sec. 9.2, at the end of the grid, which absorbs the population and thereby imitates the population leaving the grid area. In our case, we cannot use this numerical tool because the interaction region includes the total grid required for the propagations on the PECs of the 4s- and 4p-excited states. We want to probe exactly these nuclear motions by reflecting the dynamics on the final state. Applying a CAP would cut off the lower part of the time-resolved delay-dependent KER spectrum.

Due to the long propagation time of 2000 fs, we have to extrapolate the originally computed *ab initio* PECs in a range of internuclear distances between 2 Å and 90 Å, where the grid is spanned by 4000 grid points. Note that a sufficiently high density of grid points is necessary to map the process correctly. The bound state PECs for the ground state, the 3s-hole state, as well as the 4s- and 4p-excited states are fitted by Morse potentials, see Eq. (10.2), where the potential well depth D_e and the internuclear equilibrium position R_e are determined by the *ab initio* PECs. At asymptotic distances, the extrapolated PECs were adjusted to the corresponding sums of atomic energies taken from NIST [123], which were averaged over the total angular momentum components, respectively. Furthermore, to keep the nuclear dynamics of the system, the original curve-crossing points of the *ab initio* PECs were used as references to shift the PECs of the 4s- and 4p-excited states along the x-axis so that they exhibit the same crossing points with the 3s-hole state PEC as before the extrapolation. The final state PECs describe dissociation and, therefore, are fitted by $V_f = 1/R + V_f^{\infty}$, where the kinetic-energy release is approximated by $E_{KER} = 1/R$, see Ref. [100]. V_f^{∞} equals the potential energy the system has after the two cations get separated by infinite nuclear distances and stop moving. It is also determined by the sum of the corresponding atomic energies, see Ref. [123]. The PECs are not shifted because at an internuclear distance of 90 Å their kinetic energies are still high enough to separate further, and we are interested in this kinetic-energy release. Because all final-state PECs energetically lie close together and exhibit similar nuclear dynamics, we averaged over all of them and used only one final-state PEC, which simplifies the computation but does not affect the observed effects in the spectrum.

To simulate the energy transfer from $\mathrm{Ar}^{+*}(3\mathrm{s}^{-1})$-Ar to $\mathrm{Ar}^{+}(3\mathrm{p}^{-1})$-$\mathrm{Ar}^{*}(4\mathrm{s})$ and $\mathrm{Ar}^{+}(3\mathrm{p}^{-1})$-$\mathrm{Ar}^{*}(4\mathrm{p})$, taking place at the points of curve-crossings, we introduce an effective decay width, which corresponds to the energy transfer time taken from Ref. [106]. The corresponding decay width of 0.8 meV is statistically distributed to the corresponding 4s- and 4p-excited states by the multiplicity of the total angular momentum of the atomic states and approximates the population transfer at the curve-crossing points. As explained above, the used *ab initio* PECs were calculated in an adiabatic basis and were subsequently diabatized. The computations of the derivative coupling matrix elements for non-adiabatic coupling in the adiabatic picture are efforts by themselves, and the Hamiltonian in the diabatic basis, where the population transfer proceeds via potential coupling, is usually determined by a unitary transformation of the one in the adiabatic basis. By assuming an effective decay width, which begins at the internuclear distances of the curve crossings realized by step functions, we circumvent these difficulties and find a suitable approach to imitate the behavior of the population transfer. Due to the decay, the energy transfer does not occur only at internuclear distances of the same energy, but also at higher ones. To mimic the original behavior, where energy transfers take place only at the curve-crossing points, and to guarantee energy conservation, we add energy shifts to the PECs of the 4s- and 4p-excited states. These approximations allow us to use the same coupled set of time-dependent Schrödinger equations to describe the nuclear dynamics as for ICD, see Eq. (8.48). Here, $\hat{\mathcal{H}}_d$ describes the propagation on the 3s-hole state, $\hat{W}_{f\leftarrow d}$ is the transition operator between 3s-hole states and 4s- and 4p-excited states, $\hat{H}_f$ is the Hamiltonian of the 4s- and 4p-excited states and $E_{k_0'}$ marks the energy shifts.

Assuming broad-band ionization for the ionization initiated by the XUV-pump pulse, we take the ICD-Hamiltonian (see Eq. (8.48)) and perform a propagation on the 3s-hole state (blue PECs in Figs. 11.1) including the decay dynamics and simultaneously on the 4s- and 4p-excited

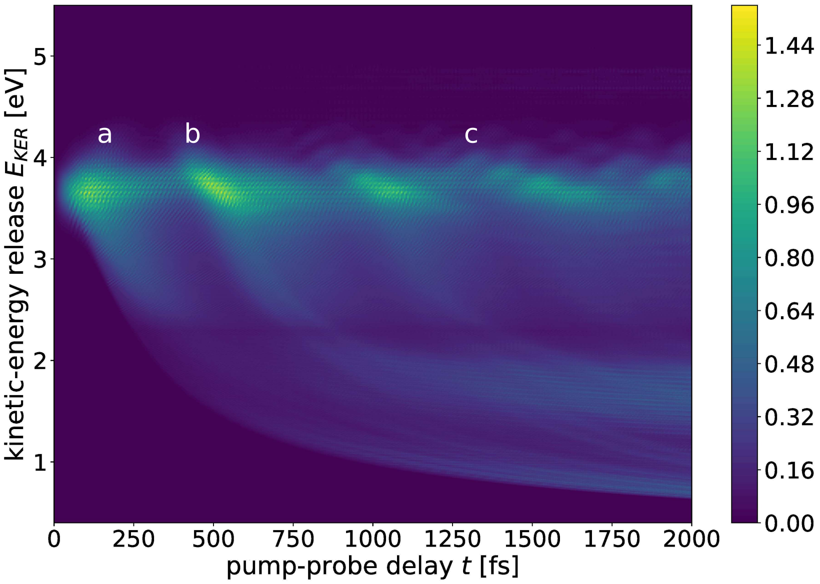

Figure 11.4: Time-resolved KER spectrum of Ar$_2$ depending on the pump-probe delay. Eq. (8.48) is used to perform the decay and the propagation on the 3s-hole states and the 4s- and 4p-excited states. The overlaps between time-dependent wave functions of the 4s- and 4p-excited states and the eigenstates of the final state give the time-resolved KER spectra for the corresponding PECs, respectively, see Eq. (8.64). Afterward, the resulting delay-time resolved KER spectra are combined. a, b, and c mark different nuclear dynamical features in the spectrum.

states (dark and light green PECs in Figs. 11.1) by applying the complex short iterative Lanczos (CSIL) integrator implemented in the MCTDH package [194]. The reduced mass of the Ar_2 dimer is 19.974 AMU. To obtain the partial KER spectrum at each time step (Δ = 5 fs), the time-dependent wave function of the corresponding 4s- or 4p-excited state is projected on the final state, which corresponds to the two remaining argon ions after the ionization by the IR-probe laser pulse. Therefore, at each time step, the overlap integrals between the time-dependent wave function and the eigenstates of the final state E_{n_f} are computed separately, see Eq. (8.64). This procedure is repeated for each gerade and ungerade transition between the 3s-hole and 4s- or 4p-excited states, where the spectra originating from the same transition but correspond to different energy shifts $E_{k'_0}$ are accumulated. Finally, the contributions of the partial KER spectra are summed incoherently. Using the method explained above, we obtained the time-resolved XUV-IR delay-dependent KER spectrum shown in Fig. 11.4.

The computed spectrum is in good agreement with the experimental one, see Fig. 11.3. The structures at 0.8 eV and 1.9 eV, associated with the probing from the 4p- and 4s-excited state, respectively, the intense islands at 3.8 eV, resulting from the oscillation of the wave packet in the $3s^{-1}$ potential well, and the lack of signal at 2.3 eV, due, as we will see, to destructive interference, are well reproduced. Instead of three islands as in the measured data, we observe four to five, suggesting different oscillation times, see Sec. 11.3. Furthermore, we observe that these structures exhibit the forms of parabolic curves, where all but the first decrease with increasing pump-probe delay. This allows us to analyze the quantum dynamics during the pre-ICD process and the various features observed in the measured KER spectrum in detail.

These islands reflect the movement of the nuclear wave packet in the 3s-hole state, and their parabolic shapes show that the curve-crossing points are reached one after the other. This effect is further enhanced by approximating the population transfer as decay process, where the transfer also occurs at internuclear distances larger than the ones of the curve-crossing points. The wave packet on the 3s-hole potential is initially localized around the equilibrium internuclear distance of the neutral dimer at 3.8 Å (marked by a red arrow in Fig. 11.5a), propagating towards the potential minimum due to the gradient and passing through all the curve crossings, where the population is transferred to the 4s- and 4p-excited states, and subsequently probed (see Fig. 11.5a). Because decreasing internuclear distances occur in the spectrum as increasing KER, the first structure appears as an increasing parabolic curve. After the population has passed the potential minimum, it returns and moves towards increasing internuclear distances, see Fig. 11.5b. Therefore, the corresponding parabolic structure decreases. Furthermore, interferences in the form of layered structures can be observed in the spectrum, resulting from wave packet portions arriving at later times and interfering with portions of the wave packet already propagating on the 4s- and 4p-excited-state PECs, compare Fig. 11.3b. Therefore, destructive interferences on the final-state PEC are the reason for the interruption of the signal at about 2.3 eV. Because during the run of the wave packet through the potential well, no population is transferred to the 4s- and 4p-excited states, resulting in no contribution to the KER spectrum, the islands appear as separated signals in the spectrum. Besides the propagation on the PEC and the population transfer, the wave packet expands over the grid, and therefore, the propagation towards decreasing internuclear distances can no longer be identified in the spectrum. Additionally, the signals blur out with increasing pump-probe delay-time, see Fig. 11.3c.

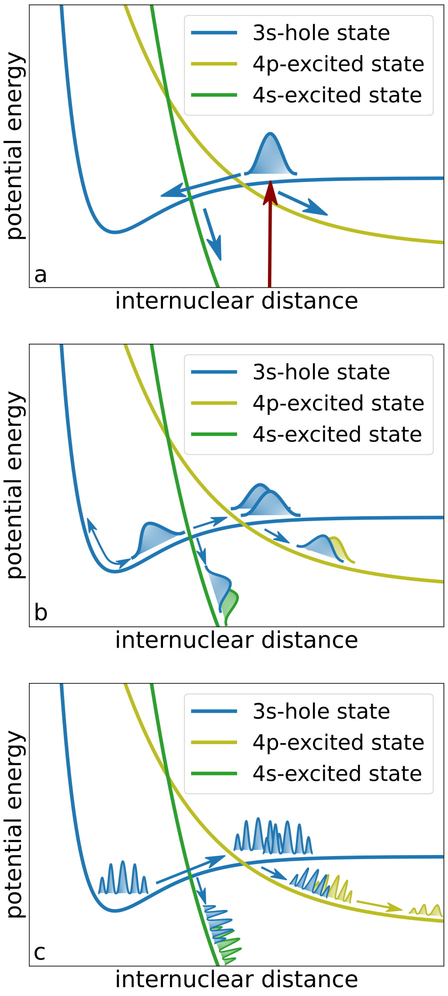

Figure 11.5: Schematic representation of nuclear dynamics during pre-ICD of the Ar$_2$ dimer in the delay-time range a, b, c, compare Fig. 11.1. The blue curve schematically represents the 3s-hole states $^2\Sigma^+_{g,u}$ (Ar^{+*}(3s^{-1})-Ar), while the dark and light green curves denote the 4s- and 4p-excited states, $^2\Sigma^+_{g,u}$ (Ar$^+$(3p^{-1})-Ar*(3p^{-1} 4s)) and $^2\Sigma^+_{g,u}$ (Ar$^+$(3p^{-1})-Ar*(3p^{-1} 4p)), respectively.

By separating the gerade and ungerade contributions of the spectrum, we receive additional insight into nuclear dynamics. Fig. 11.6 shows the contribution to the XUV-IR delay-dependent KER spectrum from the gerade states and Fig. 11.7 from the ungerade states. Both exhibit the structures corresponding to the relaxation pathways via the 4s- and 4p-excited states. The islands around 3.8 eV show the most remarkable differences. The corresponding signals in the spectrum of the ungerade states are well separated, while the signals in the spectrum of the gerade states show a wave-like structure.

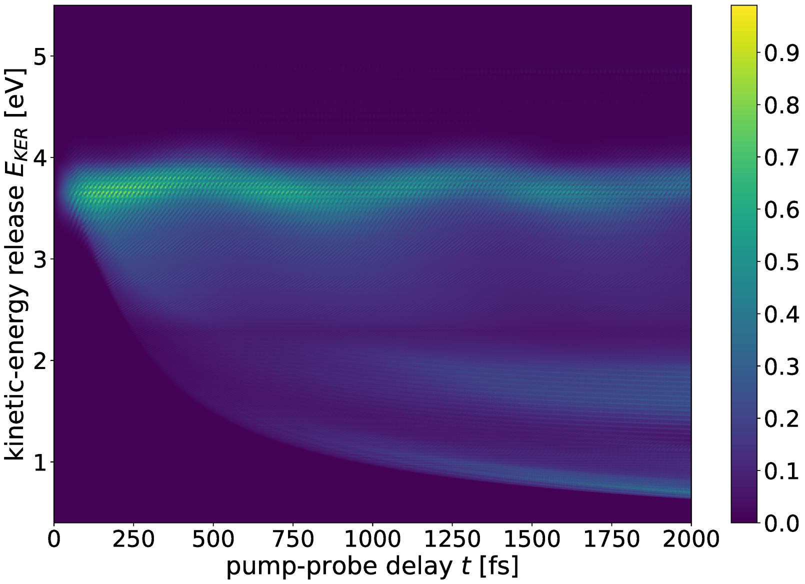

Figure 11.6: Contribution of the gerade states to the time-resolved KER spectrum of Ar_2 depending on the pump-probe delay. After the decay and the propagation on the 3s-hole states and the 4s- and 4p-excited states are performed by using Eq. (8.48), the overlaps between time-dependent wave functions of the 4s- and 4p-excited states and the eigenstates of the final state are computed for each time step, where only transitions between gerade states are considered, see Eq. (8.64). Then, the corresponding partial KER spectra are combined.

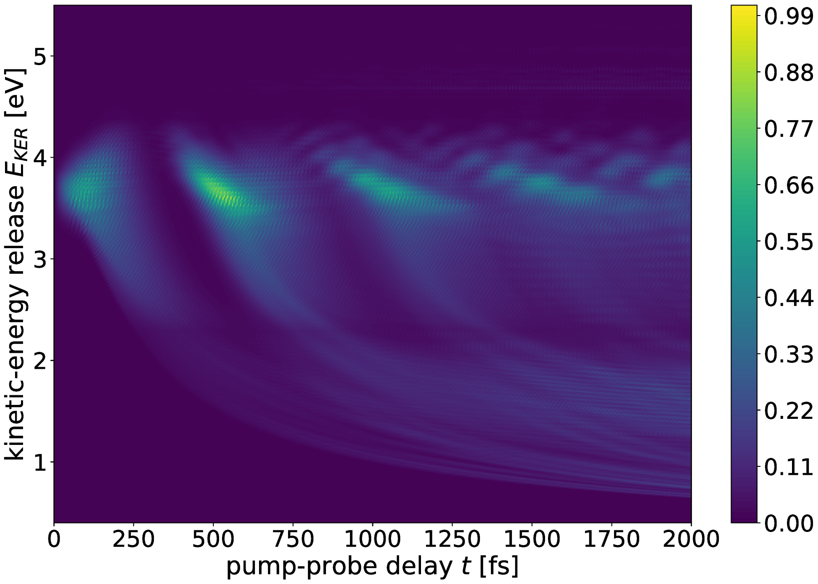

Figure 11.7: Contribution of the ungerade states to the time-resolved KER spectrum of Ar_2 depending on the pump-probe delay. After the decay and the propagation on the 3s-hole states and the 4s- and 4p-excited states are performed by using Eq. (8.48), the overlaps between time-dependent wave functions of the 4s- and 4p-excited states and the eigenstates of the final state are computed for each time step, where only transitions between ungerade states are considered, see Eq. (8.64). Then, the corresponding partial KER spectra are combined.

The reason for this lies in the shape of the 3s-hole state PEC and the positions of the curve-crossing points, which in the case of gerade states, are closer to the potential minimum and the turning point, compare Fig. 11.8. Consequently, the oscillation period for the gerade contribution is shorter than for the ungerade one. The corresponding signals in the spectrum are not clearly separated from each other, but a wave-like shape can be observed, which reflects at least the forward and backward movement of the nuclear wave packet. Due to the long oscillation period without population transfer, see Fig. 11.8, the signals in the KER spectrum from the ungerade states are clearly visible.

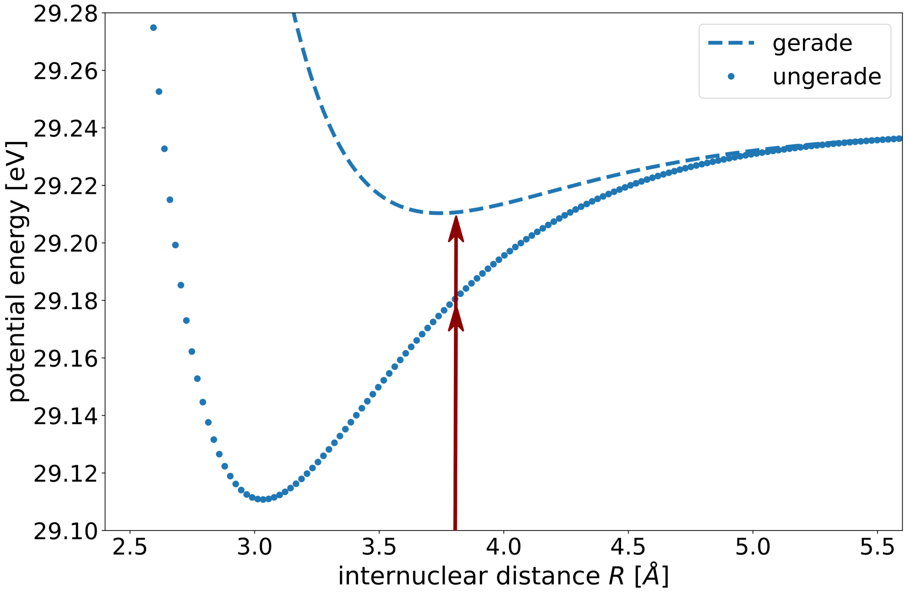

Figure 11.8: PECs of the gerade $^2\Sigma_g^+$ and ungerade $^2\Sigma_u^+$ 3s-hole state (Ar^{+*}(3s^{-1})-Ar) in comparison. The red arrows mark the equilibrium position of the ground state.

We now return to the lack of signal around 2.3 eV, appearing in both gerade and ungerade spectra, and clearly visible also in the experimental KER-trace (see Fig. 11.3). Our analysis shows that this is a result of a destructive interference taking place between different portions of the wave packet transferred to the 4s- and 4p-excited potentials at two consecutive passages through the corresponding curve-crossings. In other words, during its excursion to the inner turning point and back, the wave packet moving on the 3s^{-1} PEC accumulates a phase and when transferred to 4s and 4p potentials interferes destructively with the portions of the wave packet already propagating on these PECs (see Fig. 11.5b and c).

11.3 Adjustment to the measured time-resolved Kinetic-Energy-Release Spectrum

Comparing our time-resolved delay-dependent KER spectrum, see Fig. 11.4 with the experimental one in Fig. 11.3, makes clear that the measured KER spectrum does not exhibit four to five islands around 3.8 eV but rather three, resulting from a shorter oscillation period than in the experiment. As has been already successfully used for the PE spectrum of the NeKr dimer in Chap. 10, a better agreement between the measured and computed spectra can be achieved by adjusting the corresponding PECs. Already knowing from Fig. 11.7 that the strong separation of the islands occurs rather from ungerade transitions, we only have to model the PEC of the ungerade 3s-hole state, see Fig. 11.9. The gradient must be decreased to slow down the propagation of the population. Therefore, we fitted a Morse potential to the PEC of the ungerade 3s-hole state and then optimized its parameters such that the wave-packet motion reproduces the experimentally observed period of about 800 fs. The depth of the potential energy well D_e is halved to flatten the descent of the curve and the equilibrium position R_e and the width control parameter α are also adjusted to conserve the total shape of the curve. Consequently, the resulting PEC is less deep and has a smaller gradient to slow down the wave packet propagating through the potential well and to increase the oscillation time.

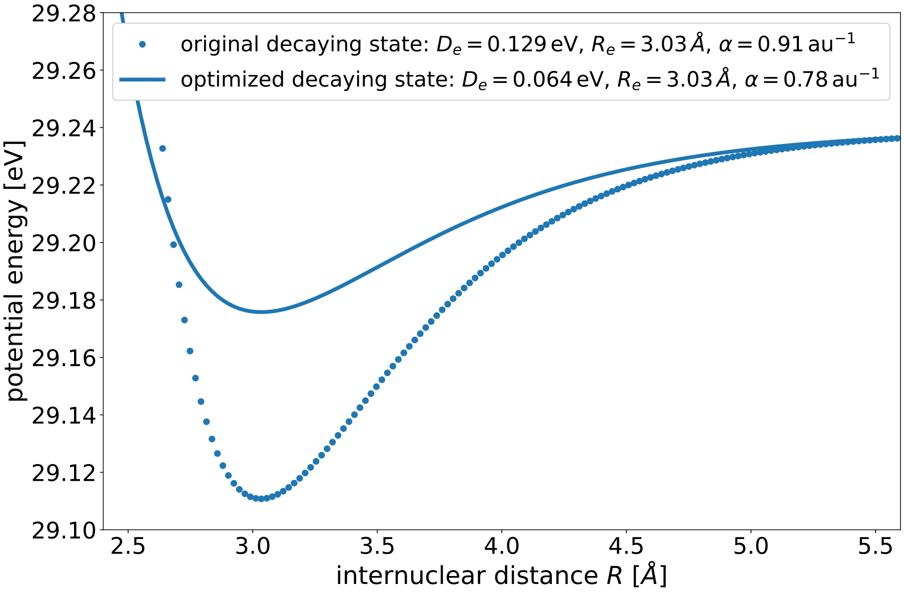

Figure 11.9: The original (dots) and the optimized (line) PEC of the ungerade ${}^2\Sigma_u^+$ 3s-hole state (Ar^{+*}(3s^{-1})-Ar) in comparison.

The computation of the time-resolved delay-dependent KER spectrum with the optimized PEC gives the result seen in Fig. 11.9. Besides the structures of the 4s- and 4p-decay channels and the lack of signal at 2.3 eV due to destructive interference, only three islands in the KER region of 3.8 eV can be observed, which reflect the nuclear dynamics in the 3s-hole state.

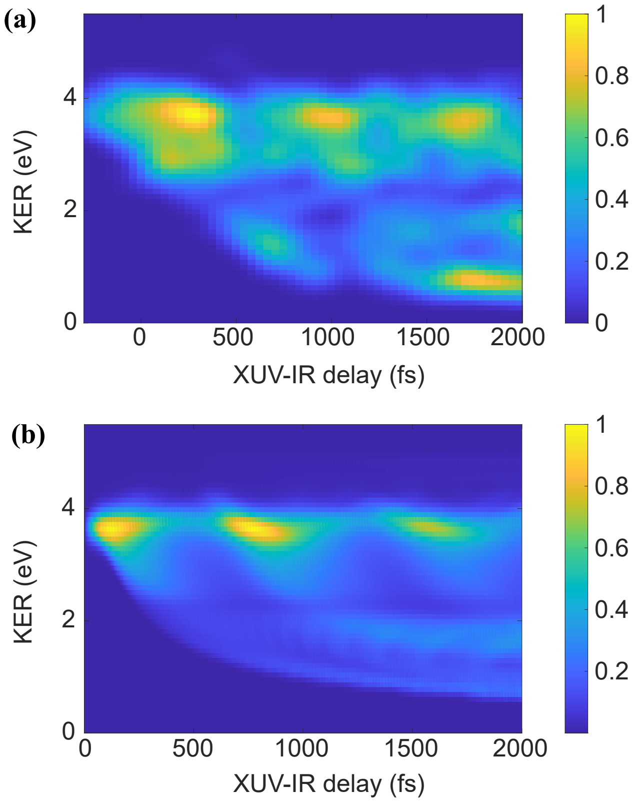

Figure 11.10: (a) Measured (Wörner and co-workers [66]) and (b) computed time-resolved KER spectrum of Ar$_2$ depending on the pump-probe delay. The depth of the PEC of the decaying state $^2\Sigma_u^+$ (Ar^{+*}(3s^{-1})-Ar) is halved from 0.128 eV to 0.064 eV to increase the oscillation time of the population around the PEC minimum. The KER spectra are calculated for each time step (Eq. (8.64)) and eventually combined.

Chapter 12

Conclusion

After introducing the investigated process of ionization followed by ICD in dimers, we presented the derivation of the time-independent formalism used to derive the PE spectrum by scattering theory as well as of the time-dependent formalism used to derive the ICD-electron and KER spectrum, whose computations are based on wave-packet propagation [104, 105, 107–112]. Furthermore, we introduced the used numerical methods. The Hamiltonians were written in sine-DVR [187, 195, 196]. Their diagonalizations equal the solving of the corresponding time-independent Schrödinger equation. The eigenvalues and eigenvectors are required for the time-independent computation of the PE spectra. For the time-dependently derived ICD-electron and KER spectra, a system of first-order differential equations has to be solved, which are coupled time-dependent Schrödinger equations, describing the time evolution of the population in the corresponding PEC, respectively. This was realized by performing the wave-packet propagation within the Heidelberger MCTDH algorithm [193]. While only the time-dependent wave function of the decaying state is needed to compute KER spectra, a CAP [194] has to be introduced to determine the flux for the computation of ICD-electron spectra.

Subsequently, the derived equations and numerical tools were applied to compute PE and ICD-electron spectra of the NeKr dimer and time-resolved KER spectra of the Ar_2 dimer. Following the 2s ionization of the NeKr dimer, the system undergoes ICD, where we concentrated on the interference effects during the ionization and the following decay. Two different sources of interference exist. Interference occurs as a result of coherently populated vibrational decaying state levels, which are differently broadened and consequently overlap due to their partial decay widths Γ_{n_d}. Furthermore, interference can be caused by nuclear dynamics in the final state, where the previous decayed population interferes with the propagating population in the final state, see Ref. [111, 112]. Additionally, we studied vibrationally selected ICD, in which the system is initially prepared in a vibrationally excited state of the electronic ground state. The delocalization of the vibrationally excited wave functions is accompanied by the decrease of the internuclear-distance dependent decay width, which enhanced the impact of interferences on the spectra. We also investigated pre-ICD in the Ar_2 dimer, where we could observe beside the two above-explained sources of interference another one. Interference also arises due to the nuclear dynamics in the decaying state. Pre-ICD differs from ICD in that the excess energy generated by the decay is not sufficient to ionize, but to excite the neighbor. Therefore, an additional energy source is required for the ionization. The calculation of the pump-probe delay-time dependent KER spectrum, gives insight into the nuclear dynamics occurring during pre-ICD in the Ar_2 dimer. Investigations of ICD in the NeKr dimer were followed by studying pre-ICD in Ar_2 dimer.

Ionization of Ne2s was investigated in the NeKr dimer. Due to the subsequent ICD and the accompanying internuclear-distance dependent decay width $\Gamma_d(\mathrm{R})$ [105], interference effects can be observed in the PE spectrum. The PE spectrum is only affected by interferences arising in the decaying state. In general, the PE spectrum sensitively reacts to changes in the PEC of the decaying state because it highly depends on the vibrational energy levels and the corresponding partial decay widths. Therefore, the adjustment of the decaying state PEC proved to be a convenient way to achieve a satisfactory agreement between the computed and measured PE spectrum, see Ref. [100]. We fitted a Morse potential to the *ab initio* PEC (Ref. [100]) and optimized its parameters by minimizing the mean-distance square between the theoretical and experimental data of the PE spectrum, see Fig. 10.2. KER spectra are often measured in experimental setups. Because they take nuclear dynamics into account, various information can be extracted from them. Thus, we used them to confirm the choice of the decaying state PEC. By using this optimized PEC and computing the different contributions of the PE spectrum, we analyzed the interference effects within the PE spectrum. We observed in Fig. 10.3 that these interferences are destructive, and therefore, the PE spectrum including interference effects is decreased in comparison to the standard PE spectrum without interferences. Furthermore, the PE spectrum including interference effects is slightly shifted to higher photoelectron energies. As explained above, the interference effects in the spectrum result from the overlaps of the coherently populated vibrational energy levels of the decaying state, caused by the broadening of the levels due to their partial decay widths. To illustrate this, we also showed the contributions to the PE spectrum computed with a halved and quartered decay width, see Figs. 10.4 and 10.5. With decreasing decay width, the contribution of the interferences decreases as well. Consequently, the PE spectra with interferences approach those without interferences. Furthermore, the PE spectra provide more structure, which leads to the conclusion that the contributions of the vibrational energy levels to the spectra can now be identified due to the reduction of the overlaps.

We also focused on ICD following 2s ionization. Therefore, we computed the vibrationally selected ICD-electron spectra, where the population is initially prepared in one of the vibrational levels of the electronic ground state, see Fig. 10.6. The five corresponding ICD-electron spectra become more delocalized the higher the initial vibrational excitation is and showe structures, comparable to the nodal structures of the initial wave functions, see Fig. 10.7. The similar shapes of the ICD-electron spectra and the initial wave functions result from the fast decay - the lifetime of $Ne^+(2s^{-1})Kr$ is about 41 fs. Instead of propagating on the PEC of the decaying state, the population decays nearly immediately and as a result, the corresponding ICD-electron spectra reflect the structure of the initial wave function. Because vibrationally selected ICD has yet to be experimentally realized, we also computed the ICD-electron spectra of the NeKr dimer at different temperatures, see Fig. 10.8. Therefore, the initial population is statistically distributed to the vibrational states of the electronic ground state. Even at 10 K, as in Ref. [100], we observed a slight impact of the first vibrationally excited state. For higher temperatures, a higher percentage of the population is in the vibrationally excited states. Consequently, the impact of the vibrationally excited states grows with increasing temperatures, and therefore, additional structures appear in the spectra. While at 10 K the spectra slightly differ, at 20 K, two additional peaks appear and the impact of the temperature on the computed spectra can no longer be neglected.

Another possibility to study ICD in the NeKr dimer is to analyze the distribution of the kinetic-energy release of the remaining ions Ne^+ and Kr^+ after the decay. In the classical picture, the ICD-electron and the KER spectrum can be represented as mirror images of each other, and even in the quantum picture, they provide complementary information. While the KER spectrum reflects the nuclear dynamics of the decaying state, the ICD-electron spectrum exhibits the nuclear dynamics of the final state, which are also affected by the decay [111, 112]. Consequently, the directly computed KER spectrum and the mirror image of the ICD spectrum of NeKr only coincide, if the interference effects in the final state are negligibly small. We showed that this is achieved only if the vibrational ground state is initially populated, see Fig. 10.9. Due to the fast decay, the population is immediately transferred to the final state and there is no time left for interferences to occur. For the third vibrationally excited ground state, see Fig. 10.10, the two spectra differ at high KER energies. Because the peaks of the mirror image of the ICD spectrum become smaller with increasing KER compared to the directly computed KER spectrum, we concluded that the final state exhibits desctructive interference. The vibrationally excited wave functions are more delocalized than the ground state wave function. Because the decay width depends on the internuclear distance, parts of the population decay slower than others and have more time to propagate in the decaying state as well as to interfere, which leads to the differences between the two spectra.

After we had performed full dynamic simulations of the ICD process in the NeKr dimer, we computed the time-resolved delay-time dependent KER spectrum of the Ar_2 dimer, which undergoes pre-ICD after 3s ionization. As mentioned before, our theoretical approach was motivated by pump-probe experiments, and therefore, we extracted the lifetime of the 3s-hole state from the measured delay-dependent KER spectrum in Ref. [106]. Assuming the existence of a corresponding decay width allowed us to use Eq. (8.48) for the propagation. By computing the overlaps between the time-dependent wave functions of the 4s- and 4p-excited states and the eigenstates of the final state, we determined the time-resolved delay-dependent KER spectrum, see Fig. 11.4. The involved PECs were taken from Ref. [106, 213] and extrapolated. Measured and computed KER spectra are in good agreement. The contributions of the two decay channels via the 4s- or 4p-excited state and the lack of signals due to destructive interference at 2.3 eV are clearly displayed. Furthermore, in the KER region of 3.8 eV, four to five separated signals occur. This KER region corresponds to the population, which is directly transferred to the final state at the crossing points, and the observed structures reflect the nuclear dynamics in the 3s-hole state. While parts of the population constantly decay, other parts of the population run through the potential well. During these oscillations, the corresponding population does not contribute to the spectrum leading to the separated signals. The blurring of the signals is caused by the broadening of the wave functions within time and by interferences between the oscillating and decaying parts of the population in the 3s-hole state due to the comparable long lifetime of 824 fs. Additionally, we presented the separate contributions to the time-resolved delay-dependent KER spectrum defined by the gerade and ungerade transitions, see Figs. 11.6 and 11.7. While the KER spectrum of the gerade transitions is continuous, the KER spectrum of the ungerade transitions is structured. These differences can be explained by the PECs of the gerade and ungerade contributions of the 3s-hole state. The potential well of the ungerade 3s-hole PEC is deeper and the minimum is shifted to lower internuclear distances compared to the PEC of the gerade 3s-hole state. Consequently, the wave packet needs longer for one oscillation through the potential well. Additionally, the crossing points of the gerade 3s-hole state PEC with the pre-ICD states PECs are located close to its minimum, whereby the oscillations of the wave packet are not clearly recognizable in the spectrum, and a wave-like structure appears. To complete our study of the nuclear dynamics during pre-ICD in the Ar_2 dimer, we finally optimized the PEC of the ungerade 3s-hole state because the measured KER spectrum shows only three islands. Therefore, the PEC of the decaying state has to be changed so that the wave packet needs longer for the oscillation through the potential well. This goal is achieved by decreasing the gradient of the potential well, which slows the population down. Consequently, our optimized potential well is less deep than the *ab initio* one. The resulting time-resolved delay-dependent KER spectrum gives excellent agreement with the experimental one, see Fig. 11.10.

Lastly, we investigated ICD in the NeKr dimer, where we focused especially on the interference effects. We also considered vibrationally selected ICD, which gave additional inside into the nuclear dynamics and interferences. Furthermore, pre-ICD in the Ar_2 dimer during a pump-probe experiment was studied and an additional source of interference was found. The nuclear dynamics during pre-ICD were analyzed.

Appendix A

Transition Amplitude of dICD via Many-Body Perturbation Theory

In this appendix, we present the complete second-order transition amplitude of our system, $T^{(2)}_{\varepsilon_k\varepsilon_{k'}ov_Aov_Bov'_B:iv_A}$, which comprises eighteen terms, and we explain how it is structured. The results presented here are also found in Ref. [64]. As mentioned in Chap. 5, the differential partial dICD decay width, as well as the corresponding transition amplitude, can also be derived by applying many-body perturbation theory [151], resulting also in Eq. (5.10). For reasons of completeness, we show here this alternative to the derivation by time-dependent second-order perturbation theory.

Since the transition between the unperturbed decaying and final state is forbidden in first order, Fermi's golden rule cannot be directly applied. Therefore, to obtain the dICD transition amplitude, we expand these states in terms of many-body perturbation theory

$$
\begin{aligned}
|\Psi_{iv_A}\rangle \quad &\approx |\Phi_{iv_A}\rangle + \frac{\hat{Q}_{iv_A}}{E^{(0)}_{iv_A} - \hat{H}_0}\hat{H}_{int}\,|\Phi_{iv_A}\rangle = |\Psi^{(0)}_{iv_A}\rangle + |\Psi^{(1)}_{iv_A}\rangle\,, \qquad \text{(A.1a)}\\
|\Psi_{\varepsilon_k\varepsilon_{k'}ov_Aov_Bov'_B}\rangle \quad &\approx |\Phi^{\varepsilon_k\varepsilon_{k'}}_{ov_Aov_Bov'_B}\rangle + \frac{\hat{Q}_{\varepsilon_k\varepsilon_{k'}ov_Aov_Bov'_B}}{E^{(0)}_{\varepsilon_k\varepsilon_{k'}ov_Aov_Bov'_B} - \hat{H}_0}\hat{H}_{int}\,|\Phi^{\varepsilon_k\varepsilon_{k'}}_{ov_Aov_Bov'_B}\rangle\\
&= |\Psi^{(0)}_{\varepsilon_k\varepsilon_{k'}ov_Aov_Bov'_B}\rangle + |\Psi^{(1)}_{\varepsilon_k\varepsilon_{k'}ov_Aov_Bov'_B}\rangle\,, \qquad \text{(A.1b)}
\end{aligned}
$$

where $\hat{Q}_{iv_A}$ and $\hat{Q}_{\varepsilon_k\varepsilon_{k'}ov_Aov_Bov'_B}$ are projectors in the configuration space of the form $\hat{Q}_{iv_A} = \mathbb{1} - |\Phi_{iv_A}\rangle\langle\Phi_{iv_A}|$ and $\hat{Q}_{\varepsilon_k\varepsilon_{k'}ov_Aov_Bov'_B} = \mathbb{1} - |\Phi^{\varepsilon_k\varepsilon_{k'}}_{ov_Aov_Bov'_B}\rangle\langle\Phi^{\varepsilon_k\varepsilon_{k'}}_{ov_Aov_Bov'_B}|$, respectively. By subtracting $|\Phi_{iv_A}\rangle$ and $|\Phi^{\varepsilon_k\varepsilon_{k'}}_{ov_Aov_Bov'_B}\rangle$ from the resolution of identity, many-body perturbation theory prevents vanishing energy denominators. The transition amplitude between the initial 1h-state $|\Psi_{iv_A}\rangle$ and the final 2p3h-state $|\Psi_{\varepsilon_k\varepsilon_{k'}ov_Aov_Bov'_B}\rangle$ becomes

$$
T^{(2)}_{\varepsilon_k\varepsilon_{k'}ov_Aov_Bov'_B:iv_A} = \langle\Phi^{\varepsilon_k\varepsilon_{k'}}_{ov_Aov_Bov'_B}|\hat{H}_{int}|\Psi^{(1)}_{iv_A}\rangle + \langle\Psi^{(1)}_{\varepsilon_k\varepsilon_{k'}ov_Aov_Bov'_B}|\hat{H}_{int}|\Phi_{iv_A}\rangle\,. \qquad \text{(A.2)}
$$

Inserting the first-order states as well as the projector operators results in

$$T^{(2)}_{\varepsilon_k\varepsilon_{k'}ov_Aov_Bov'_B:iv_A} = \sum_N \Big[\langle\Phi^{\varepsilon_k\varepsilon_{k'}}_{ov_Aov_Bov'_B}|\hat{H}_{int}\frac{|\Phi_N\rangle\langle\Phi_N| - |\Phi_{iv_A}\rangle\langle\Phi_{iv_A}|}{E^{(0)}_{iv_A} - \hat{H}_0}\hat{H}_{int}|\Phi_{iv_A}\rangle$$
$$+ \langle\Phi^{\varepsilon_k\varepsilon_{k'}}_{ov_Aov_Bov'_B}|\hat{H}_{int}\frac{|\Phi_N\rangle\langle\Phi_N| - |\Phi_{\varepsilon_k\varepsilon_{k'}ov_Aov_Bov'_B}\rangle\langle\Phi_{\varepsilon_k\varepsilon_{k'}ov_Aov_Bov'_B}|}{E^{(0)}_{\varepsilon_k\varepsilon_{k'}ov_Aov_Bov'_B} - \hat{H}_0}\hat{H}_{int}|\Phi_{iv_A}\rangle\Big]. \tag{A.3}$$

The contributing virtual states $|\Phi_N\rangle$ are 1p2h- and 2p3h-states, listed in Tabs. A.1 and A.2.

	$\sum_p$	$\sum_h$
1	$\Phi^{p}_{ov_Aov_B}$	$\Phi^{\varepsilon_k}_{ov_Ah}$
2	$\Phi^{p}_{ov_Bov'_B}$	$\Phi^{\varepsilon_k}_{ov_Bh}$
3	$\Phi^{p}_{ov'_Bov_A}$	$\Phi^{\varepsilon_k}_{ov'_Bh}$
4		$\Phi^{\varepsilon_{k'}}_{ov_Ah}$
5		$\Phi^{\varepsilon_{k'}}_{ov_Bh}$
6		$\Phi^{\varepsilon_{k'}}_{ov'_Bh}$

Table A.1: Virtual 1p2h-states which couple the initial and the final state in second order. Free index h (p) runs over all occupied (unoccupied) orbitals.

	$\sum_p$	$\sum_h$
1	$\Phi^{\varepsilon_kp}_{ov_Aov_Biv_A}$	$\Phi^{\varepsilon_k\varepsilon_{k'}}_{ov_Ahiv_A}$
2	$\Phi^{\varepsilon_kp}_{ov_Bov'_Biv_A}$	$\Phi^{\varepsilon_k\varepsilon_{k'}}_{ov_Bhiv_A}$
3	$\Phi^{\varepsilon_kp}_{ov'_Bov_Aiv_A}$	$\Phi^{\varepsilon_k\varepsilon_{k'}}_{ov'_Bhiv_A}$
4	$\Phi^{p\varepsilon_{k'}}_{ov_Aov_Biv_A}$	
5	$\Phi^{p\varepsilon_{k'}}_{ov_Bov'_Biv_A}$	
6	$\Phi^{p\varepsilon_{k'}}_{ov'_Bov_Aiv_A}$	

Table A.2: Virtual 2p3h-states which couple the initial and the final state in second order. Free index h (p) runs over all occupied (unoccupied) orbitals.

Note that one of the holes of the 2p3h-states has to be iv_A, so that only four spin-orbitals change during one transition, and the coupling to the initial 1h-state $|\Phi_{iv_A}\rangle$ via the two-particle Coulomb operator is possible. 1h-states vanish because the contribution of the averaged potential $\hat{v}^{HF}$ and the one-particle contribution of the Coulomb operator $\hat{V}$ cancel each other in Hartree-Fock approximation[219, 220]

$$\langle\Phi_n|\hat{H}_{int}|\Phi_{iv_A}\rangle = v^{HF}_{n\,iv_A} + \sum_k V_{nk[iv_A\,k]} = 0. \tag{A.4}$$

Using perturbation theory in the Hartree-Fock approximation gives an unperturbed Hamiltonian, which equals the Fock operator $\hat{H}_0 = \hat{F} = \hat{T} + \hat{W} + \hat{v}^{HF}$, where $\hat{T}$ is the kinetic-energy operator, $\hat{W}$ describes the interaction between nuclei and electrons and $\hat{v}^{HF}$ is the averaged electron potential. The interaction Hamiltonian is given by $\hat{H}_{int} = \hat{V} - \hat{v}^{HF}$, where $\hat{V}$ is the Coulomb operator. By combining the unperturbed and the interaction Hamiltonian, we get $\hat{H} = \hat{H}_0 - \hat{V} - \hat{v}^{HF} = \hat{T} + \hat{W} + \hat{V}$. It follows for the averaged potential $-\hat{v}^{HF} = \hat{T} + \hat{W} - \hat{H}_0$. The corresponding matrix elements now read $\langle \Phi_n | - \hat{v}^{HF} | \Phi_{iv_A} \rangle = \langle \Phi_n | \hat{T} + \hat{W} | \Phi_{iv_A} \rangle - \langle \Phi_n | \hat{H}_0 | \Phi_{iv_A} \rangle$. The Hartree-Fock equation [219] can be inserted for the matrix element of unperturbed Hamiltonian, which gives

$$-v^{HF}_{niv_A} = T_{niv_A} + W_{niv_A} - (T_{niv_A} + W_{niv_A} + \sum_k V_{nk[iv_Ak]}) = -\sum_k V_{nk[iv_Ak]}. \tag{A.5}$$

Consequently, $v^{HF}_{niv_A} = \sum_k V_{nk[iv_Ak]}$ and the matrix element in Eq. (A.4) vanishes. The corresponding transitions do not contribute to the transition amplitude.

The expressions of the transition amplitudes resulting from time-dependent (5.10) and time-independent many-body (A.3) perturbation theory have to be equal. Therefore, we follow the many-body perturbation theory treatment of the double Auger and SPDI processes [72, 73, 76]. We remove all 1p2h-states (see Tab. A.1) from the expansion of the initial state and all 2p3h-states (see Tab. A.2) from the expansion of the final state. This procedure is in conformity with the derivation of transition amplitudes for double Auger and SPDI. In double Auger including the corresponding 1p2h- and 2p3h-states results in negligible contributions to transition amplitudes due to large energy denominators and small Coulomb integrals. In the description of the SPDI process, the initial state contains no 1p2h configurations due to Brillouin's theorem [219], while in the final state expansion, the 2p3h configurations do not contribute because they do not couple to the ground state via the dipole operator, see App. C. If we consider the asymptotic dICD amplitude, see Eq. (3.25) in Chap. 5, this procedure for constructing the SPDI states directly translates into our approach for describing the transition amplitude of dICD.

We would also like to mention that without excluding some states from the perturbative expansions, an additional factor 2 appears in the transition amplitude because the perturbative expansions of the initial and the final state produce the same contribution.

Returning to the derivation of the transition amplitude, we insert the resolution of unperturbed states into Eq. (A.2), where only the states in Tabs. A.1 and A.2 give non-zero contributions. Evaluating the Coulomb integrals finally gives the following transition amplitude

$$T^{(2)}_{\varepsilon_k \varepsilon_{k'} \mathrm{o}v_A \mathrm{o}v_B \mathrm{o}v'_B ; i v_A}$$

$$= \sum_p \Bigg[+ \frac{V_{\varepsilon_k \, \varepsilon_{k'} \, [\mathrm{o}v'_B \, p]}}{\varepsilon_k + \varepsilon_{k'} - \varepsilon_{\mathrm{o}v'_B} - \varepsilon_p + i0^+} V_{p \, i v_A \, [\mathrm{o}v_A \, \mathrm{o}v_B]}$$

$$+ \frac{V_{\varepsilon_k \, \varepsilon_{k'} \, [\mathrm{o}v_A \, p]}}{\varepsilon_k + \varepsilon_{k'} - \varepsilon_{\mathrm{o}v_A} - \varepsilon_p + i0^+} V_{p \, i v_A \, [\mathrm{o}v_B \, \mathrm{o}v'_B]}$$

$$+ \frac{V_{\varepsilon_k \, \varepsilon_{k'} \, [\mathrm{o}v_B \, p]}}{\varepsilon_k + \varepsilon_{k'} - \varepsilon_{\mathrm{o}v_B} - \varepsilon_p + i0^+} V_{p \, i v_A \, [\mathrm{o}v'_B \, \mathrm{o}v_A]} \Bigg]$$

$$+ \sum_h \Bigg[- V_{i v_A \, \varepsilon_k \, [\mathrm{o}v_A \, h]} \frac{V_{h \, \varepsilon_{k'} \, [\mathrm{o}v_B \, \mathrm{o}v'_B]}}{\varepsilon_h + \varepsilon_{k'} - \varepsilon_{\mathrm{o}v_B} - \varepsilon_{\mathrm{o}v'_B}}$$

$$- V_{i v_A \, \varepsilon_k \, [\mathrm{o}v_B \, h]} \frac{V_{h \, \varepsilon_{k'} \, [\mathrm{o}v'_B \, \mathrm{o}v_A]}}{\varepsilon_h + \varepsilon_{k'} - \varepsilon_{\mathrm{o}v'_B} - \varepsilon_{\mathrm{o}v_A}}$$

$$- V_{i v_A \, \varepsilon_k \, [\mathrm{o}v'_B \, h]} \frac{V_{h \, \varepsilon_{k'} \, [\mathrm{o}v_A \, \mathrm{o}v_B]}}{\varepsilon_h + \varepsilon_{k'} - \varepsilon_{\mathrm{o}v_A} - \varepsilon_{\mathrm{o}v_B}}$$

$$+ V_{i v_A \, \varepsilon_{k'} \, [\mathrm{o}v_A \, h]} \frac{V_{h_B \, \varepsilon_k \, [\mathrm{o}v_B \, \mathrm{o}v'_B]}}{\varepsilon_h + \varepsilon_k - \varepsilon_{\mathrm{o}v_B} - \varepsilon_{\mathrm{o}v'_B}}$$

$$+ V_{i v_A \, \varepsilon_{k'} \, [\mathrm{o}v_B \, h]} \frac{V_{h_B \, \varepsilon_k \, [\mathrm{o}v'_B \, \mathrm{o}v_A]}}{\varepsilon_h + \varepsilon_k - \varepsilon_{\mathrm{o}v'_B} - \varepsilon_{\mathrm{o}v_A}}$$

$$+ V_{i v_A \, \varepsilon_{k'} \, [\mathrm{o}v'_B \, h]} \frac{V_{h \, \varepsilon_k \, [\mathrm{o}v_A \, \mathrm{o}v_B]}}{\varepsilon_h + \varepsilon_k - \varepsilon_{\mathrm{o}v_A} - \varepsilon_{\mathrm{o}v_B}} \Bigg]$$

$$+ \sum_p \Bigg[+ V_{i v_A \, \varepsilon_{k'} \, [\mathrm{o}v'_B \, p]} \frac{V_{p \, \varepsilon_k \, [\mathrm{o}v_A \, \mathrm{o}v_B]}}{\varepsilon_p + \varepsilon_k - \varepsilon_{\mathrm{o}v_A} - \varepsilon_{\mathrm{o}v_B}}$$

$$+ V_{i v_A \, \varepsilon_{k'} \, [\mathrm{o}v_A \, p]} \frac{V_{p \, \varepsilon_k \, [\mathrm{o}v_B \, \mathrm{o}v'_B]}}{\varepsilon_p + \varepsilon_k - \varepsilon_{\mathrm{o}v_B} - \varepsilon_{\mathrm{o}v'_B}}$$

$$+ V_{i v_A \, \varepsilon_{k'} \, [\mathrm{o}v_B \, p]} \frac{V_{p \, \varepsilon_k \, [\mathrm{o}v'_B \, \mathrm{o}v_A]}}{\varepsilon_p + \varepsilon_k - \varepsilon_{\mathrm{o}v'_B} - \varepsilon_{\mathrm{o}v_A}}$$

$$- V_{i v_A \, \varepsilon_k \, [\mathrm{o}v'_B \, p]} \frac{V_{p \, \varepsilon_{k'} \, [\mathrm{o}v_A \, \mathrm{o}v_B]}}{\varepsilon_p + \varepsilon_{k'} - \varepsilon_{\mathrm{o}v_A} - \varepsilon_{\mathrm{o}v_B}}$$

$$- V_{i v_A \, \varepsilon_k \, [\mathrm{o}v_A \, p]} \frac{V_{p \, \varepsilon_{k'} \, [\mathrm{o}v_B \, \mathrm{o}v'_B]}}{\varepsilon_p + \varepsilon_{k'} - \varepsilon_{\mathrm{o}v_B} - \varepsilon_{\mathrm{o}v'_B}}$$

$$- V_{i v_A \, \varepsilon_k \, [\mathrm{o}v_B \, p]} \frac{V_{p \, \varepsilon_{k'} \, [\mathrm{o}v'_B \, \mathrm{o}v_A]}}{\varepsilon_p + \varepsilon_{k'} - \varepsilon_{\mathrm{o}v'_B} - \varepsilon_{\mathrm{o}v_A}} \Bigg]$$

$$
\begin{aligned}
+\sum_{h}\Bigg[&+ \frac{V_{\varepsilon_k\,\varepsilon_{k'}\,[\mathrm{ov}_A\,h]}}{\varepsilon_k+\varepsilon_{k'}-\varepsilon_{\mathrm{ov}_A}-\varepsilon_h} V_{h\,i v_A\,[\mathrm{ov}_B\,\mathrm{ov}'_B]} \\
&+ \frac{V_{\varepsilon_k\,\varepsilon_{k'}\,[\mathrm{ov}_B\,h]}}{\varepsilon_k+\varepsilon_{k'}-\varepsilon_{\mathrm{ov}_B}-\varepsilon_h} V_{h\,i v_A\,[\mathrm{ov}'_B\,\mathrm{ov}_A]} \\
&+ \frac{V_{\varepsilon_k\,\varepsilon_{k'}\,[\mathrm{ov}'_B\,h]}}{\varepsilon_k+\varepsilon_{k'}-\varepsilon_{\mathrm{ov}'_B}-\varepsilon_h} V_{h\,i v_A\,[\mathrm{ov}_A\,\mathrm{ov}_B]} \Bigg]. \qquad \text{(A.6)}
\end{aligned}
$$

The total expression for the perturbative dICD transition amplitude in Eq. (A.6) is structured as follows. The first two sums feature the coupling of the initial-hole state to the 1p2h-states (as in Fig. 5.1), whereby the first sum over particle orbitals in the continuum has a singularity as explained in Chap. 5. The first sum over particle orbitals and the second over hole orbitals are the knock-out and the shake-off amplitudes, respectively. The 3rd and 4th sums correspond to the coupling to the unperturbed 2p3h-states with one hole in iv_A (as in Fig. 5.2) and belong to the ground-state-correlation mechanisms.

Appendix B

The limes $R \rightarrow \infty$ of the perturbatively derived expression for Γ_{dICD}

In the following, we want to show the perturbatively derived transition amplitude in the various processes of A and B for $R \rightarrow \infty$ in more detail than in Sec. 5.5. The here shown results are reported in Ref. [64]. Assuming a large distance R between the species makes several assumptions valid. All terms with a Coulomb integral corresponding to electron transfer, for example $\sum_p + V_{\varepsilon_k \varepsilon_{k'} [ov_A\, p]} \left(\frac{1}{\varepsilon_k + \varepsilon_{k'} - \varepsilon_{ov_A} - \varepsilon_p + i0^+} \right) V_{p\, iv_A\, [ov_B\, ov'_B]}$, can be neglected because they decay exponentially with R. The second Coulomb integral describes electron transfer independent of the localization site of p. Note that other Coulomb integrals also describe electron transfer, if the appearing sum runs only over hole or particle states of A, like in $\sum_{h_A} - V_{iv_A\, \varepsilon_k\, [ov_A\, h_A]} V_{h_A\, \varepsilon_{k'}\, [ov_B\, ov'_B]} \left(\frac{1}{\varepsilon_{h_A} + \varepsilon_{k'} - \varepsilon_{ov_B} - \varepsilon_{ov'_B}} \right)$ (compare Eq. (5.13)), while the sum of states on B by itself gives a non-vanishing contribution. If electron transfer is neglected, the Coulomb-exchange terms presenting non-local processes vanish, too. In this case, the corresponding anti-symmetrization brackets in the 4-index integrals can be skipped. We expand the interaction Coulomb operator $\hat{V}_{AB}$ (see Eq. (5.20)) and take the leading term which behaves as R^{-3}. Concerning B, only matrix elements presenting local processes are left, which are independent of R. Therefore, all leading terms are combinations of an interaction between A and B and a local process on B and scale as R^{-3}. In these approximations, the transition amplitude, Eq. (B.1), takes on the form:

$$T^{(R\rightarrow\infty)}_{\varepsilon_k \varepsilon_{k'} ov_A ov_B ov'_B; iv_A}$$

$$= \sum_{p_B} \Bigg[- \frac{V_{\varepsilon_k\, \varepsilon_{k'}\, [ov'_B\, p_B]}}{\varepsilon_k + \varepsilon_{k'} - \varepsilon_{ov'_B} - \varepsilon_{p_B} + i0^+} V_{p_B\, iv_A\, ov_B\, ov_A} + \frac{V_{\varepsilon_k\, \varepsilon_{k'}\, [ov_B\, p_B]}}{\varepsilon_k + \varepsilon_{k'} - \varepsilon_{ov_B} - \varepsilon_{p_B} + i0^+} V_{p_B\, iv_A\, ov'_B\, ov_A} \Bigg]$$

$$
\begin{aligned}
&+\sum_{h_B}\Bigg[-V_{iv_A\,\varepsilon_k\,\mathrm{ov}_A\,h_B}\frac{V_{h_B\,\varepsilon_{k'}\,[\mathrm{ov}_B\,\mathrm{ov}'_B]}}{\varepsilon_{h_B}+\varepsilon_{k'}-\varepsilon_{\mathrm{ov}_B}-\varepsilon_{\mathrm{ov}'_B}}\\
&\qquad\quad+V_{iv_A\,\varepsilon_{k'}\,\mathrm{ov}_A\,h_B}\frac{V_{h_B\,\varepsilon_k\,[\mathrm{ov}_B\,\mathrm{ov}'_B]}}{\varepsilon_{h_B}+\varepsilon_k-\varepsilon_{\mathrm{ov}_B}-\varepsilon_{\mathrm{ov}'_B}}\Bigg]\\
&+\sum_{p_B}\Bigg[+V_{iv_A\,\varepsilon_{k'}\,\mathrm{ov}_A\,p_B}\frac{V_{p_B\,\varepsilon_k\,[\mathrm{ov}_B\,\mathrm{ov}'_B]}}{\varepsilon_{p_B}+\varepsilon_k-\varepsilon_{\mathrm{ov}_B}-\varepsilon_{\mathrm{ov}'_B}}\\
&\qquad\quad-V_{iv_A\,\varepsilon_k\,\mathrm{ov}_A\,p_B}\frac{V_{p_B\,\varepsilon_{k'}\,[\mathrm{ov}_B\,\mathrm{ov}'_B]}}{\varepsilon_{p_B}+\varepsilon_{k'}-\varepsilon_{\mathrm{ov}_B}-\varepsilon_{\mathrm{ov}'_B}}\Bigg]\\
&+\sum_{h_B}\Bigg[+\frac{V_{\varepsilon_k\,\varepsilon_{k'}\,[\mathrm{ov}_B\,h_B]}}{\varepsilon_k+\varepsilon_{k'}-\varepsilon_{\mathrm{ov}_B}-\varepsilon_{h_B}}V_{h_B\,iv_A\,\mathrm{ov}'_B\,\mathrm{ov}_A}\\
&\qquad\quad-\frac{V_{\varepsilon_k\,\varepsilon_{k'}\,[\mathrm{ov}'_B\,h_B]}}{\varepsilon_k+\varepsilon_{k'}-\varepsilon_{\mathrm{ov}'_B}-\varepsilon_{h_B}}V_{h_B\,iv_A\,\mathrm{ov}_B\,\mathrm{ov}_A}\Bigg]. \qquad (\mathrm{B.1})
\end{aligned}
$$

The Coulomb integrals describing the interaction between A and B read

$$
V_{p_B iv_A h_B \mathrm{ov}_A}=\int\!\!\int \varphi^*_{iv_A}(\boldsymbol{r}^{(A)})\varphi^*_{p_B}(\boldsymbol{r}^{(B)})\,\frac{\mathrm{e}^2}{|\boldsymbol{r}^{(B)}-\boldsymbol{r}^{(A)}|}\,\varphi_{\mathrm{ov}_A}(\boldsymbol{r}^{(A)})\varphi_{h_B}(\boldsymbol{r}^{(B)})\,d\boldsymbol{r}^{(A)}d\boldsymbol{r}^{(B)}. \qquad (\mathrm{B.2})
$$

As described above, the interaction Coulomb operator can be multipole-expanded for $R \to \infty$ (see Eq. (3.5)), where the expansion is broken off after the dipol term, which is the first giving a contribution. Choosing $\boldsymbol{e_R} = \boldsymbol{e_z}$ and inserting the expansion $\hat{V}_{AB} \approx \mathrm{e}^2/R^3\big[\boldsymbol{\xi r} - 3(\boldsymbol{\xi e_R})(\boldsymbol{r e_R})\big]$ into Eq. (B.2), gives

$$
\begin{aligned}
V_{p_B iv_A h_B \mathrm{ov}_A} \approx \frac{1}{R^3}\Bigg[&\langle\varphi_{iv_A}|\hat{d}_x^{(A)}|\varphi_{\mathrm{ov}_A}\rangle\langle\varphi_{p_B}|\hat{d}_x^{(B)}|\varphi_{h_B}\rangle+\langle\varphi_{iv_A}|\hat{d}_y^{(A)}|\varphi_{\mathrm{ov}_A}\rangle\langle\varphi_{p_B}|\hat{d}_y^{(B)}|\varphi_{h_B}\rangle\\
&-2\,\langle\varphi_{iv_A}|\hat{d}_z^{(A)}|\varphi_{\mathrm{ov}_A}\rangle\langle\varphi_{p_B}|\hat{d}_z^{(B)}|\varphi_{h_B}\rangle\Bigg], \qquad (\mathrm{B.3})
\end{aligned}
$$

where $\hat{d}_x$, $\hat{d}_y$ and $\hat{d}_z$ are the components of the one-particle dipole operator. The Coulomb integrals of the form $V_{p_B iv_A h_B \mathrm{ov}_A}$ in Eq. (B.1) are replaced by the approximation of Eq. (B.3). For simplicity, we only show the transformations of the perturbative amplitude by the first term of Eq. (B.1), P_1. The procedure is analog for the other terms and thus, we can later generalize our findings to get the total transition amplitude. After inserting the expansion of the interaction Coulomb operator, P_1 becomes

$$
P_1=\frac{1}{R^3}T_1=\frac{1}{R^3}\Bigg[\langle\varphi_{iv_A}|\hat{d}_x^{(A)}|\varphi_{\mathrm{ov}_A}\rangle\,T_x^{(B)}+\langle\varphi_{iv_A}|\hat{d}_y^{(A)}|\varphi_{\mathrm{ov}_A}\rangle\,T_y^{(B)}-2\,\langle\varphi_{iv_A}|\hat{d}_z^{(A)}|\varphi_{\mathrm{ov}_A}\rangle\,T_z^{(B)}\Bigg]. \qquad (\mathrm{B.4})
$$

$T_x^{(B)}$, $T_y^{(B)}$ and $T_z^{(B)}$ can be identified as the components of the single-photon double-ionization transition amplitude (see Refs. [72, 73]) describing the knock-out mechanism

$$T_x^{(B)} = \sum_{p_B} \langle \varphi_{p_B} | \hat{d}_x^{\,(B)} | \varphi_{\mathrm{ov}_B} \rangle \frac{V_{\varepsilon_k \varepsilon_{k'} [\mathrm{ov}'_B p_B]}}{\varepsilon_k + \varepsilon_{k'} - \varepsilon_{p_B} - \varepsilon_{\mathrm{ov}'_B} + i0^+}, \tag{B.5a}$$

$$T_y^{(B)} = \sum_{p_B} \langle \varphi_{p_B} | \hat{d}_y^{\,(B)} | \varphi_{\mathrm{ov}_B} \rangle \frac{V_{\varepsilon_k \varepsilon_{k'} [\mathrm{ov}'_B p_B]}}{\varepsilon_k + \varepsilon_{k'} - \varepsilon_{p_B} - \varepsilon_{\mathrm{ov}'_B} + i0^+}, \tag{B.5b}$$

$$T_z^{(B)} = \sum_{p_B} \langle \varphi_{p_B} | \hat{d}_z^{\,(B)} | \varphi_{\mathrm{ov}_B} \rangle \frac{V_{\varepsilon_k \varepsilon_{k'} [\mathrm{ov}'_B p_B]}}{\varepsilon_k + \varepsilon_{k'} - \varepsilon_{p_B} - \varepsilon_{\mathrm{ov}'_B} + i0^+}. \tag{B.5c}$$

For an atomic system, the absolute value squared of the transition amplitude T_1 in Eq. (B.4) is averaged and summed over the spin and spatial degeneracies of the initial and the finals state, respectively.

$$\overline{|T_1|^2} = \frac{1}{2\, l_{iv_A} + 1} \frac{1}{2\, s_{iv_A} + 1} \sum_{\substack{m_{l_{iv_A}} m_{l_{\mathrm{ov}_A}} \\ m_{l_{\mathrm{ov}_B}} m_{l_{\mathrm{ov}'_B}}}} \sum_{\eta\lambda\delta\nu\mu\sigma} |T_1|^2, \tag{B.6}$$

where mixed terms vanish and quadratic terms give the same contribution, which leads to an additional factor 6 due to six quadratic terms of the transition amplitude. Therefore, we can rewrite Eq. (B.6) in terms of the z-component as

$$\overline{|T_1|^2} = 6\, \overline{| \langle \varphi_{iv_A} | \hat{d}_z^{\,(A)} | \varphi_{\mathrm{ov}_A} \rangle \, T_z^{(B)} |^2}. \tag{B.7}$$

Using the fact that the three components of the dipole operators give the same contribution, allows us to rewrite $\overline{| \langle \varphi_{iv_A} | \hat{d}_z^{\,(A)} | \varphi_{\mathrm{ov}_A} \rangle |^2} = 1/3 \overline{| \langle \varphi_{iv_A} | \hat{\boldsymbol{d}}_A | \varphi_{\mathrm{ov}_A} \rangle |^2}$ and $\overline{|T_z^{(B)}|^2} = 1/3 \overline{|\boldsymbol{T}_B|^2}$ in terms of the full dipole operators. Finally, the first term P_1 (compare Eq. (B.4)) of Eq. (B.1) reads, in its reduced form,

$$P_1 = \frac{2}{3R^6} \overline{| \langle \varphi_{iv_A} | \hat{\boldsymbol{d}}_A | \varphi_{\mathrm{ov}_A} \rangle \, \boldsymbol{T}_B |^2}. \tag{B.8}$$

Returning to the complete transition amplitude and generalizing it, gives

$$\overline{|T^{(R\rightarrow\infty)}_{\varepsilon_k \varepsilon_{k'} \mathrm{ov}_A \mathrm{ov}_B \mathrm{ov}'_B; iv_A}|^2} = \frac{2}{3R^6} \overline{| \langle \varphi_{iv_A} | \hat{\boldsymbol{d}}_A | \varphi_{\mathrm{ov}_A} \rangle \left(\boldsymbol{T}(KO) + \boldsymbol{T}(SO) + \boldsymbol{T}(GSC_p) + \boldsymbol{T}(GSC_h) \right) |^2}. \tag{B.9}$$

As shown in App. C, by using many-body perturbation theory in the present nomenclature, $\boldsymbol{T}(KO)$, $\boldsymbol{T}(SO)$, $\boldsymbol{T}(GSC_p)$ and $\boldsymbol{T}(GSC_h)$ of Eq. (B.9) are transition amplitudes (see Refs. [72, 73]) of single-photon double ionization. The four transition amplitudes belong to the different mechanisms: knock-out (KO), shake-off (SO) and ground-state correlations (GSC_p/GSC_h). The transition amplitudes read

$$\boldsymbol{T}(KO) = \sum_{p_B} \Bigg[\langle \varphi_{p_B} | \hat{\boldsymbol{d}}_B | \varphi_{\mathrm{ov}_B} \rangle \frac{V_{\varepsilon_k \, \varepsilon_{k'} \, [\mathrm{ov}'_B \, p_B]}}{\varepsilon_k + \varepsilon_{k'} - \varepsilon_{p_B} - \varepsilon_{\mathrm{ov}'_B} + i0^+} - \langle \varphi_{p_B} | \hat{\boldsymbol{d}}_B | \varphi_{\mathrm{ov}'_B} \rangle \frac{V_{\varepsilon_k \, \varepsilon_{k'} \, [\mathrm{ov}_B \, p_B]}}{\varepsilon_k + \varepsilon_{k'} - \varepsilon_{p_B} - \varepsilon_{\mathrm{ov}_B} + i0^+} \Bigg], \tag{B.10}$$

$$\boldsymbol{T}(SO) = \sum_{h_B} \Bigg[\langle \varphi_{\varepsilon_k} | \hat{\boldsymbol{d}}_B | \varphi_{h_B} \rangle \frac{V_{h_B \, \varepsilon_{k'} \, [\mathrm{ov}_B \, \mathrm{ov}'_B]}}{\varepsilon_{k'} + \varepsilon_{h_B} - \varepsilon_{\mathrm{ov}_B} - \varepsilon_{\mathrm{ov}'_B}} - \langle \varphi_{\varepsilon_{k'}} | \hat{\boldsymbol{d}}_B | \varphi_{h_B} \rangle \frac{V_{h_B \, \varepsilon_k \, [\mathrm{ov}_B \, \mathrm{ov}'_B]}}{\varepsilon_k + \varepsilon_{h_B} - \varepsilon_{\mathrm{ov}_B} - \varepsilon_{\mathrm{ov}'_B}} \Bigg], \tag{B.11}$$

$$\boldsymbol{T}(GSC_p) = \sum_{p_B} \Bigg[\langle \varphi_{\varepsilon_{k'}} | \hat{\boldsymbol{d}}_B | \varphi_{p_B} \rangle \frac{V_{p_B \, \varepsilon_k \, [\mathrm{ov}_B \, \mathrm{ov}'_B]}}{\varepsilon_k + \varepsilon_{p_B} - \varepsilon_{\mathrm{ov}_B} - \varepsilon_{\mathrm{ov}'_B}} - \langle \varphi_{\varepsilon_k} | \hat{\boldsymbol{d}}_B | \varphi_{p_B} \rangle \frac{V_{p_B \, \varepsilon_{k'} \, [\mathrm{ov}_B \, \mathrm{ov}'_B]}}{\varepsilon_{k'} + \varepsilon_{p_B} - \varepsilon_{\mathrm{ov}_B} - \varepsilon_{\mathrm{ov}'_B}} \Bigg], \tag{B.12}$$

$$\boldsymbol{T}(GSC_h) = \sum_{h_B} \Bigg[\langle \varphi_{h_B} | \hat{\boldsymbol{d}}_B | \varphi_{\mathrm{ov}'_B} \rangle \frac{V_{\varepsilon_k \, \varepsilon_{k'} \, [\mathrm{ov}_B \, h_B]}}{\varepsilon_k + \varepsilon_{k'} - \varepsilon_{\mathrm{ov}_B} - \varepsilon_{h_B}} - \langle \varphi_{h_B} | \hat{\boldsymbol{d}}_B | \varphi_{\mathrm{ov}'_B} \rangle \frac{V_{\varepsilon_k \, \varepsilon_{k'} \, [\mathrm{ov}'_B \, h_B]}}{\varepsilon_k + \varepsilon_{k'} - \varepsilon_{\mathrm{ov}_B} - \varepsilon_{h_B}} \Bigg]. \tag{B.13}$$

The transition amplitude of SPDI consists of these four processes. The corresponding single-differential partial SPDI cross section is given by

$$\frac{d\sigma_B^{++}(\omega)}{d\varepsilon_{k'}} = \frac{4\pi^2}{3} \frac{\omega}{c} \sum_{\mathrm{ov}_B \mathrm{ov}'_B} \overline{\big| \big(T(KO) + T(SO) + T(GSC_p) + T(GSC_h) \big) \big|^2}, \tag{B.14}$$

and describes the single-photon double ionization of species B for photon energy $\hbar\omega$.

Appendix C

Derivation of the SPDI transition amplitude by Many-Body Perturbation Theory

The derivation of the dICD decay width is explained in the main text Chap. 5 and the above appendices Apps. A and B in much detail. Now, we want to derive the perturbative expression of the SPDI transition amplitude, which is already well-known [72, 73], in our nomenclature for the species B. The below presented derivation is also found in Ref. [64]. As usual, the unperturbed initial and final state are Hartree-Fock ground states of B with annihilation and creation operators acting on them

$$|\Phi_0\rangle = |\Phi_0^B\rangle\,, \tag{C.1}$$

$$|\Phi_{ov_Bov'_B}^{\varepsilon_k\varepsilon_{k'}}\rangle = c_{\varepsilon_k}^{\dagger} c_{\varepsilon_{k'}}^{\dagger} c_{ov_B} c_{ov'_B} |\Phi_0^B\rangle\,, \tag{C.2}$$

where B is initially in its ground state and finally doubly ionized, the two emitted electrons being indicated by ε_k and $\varepsilon_{k'}$ and the resulting holes by ov_B and ov'_B. Again, the Hartree-Fock approximation is applied in the context of perturbation theory. The initial and final state in zeroth order give no contribution. To obtain the transition amplitude $T^{(1|1)}_{\varepsilon_k\varepsilon_{k'}ov_Bov'_B}$ of SPDI, the states have to be expanded perturbatively through first order,

$$\begin{aligned} T^{(1|1)}_{\varepsilon_k\varepsilon_{k'}ov_Bov'_B} &= \langle\Phi_{ov_Bov'_B}^{\varepsilon_k\varepsilon_{k'}}|\hat{\boldsymbol{D}}_B \frac{\hat{Q}_0}{E_0^{(0)} - \hat{H}_0^B} \hat{H}_{int}^B |\Phi_0^B\rangle \\ &+ \langle\Phi_{ov_Bov'_B}^{\varepsilon_k\varepsilon_{k'}}|\hat{H}_{int}^B \frac{\hat{Q}_{\varepsilon_k\varepsilon_{k'}ov_Bov'_B}}{E^{(0)}_{\varepsilon_k\varepsilon_{k'}ov_Bov'_B} - \hat{H}_0^B} \hat{\boldsymbol{D}}_B |\Phi_0^B\rangle\,. \end{aligned} \tag{C.3}$$

Note that $(1|1)$ is used to denote the perturbative order of the transition amplitude because the dipole operator as well as the interaction Hamiltonian involved in the expansion of the states are applied. Here, the first term corresponds to the initial-state expansion, and the second term to the final-state expansion. $\hat{Q}_0$ and $\hat{Q}^{\varepsilon_k\varepsilon_{k'}}_{ov_Bov'_B}$ are projector operators of the form $\hat{Q} = \mathbb{1} - |\Phi_0\rangle\langle\Phi_0|$ and $\hat{Q} = \mathbb{1} - |\Phi_{ov_Bov'_B}^{\varepsilon_k\varepsilon_{k'}}\rangle\langle\Phi_{ov_Bov'_B}^{\varepsilon_k\varepsilon_{k'}}|$, respectively. $\hat{\boldsymbol{D}}_B$ and $\hat{H}_{int}$ are the dipole operator and the interaction Hamiltonian of B, respectively. The resolution of the unperturbed states in the form $\mathbb{1} = \sum_N |\Phi_N\rangle \langle\Phi_N|$, where N denotes the different configurations, is inserted to achieve the explicit expression of the SPDI transition amplitude. Formally, 1p1h- and 2p2h-states can be inserted. A closer look at the initial-state expansion makes clear that only 2p2h-states give a non-vanishing contribution. Matrix elements like $\langle\Phi^{p_1}_{h_1}|\hat{H}_{int}|\Phi_0\rangle$ vanish, because in Hartree-Fock: $\langle\Phi^{p_1}_{h_1}|\hat{H}_{int}|\Phi_0\rangle = v^{HF}_{p_1 h_1} + \sum_k V_{p_1 k[h_1 k]} = 0$, as known from Brillouin's theorem [219]. In the final state expansion only 1p1h-states contribute, while for 2p2h-state terms the transition matrix elements vanish, $\langle\Phi^{\varepsilon_k\varepsilon_{k'}}_{ov_B ov'_B}|\hat{\boldsymbol{D}}_B|\Phi_0\rangle = 0$, as $\hat{\boldsymbol{D}}_B$ is a one-particle-operator. Note that the above explanation is only valid for atoms. For molecules, $\langle\Phi_0|\hat{\boldsymbol{D}}_B|\Phi_0\rangle$ is not dipole-forbidden and also contributes. This additional contribution is compensated by $\langle\Phi^{\varepsilon_k\varepsilon_{k'}}_{ov_B ov'_B}|\hat{\boldsymbol{D}}_B|\Phi^{\varepsilon_k\varepsilon_{k'}}_{ov_B ov'_B}\rangle = \langle\Phi_0|\hat{\boldsymbol{D}}_B|\Phi_0\rangle - \boldsymbol{D}_{ov_B ov_B} - \boldsymbol{D}_{ov'_B ov'_B} + \boldsymbol{D}_{\varepsilon_k\varepsilon_k} + \boldsymbol{D}_{\varepsilon_{k'}\varepsilon_{k'}}$ leading to the same result for the transition amplitude as for atoms. After inserting the resolution of unperturbed states and evaluating the respective matrix elements, one gets the following expression for the SPDI transition amplitude:

$$
\begin{aligned}
&T^{(1|1)}_{\varepsilon_k\varepsilon_{k'} ov_B ov'_B} \\
&= \sum_{p_B} \left[+ \frac{V_{\varepsilon_k\,\varepsilon_{k'}\,[ov'_B\,p_B]}}{\varepsilon_k + \varepsilon_{k'} - \varepsilon_{ov'_B} - \varepsilon_{p_B} + i0^+} \boldsymbol{D}_{p_B\,ov_B} \right. \\
&\qquad \left. - \frac{V_{\varepsilon_k\,\varepsilon_{k'}\,[ov_B\,p_B]}}{\varepsilon_k + \varepsilon_{k'} - \varepsilon_{ov_B} - \varepsilon_{p_B} + i0^+} \boldsymbol{D}_{p_B\,ov'_B} \right] \\
&+ \sum_{h_B} \left[+ \boldsymbol{D}_{\varepsilon_k\,h_B} \frac{V_{h_B\,\varepsilon_{k'}\,[ov_B\,ov'_B]}}{\varepsilon_{h_B} + \varepsilon_{k'} - \varepsilon_{ov_B} - \varepsilon_{ov'_B}} \right. \\
&\qquad \left. - \boldsymbol{D}_{\varepsilon_{k'}\,h_B} \frac{V_{h_B\,\varepsilon_k\,[ov_B\,ov'_B]}}{\varepsilon_{h_B} + \varepsilon_k - \varepsilon_{ov_B} - \varepsilon_{ov'_B}} \right] \\
&+ \sum_{p_B} \left[- \boldsymbol{D}_{\varepsilon_{k'}\,p_B} \frac{V_{p_B\,\varepsilon_k\,[ov_B\,ov'_B]}}{\varepsilon_{p_B} + \varepsilon_k - \varepsilon_{ov_B} - \varepsilon_{ov'_B}} \right. \\
&\qquad \left. + \boldsymbol{D}_{\varepsilon_k\,p_B} \frac{V_{p_B\,\varepsilon_{k'}\,[ov_B\,ov'_B]}}{\varepsilon_{p_B} + \varepsilon_{k'} - \varepsilon_{ov_B} - \varepsilon_{ov'_B}} \right] \\
&+ \sum_{h_B} \left[- \frac{V_{\varepsilon_k\,\varepsilon_{k'}\,[ov_B\,h_B]}}{\varepsilon_k + \varepsilon_{k'} - \varepsilon_{ov_B} - \varepsilon_{h_B}} \boldsymbol{D}_{h_B\,ov'_B} \right. \\
&\qquad \left. + \frac{V_{\varepsilon_k\,\varepsilon_{k'}\,[ov'_B\,h_B]}}{\varepsilon_k + \varepsilon_{k'} - \varepsilon_{ov'_B} - \varepsilon_{h_B}} \boldsymbol{D}_{h_B\,ov_B} \right] .
\end{aligned}
\tag{C.4}
$$

The first two sums arise from the final-state expansions and can be identified as knock-out and shake-off mechanisms. The knock-out terms can have singularities, because $\varepsilon_{p_B} = \varepsilon_k + \varepsilon_{k'} - \varepsilon_{ov_B}/\varepsilon_{ov'_B}$, and therefore, $+i0^+$ is inserted into the energy denominator. The last two sums come from the initial-state expansion and describe the ground-state correlations. Before the single-differential partial cross section $\frac{d\sigma_B^{++}(\omega)}{d\varepsilon_{k'}}$ is derived, one has to average over the initial-state degeneracies, which is omitted in the case of the non-degenerate ground state, and sum over the final-state degeneracies, see App. B.

Appendix D

Morse fit

The results presented here are reported in Ref. [65].

As explained in Sec. 10.1, a Morse potential is fitted to the *ab initio* PEC of the decaying state, and its parameters are then adjusted such that the computed PE spectrum reproduces best the experimentally measured one. An important characteristic of this state is its decay width $\Gamma_d(R)$, which was computed by the Fano-ADC-Stieltjes method but was also adjusted by comparing it to the experimental PE spectrum. The best agreement we find for a Morse potential with parameters $D_e = 0.16$ eV, $R_e = 3.01\,\text{Å}$, and $\alpha = 1.09$ au^{-1}, and a decay width scaled by 0.8. Due to the huge amount of parameter combinations and the sensitivity of the PE spectrum to changes in the decaying-state PEC, there are several different sets of parameters that provide a good agreement with the experiment. Here, we would like to discuss, why we chose this particular set of parameters for our working Morse potential, and how the different parameters influence the PE and KER spectra.

Let us start with why it is necessary to scale the decay width. The Fano-ADC-Stieltjes method usually overestimates the decay width [46, 210]. Due to the resulting large broadening of the vibrational energy levels, they greatly overlap, which leads to stronger interference effects. In Fig. D.1 we show a comparison between a PE spectrum computed via Eq. (8.36) for our working Morse potential, but with an unscaled decay width. To better expound the effect of the larger decay width on the PE spectrum, we do not convolve with a Gaussian to account for the experimental resolution. The spectrum is computed under the assumption that only the vibrational ground state is initially populated.

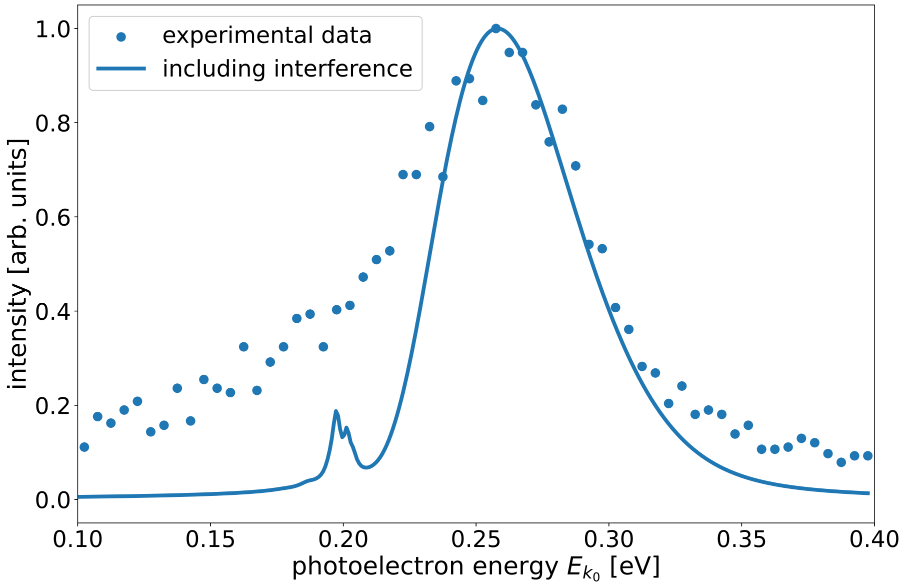

Figure D.1: Computed PE spectrum with interference effects and unscaled decay width (line) compared to experimentally measured PE spectrum taken from Ref. [100] (dots) for a photon energy of 48.68 eV. The PE spectrum is calculated by Eq. (8.36) for a NeKr dimer of the most frequently occurring isotope-mass combination in nature of 16.15 AMU (reduced mass) and scaled by its highest intensity. The population is initially in the ground state.

One can observe that besides the main peak, which agrees well with the experiment, the computed PE spectrum exhibits an additional smaller peak at lower energies, which is not observed experimentally. We note that due to the PCI effect, the low-energy part of the experimental PE spectrum exhibits a smooth tail because the faster ICD electrons overtake the slower photoelectrons, which are decelerated due to the missing shielding of the ICD electrons. As in our computations, we do not take the PCI effect into account, we use for the optimization of the decaying-state PEC V_d only the higher-energy part of the experimental spectrum. Importantly, the small peak at 0.2 eV appears solely due to the interference effects, which are suppressed if the decay width is smaller. The peak disappears if we take only 80 % of the originally computed decay width.

Now we return to the parameters, which define the Morse potential. The results of the grid search highly depend on the initial guess and the given ranges for the parameters. For the PEC, we finally use in this work, we define parameter ranges close to the Morse fit of the *ab initio* PEC. Allowing more variation of the parameters or using a slightly different starting parameter combination, lead to different results. However, as explained above, several parameter combinations give good agreement between the theoretical and experimental PE spectrum. In Fig. D.2, we present an interfering PE spectrum computed with a slightly shifted Morse potential with a narrower potential well, to which we refer in the following as alternative Morse potential ($D_e = 0.16\,\mathrm{eV}$, $R_e = 3.18\,\text{Å}$, $\alpha = 1.51\,\mathrm{au}^{-1}$ and $\mathrm{sc} = 0.8$).

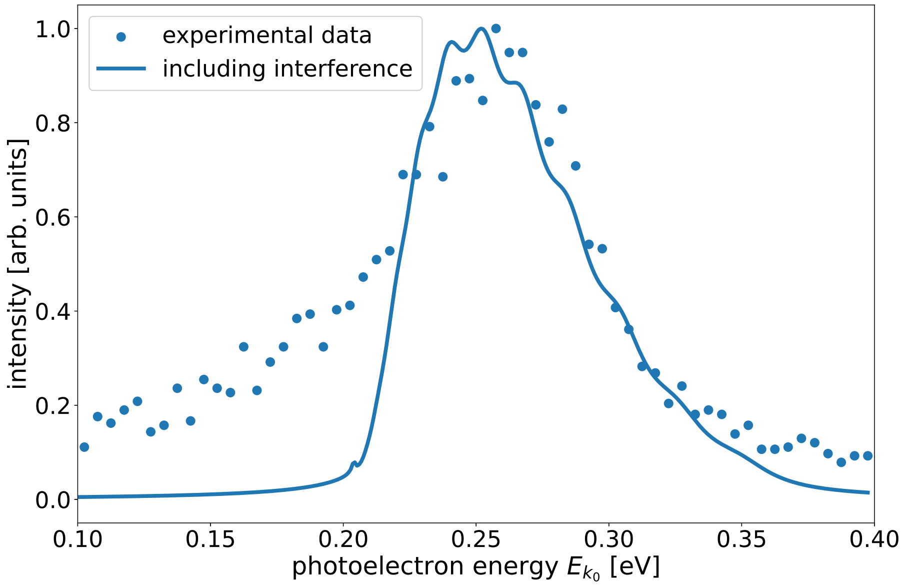

Figure D.2: Computed PE spectrum with interference effects using the alternative Morse potential (D_e = 0.16 eV, R_e = 3.18 Å, α = 1.51 au^{-1}, and sc = 0.8) compared to the experimentally measured PE spectrum taken from Ref. [100] (dots) for a photon energy of 48.68 eV. The PE spectrum is calculated by Eq. (8.36) for a NeKr dimer of the most frequently occurring isotope-mass combination in nature of 16.15 AMU (reduced mass) and scaled by its highest intensity. The population is initially in the ground state. The spectrum is not convolved by a Gaussian to preserve the good agreement between theoretical and experimental data.

Again, only the vibrational ground state of the neutral dimer is assumed to be initially populated, and we do not convolve the resulting spectrum with a Gaussian. The spectrum shows more structure, which, however, cannot be resolved experimentally. The agreement between the computed and measured spectrum is even better for the alternative Morse potential than for the working Morse potential. The PE spectrum, however, reflects only the initial step of the dynamics triggered by the Ne2s ionization. The KER spectrum of the Coulomb explosion following the ICD process is also very sensitive to the decaying-state potential, as it actually reflects the nuclear dynamics in the Ne$^+$(2s^{-1})Kr state (see, Eq. (8.48). We, therefore, should also take the KER spectrum into account when determining the optimum parameters of the decaying-state Morse potential.

Fig. D.3 shows the KER spectrum with the alternative Morse potential compared to the experimental data taken from Ref. [100]. The vibrational ground state is initially populated. The computed spectrum shows a structure at about 4.5 eV, which is not observed experimentally. We can, therefore, conclude that the PE spectrum does not contain sufficient information to fully reconstruct the decaying state PEC. A comparison between the KER spectrum computed with the alternative Morse potential and the working Morse potential, see App. F, confirms that other experimental observables such as the KER spectrum could be very useful in this case.

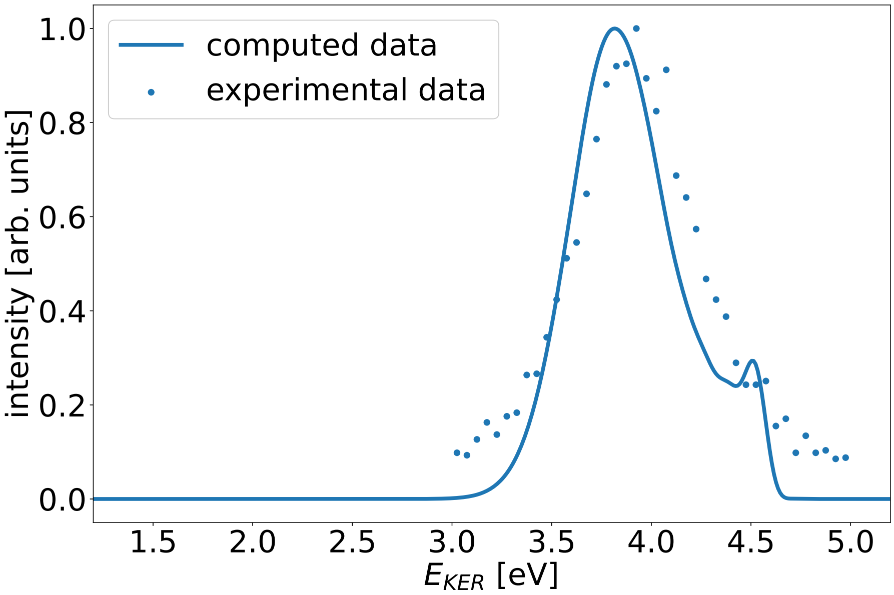

Figure D.3: Computed KER spectrum corresponding to the alternative Morse potential ($D_e = 0.16\,\mathrm{eV}$, $R_e = 3.18\,\text{Å}$, $\alpha = 1.51\,\mathrm{au}^{-1}$ and sc = 0.8) compared to experimentally measured KER spectrum taken from Ref. [100]. The KER spectrum is calculated by Eq. (8.63) for a NeKr dimer of the most frequently occurring isotope-mass combination in nature of 16.15 AMU (reduced mass) and scaled by its highest intensity. The population is initially in the ground state.

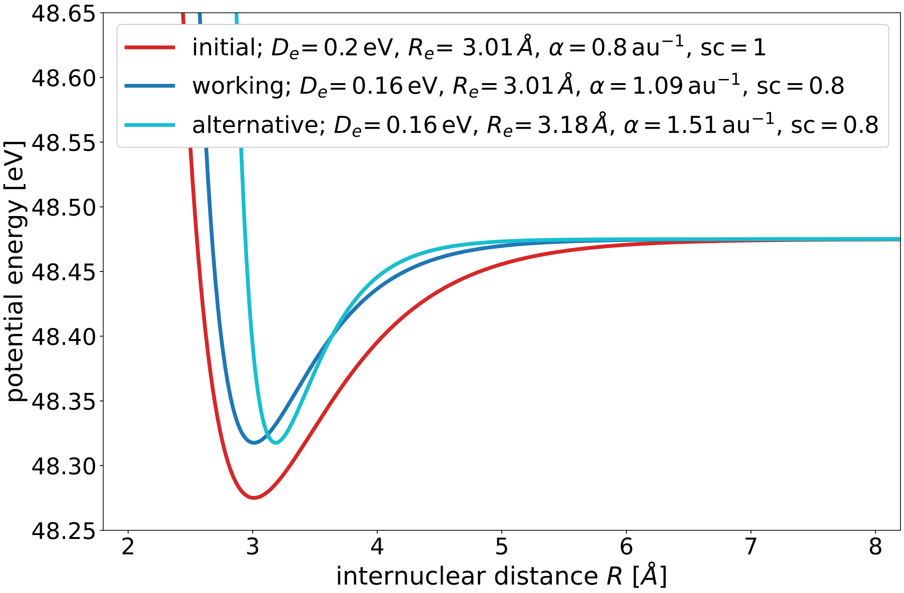

Figure D.4: PECs of the $\mathrm{Ne}^{+}(2\mathrm{s}^{-1})\mathrm{Kr}$ state for the different Morse fits. The fit to the original *ab initio* potential (red), the working Morse potential (dark blue), and the alternative Morse potential (light blue). The Morse potential is given by Eq. (10.2) and the corresponding parameters are listed in the legend.

If one compares this KER spectrum to the ones in App. F, it will seem that the spectrum is cut off at higher KER energies. A close look at the different Morse PECs immediately provides an explanation for this behavior. In Fig. D.4, the red curve is the *ab initio* PEC of the decaying state fitted by a Morse potential. We refer to it as initial Morse fit. The dark blue PEC corresponds to the working Morse potential. The light blue PEC represents the alternative Morse potential. The latter PEC belongs to the calculations of the PE and KER spectra in Fig. D.2 and Fig. D.3. Its potential-well width is only about half of that of the working Morse potential. Consequently, the wave packet cannot propagate to as small internuclear distances as it can in the case of the initial Morse fit and the working Morse potential. Therefore, the decay takes place at higher internuclear distances, which correspond to smaller KER energies.

Appendix E

Impact of isotope masses

In this appendix, we analyze the impact of the nuclear mass on the PE spectrum. The results presented here are reported in Ref. [65]. If only the vibrational ground state is initially populated, the effect of the different isotope masses on the PE spectrum is negligibly small. More interesting are the PE spectra obtained by ionizing already vibrationally excited neutral dimers (vibrationally selected PE spectrum). The results for the PE spectra of a dimer being initially in its first excited vibrational state are shown in Fig. E.1, where different isotope-mass combinations are considered.

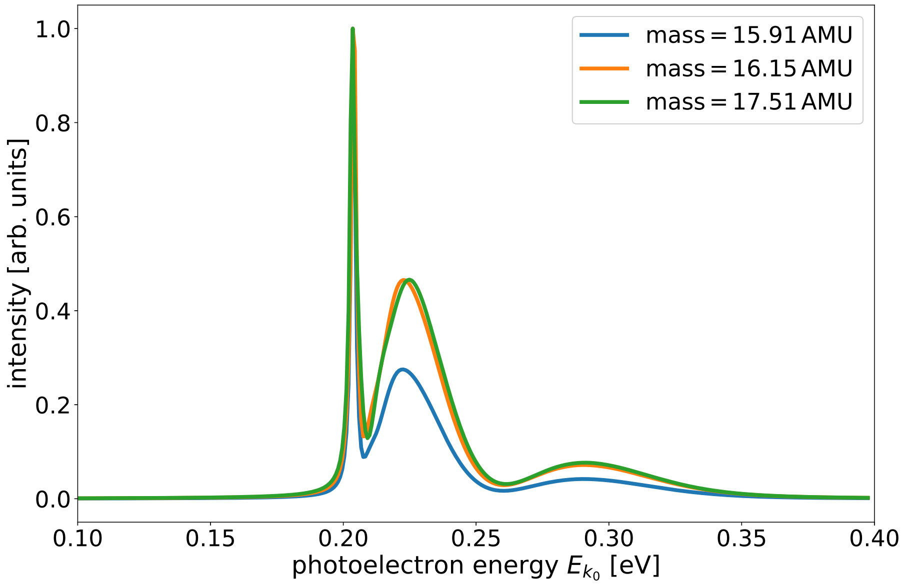

Figure E.1: Computed vibrationally selected ($\nu = 1$) PE spectra of the NeKr dimer including interference effects for different isotope-mass combinations. The lowest (blue), the highest (green), and the most frequently occurring (orange) isotope-mass combinations are shown. The corresponding reduced masses are given in the legend. The PE spectra are computed by Eq. (8.36) and scaled by their highest intensities. A photon energy of 48.68 eV is assumed.

The spectra corresponding to the lowest possible (reduced mass of 15.91 AMU), the highest possible (reduced mass 17.51 AMU), and the most frequently occurring (reduced mass 16.15 AMU) isotope-mass combinations are displayed. All spectra include interference effects and are scaled by their highest intensity value. The spectra are computed by Eq. (8.36). We see that the spectra are markedly different. One can identify three peaks, whose intensities vary depending on the isotopic combination of Ne and Kr. While the spectra for 16.15 AMU and 17.51 AMU are similar, the spectrum for the lowest isotope-mass combination of 15.91 AMU is less intense at photoelectron energies of 0.23 eV and 0.29 eV. These discrepancies demonstrate that the vibrationally selected PE spectrum can be sensitive to the isotope-mass composition of the dimer.

This high sensitivity shows that for vibrationally selected PE spectra, the usual way to take the isotope effect into account, namely to average the reduced mass (being 16.26 AMU in the present case) might not be a good approximation. Instead, one needs to compute the spectrum (Eq. (8.36)) for every isotope combination and average afterward, weighting with the natural abundance of the corresponding isotopes. In Fig. E.2, we compare the vibrationally selected ($\nu = 1$) PE spectra obtained by averaging the reduced mass (orange) and by averaging the weighted spectra of every mass combination (blue). Both spectra take interference effects into account and are scaled by their highest intensity value, respectively.

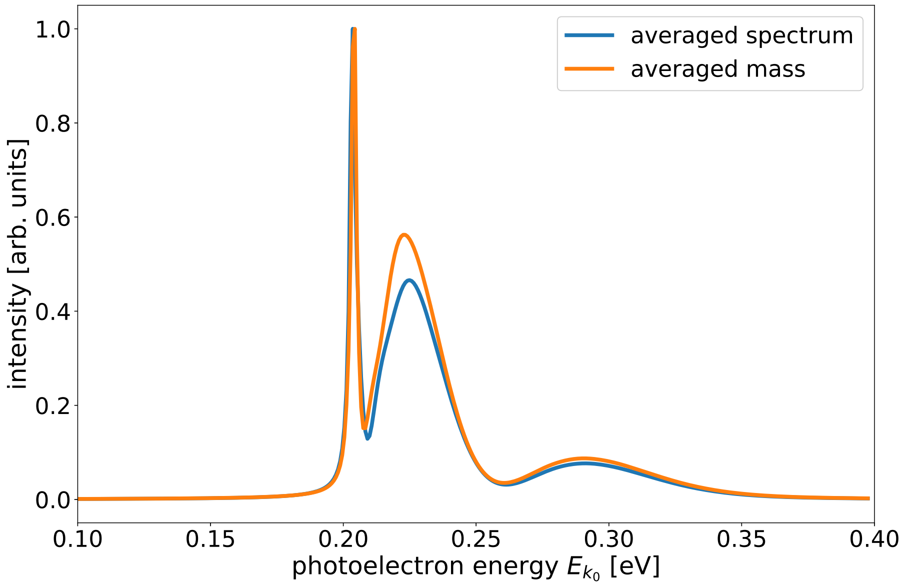

Figure E.2: Computed vibrationally selected ($\nu = 1$) PE spectra of the NeKr dimer including interference effects, obtained by averaging the reduced mass (orange) and by averaging the weighted spectra of every mass combination (blue). The average reduced mass used is 16.26 AMU. The PE spectra are computed by Eq. (8.36) and scaled by their highest intensities. A Photon energy of 48.68 eV is assumed.

The peaks at 0.21 eV and 0.29 eV of the spectrum corresponding to the averaged reduced mass and the spectrum considering all isotope-mass combinations coincide, while the peak at 0.23 eV of the spectrum approximating the mass is dominant. We see that the two averaging procedures can lead to substantial differences in peak intensities and thus for the vibrationally selected ICD processes, we cannot use the averaged reduced mass to calculate the spectra. We, therefore, used in the present work the most frequently occurring isotope combination and its reduced mass of 16.15 AMU.

Appendix F

Kinetic-Energy-Release Spectrum

The results presented here are reported in Ref. [65].

After ICD has taken place, the NeKr dimer undergoes a Coulomb explosion, where the Ne and Kr ions fly apart. The KER spectrum gives the distribution of kinetic energies of the two cations. Thereby, the KER is the difference between the final-state potential at nuclear distances of the decay and at infinity, $E_{KER} = E_{n_f} - V_f^{\infty}$. The KER spectrum, however, reflects the nuclear dynamics in the decaying state by projecting the wave packet propagating in the decaying state on the final state, see, Eq. (8.63). No interference effects in the final state appear in the KER spectrum.

In the following, we similarly proceed for the KER as for the ICD-electron spectrum, see Sec. 10.1. We report the KER spectra following a vibrationally selected ICD process, where the NeKr dimer is in one of the five vibrational levels of its electronic ground state at the moment of photoionization. The resulting KER spectra are shown in, see Fig. F.1. The KER energies lie between 1.2 eV and 5.2 eV, depending on the vibrationally selected channel. As for the ICD-electron spectrum, the KER spectrum associated with the vibrational ground state gives the highest contribution due to the most localized wave function and is therefore used for the scaling. Due to the ultrafast ICD process, the KER spectra reflect the initial vibrational wave functions and reproduce their nodal structures.

For completeness, we also report here the dependence of the KER spectra on the temperature of the NeKr dimer. As explained in Sec. 10.1, the population is statistically distributed within the vibrational levels depending on the temperature. The corresponding KER spectra at different temperatures are displayed in Fig. F.2. As for the ICD-electron spectrum, a small impact of the temperature can be observed already at 10 K. The effect increases with the increase in temperature and becomes clearly visible at 20 K, where the processes initiated from the excited vibrational states start to contribute more substantially. New peaks at 1.75 eV and 3 eV appear at higher temperatures.

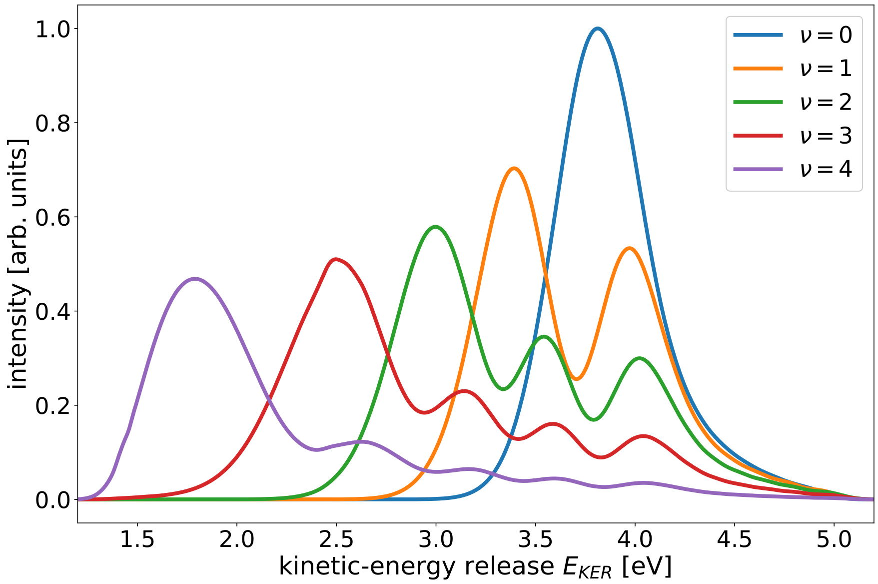

Figure F.1: Computed vibrationally selected KER spectra of the NeKr dimer. The spectra are calculated by Eq. (8.63) assuming that before the photoionization the system is in one of the five vibrational levels of the electronic ground state, $\nu = 0$ to 4. Because the spectrum, which corresponds to the initially populated vibrational ground state, is the most localized one and has consequently the highest intensity contribution, its maximum value is used for the scaling of the other spectra. The most frequently occurring isotope-mass combination of 16.15 AMU (reduced mass) is used for the computation.

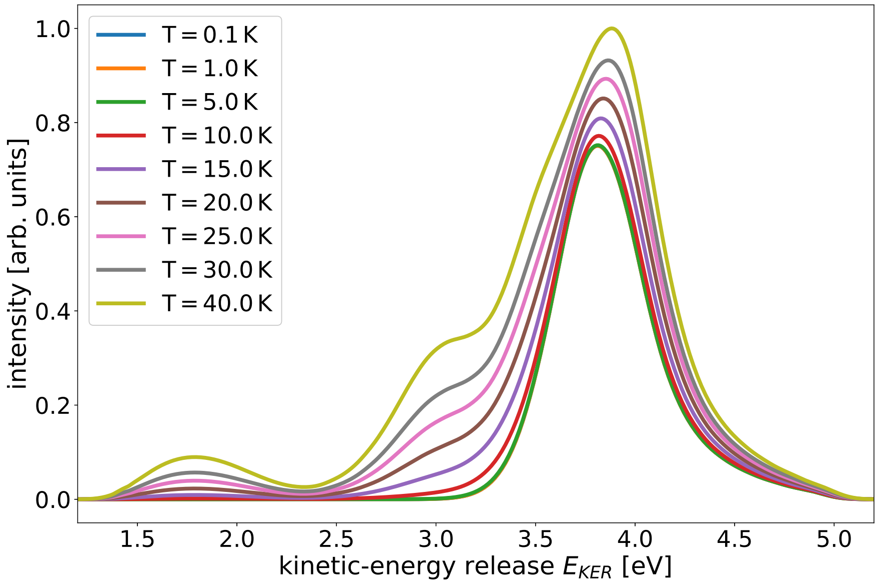

Figure F.2: Computed KER spectra of the NeKr dimer at different temperatures. The spectra are calculated by using Eq. (8.63) in combination with the Boltzman distribution explained in Sec. 10.2. The spectrum at the highest temperature has the highest maximum and is therefore used for the scaling of the spectra. The most frequently occurring isotope-mass combination of 16.15 AMU (reduced mass) is used for the computation.

List of Publications

Publications considered in this thesis

[a] J. Fedyk, K. Gokhberg, and L. S. Cederbaum, Phys. Rev. A **103**, 022816 (2021)
[b] J. Fedyk, K. Gokhberg, T. Miteva, L. S. Cederbaum, and A. I. Kuleff, Phys. Rev. A **107**, 023109 (2023)
[c] M. Han, J. Fedyk, J.-B. Ji, V. Despré, A. I. Kuleff, H. J. Wörner, arXiv:2303.04844 (2023)

Further Publications

[d] L. S. Cederbaum, J. Fedyk, arXiv:2212.07309 (2022)
[e] J. Fedyk, A. B. Voitkiv, and C. Müller, Phys. Rev. A **98**, 033418 (2018)

Bibliography

[1] L. S. Cederbaum, J. Zobeley, F. Tarantelli, *Phys. Rev. Lett.* **1997**, *79*, 4778–4781.

[2] S. Marburger, O. Kugeler, U. Hergenhahn, T. Möller, *Phys. Rev. Lett.* **2003**, *90*, 203401.

[3] T. Jahnke, A. Czasch, M. S. Schöffler, S. Schössler, A. Knapp, M. Käsz, J. Titze, C. Wimmer, K. Kreidi, R. E. Grisenti, A. Staudte, O. Jagutzki, U. Hergenhahn, H. Schmidt-Böcking, R. Dörner, *Phys. Rev. Lett.* **2004**, *93*, 163401.

[4] G. Öhrwall, M. Tchaplyguine, M. Lundwall, R. Feifel, H. Bergersen, T. Rander, A. Lindblad, J. Schulz, S. Peredkov, S. Barth, S. Marburger, U. Hergenhahn, S. Svensson, O. Björneholm, *Phys. Rev. Lett.* **2004**, *93*, 173401.

[5] V. Averbukh, P. Demekhin, P. Kolorenč, S. Scheit, S. Stoychev, A. Kuleff, Y.-C. Chiang, K. Gokhberg, S. Kopelke, N. Sisourat, L. Cederbaum, *Journal of Electron Spectroscopy and Related Phenomena* **2011**, *183*, Electron Spectroscopy Kai Siegbahn Memorial Volume, 36–47.

[6] U. Hergenhahn, *Journal of Electron Spectroscopy and Related Phenomena* **2011**, *184*, 78–90.

[7] T. Jahnke, *Journal of Physics B: Atomic Molecular and Optical Physics* **2015**, *48*, 082001.

[8] T. Jahnke, U. Hergenhahn, B. Winter, R. Dörner, U. Frühling, P. V. Demekhin, K. Gokhberg, L. S. Cederbaum, A. Ehresmann, A. Knie, A. Dreuw, *Chemical Reviews* **2020**, *120*, 11295–11369.

[9] N. Sisourat, N. V. Kryzhevoi, P. Kolorenč, S. Scheit, T. Jahnke, L. S. Cederbaum, *Nature Physics* **2010**, *6*, 508–511.

[10] T. Havermeier, T. Jahnke, K. Kreidi, R. Wallauer, S. Voss, M. Schöffler, S. Schössler, L. Foucar, N. Neumann, J. Titze, H. Sann, M. Kühnel, J. Voigtsberger, J. H. Morilla, W. Schöllkopf, H. Schmidt-Böcking, R. E. Grisenti, R. Dörner, *Phys. Rev. Lett.* **2010**, *104*, 133401.

[11] R. Santra, J. Zobeley, L. S. Cederbaum, N. Moiseyev, *Phys. Rev. Lett.* **2000**, *85*, 4490–4493.

[12] R. Santra, J. Zobeley, L. S. Cederbaum, *Phys. Rev. B* **2001**, *64*, 245104.

[13] S. Scheit, V. Averbukh, H.-D. Meyer, N. Moiseyev, R. Santra, T. Sommerfeld, J. Zobeley, L. S. Cederbaum, *The Journal of Chemical Physics* **2004**, *121*, 8393–8398.

[14] A. M. Dias, *Physica B: Condensed Matter* **2008**, *403*, 3490–3494.

[15] J. Zobeley, R. Santra, L. S. Cederbaum, *J. Chem. Phys.* **2001**, *115*, 5076–5088.

[16] A. Hans, P. Schmidt, C. Ozga, C. Richter, H. Otto, X. Holzapfel, G. Hartmann, A. Ehresmann, U. Hergenhahn, A. Knie, *The Journal of Physical Chemistry Letters* **2019**, *10*, 1078–1082.

[17] T. Ouchi, K. Sakai, H. Fukuzawa, X.-J. Liu, I. Higuchi, Y. Tamenori, K. Nagaya, H. Iwayama, M. Yao, D. Zhang, D. Ding, A. I. Kuleff, S. D. Stoychev, P. V. Demekhin, N. Saito, K. Ueda, *Phys. Rev. Lett.* **2011**, *107*, 053401.

[18] E. Fasshauer, M. Förstel, S. Pallmann, M. Pernpointner, U. Hergenhahn, *New Journal of Physics* **2014**, *16*, 103026.

[19] P. O'Keeffe, A. Ciavardini, E. Ripani, P. Bolognesi, M. Coreno, L. Avaldi, M. Devetta, M. Di Fraia, C. Callegari, K. C. Prince, R. Richter, *Phys. Rev. A* **2014**, *90*, 042508.

[20] M. Pernpointner, N. V. Kryzhevoi, S. Urbaczek, *The Journal of Chemical Physics* **2008**, *129*, 024304.

[21] F. Trinter, J. B. Williams, M. Weller, M. Waitz, M. Pitzer, J. Voigtsberger, C. Schober, G. Kastirke, C. Müller, C. Goihl, P. Burzynski, F. Wiegandt, R. Wallauer, A. Kalinin, L. P. H. Schmidt, M. S. Schöffler, Y.-C. Chiang, K. Gokhberg, T. Jahnke, R. Dörner, *Phys. Rev. Lett.* **2013**, *111*, 233004.

[22] A. Mhamdi, F. Trinter, C. Rauch, M. Weller, J. Rist, M. Waitz, J. Siebert, D. Metz, C. Janke, G. Kastirke, F. Wiegandt, T. Bauer, M. Tia, B. Cunha de Miranda, M. Pitzer, H. Sann, G. Schiwietz, M. Schöffler, M. Simon, K. Gokhberg, R. Dörner, T. Jahnke, P. V. Demekhin, *Phys. Rev. A* **2018**, *97*, 053407.

[23] H. Sann, T. Havermeier, H.-K. Kim, F. Sturm, F. Trinter, M. Waitz, S. Zeller, B. Ulrich, M. Meckel, S. Voss, T. Bauer, D. Schneider, H. Schmidt-Böcking, R. Wallauer, M. Schöffler, J. Williams, R. Dörner, T. Jahnke, *Chemical Physics* **2017**, *482*, 221–225.

[24] P. Zhang, C. Perry, T. T. Luu, D. Matselyukh, H. J. Wörner, *Phys. Rev. Lett.* **2022**, *128*, 133001.

[25] I. B. Müller, L. S. Cederbaum, *The Journal of Chemical Physics* **2006**, *125*, 204305.

[26] M. Mucke, M. Braune, S. Barth, M. Förstel, T. Lischke, V. Ulrich, T. Arion, U. Becker, A. Bradshaw, U. Hergenhahn, *Nat. Phys.* **2010**, *6*, 143–146.

[27] T. Jahnke, H. Sann, T. Havermeier, K. Kreidi, C. Stuck, M. Meckel, M. Schöffler, N. Neumann, R. Wallauer, S. Voss, A. Czasch, O. Jagutzki, A. Malakzadeh, F. Afaneh, T. Weber, H. Schmidt-Böcking, R. Dörner, *Nat. Phys.* **2010**, *6*, 139–142.

[28] P. H. P. Harbach, M. Schneider, S. Faraji, A. Dreuw, *The Journal of Physical Chemistry Letters* **2013**, *4*, 943–949.

[29] E. Alizadeh, T. M. Orlando, L. Sanche, *Annual Review of Physical Chemistry* **2015**, *66*, 379–398.

[30] X. Ren, E. Wang, A. D. Skitnevskaya, A. B. Trofimov, K. Gokhberg, A. Dorn, *Nature Physics* **2018**, *14*, 1062–1066.

[31] I. Cherkes, N. Moiseyev, *Phys. Rev. B* **2011**, *83*, 113303.

[32] A. Bande, K. Gokhberg, L. S. Cederbaum, *The Journal of Chemical Physics* **2011**, *135*, 144112.

[33] H. Agueny, M. Pesche, B. Lutet-Toti, T. Miteva, A. Molle, J. Caillat, N. Sisourat, *Phys. Rev. B* **2020**, *101*, 195431.

[34] A. Bande, *Molecular Physics* **2019**, *117*, 2014–2028.

[35] L. S. Cederbaum, A. I. Kuleff, *Nature Communications* **2021**, *12*, 4083.

[36] B. Najjari, A. B. Voitkiv, C. Müller, *Phys. Rev. Lett.* **2010**, *105*, 153002.

[37] E. Fasshauer, L. B. Madsen, *Phys. Rev. A* **2020**, *101*, 043414.

[38] C. Hoffmeister, C. Müller, A. B. Voitkiv, *Phys. Rev. A* **2022**, *105*, 042803.

[39] L. S. Cederbaum, *Phys. Rev. Lett.* **2018**, *121*, 223001.

[40] R. Santra, L. S. Cederbaum, *Phys. Rev. Lett.* **2003**, *90*, 153401.

[41] K. Kreidi, T. Jahnke, T. Weber, T. Havermeier, X. Liu, Y. Morisita, S. Schössler, L. P. H. Schmidt, M. Schöffler, M. Odenweller, N. Neumann, L. Foucar, J. Titze, B. Ulrich, F. Sturm, C. Stuck, R. Wallauer, S. Voss, I. Lauter, H. K. Kim, M. Rudloff, H. Fukuzawa, G. Prümper, N. Saito, K. Ueda, A. Czasch, O. Jagutzki, H. Schmidt-Böcking, S. Stoychev, P. V. Demekhin, R. Dörner, *Phys. Rev. A* **2008**, *78*, 043422.

[42] P. O'Keeffe, E. Ripani, P. Bolognesi, M. Coreno, M. Devetta, C. Callegari, M. Di Fraia, K. C. Prince, R. Richter, M. Alagia, A. Kivimäki, L. Avaldi, *The Journal of Physical Chemistry Letters* **2013**, *4*, 1797–1801.

[43] K. Gokhberg, P. Kolorenč, A. I. Kuleff, L. S. Cederbaum, *Nature* **2013**, *505*, 661.

[44] F. Trinter, M. S. Schöffler, H.-K. Kim, F. P. Sturm, K. Cole, N. Neumann, A. Vredenborg, J. Williams, I. Bocharova, R. Guillemin, M. Simon, A. Belkacem, A. L. Landers, T. Weber, H. Schmidt-Böcking, R. Dörner, T. Jahnke, *Nature* **2013**, *505*, 664.

[45] V. Stumpf, K. Gokhberg, L. S. Cederbaum, *Nat. Chem.* **2016**, *8*, 237–241.

[46] T. Ouchi, K. Sakai, H. Fukuzawa, I. Higuchi, P. V. Demekhin, Y.-C. Chiang, S. D. Stoychev, A. I. Kuleff, T. Mazza, M. Schöffler, K. Nagaya, M. Yao, Y. Tamenori, N. Saito, K. Ueda, *Phys. Rev. A* **2011**, *83*, 053415.

[47] I. B. Müller, L. S. Cederbaum, *The Journal of Chemical Physics* **2005**, *122*, 094305.

[48] I. Unger, R. Seidel, S. Thürmer, M. N. Pohl, E. F. Aziz, L. S. Cederbaum, E. Muchová, P. Slavíček, B. Winter, N. V. Kryzhevoi, *Nature Chemistry* **2017**, *9*, 708–714.

[49] T. Ouchi, H. Fukuzawa, K. Sakai, T. Mazza, M. Schöffler, K. Nagaya, Y. Tamenori, N. Saito, K. Ueda, *Chemical Physics* **2017**, *482*, 244–248.

[50] M. N. Pohl, C. Richter, E. Lugovoy, R. Seidel, P. Slavíček, E. F. Aziz, B. Abel, B. Winter, U. Hergenhahn, *The Journal of Physical Chemistry B* **2017**, *121*, 7709–7714.

[51] K. Gokhberg, L. S. Cederbaum, *Journal of Physics B: Atomic Molecular and Optical Physics* **2009**, *42*, 231001.

[52] K. Gokhberg, L. S. Cederbaum, *Phys. Rev. A* **2010**, *82*, 052707.

[53] A. Eckey, A. Jacob, A. B. Voitkiv, C. Müller, *Phys. Rev. A* **2018**, *98*, 012710.

[54] F. M. Pont, A. Molle, E. R. Berikaa, S. Bubeck, A. Bande, *Journal of Physics: Condensed Matter* **2019**, *32*, 065302.

[55] A. Molle, E. R. Berikaa, F. M. Pont, A. Bande, *The Journal of Chemical Physics* **2019**, *150*, 224105.

[56] K. Gokhberg, L. S. Cederbaum, *Journal of Physics B: Atomic Molecular and Optical Physics* **2009**, *42*, 231001.

[57] N. Sisourat, T. Miteva, J. D. Gorfinkiel, K. Gokhberg, L. S. Cederbaum, *Phys. Rev. A* **2018**, *98*, 020701.

[58] H.-K. Kim, H. Gassert, M. S. Schöffler, J. N. Titze, M. Waitz, J. Voigtsberger, F. Trinter, J. Becht, A. Kalinin, N. Neumann, C. Zhou, L. P. H. Schmidt, O. Jagutzki, A. Czasch, H. Merabet, H. Schmidt-Böcking, T. Jahnke, A. Cassimi, R. Dörner, *Phys. Rev. A* **2013**, *88*, 042707.

[59] A. Jacob, C. Müller, A. B. Voitkiv, *Phys. Rev. A* **2021**, *103*, 042804.

[60] J. Titze, M. S. Schöffler, H.-K. Kim, F. Trinter, M. Waitz, J. Voigtsberger, N. Neumann, B. Ulrich, K. Kreidi, R. Wallauer, M. Odenweller, T. Havermeier, S. Schössler, M. Meckel, L. Foucar, T. Jahnke, A. Czasch, L. P. H. Schmidt, O. Jagutzki, R. E. Grisenti, H. Schmidt-Böcking, H. J. Lüdde, R. Dörner, *Phys. Rev. Lett.* **2011**, *106*, 033201.

[61] S. Yan, P. Zhang, X. Ma, S. Xu, B. Li, X. L. Zhu, W. T. Feng, S. F. Zhang, D. M. Zhao, R. T. Zhang, D. L. Guo, H. P. Liu, *Phys. Rev. A* **2013**, *88*, 042712.

[62] S. Yan, P. Zhang, X. Ma, S. Xu, S. X. Tian, B. Li, X. L. Zhu, W. T. Feng, D. M. Zhao, *Phys. Rev. A* **2014**, *89*, 062707.

[63] F. Grüll, A. B. Voitkiv, C. Müller, *Phys. Rev. A* **2019**, *100*, 032702.

[64] J. Fedyk, K. Gokhberg, L. S. Cederbaum, *Phys. Rev. A* **2021**, *103*, 022816.

[65] J. Fedyk, K. Gokhberg, T. Miteva, L. S. Cederbaum, A. I. Kuleff, *Phys. Rev. A* **2023**, *107*, 023109.

[66] M. Han, J. Fedyk, J.-B. Ji, V. Despré, A. I. Kuleff, H. J. Wörner, *arXiv:2303.04844* **2023**.

[67] V. Averbukh, L. S. Cederbaum, *Phys. Rev. Lett.* **2006**, *96*, 053401.

[68] A. C. LaForge, M. Shcherbinin, F. Stienkemeier, R. Richter, R. Moshammer, T. Pfeifer, M. Mudrich, *Nat. Phys.* **2019**, *15*, 247–250.

[69] A. Eckey, A. B. Voitkiv, C. Müller, *Journal of Physics B: Atomic Molecular and Optical Physics* **2020**, *53*, 055001.

[70] J. Zhou, X. Yu, S. Luo, X. Xue, S. Jia, X. Zhang, Y. Zhao, X. Hao, L. He, C. Wang, D. Ding, X. Ren, *Nature Communications* **2022**, *13*, 5335.

[71] R. Dörner, H. Schmidt-Böcking, T. Weber, T. Jahnke, M. Schöffler, A. Knapp, M. Hattass, A. Czasch, L. Ph. H. Schmidt, O. Jagutzki, *Radiat. Phys. Chem.* **2004**, *70*, 191–206.

[72] T. N. Chang, R. T. Poe, *Phys. Rev. A* **1975**, *12*, 1432–1439.

[73] K.-i. Hino, T. Ishihara, F. Shimizu, N. Toshima, J. H. McGuire, *Phys. Rev. A* **1993**, *48*, 1271–1276.

[74] C. Pan, H. P. Kelly, *Journal of Physics B: Atomic Molecular and Optical Physics* **1995**, *28*, 5001–5012.

[75] R. Wehlitz, P. N. Jurani ć, D. V. Luki ć, *Phys. Rev. A* **2008**, *78*, 033428.

[76] M. Y. Amusia, I. S. Lee, V. A. Kilin, *Phys. Rev. A* **1992**, *45*, 4576–4587.

[77] P. Kolorenč, V. Averbukh, R. Feifel, J. Eland, *Journal of Physics B: Atomic Molecular and Optical Physics* **2016**, *49*, 082001.

[78] F. Zhou, Y. Ma, Y. Qu, *Phys. Rev. A* **2016**, *93*, 060501.

[79] Y. Ma, F. Zhou, L. Liu, Y. Qu, *Phys. Rev. A* **2017**, *96*, 042504.

[80] J. Viefhaus, A. Grum-Grzhimailo, N. Kabachnik, U. Becker, *Journal of Electron Spectroscopy and Related Phenomena* **2004**, *141*, 121–126.

[81] P. Berman, E. Arimondo, C. Lin, *Advances in Atomic, Molecular, and Optical Physics*, Elsevier Science, **2010**.

[82] R. Wehlitz, F. Heiser, O. Hemmers, B. Langer, A. Menzel, U. Becker, *Phys. Rev. Lett.* **1991**, *67*, 3764–3767.

[83] T. Hartman, P. N. Jurani ć, K. Collins, B. Reilly, E. Makoutz, N. Appathurai, R. Wehlitz, *Phys. Rev. A* **2013**, *87*, 063403.

[84] A. S. Kheifets, I. Bray, *Phys. Rev. A* **2007**, *75*, 042703.

[85] M. S. Pindzola, C. P. Ballance, S. A. Abdel-Naby, F. Robicheaux, G. S. J. Armstrong, J. Colgan, *Journal of Physics B: Atomic Molecular and Optical Physics* **2013**, *46*, 035201.

[86] F. L. Yip, T. N. Rescigno, C. W. McCurdy, *Phys. Rev. A* **2016**, *94*, 063414.

[87] J. Zeng, P. Liu, W. Xiang, J. Yuan, *Phys. Rev. A* **2013**, *87*, 033419.

[88] T. Hayaishi, E. Murakami, Y. Morioka, E. Shigemasa, A. Yagishita, F. Koike, *Journal of Physics B: Atomic Molecular and Optical Physics* **1995**, *28*, 1411–1420.

[89] R. Wehlitz, *Journal of Physics B: Atomic Molecular and Optical Physics* **2016**, *49*, 222004.

[90] V. Averbukh, I. B. Müller, L. S. Cederbaum, *Phys. Rev. Lett.* **2004**, *93*, 263002.

[91] K. Gokhberg, S. Kopelke, N. V. Kryzhevoi, P. Kolorenč, L. S. Cederbaum, *Phys. Rev. A* **2010**, *81*, 013417.

[92] C. Müller, M. A. Macovei, A. B. Voitkiv, *Phys. Rev. A* **2011**, *84*, 055401.

[93] J. L. Hemmerich, R. Bennett, S. Y. Buhmann, *Nat. Commun.* **2018**, *9*, 2934.

[94] S. Scheit, L. S. Cederbaum, H.-D. Meyer, *The Journal of Chemical Physics* **2003**, *118*, 2092–2107.

[95] K. Schnorr, A. Senftleben, M. Kurka, A. Rudenko, L. Foucar, G. Schmid, A. Broska, T. Pfeifer, K. Meyer, D. Anielski, R. Boll, D. Rolles, M. Kübel, M. F. Kling, Y. H. Jiang, S. Mondal, T. Tachibana, K. Ueda, T. Marchenko, M. Simon, G. Brenner, R. Treusch, S. Scheit, V. Averbukh, J. Ullrich, C. D. Schröter, R. Moshammer, *Phys. Rev. Lett.* **2013**, *111*, 093402.

[96] N. Moiseyev, R. Santra, J. Zobeley, L. S. Cederbaum, *The Journal of Chemical Physics* **2001**, *114*, 7351–7360.

[97] N. Sisourat, N. V. Kryzhevoi, P. Kolorenč, S. Scheit, L. S. Cederbaum, *Phys. Rev. A* **2010**, *82*, 053401.

[98] T. Havermeier, K. Kreidi, R. Wallauer, S. Voss, M. Schöffler, S. Schössler, L. Foucar, N. Neumann, J. Titze, H. Sann, M. Kühnel, J. Voigtsberger, N. Sisourat, W. Schöllkopf, H. Schmidt-Böcking, R. E. Grisenti, R. Dörner, T. Jahnke, *Phys. Rev. A* **2010**, *82*, 063405.

[99] S. Scheit, V. Averbukh, H.-D. Meyer, J. Zobeley, L. S. Cederbaum, *The Journal of Chemical Physics* **2006**, *124*, 154305.

[100] F. Trinter, T. Miteva, M. Weller, A. Hartung, M. Richter, J. B. Williams, A. Gatton, B. Gaire, J. Sartor, A. L. Landers, B. Berry, I. Ben-Itzhak, N. Sisourat, V. Stumpf, K. Gokhberg, R. Dörner, T. Jahnke, T. Weber, *Chem. Sci.* **2022**, *13*, 1789–1800.

[101] A. Niehaus, *Journal of Physics B: Atomic and Molecular Physics* **1977**, *10*, 1845–1857.

[102] F. Trinter, J. B. Williams, M. Weller, M. Waitz, M. Pitzer, J. Voigtsberger, C. Schober, G. Kastirke, C. Müller, C. Goihl, P. Burzynski, F. Wiegandt, T. Bauer, R. Wallauer, H. Sann, A. Kalinin, L. P. H. Schmidt, M. Schöffler, N. Sisourat, T. Jahnke, *Phys. Rev. Lett.* **2013**, *111*, 093401.

[103] R. Dörner, V. Mergel, O. Jagutzki, L. Spielberger, J. Ullrich, R. Moshammer, H. Schmidt-Böcking, *Physics Reports* **2000**, *330*, 95–192.

[104] F. Kaspar, W. Domcke, L. Cederbaum, *Chemical Physics* **1979**, *44*, 33–44.

[105] S. Scheit, L. S. Cederbaum, *Phys. Rev. Lett.* **2006**, *96*, 233001.

[106] T. Mizuno, P. Cörlin, T. Miteva, K. Gokhberg, A. Kuleff, L. S. Cederbaum, T. Pfeifer, A. Fischer, R. Moshammer, *The Journal of Chemical Physics* **2017**, *146*, 104305.

[107] S. Scheit, Ph.D. thesis, Ruprecht-Karls-Universität Heidelberg, **2007**.

[108] Y.-C. Chiang, Ph.D. thesis, Ruprecht-Karls-Universität Heidelberg, **2012**.

[109] E. Pahl, H.-D. Meyer, L. S. Cederbaum, *Zeitschrift für Physik D Atoms Molecules and Clusters* **1996**, *38*, 215–232.

[110] L. S. Cederbaum, F. Tarantelli, *The Journal of Chemical Physics* **1993**, *98*, 9691–9706.

[111] Y.-C. Chiang, F. Otto, H.-D. Meyer, L. S. Cederbaum, *Phys. Rev. Lett.* **2011**, *107*, 173001.

[112] Y.-C. Chiang, F. Otto, H.-D. Meyer, L. S. Cederbaum, *The Journal of Chemical Physics* **2012**, *136*, 114111.

[113] A. I. Kuleff, K. Gokhberg, S. Kopelke, L. S. Cederbaum, *Phys. Rev. Lett.* **2010**, *105*, 043004.

[114] F. Trinter, M. S. Schöffler, H.-K. Kim, F. P. Sturm, K. Cole, N. Neumann, A. Vredenborg, J. Williams, I. Bocharova, R. Guillemin, M. Simon, A. Belkacem, A. L. Landers, T. Weber, H. Schmidt-Böcking, R. Dörner, T. Jahnke, *Nature* **2014**, *505*, 664–666.

[115] K. Gokhberg, P. Kolorenč, A. I. Kuleff, L. S. Cederbaum, *Nature* **2014**, *505*, 661–663.

[116] H. Friedrich, *Theoretische Atomphysik*, Springer, 2. Edition, **1994**.

[117] I. Sobel'man, *Introduction of the Theory of Atomic Spectra*, Pergamon Press, **1972**.

[118] F. Mertins, Ph.D. thesis, Ruprecht-Karls-Universität Heidelberg, **1995**.

[119] J. C. Tully, R. S. Berry, B. J. Dalton, *Phys. Rev.* **1968**, *176*, 95–105.

[120] M.-S. Son, Y. Kiel Sung, *Chem. Phys. Lett.* **1995**, *245*, 113–118.

[121] V. Srdanov, A. Saab, D. Margolese, E. Poolman, K. Khemani, A. Koch, F. Wudl, B. Kirtman, G. Stucky, *Chem. Phys. Lett.* **1992**, *192*, 243–248.

[122] M. C. Böhm, T. Schedel-Niedrig, H. Werner, R. Schlögl, J. Schulte, J. Schütt, *Zeitschrift für Naturforschung A* **1996**, *51*, 283–298.

[123] National Institute of Standards and Technology Atomic Spectra Database, `https://www.nist.gov/pml/atomic-spectra-database`, Last Update: October 2022.

[124] P. N. Jurani ć, D. Luki ć, K. Barger, R. Wehlitz, *Phys. Rev. A* **2006**, *73*, 042701.

[125] R. Wehlitz, private communication, **2019**.

[126] A. Reinköster, S. Korica, G. Prümper, J. Viefhaus, K. Godehusen, O. Schwarzkopf, M. Mast, U. Becker, *Journal of Physics B: Atomic Molecular and Optical Physics* **2004**, *37*, 2135–2144.

[127] A. Lyras, H. Bachau, *Journal of Physics B: Atomic Molecular and Optical Physics* **2005**, *38*, 1119–1131.

[128] B. Karaçoban Usta, *Can. J. Phys.* **2019**, *97*, 828–841.

[129] A. M. Weigold, J. A. Piper, *Opt. Lett.* **1990**, *15*, 1209–1211.

[130] V. Pejcev, T. W. Ottley, D. Rassi, K. J. Ross, *J. Phys. B: At. Mol. Opt. Phys.* **1977**, *10*, 2389–2398.

[131] R. Wehlitz, J. Colgan, M. Martinez, J. Bluett, D. Lukić, S. Whitfield, *J. Electron Spectrosc. Relat. Phenom.* **2005**, *144-147*, 59–62.

[132] P. N. Jurani ć, J. Nordberg, R. Wehlitz, *Phys. Rev. A* **2006**, *74*, 042707.

[133] B. Rouvellou, L. Journel, J. M. Bizau, D. Cubaynes, F. J. Wuilleumier, M. Richter, K.-H. Selbmann, P. Sladeczek, P. Zimmermann, *Phys. Rev. A* **1994**, *50*, 4868–4876.

[134] J. A. R. Samson, W. C. Stolte, Z.-X. He, J. N. Cutler, Y. Lu, R. J. Bartlett, *Phys. Rev. A* **1998**, *57*, 1906–1911.

[135] R. Wehlitz, I. A. Sellin, O. Hemmers, S. B. Whitfield, P. Glans, H. Wang, D. W. Lindle, B. Langer, N. Berrah, J. Viefhaus, U. Becker, *Journal of Physics B: Atomic Molecular and Optical Physics* **1997**, *30*, L51–L58.

[136] R. Dörner, T. Vogt, V. Mergel, H. Khemliche, S. Kravis, C. L. Cocke, J. Ullrich, M. Unverzagt, L. Spielberger, M. Damrau, O. Jagutzki, I. Ali, B. Weaver, K. Ullmann, C. C. Hsu, M. Jung, E. P. Kanter, B. Sonntag, M. H. Prior, E. Rotenberg, J. Denlinger, T. Warwick, S. T. Manson, H. Schmidt-Böcking, *Phys. Rev. Lett.* **1996**, *76*, 2654–2657.

[137] A. S. Kheifets, I. Bray, *Phys. Rev. A* **1998**, *58*, 4501–4511.

[138] A. Kheifets, private communication, **2019**.

[139] J. Bouwman, P. Castellanos, M. Bulak, J. Terwisscha van Scheltinga, J. Cami, H. Linnartz, A. G. G. M. Tielens, *A&A* **2019**, *621*, A80.

[140] D. K. Bohme, *Chem. Rev.* **1992**, *92*, 1487–1508.

[141] Y. Xie, L. C. Ho, *ApJ* **2019**, *884*, 136.

[142] D. C. Griffin, D. M. Mitnik, N. R. Badnell, *Journal of Physics B: Atomic Molecular and Optical Physics* **2001**, *34*, 4401–4415.

[143] A. Picón, C. Buth, G. Doumy, B. Krässig, L. Young, S. H. Southworth, *Phys. Rev. A* **2013**, *87*, 013432.

[144] N. Rohringer, R. Santra, *Phys. Rev. A* **2008**, *77*, 053404.

[145] M. Coreno, L. Avaldi, R. Camilloni, K. C. Prince, M. de Simone, J. Karvonen, R. Colle, S. Simonucci, *Phys. Rev. A* **1999**, *59*, 2494–2497.

[146] M. Bartolomei, E. Carmona-Novillo, M. I. Hernandez, J. Campos-Martinez, F. Pirani, *J. Phys. Chem. C* **2013**, *117*, 10512–10522.

[147] O. Stauffert, S. Izadnia, F. Stienkemeier, M. Walter, *J. Chem. Phys.* **2019**, *150*, 244703.

[148] T. Brupbacher, H. Lüthi, A. Bauder, *Chem. Phys. Lett.* **1992**, *195*, 482–486.

[149] A. Hans, C. Küstner-Wetekam, P. Schmidt, C. Ozga, X. Holzapfel, H. Otto, C. Zindel, C. Richter, L. S. Cederbaum, A. Ehresmann, U. Hergenhahn, N. V. Kryzhevoi, A. Knie, *Phys. Rev. Research* **2020**, *2*, 012022.

[150] A. S. Davydov, *Quantum Mechanics*, Pergamon Press, 2nd Edition, **1976**.

[151] N. March, W. Young, S. Sampanther, *The Many-Body Problem in Quantum Mechanics*, Cambridge University Press, London, **1967**.

[152] D. M. Bishop in Advances in Quantum Chemistry, Academic Press, **1967**, pp. 25–59.

[153] P. V. Demekhin, A. Ehresmann, V. L. Sukhorukov, *The Journal of Chemical Physics* **2011**, *134*, 024113.

[154] C. Dal Cappello, H. Le Rouzo, *Phys. Rev. A* **1991**, *43*, 1395–1404.

[155] F. Maulbetsch, J. S. Briggs, *Journal of Physics B: Atomic Molecular and Optical Physics* **1993**, *26*, 1679.

[156] S. Keller, B. Bapat, R. Moshammer, J. Ullrich, R. M. Dreizler, *Journal of Physics B: Atomic Molecular and Optical Physics* **2000**, *33*, 1447.

[157] M. Brauner, J. S. Briggs, H. Klar, *Journal of Physics B: Atomic Molecular and Optical Physics* **1989**, *22*, 2265.

[158] J. Berakdar, H. Klar, *Journal of Physics B: Atomic Molecular and Optical Physics* **1993**, *26*, 4219.

[159] J. Berakdar, *Phys. Rev. A* **1996**, *54*, 1480–1486.

[160] S. P. Lucey, J. Rasch, C. T. Whelan, *Proceedings of the Royal Society of London. Series A: Mathematical Physical and Engineering Sciences* **1999**, *455*, 349–383.

[161] I. Bray, A. T. Stelbovics, *Phys. Rev. A* **1992**, *46*, 6995–7011.

[162] I. Bray, D. V. Fursa, A. S. Kheifets, A. T. Stelbovics, *Journal of Physics B: Atomic Molecular and Optical Physics* **2002**, *35*, R117.

[163] M. S. Pindzola, F. Robicheaux, S. D. Loch, J. C. Berengut, T. Topcu, J. Colgan, M. Foster, D. C. Griffin, C. P. Ballance, D. R. Schultz, T. Minami, N. R. Badnell, M. C. Witthoeft, D. R. Plante, D. M. Mitnik, J. A. Ludlow, U. Kleiman, *Journal of Physics B: Atomic Molecular and Optical Physics* **2007**, *40*, R39.

[164] J. Tennyson, *Physics Reports* **2010**, *491*, 29–76.

[165] A. Molle, A. Dubois, J. D. Gorfinkiel, L. S. Cederbaum, N. Sisourat, *Phys. Rev. A* **2021**, *104*, 022818.

[166] C. C. Jia, T. Kirchner, J. W. Gao, Y. Wu, J. G. Wang, N. Sisourat, *Phys. Rev. A* **2023**, *107*, 012808.

[167] J. Wragg, J. S. Parker, H. W. van der Hart, *Phys. Rev. A* **2015**, *92*, 022504.

[168] A. S. Kheifets, I. Bray, *Phys. Rev. A* **1996**, *54*, R995–R997.

[169] S. Otranto, C. R. Garibotti, *The European Physical Journal D - Atomic Molecular Optical and Plasma Physics* **2003**, *27*, 215–221.

[170] A. S. Kheifets, I. Bray, *Phys. Rev. A* **2001**, *65*, 012710.

[171] M. Foster, J. Colgan, *Journal of Physics B: Atomic Molecular and Optical Physics* **2006**, *39*, 5067.

[172] V. Averbukh, L. S. Cederbaum, *The Journal of Chemical Physics* **2005**, *123*, 204107.

[173] V. Averbukh, L. S. Cederbaum, *J. Chem. Phys.* **2006**, *125*, 094107.

[174] P. Kolorenč, N. V. Kryzhevoi, N. Sisourat, L. S. Cederbaum, *Phys. Rev. A* **2010**, *82*, 013422.

[175] S. Kopelke, K. Gokhberg, V. Averbukh, F. Tarantelli, L. S. Cederbaum, *J. Chem. Phys.* **2011**, *134*, 094107.

[176] P. Kolorenč, V. Averbukh, *J. Chem. Phys.* **2020**, *152*, 214107.

[177] A. Y. Istomin, N. L. Manakov, A. F. Starace, *Journal of Physics B: Atomic Molecular and Optical Physics* **2002**, *35*, L543–L552.

[178] S. P. Lucey, J. Rasch, C. T. Whelan, H. R. J. Walters, *Journal of Physics B: Atomic Molecular and Optical Physics* **1998**, *31*, 1237–1258.

[179] F. Maulbetsch, J. S. Briggs, *Journal of Physics B: Atomic Molecular and Optical Physics* **1994**, *27*, 4095–4104.

[180] N. V. Kryzhevoi, V. Averbukh, L. S. Cederbaum, *Phys. Rev. B* **2007**, *76*, 094513.

[181] V. Stumpf, C. Brunken, K. Gokhberg, *J. Chem. Phys.* **2016**, *145*, 104306.

[182] L. Liu, P. Kolorenč, K. Gokhberg, *Phys. Rev. A* **2020**, *101*, 033402.

[183] W. Pokapanich, N. V. Kryzhevoi, N. Ottosson, S. Svensson, L. S. Cederbaum, G. Öhrwall, O. Björneholm, *J. Am. Chem. Soc.* **2011**, *133*, 13430–13436.

[184] R. P. Madden, K. Codling, *Phys. Rev. Lett.* **1963**, *10*, 516–518.

[185] J. M. Rost, K. Schulz, M. Domke, G. Kaindl, *J. Phys. B: At. Mol. Opt. Phys.* **1997**, *30*, 4663–4694.

[186] G. Jabbari, K. Gokhberg, L. S. Cederbaum, *Chem. Phys. Lett.* **2020**, *754*, 137571.

[187] D. J. Tannor, *Introduction to Quantum Mechanics A Time-Dependent Perspective*, University Science Books, **2007**.

[188] J. R. Taylor, *Scattering Theory: The Quantum Theory on Nonrelativistic Collisions*, John Wiley & Sons, Inc., **1972**.

[189] J. N. Bardsley, A. Herzenberg, F. Mandl, *Proceedings of the Physical Society* **1966**, *89*, 321.

[190] T. F. O'Malley, *Phys. Rev.* **1966**, *150*, 14–29.

[191] L. S. Cederbaum, W. Domcke, *Journal of Physics B: Atomic and Molecular Physics* **1981**, *14*, 4665–4690.

[192] N. Moiseyev, P. Certain, F. Weinhold, *Molecular Physics* **1978**, *36*, 1613–1630.

[193] M. Beck, A. Jäckle, G. Worth, H.-D. Meyer, *Physics Reports* **2000**, *324*, 1–105.

[194] M. H. Beck, H.-D. Meyer, *Zeitschrift für Physik D Atoms Molecules and Clusters* **1997**, *42*, 113–129.

[195] H.-D. Meyer, Lecture notes in Numerical Methods of Quantum Dynamics Discrete Variable Representation (DVR) Integrators, **2017**.

[196] M. Schröder, Lecture notes in Computational Modeling in Python, **2021**.

[197] H.-D. Meyer, Lecture notes in Introduction to MCTDH, **2018**.

[198] J. C. Light, I. P. Hamilton, J. V. Lill, *The Journal of Chemical Physics* **1985**, *82*, 1400–1409.

[199] A. S. Dickinson, P. R. Certain, *The Journal of Chemical Physics* **1968**, *49*, 4209–4211.

[200] C. C. Marston, G. G. Balint-Kurti, *The Journal of Chemical Physics* **1989**, *91*, 3571–3576.

[201] D. T. Colbert, W. H. Miller, *The Journal of Chemical Physics* **1992**, *96*, 1982–1991.

[202] C. Leforestier, R. E. Wyatt, *The Journal of Chemical Physics* **1983**, *78*, 2334–2344.

[203] U. V. Riss, H.-D. Meyer, *Journal of Physics B: Atomic Molecular and Optical Physics* **1993**, *26*, 4503.

[204] U. V. Riss, H.-D. Meyer, *The Journal of Chemical Physics* **1996**, *105*, 1409–1419.

[205] R. W. Hamming, *Numerical Methods for Scientists and Engineers*, Dover Publications Inc, **1987**.

[206] D. A. Barrow, M. J. Slaman, R. A. Aziz, *The Journal of Chemical Physics* **1989**, *91*, 6348–6358.

[207] J. Schirmer, L. S. Cederbaum, O. Walter, *Phys. Rev. A* **1983**, *28*, 1237–1259.

[208] J. Schirmer, A. B. Trofimov, G. Stelter, *The Journal of Chemical Physics* **1998**, *109*, 4734–4744.

[209] J. Schirmer, A. Barth, *Zeitschrift für Physik A Atoms and Nuclei* **1984**, *317*, 267–279.

[210] P. V. Demekhin, Y.-C. Chiang, S. D. Stoychev, P. Kolorenč, S. Scheit, A. I. Kuleff, F. Tarantelli, L. S. Cederbaum, *The Journal of Chemical Physics* **2009**, *131*, 104303.

[211] P. Lablanquie, T. Aoto, Y. Hikosaka, Y. Morioka, F. Penent, K. Ito, *The Journal of Chemical Physics* **2007**, *127*, 154323.

[212] R. Thissen, P. Lablanquie, R. I. Hall, M. Ukai, K. Ito, *The European Physical Journal D - Atomic Molecular Optical and Plasma Physics* **1998**, *4*, 335–342.

[213] T. Miteva, Y.-C. Chiang, P. Kolorenč, A. I. Kuleff, K. Gokhberg, L. S. Cederbaum, *The Journal of Chemical Physics* **2014**, *141*, 064307.

[214] X. Ren, E. Jabbour Al Maalouf, A. Dorn, S. Denifl, *Nature Communications* **2016**, *7*, 11093.

[215] J. Rist, T. Miteva, B. Gaire, H. Sann, F. Trinter, M. Keiling, N. Gehrken, A. Moradmand, B. Berry, M. Zohrabi, M. Kunitski, I. Ben-Itzhak, A. Belkacem, T. Weber, A. Landers, M. Schöffler, J. Williams, P. Kolorenč, K. Gokhberg, T. Jahnke, R. Dörner, *Chemical Physics* **2017**, *482*, 185–191.

[216] N. Saito, Y. Morishita, I. Suzuki, S. Stoychev, A. Kuleff, L. Cederbaum, X.-J. Liu, H. Fukuzawa, G. Prümper, K. Ueda, *Chemical Physics Letters* **2007**, *441*, 16–19.

[217] R. Johnsen, M. A. Biondi, *Phys. Rev. A* **1978**, *18*, 996–1003.

[218] J. Ullrich, R. Moshammer, A. Dorn, R. Dörner, L. P. H. Schmidt, H. Schmidt-Böcking, *Reports on Progress in Physics* **2003**, *66*, 1463.

[219] A. Szabo, N. Ostlund, *Modern Quantum Chemistry: Introduction to Advanced Electronic Structure Theory*, Dover Publications, **2012**.

[220] J. Schirmer, *Many-Body Methods for Atoms, Molecules and Clusters*, Springer International Publishing, **2018**.

Eidesstattliche Erklärung

Ich versichere hiermit die vorgelegte Dissertation selbstständig und lediglich unter Benutzung der angegebenen Quellen und Hilfsmittel verfasst zu haben. Insbesondere habe ich wörtlich oder sinngemäß aus anderen Werken übernommene Inhalte als solche kenntlich gemacht.

Ich erkläre weiterhin, dass ich an keiner anderen Hochschule ein Prüfungsverfahren beantragt habe und dass ich die vorliegende Arbeit oder Teile davon nicht anderweitig als Prüfungsarbeit verwendet oder als Dissertation eingereicht habe.

Heidelberg, April 25th, 2023

(Jacqueline Fedyk)